UNIVERSITÀ DI PARMA

Università degli Studi di Parma

Dottorato di Ricerca in
Ingegneria Civile e Architettura

Ciclo XXXII

Mixing processes and buoyancy transport in stratified turbulent flows

Coordinatore:
Prof. Andrea Carpinteri

Supervisor:

Prof. Sandro G. Longo, PhD

Co-Supervisors:

Prof. Andrew W. Woods, PhD
Prof. Luca Chiapponi, PhD

Candidata: Diana Petrolo

Anni 2016-2019

Acknowledgments

Alla fine di questo triennio, non posso fare a meno di ringraziare il Prof. Sandro Longo, tutor della mia tesi di dottorato e paziente consigliere. Il suo supporto quotidiano è stato fondamentale per attenuare l'ansia che la realtà competitiva accademica mi trasmette. Anche se la mia indole è ancora un po' capricciosa, so che i suoi consigli sono sempre preziosi e genuini. Lui mi ha dato l'opportunità di entrare più a stretto contatto con l'Idraulica, una materia da cui, prima di allora, distoglievo sempre lo sguardo. Se il mio percorso non si è ancora concluso, non posso che sentirmi fortunata e enormemente gratificata.

A heartfelt thanks to Prof Andy Woods, who hosted me in the BP Institute for more than a year. He has been the inspiration of this work, a precious guidance, endless supply of brilliant ideas. I should thank him for his enthusiasm and numerous fruitful discussions.

I would also like to thank Lotty, Patrick and Andrew for their experimental and technical support in the laboratory, Dudley and Caroline for being always there to encourage me, and my close friends C.K., Julia, Jan and Nicola for filling my days with laughs, company and invaluable support. You all made my days brighter.

Un prezioso ringraziamento a Luca, che pazientemente mi ascolta e sopporta. È il motore delle nostre attività. Mi auguro che la luce in fondo al tunnel sia per lui in realtà molto più vicina di quanto già non immaginiamo.

Fabio e Michele, compagni di viaggio, grazie per i vostri consigli e la vostra presenza.

Alla mia famiglia e a Federico, vi voglio bene.

Abstract

This thesis attempts to increase the overall understanding of turbulent mixing by exploring the controls on the vertical buoyancy transport in a stratified turbulent Taylor-Couette flow. The inner cylinder of the tank, of radius R_1, rotates, while the outer cylinder, of radius R_2, is fixed, and the gap $\Delta R = R_2 - R_1$ is filled with fluid up to a depth H, so that the aspect ratio $H/\Delta R = 2.7 - 2.8$.

In order to simulate the global overturning circulation that perpetually carries and redistributes heat, salt and carbon between ocean basins at different rates, we conduct a series of experiments where we vary the rotation of the inner cylinder, Ω. In addition, we model rainfall and ice melting on the ocean surface by supplying a fresh water flux at the top of the tank, while the dense currents released by ice formation at the Antartica are modeled by a saline water flux supplied at the base of the tank. At the same time, we vent the same flux as the supply by two sinks located at the same depth of the respective sources. In our stylized experiments, the diapycnal mixing through isopycnal surfaces can be associated to the salt flux extracted at the top, whereas the upwelling flux can be measured by the fluid extracted at the bottom. In our experiments, we also vary the salinity of the bottom source, in order to simulate different interglacial periods.

Firstly, we found that in the *unsaturated* regime, the vertical buoyancy flux is rate-limited by the salinity of the bottom source and it depends linearly on the buoyancy frequency, N, while in the *saturated* regime, it is rate-limited by turbulence, it is independent on N and proportional to Ω^3, matching the equivalent flux through a two-layer or multi-layer stratification, or though the interfaces that spontaneously form in a linear stratified fluid, for sufficiently high initial stratification. In this thesis, we will also discuss the influence of the initial condition and of the position of the sources and sinks on the steady-state stratification, as well as the effects of a coupling between turbulence and advection on the diffusivity $\mathcal{D}$.

Secondly, we look in more detail at the mixing mechanisms responsible

for mixing and buoyancy transport across a density interface. The density interfaces are very common in the natural environment. A typical example is the thermocline, which separates the upper mixed region of the ocean from the stratified ocean interior. In our experiments, in order to prevent homogenization, we stabilize the density interface by adding a source of fresh water and a source of dense water at the top and bottom of the tank respectively. Analogously to the prior set-up, we withdraw the same volume flux as the supply by two sinks, and wait for the steady state before measuring the density and velocity field and recording videos of the visible mixing phenomena.

We find that the dominant mixing mechanism is localized at the interface and it is diffusive, as the time averaged correlation $\overline{\rho' w'}$ of density ρ' and vertical velocity w' fluctuations at the interface is a good approximation of the total vertical salt transport. We will also present the velocity and turbulence field, as well as the macro (integral) and micro (Taylor) length scales in the vertical, radial and azimuthal direction.

The mixing mechanism in a two-layer fluid also involves a single wake-like perturbation that originates at the interface, close to the inner cylinder, and spreads out radially and azimuthally, with a peak period $T_p \propto \Omega^{-1}$, and a coefficient of proportionality equal to 12π. From the shadow-graph images we infer that the mixing phenomenon, able to break the sharp gradients and to promote classical diffusion, is intermittent and lasts for approximately 40% of the peak period, causing the interface to fade away and letting parcels of intermediate density be vertically transported. Finally, we develop a model for the salt diffusivity based on diffusion inside the trailing edges of the wake.

Contents

List of Figures

List of Tables

Chapter 1

Introduction

All the pathways and energetics that drive the ocean circulation are still not fully understood. Although the global overturning circulation plays a fundamental role in the climate change and for this numerical simulations, field observations and experimental models are continuously improved, we all need to fight against expensive or time consuming facilities and the impossibility (for now) to investigate accurately all way through a 4000 m deep and 360 million km^2 wide surface.

1.1 How the ocean looks like

Figure 1.1 is a very large scale picture of the stratification of the Atlantic Ocean interior, captured across the mid-Atlantic ridge, as a result of the WOCE Hydrographic Programme (WHP). The WOCE (World Ocean Circulation Experiment) is part of the World Climate Research Programme (WCRP) and it aims at proving necessary oceanic data set about salinity, temperature and neutral density fields acquired during different series of cruises, in order to represent the state of the oceans. These data are continuously updated in order to improve the models that describe the oceanic circulation and ocean-atmosphere interactions and forecast climate changes (Sparrow et al., 2005).

The first thing to notice from figure 1.1*a* is that there are a lot of variations in salinity with depth and latitude of the ocean. Water is in general saltier in the subtropical surface region, where it is partially removed by evaporation. It can also be seen that the water in the deep Southern Ocean is quite fresh and in contact with the surface, while there is some salty water at mid to deep depths in the North Atlantic. This salty water at the inter-

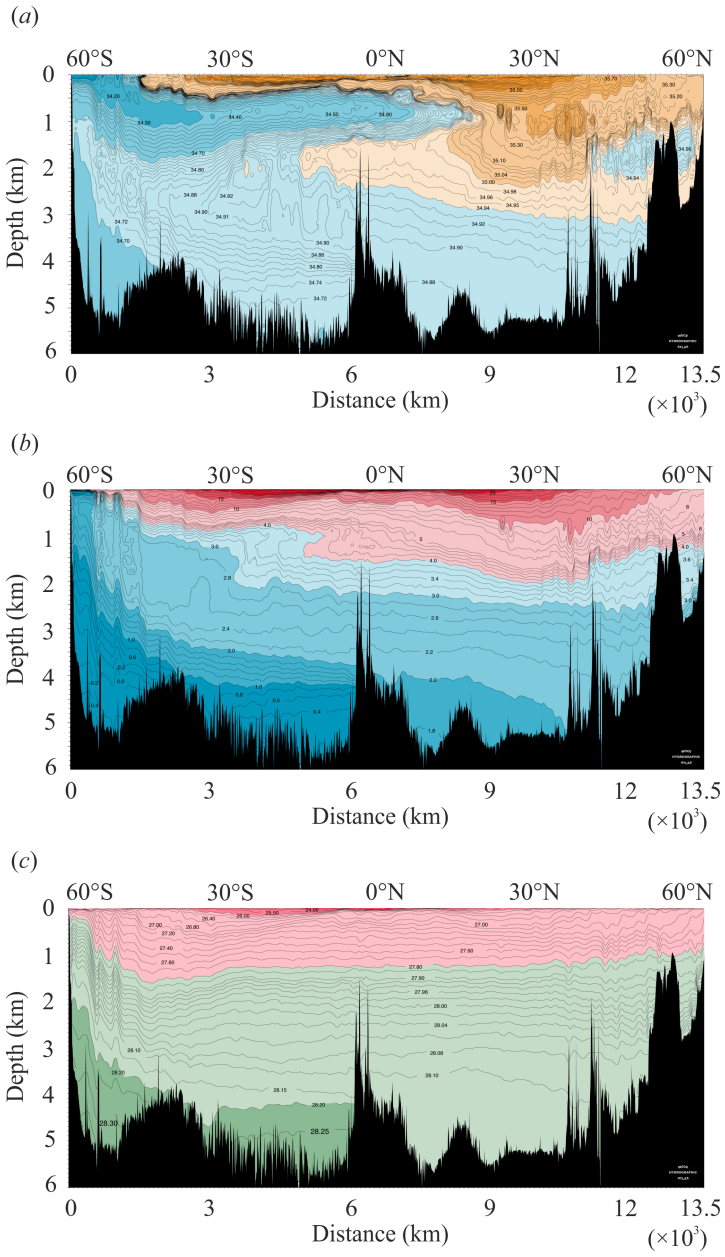

Figure 1.1: (*a*) Salinity, (*b*) potential temperature and (*c*) neutral density across the A16 30° W section of the Atlantic Sea. WOCE Atlantic Ocean Hydrographic Atlas (http://whp-atlas.ucsd.edu/atlantic/sections.htm).

mediate is a signal of the Mediterranean Sea which acts like an evaporation basin: the flow coming in from North Atlantic loses most of its water and flows out with pretty much higher salinity, it is denser than the initial flow so it starts filling intermediate depths. In terms of temperature, we can see from figure 1.1*b* that the coldest water is formed at the Southern Ocean and extends through the ocean floor. Slightly less cold water is at shallower depths in North Atlantic, while the warmest water, radiated by sunlight, is at the surface.

So in the ocean, density is not a function of just temperature but it is also influenced by salinity and compressibility (i.e. pressure). A variable that oceanographers often link to the ocean interior pattern is the neutral density, which is a function of the three state variables (salinity, temperature and pressure) and the local density gradient. If a parcel moves along the neutral density surfaces, it flows remaining neutrally buoyant, as the neutral density is conserved. In neutral density terms, the ocean is stably stratified: the densest water is at the bottom, which is indeed the coldest and not the saltiest, and the lightest water is at the top.

The neutral density surfaces are more commonly known as isopycnals and because of their near-horizontality, the stratification is almost vertical everywhere in the ocean, with the exceptions of the Southern Ocean regions where isopycnals slope up to the atmosphere (see figure 1.1*c*).

In most of the ocean, the density increases with depth monotonically. A measure of the strength of the stratification is represented by the buoyancy frequency, N, or the angular frequency of the oscillations of a displaced parcel in a stable stratified ambient fluid:

$$N = \sqrt{-\frac{g}{\rho_0}\frac{\partial \rho}{\partial z}}, \tag{1.1}$$

where g is the acceleration due to gravity, ρ_0 is a reference for density, and $\partial\rho/\partial z$ is the vertical density gradient in the ocean. N seems to reach a maximum just below the surface and then gets smaller with depth (Kang and Curchitser, 2015; Lozovatsky et al., 2015; Mashayek et al., 2017). This means that the deep ocean is more weakly stratified than the upper region, the thermocline, where the buoyancy frequency is maximum.

In the ocean there are also places that are not stably stratified: the mixing layers at the bottom and top boundary layers, expressions of strong turbulent mixing processes that lead to a relatively uniform distribution of density and temperature. The mass, momentum and heat transfer across these well-mixed layers are the dominant sources of all the small scale motions in the ocean interior. The mixing layers depth varies over different

time intervals (i.e. daily and annually) (Kara et al., 2003) and it results deeper around Antartica and in North Atlantic (De Boyer Montégut et al., 2004).

The three main surface drivers of the ocean circulation are (i) the heat flux, (ii) freshwater flux and (iii) surface wind stress. The combination of heat and freshwater flux sets the buoyancy flux at the surface ocean. Figure 1.2 represent the distribution of the mean net surface heat flux and freshwater flux on the oceanic surface, obtained by the metereological and oceanic measurements collected by the Ocean Climate Stations Project (OCS) and Pacific Marine Environmental Laboratory (PMEL).

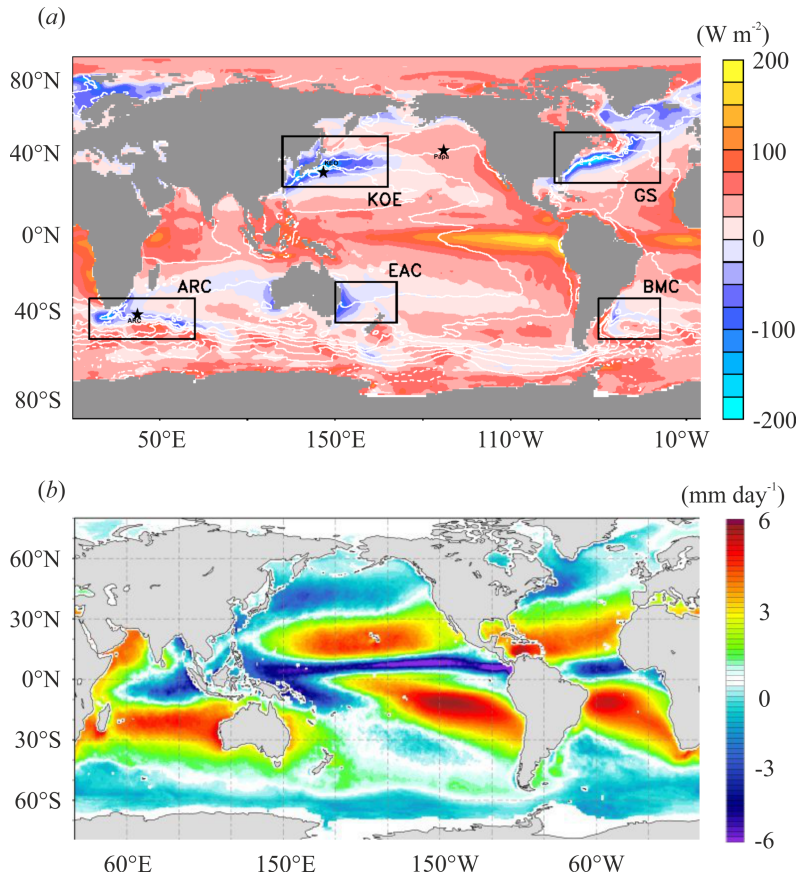

Figure 1.2: (*a*) Mean net surface heat flux (https://www.pmel.noaa.gov); (*b*) net freshwater flux (http://hoaps.cen.uni-hamburg.de).

Regarding the heat flux, in figure 1.2*a* red colors refer to heat penetrating into the ocean, while blue colors refer to heat leaving the ocean.

As we could expect, at the Equatorial regions, where there is more intense sunlight, there is a heat gain. However, this incoming heat flux is not longitudinally homogeneous: there is more heat going into the ocean near the west South America coast than Oceania. The reason is that in the East Pacific there is more cold upwelling water so there is a huge heat transfer between the atmosphere and the ocean interior. On the other hand, the western boundaries, the blue regions inside rectangles, are made of warm currents that release heat to the atmosphere.

On the other side, the freshwater flux is not affected by the salinity of the ocean underneath, and it is a primarily function of the atmospheric circulation. River run-off, ice-melting and precipitations are the most important sources of freshwater at the surface of the ocean. The dark blue regions in figure 1.2*b* represent the areas where rain and storms are more concentrated, while light blue regions where ice melts surround the Poles. In the orange regions a lot of water evaporates and leaves the ocean. There are regions of competition, in terms of buoyancy forces, between heat flux and freshwater flux. For instance, at the Equator, where heat is gained by the ocean so surface water tends to become more dense, there is also a freshwater input which makes water less dense. As a consequence, it is really hard to guess how the density field evolves in time and space.

Finally, wind stress does not affect the water buoyancy but it tends to mix surface water together with surface waves. Figure 1.3*a*-*b* is a contour plot of wind speed and direction estimated by Risien and Chelton (2008), in winter and summer respectively.

As it can be seen from figure 1.3, the wind vigorously flows eastward along the Antartic continent boundary. This wind flow is the cause that drives the Southern Ocean upwelling of dense deep currents. We shall return to this point later on in section 1.3. Generally speaking, in places where wind stress is stronger, the top mixing layer is deeper (i.e. the Antartica) (De Boyer Montégut et al., 2004).

The most important thing to highlight is that all this buoyancy forcing is limited to the surface, so once the surface water mass has its density set, advects and turns down in the ocean interior, it retains that buoyancy signal unless it meets parcels with different density with which it exchanges buoyancy.

Oxygen concentration contours are very useful in the case we would like to know how recently that amount of water approached the surface. Oxygen is entrained and dissolved into surface water by breaking waves and bubbles and lately removed by bio-geochemical processes or dispersed by mixing events associated with upwelling (Stefánsson and Richards, 1964).

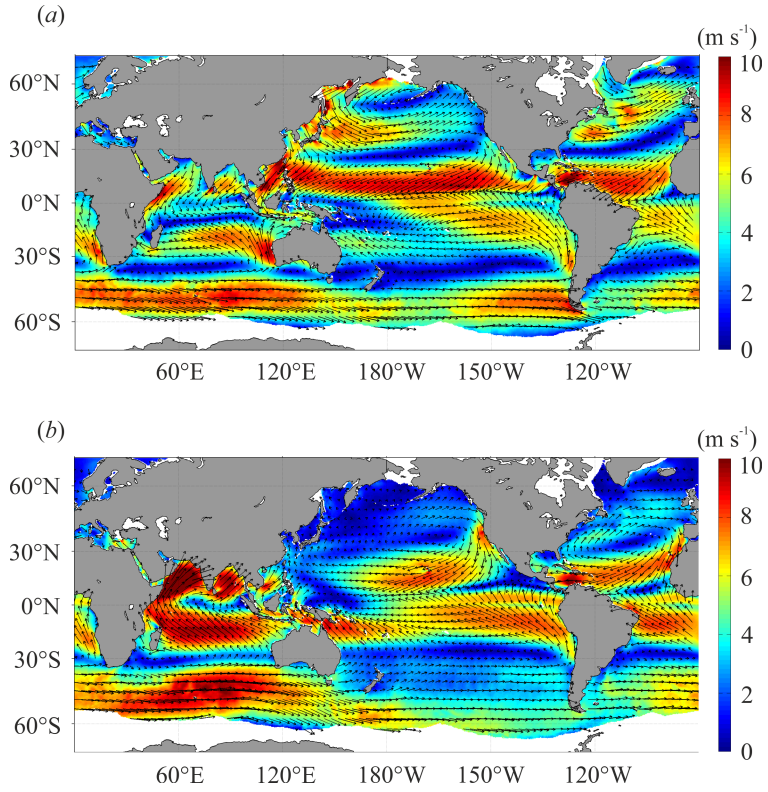

Figure 1.3: (*a*) Average wind speed in January; (*b*) average wind speed in July (Risien and Chelton, 2008).

The ocean mass that goes all way through the Atlantic interior has a much higher oxygen content (purple area) than the water above it (yellow areas), which means that the deep Atlantic water is actually much more younger than the surface (figure 1.4*a*). The densest water does not have its origin in those deep mixing layers, but rather from water that is cooled in shallower regions (i.e. the coastal shelves of Antartica). It is quite interesting to notice that Atlantic deep water is fed by mixing layers of both Northern and Southern high latitudes, while Pacific deep water is sourced by upwelled bottom water from South only. As a result, deep North Pacific has a very low oxygen content (figure 1.4b), so no deep convection occurs here, taking recently oxygenated water into the interior. In other words, the return path of the water that has sunk in the deep North Pacific, changes its density and raises up to the surface, is very slow.

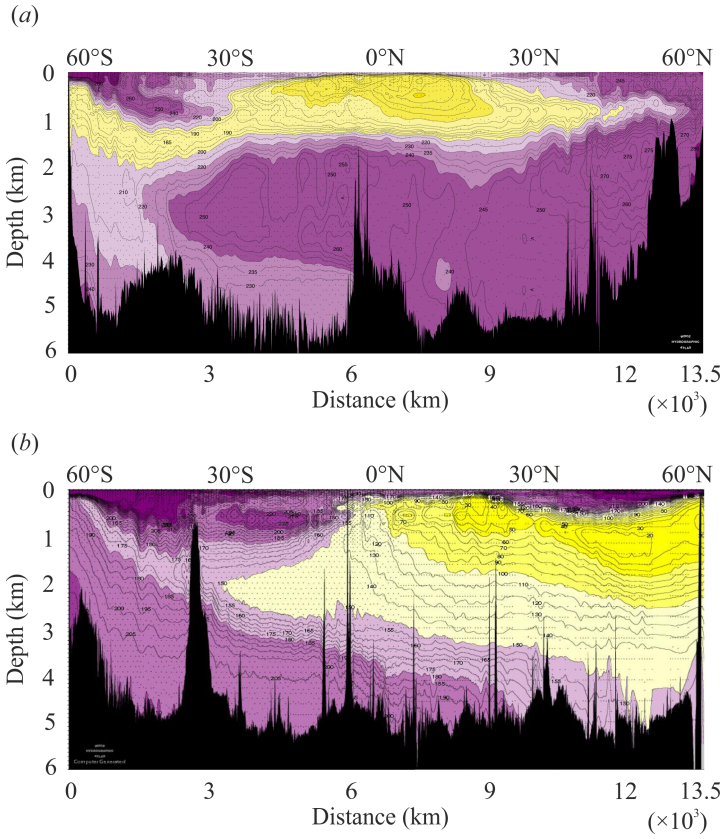

Figure 1.4: (*a*) Oxygen content in the Atlantic Ocean and (*b*) in the Pacific Ocean. Purple/yellow colours refer to high/low oxygen content. WOCE Atlantic Ocean Hydrographic Atlas.

1.2 The global overturning circulation and thermohaline circulation

The thermohaline circulation (THC) is the part of the ocean circulation that is driven by difference in density (i.e. in salinity or temperature) and it is primarily affected by heat and freshwater fluxes across the surface. THC is linked to the meridional overturning circulation (MOC), which is wind-driven instead and it can be represented by an east-west integrated streamfunction of north-south flows as a function of latitude and depth (Rahmstorf, 2006).

The global overturning circulation (GOC) is sustained by two intercon-

nected cells (Schmitz, 1995; Lumpkin and Speer, 2007; Marshall and Speer, 2012): the North Atlantic Deep Water (NADW) cell and the Antartic Bottom water (AABW) cell.

The sources of NADW cell come from the Pacific (via Drake Passage) and Indian Oceans (via Agulhas) and are composed of upwelled deep water and subducted upper water from Indian and Pacific Oceans. The upper water (thermocline and above) moves to North Atlantic, cools and sinks around Nordic Seas, Labrador Sea and Mediterranean Sea, generating NADW. The NADW moves southward flowing in the Southern Ocean, where a small branch joins the upwelling deep water in the Indian and Pacific Oceans and another branch goes back to the surface. The rest participates in the Antartic Circumpolar Current (ACC), where it reaches the sea surface and contributes to the dense water formations around Antartica.

At this point the global AABW begins. The AABW forms nearby the Antartic continental shelf after cooling processes. Cooling generates sea ice, which has lower salinity than the water it was formed from, so sea water ends up to be saltier and denser, and flows off the coastal shelves filling the bottom of the Atlantic, Pacific and Indian Oceans. Then it spreads out upwelling into the local deep water. AABW has to change its density in order to flow back up to the surface and this is where stratified mixing comes in.

Talley (2013) provides numbers for the mass and heat transports of the GOC. A total amount of 29 Sv of AABW (1 Sverdrup (Sv) = 10^6 m^3 s^{-1}) forms from 13Sv of adiabatically upwelling NADW and 16Sv of south-ward-moving IDW/PDW, Other 5 Sv of the upwelling NADW reaches the Indian Ocean, then moves to higher latitudes in the Atlantic and combines with 6 Sv of the IDW-PDW formation after AABW wind-driven upwelling. In heat transport terms, half of the heating (0.13 PW) occurs at the surface of the Southern Ocean and another half (0.13 - 0.14 PW) is due to the interior diapycnal mixing. The second half takes into account 0.23 PW of intermediate-depth diapycnal diffusion, 0.6 PW of thermocline mixing and internal wave turbulence and -0.7 PW of surface cooling.

Sandstrom's pioneering work (Sandström, 1908) suggested that, considering only buoyancy forces, a deep overturning circulation cannot be established if both the heating and cooling arise at the surface, but only if heating is situated at higher depth (i.e. larger pressure) than cooling. Although Jeffreys (1925) pointed out that diffusion should be taken into account, it should be noted that molecular processes are quite negligible, as they imply a "resident time" of 100 million years over a depth of 3 km, the effects of surface heating and freshwater fluxes on the turbulence at the

bottom boundaries are very week, so they are not sufficient to drive the entire deep water circulation. The consequence, already drawn by Sandstrom, is that mixing along the ocean ridges, where it is more intensified, involves additional mechanical energy sources that raise potential energy pulling the dense fluid upward and the light downward. Munk and Wunsch (1998) stated that, of the total amount of energy (2 TW) needed to maintain the global density distribution, about a half is provided by wind. Egbert and Ray (2000) answered to their question whether tides could provide the other half, saying that this scenario is plausible and tides dissipate not only frictionally in shallow areas around continental shelves, but also in open ocean through scattering of internal waves, induced by tidal flow, over rough topographies.

A good point to start with in order to close the energetic balance is to know the atmospheric wind patterns all over the surface and the tidal distribution, which may also change in geological times, affecting the climate and the oceanic heat transport. Some climate models try to predict the consequences of a possible switching off of the NADW formation, which will release a large freshwater input or ice-melting in the North Atlantic. The North-Atlantic sea level would rise by up to 1 meter if deep water formations are brought to a halt, the northern hemisphere would cool reaching a maximum gradient of ≈ 10 K and the southern would warm. This is probably what happened to Greenland during de-glaciation (Rahmstorf, 2006). Nevertheless, the NADW cell seems to never stop: NADW flows become shallower in cold periods at most, and the abyssal ocean is filled with AABW pushed north. After a second freshwater perturbation, NADW would moderately warm again, due to a convective rather than advective feedback of a self-sustaining process (Rahmstorf, 1994).

It is in general agreed that air-ice-sea interactions in the Artic are affected by summer meltwater: the stratification in the upper 50 m increases and the mixed-layer depth decreases, leading to stronger dissipation and weaker diffusivity. Diapycnal mixing will appreciably decrease as melt rates increase (Randelhoff et al., 2017).

1.3 How and where mixing occurs

One of the main processes that lead to stratification is diapycnal mixing (mixing across surfaces of equal density) caused by breaking of internal waves generated by wind in the surface mixing layer, tidal flows over topography, interactive processes of large-scale currents and mesoscale eddies with the ocean floor. The big issue with the parametrization of internal waves

is that they can generate in one place but propagate very far throughout the ocean and break somewhere else. A global non-local problem should be figured out, as mixing can happen both near and far from the generation site.

Before we knew much about where mixing is happening in the ocean, Walter Munk (Munk, 1966) came up with a one-dimensional estimate of the connection between downward propagation of dense and cold water and upwelling of fresher and warmer water. He knew that dense water could form in the North Atlantic or around Antartica and sink down to the ocean floor, so some return flow was expected to occur somewhere else. In the interior, away from the surface region, the density surfaces are nearly horizontal, so the upwelling is nearly vertical. Assuming that all the diffusion processes occur along the vertical direction, Munk came out with a diffusion coefficient of $\kappa = 10^{-4}\,\mathrm{m^2\,s^{-1}}$.

Firstly assuming this one-dimensional model correct, if the diffusivity coefficient is constant with depth, does it influence the upwelling? If κ is very low ($\sim 10^{-6}\,\mathrm{m^2\,s^{-1}}$), the ocean ends up with an almost stagnant deep dense water, and a very strong stratification near the surface with no mixing across density surfaces. Since the ocean is both heated and cooled at the surface, in the limit of very small and uniform diffusivity, the whole ocean would fill with cold fluid, with only a thin layer of warm water at the top. If κ is a little bit larger, ($\sim 10^{-5}\,\mathrm{m^2\,s^{-1}}$), the overturning circulation is strong enough to modify the density of the water near the bottom of the sea, but still smaller than the wind-driven circulation. The stratification extends further down into the interior and it is more diffused. If $\kappa \sim 10^{-4}\,\mathrm{m^2\,s^{-1}}$, the overturning is more intense and the stratification is deeper as they are controlled by both dyapicnal mixing and winds (Nikurashin and Vallis, 2011).

However, although Munk's value is still adopted as a basin-wide spatial avarage (Munk and Wunsch, 1998), this estimate is much larger than observed in most of the ocean interior and much lower than bottom rough boundaries. Smaller values of $\mathcal{O}\left(10^{-5}\right)$ are justified over abyssal plains and smooth structures, while two-order of magnitude higher values occur over rough bottom topography and ridges (Wunsch and Ferrari, 2004; Lumpkin and Speer, 2007; Waterhouse et al., 2014). Moreover, right along the bottom boundary layer (BBL), mixing vanishes. Water parcels become lighter and start flowing upward. Because the BBL is sloped, this diapycnal up-welling flow has a vertical velocity component that must be greater than the interior sinking in order to allow abyssal water to rise towards the sea surface in the net. On this basis, what happens if we assume that the diffusivity increases towards the bottom and rapidly decreases to zero right at the bottom? Up-

welling of lightened water masses occur at the side walls, down-welling in the interior and the net conversion is a small residual if the boundary is sloped. In contrast, simpler models with constant diffusivity in the ocean interior and vertical side walls suggest upwelling throughout the ocean, with hardly any abyssal stratification. In this limit, the internal wave field and the associated mixing would disappear, which is not consistent with observations (Ferrari et al., 2016).

Diapycnal mixing is not the only process that drives the deepwater masses upwelling, but also the winds blowing over the Southern Ocean, known as the Roaring Forties. What is special about this place is that the latitude band surrounding Antartica, crossing the Drake Passage between South America and Antartica, is the only horizontal ring of the Earth, with the exception of the Artica, with no topographic barriers down to a depth of about 2500 m. The zonally averaged zonal pressure gradient must be zero, so no geostrophic flow can be sustained. The only potential energy required for mixing is supplied in the bottom 2000 m (the characteristic height of the major ocean ridges), then the Roaring Forties lift water up to the surface along surfaces of constant density, requiring no mixing (Kuhlbrodt et al., 2007; Ferrari, 2014).

This upwelling branch of the MOC governs the communication between deep and shallow waters. During glacial periods, the upwelling rate is reduced, maybe due to the increase of sea ice cover or Southern wind shifting equatorward, leading to a more salty and stratified ocean and accumulation of CO_2 at the bottom. On the opposite, a huge amount of CO_2 released to the atmosphere is a symptom of a large exchange between deep ocean and the atmosphere and contributes to the global warming (Marshall and Speer, 2012). What is more, westerlies are strongly dependent on the temperature difference in the middle of the atmosphere, rather than at the surface. CO_2 warms the tropical and subtropical surface and cools the the envelope of cold air above, increasing the thermal contrast and consequently, the strength of the wind and the overturning (Toggweiler and Russell, 2008).

1.4 Climate Change

The natural environment - both oceans and lands - has been affected by climate changes, which mainly derive from the increasing emissions of greenhouse gases since the industrial revolution.

The main consequence of the increasing level of CO_2 is the global warming, which has had a grater impact on lands rather than waters. Over the last 10 years (1998-2018) the average temperature on lands was approxi-

mately 1.5°C higher than the previous decade, and more than 0.5°C higher than the global mean temperature change. This global warming has implicated a change in the precipitation pattern and in the start/end of the crop growing season. Desertification of many lands and tree destruction were caused by unavailability of freshwater. Moreover, the current extension of lands has been undergoing a human abuse. The amount of daily food calories per person has grown consistently and so the water for irrigation, inorganic nitrogen fertilizer and livestock farming activities. Cropland even extend to 12-14% of the glacial ice-free surface (Pachauri et al., 2014).

On the other hand, more than 90% of the increased energy stored in the climate system is controlled by the ocean warming, which is concentrated in the upper 75 m close to the sea surface. The increase of oceanic temperature has led to an increase in salinity of salty water where evaporation is intense and a decrease in salinity in areas of fresher waters. Greenland and Antartic ice has been melting at a higher rate and the Artic sea-ice extend is also reducing more rapidly in the last 40 years. The ocean also entrains CO_2 which has contributed to an increase of 26% of the ocean acidification (Pachauri et al., 2014).

Other extreme events connected to climate change like heat waves, cycloneas and wildfires also have a significant impact on ecosystems and human activity.

Reduction of greenhouse-gases emissions and mitigation-adaptation approaches can limit the risks of climate change, but only under cooperative political and societal policies, as no single option is sufficient by itself and every single person is wholeheartedly invited to save the planet. The Intergovernmental Panel on Climate Change (ICPP) is currently in its Sixth Assessment cycle and is working on the Sixth Assessment Report (AR6) which will be finalizes in 2022.

1.5 Thesis Outline

As we have seen above, the pathways of the ocean circulation are very complex as they involve upwelling of deep waters to the sea surface, sinking of dense water to the ocean floor and variegate mixing phenomena between such flows.

The aim of the first part of this thesis is to study the vertical buoyancy transport in a stable stratified turbulent flow, in order to model the partitioning between the upwelling and the diapycnal mixing under different climate conditions.

To this end, we firstly generate non invasive turbulence in a Taylor-Couette tank, which consists of a steady outer cylinder and a rotating inner cylinder. We fill the annulus with fluid which reproduces the ocean interior. We then supply a flux of fresh water at the top of the tank to simulate rain-fall and river run-off, and a flux of saline fluid at the bottom of the tank to simulate dense water forming after ice formation at the poles. In our experiments, we vary the rotation rate of the inner cylinder in order to test different turbulent levels and the salinity of the bottom source of fluid to test different levels of external buoyancy forces. In order to maintain a constant volume in the tank, we also introduce two sinks, one at the top and one at the bottom of the tank. Once we turn on the sources and sinks of fluid, we wait for the steady state condition. In equilibrium, the vertical buoyancy transport will lead to a certain density stratification in the fluid and the vertical transport of salt will be extracted by the sink at the top of the tank. This flux could represent the diapycnal mixing. On the other hand, the flux extracted at the bottom can be a measure of the flux that is lifted up without any change in density (i.e. the upwelling flux). This experimental model is rather simplified, as between upwelling and ambient fluid there could be diapycnal mixing and the density of the upwelling fluid may indeed vary over long time. In our experiments, we also change the initial stratification of the fluid (well mixed, linear stratified or multi-layer stratified) in order to understand how the initial state of the ocean could be modified by diverse climate conditions or turbulent intensities. We also study how the mixing efficiency could depend on the density stratification and velocity length-scale of the fluid.

Secondly, we study the total vertical buoyancy flux in some turbulent-advective scenarios, by unbalancing the flow rate of the two sinks. If the flow rate of the top sink is greater than the bottom, the external advection is positive (upward) and vice versa.

Finally we devote attention to the dye dispersion in the vertical direction by adding dye to the bottom source fluid.

I carried out this part of the thesis at the British Petroleum Institute (BP Institute) and Bullard Laboratories, Department of Earth Science, University of Cambridge, under the supervision of Prof. Andrew W. Woods.

The second part of this thesis aims at the study of the density and velocity field in a two-layer fluid in steady state condition, in a turbulent Taylor-Couette flow. In order to stabilize the density difference between the two layers of fluid, we supply a source of fresh water at the top and a source of very salty water at the bottom of the tank, analogously to previous experiments. We use a set of Ultrasound Velocity Profilers aligned in the vertical,

radial and azimuthal direction to reconstruct the three dimensional velocity field and understand where the main mixing events occur. We evaluate the influence of the interface on the macro and mciro length-scales in the three principal direction (vertical, radial and azimuthal). We also analyze the turbulent kinetic energy field and how it is transformed into potential energy. Then we look in more details at the mixing mechanisms across the density interface, building an ad-hoc conductivity probe and recording videos from top and lateral views.

I carried out this part of the thesis at the Hydraulic Laboratory, Department of Engineering and Architecture, University of Parma, under the supervision of Prof. Sandro Longo, with a Taylor-Couette tank similar to the one used in Cambridge.

This thesis is organized as follows. Chapter 2 contains a review of the most significant theoretical and experimental background on mixing phenomena in turbulent stratified flows, which have laid the foundations for the present study. Chapter 3 deals with the experimental apparatus and calibration techniques. In chapter 4 we report and discuss the results of the first part of the thesis, while in chapter 5 we analyze the results of the second part. In chapter 6 we give the general conclusions and suggestions for future work.

The road map of the experimental activity is shown in figure 1.5.

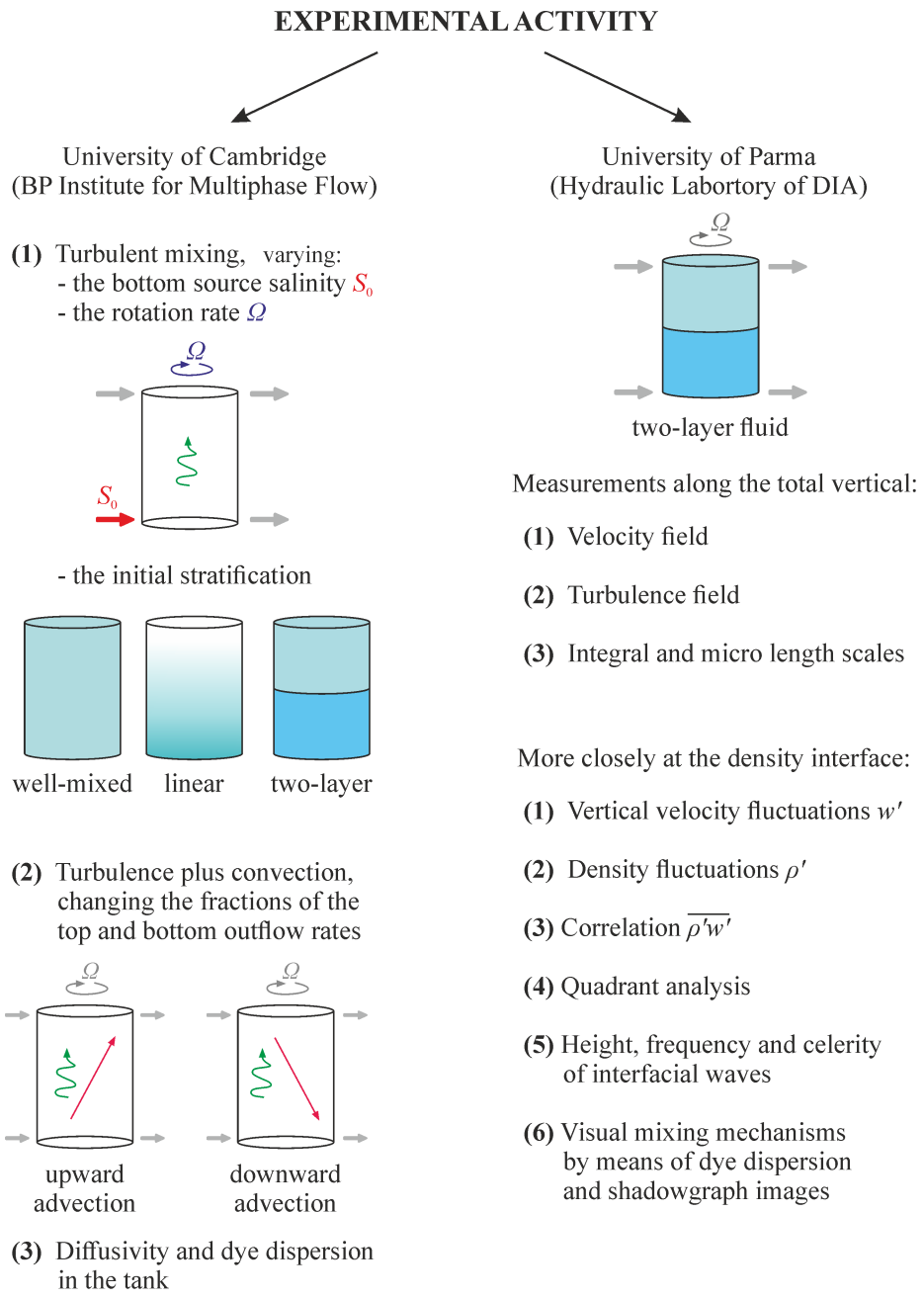

Figure 1.5: Road map of the experimental activity.

Chapter 2

Theoretical and experimental background

Many experimental, theoretical, field and numerical studies have been motivated by the investigation of the controls on the vertical mixing in the ocean, the fundamental mechanism that transfers heat from the sea surface downwards and salt from the bottom upwards through the ocean interior.

This chapter is going to review the most illuminating findings in the literature background. Some of the first experiments date back to the 80's and deal with mixing across a density interface between two homogeneous layers or in a linearly stratified fluids in a tank, where turbulence is generated by a thermal gradient (Turner, 1965) or mechanical oscillations of grids in the vertical direction (Linden, 1980; Fernando and Long, 1985, 1988) or rods in the horizontal direction (Fernando and Long, 1988; Park et al., 1994; Whitehead and Stevenson, 2007; Thorpe, 2016). Other studies investigate non-invasive mixing in a Taylor-Couette flow (Woods et al., 2010; Oglethorpe et al., 2013).

2.1 Mixing across a density interface

Stable density interfaces that separate upper lighter layers from lower denser layers are ubiquitous in the natural environment and they form spontaneously both in the ocean and in the atmosphere. Generally in the ocean, density interfaces are very frequent both at small and large depths (Cooper, 1967; Tait and Howe, 1968). Some of the most important examples of density interface in nature are: (i) the thermocline, which is the density interface between the ocean upper mixed layer and the stratified pycnocline, (ii) the

planetary boundary layer, which extends from the free atmosphere to the Earth surface, and (iii) interfaces that develop between gravity currents of denser fluids released into lighter ambient fluids and the ambient fluid itself. The refractive index changes with the fluid density, but when the density difference is not so large, the interface may not be visible to the human eye. On the opposite side, the density interface that separate air, a very light fluid, from sea water is very distinct and very well-defined.

We have seen from chapter 1 the key role played by turbulent mixing processes in the ocean circulation. The time scales for the abyssal waters to warm and upwell the ocean is of order of centuries, and in this time a lot of turbulent processes arise over the numerous pathways. Understanding the processes and the pathways is essential to parametrize the mixing phenomena (Alford et al., 2013). Those that may occur across density interfaces differ in accordance with the nature of turbulence and the stratification of the fluid. The first major difference is between shear-free and sheared density interfaces: in the first case, mixing is caused by external forces far from the interface that produce and diffuse turbulence, like wind stress and surface wave breaking are responsible for the deepening and mixing of the ocean upper mixed layer. On the other hand, in case of gravity currents, and counter-flowing currents in general, or imposed shear stress over a surface, the interface is affected not only by a density or temperature gap, but also by a velocity jump. Kelvin-Helmotz and Holmboe instability are typical examples of instabilities in shear driven flows that lead to a formation of a progressively deepening of an intermediate layer with a linear velocity and density gradient (Thorpe, 1973).

The influence of the background stratification over the flow shear also affects the mixing phenomena at interfaces and it is represented by the bulk Richardson number

$$Ri_B = g\frac{\Delta\rho\, d}{\rho\, u^2}, \tag{2.1}$$

where d and u are a length and velocity scale, $\Delta\rho > 0$ is the density difference over the vertical extent of the flow and ρ is a reference for density. Ri_B represents the ratio between buoyancy forces ($\sim g\Delta\rho$) to the intertial forces ($\sim \rho u^2/d$) or the ratio of the potential energy required for mixing ($\sim g\Delta\rho\, d$) to the available kinetic energy ($\sim \rho\, u^2$). For strong stratification (large density gap, hence, large Ri_B), the buoyancy forces act as restoring forces on vertical displacement, and the density interface is a rigid surface, scoured by turbulent eddies that bump against it and flatten. Turbulence is anisotropic at the interface as energy is transferred from vertical velocity to the horizontal component (Hannoun et al., 1988). In addition, entrainment

is mainly due to a wide variety of wave breaking mechanisms (Fernando and Long, 1988; Troy and Koseff, 2005). In contrast, for weak stratification, the available kinetic energy is sufficient to mix the fluid. Turbulent eddies are more capable to penetrate the interface and overturn, raising heavy fluid in the buoyant surrounding through splashing mechanisms (Briggs et al., 1998; Fernando, 1991).

The local Richardson number,

$$Ri = \frac{N^2}{\left(\frac{\partial u}{\partial z}\right)^2}, \tag{2.2}$$

is the ratio between the buoyancy frequency, N, given by equation 1.1 and the vertical shear, $\partial u/\partial z$. It takes into account the local stability of the flow instead of the bulk properties of the flow.

The influence of the molecular diffusivity of passive scalars, κ, on interfacial entrainment has also been examined. Turner (1965) used the ratio between the density difference due to salinity and that of temperature as a stability parameter to study the rate of heat and salt transfer across a sharp density interface. He found out that the initial density interface between two layers of different salt concentration and same temperature, persists while the fluid is being heated from below. He also found that with increasing stability, salt transfer becomes slower than heat and salt diffusion inhibits heat transfer. In this case, when the heat transport is reduced by the salt flux, a constant fraction of the potential energy of temperature is used to lift the salt. The effective turbulent transfer coefficients for salt and heat eventually approach the molecular values, with the heat molecular diffusivity being greater than the salt. Later on, Wolanski and Brush Jr (1975), using heat, salt, sugar, suspension of Silica spheres and clay as passive scalars with respectively decreasing molecular diffusivity, confirmed that the entrainment velocity (E, the rate of change in concentration in one of the two layers) decays with κ at fixed Ri, hence $E = E(Ri, Pr)$, with $Pr = \nu/\kappa$, where Pr is the Prandtl number and ν is the kinematic viscosity of the passive scalar.

2.1.1 Grid-generated turbulence

A series of experiments have been carried out in a tank where turbulence is generated in a two-layer fluid by a grid oscillating in the vertical.

If the horizontal grid falls freely from the the surface to the base of the tank, crossing the sharp density interface, the interface becomes more disturbed and thicker and generates internal waves. The mixing efficiency

can be evaluated by the flux Richardson number, Ri_f, which is the fraction of the available kinetic energy spent for mixing (the remainder is dissipated by viscosity) and converted into potential energy. If the rate of change of potential energy is $1/2\,(g\Delta\rho/\rho_0)\,u_e$, and the rate of supply kinetic energy is $1/2(u^2\,u/d)$, then

$$Ri_f \propto \frac{u_e}{u}\frac{g\Delta\rho}{\rho_0}\frac{d}{u^2} \propto ERi_B. \tag{2.3}$$

Ri_f depends on the bulk Richardson number (often called overall Richardson number Ri_0) $Ri_B = g\Delta\rho M/\rho U^2$ based on the mesh grid M and the grid velocity U as length and velocity scale respectively. For small values of Ri_B, Ri_f increases with Ri_B, as turbulence does more work against the buoyancy forces and support mixing, leading to a reduction of the density gradient. In contrast, Ri_f decays for larger values of Ri_B: less energy is spent for mixing and mass tends to accumulate in high density gradient regions (where mixing is least), making these gradient higher. Ri_f has then a maximum of $Ri_f = 0.12$ at $Ri_B \approx 1.3$ (Linden, 1979, 1980), meaning that viscosity dissipates almost 90% of the available kinetic energy.

The mixing efficiency can also be interpreted in terms of entrainment coefficient E, as the ratio between the velocity of the entrainment of fluid across the interface, u_e, and a characteristic velocity, u, so

$$\frac{Ri_f}{Ri_B} \propto E = \frac{u_e}{u}. \tag{2.4}$$

Turner (1968) expressed the entrainment velocity as the rate of advancing of the lower (upper) layer, on the basis of which layer was stirred, as:

$$u_e = \frac{\mathrm{d}h}{\mathrm{d}t} = -\frac{h}{\Delta\rho}\frac{\mathrm{d}\rho_l}{\mathrm{d}t}, \tag{2.5}$$

where h is the height of the stirred layer, $\Delta\rho = \rho_l - \rho_u$ the density difference between the lower and upper layer. If both layers are stirred at the same rate, the fluid entrained in the upper layer equals the fluid entrained by the lower layer ad the density interface does not move. The entrainment coefficient E is the same, no matter whether only one layer or both layers are being stirred by the grid (Turner, 1968).

In the grid mixing experiments in a stratified flow, turbulence decays with distance from the interface. The entrainment law has the form

$$E \propto Ri_B^{-n} \tag{2.6}$$

with $n > 1$ and $Ri_0 > 1.3$. Then

$$R_f \propto Ri_B^{1-n}. \tag{2.7}$$

In case of temperature differences between layers caused by heating from below, $n = 1$, so R_f remains constant for increasing Ri_B, while in case of density differences produced by salinity $n = 3/2$, therefore R_f decreases for increasing Ri_B (Turner, 1968). For large values of Ri_0, $n = 7/4$ within the mixed layer and $n = 3/4$ in the region of the interfacial layer close to the mixed layer (Fernando and Long, 1985). When a steady buoyancy flux is imposed to stabilize the interface by a source of fresh water in the top layer and salty water in the bottom layer, $n = 1$ (Fernando and Long, 1988).

In the experiments of Zellouf et al. (2005) which were very similar to Turner (1968), the salt flux increases while the heat flux decreases with decreasing density difference between the layers. In case of strong salt stratification, the interface is much more stable and more energy is required to destabilize it. When the stratification is weaker, the turbulent structures are more capable to penetrate the interface. When $Ri_B < 10$, the entrainment velocity rate for heat and salt approach the same value, while for $Ri_B > 10$, the exponent n of equation 2.6 are the same of Turner (1968).

Direct numerical simulations were performed by Briggs et al. (1996, 1998) who characterized turbulence structure by local vertical Froude number $Fr_v = w'/(Nl')$, where w' is the vertical velocity fluctuation, l' the vertical turbulent length scale and N the buoyancy frequency. The vertical mixing efficiency, η_v, increases to a maximum value of ≈ 0.3 when $Fr_v = 1$, and decreases under weak stratification ($Fr_v > 1$). The bell-shaped curve is analogous to the earlier findings, considering that the Froude number is the square root of the inverse of Richardson number. So $\eta_v \to 0$ when $Fr_v \to \infty$ because a weakly stratified fluid is vigorously mixed by turbulence and becomes well mixed, and when $Fr_v \to 0$ because strong buoyancy cannot let turbulent eddies stir the fluid. In addition, η_v takes into account the anisotropy of turbulence produced by vertically oscillating grid experiments, expressed by the ratio of vertical and horizontal velocity oscillations w'/u', which is large close to the source of turbulence and decays far from the grid.

Crapper and Linden (1974) paid attention to the evolution of the thickness of the density interface, h, (non-dimensionalized with respect to the turbulent length scale, l) in a wide range of Ri and Péclet number $Pe = ul/\kappa$, where u is again a velocity scale and κ the molecular diffusivity for salt or heat. Pe is a measure of the effects of the advective component to the diffusive component. The ratio h/l does not depend on Ri but decreases with increasing Pr in a region of Pe where transport is mainly driven by molecular diffusion, approaching a constant value of 1.5 at $Pr \approx 200$ when diffusion becomes unimportant. At low Pe, the constant temperature gradi-

ent in the center of the interface implies a constant heat flux across it. This region is characterized by "diffusive core" where the diffusive flux matched the entrainment heat flux at the edges of the layers. When Pe increases, the thickness of the interface reduces and the interface sharpens, leading to an increase of the temperature gradient.

2.1.2 Rod-generated turbulence

In the work of Whitehead and Stevenson (2007), turbulence was generated by vertical rods oscillating in the horizontal direction. They found that if the two initial homogeneous layers are stirred throughout the full depth, the density profiles are self-similar and collapse into one universal profile. The initial sharp interface widens when the mixing starts, and the density gradient becomes continuous along the depth until the whole fluid becomes well-mixed. The vertical flux is greater at the interface and smaller inside the homogeneous layers, and increases with the internal Richardson number, $Ri_i = N^2 d^2/U^2$, where d and U are the diameter and the speed of the rods, the turbulent source.

Other experiments which were conducted in a linearly stratified fluid will be discussed in section 2.2.

2.2 Mixing in a linear stratified fluid

A constant linear density gradient may become unstable under small vertical perturbations. If the flux depends on the local properties of the flow, in the regions where the density gradient is a little steepened, the flux becomes more intense and further reduces the vertical gradient. In other regions where the flux is decreased after a flattening of the density gradient, the density gradient further increases in order to maintain an overall mean value of flux. The result is a staircase of uniform layers separated by sharp density interfaces, which is a common feature in the ocean environment (Phillips, 1972; Posmentier, 1977).

In this section we will often refer to an overall Richardson number

$$Ri_0 = \frac{N_0 d^2}{u^2}, \tag{2.8}$$

based on a turbulent lengthscale d and velocity scale u and a buoyancy frequency N_0 depending on the initial linear stratification.

One of the first studies that saw the development of a layered structure was conducted by Turner and Stommel (1964) in a tank of a linear stratified

fluid heated from below. A first turbulent layer formed at the bottom of the tank, and a second one above it later in time. The density interfaces move upward, while layers appear at the bottom, merging and becoming uniform. Because heat diffusion is greater than salt diffusion, heat drives convective motions faster than salt, which enhances the stability of the underlying layer.

Kato and Phillips (1969) simulated the effects of wind stress on a laboratory scale, applying a constant stress in circumferential direction on the surface of a uniformly stratified fluid in an annular tank. They studied the formation and growth of the upper turbulent well-mixed layer: the interface appears to be irregular and unsteady, affected by the overturning motion of the turbulent eddies in the layer above, until the mixed layer become so deep that the density jump across the interface is large enough to reduce the amplitude of the oscillations. The rate of deepening of the upper mixed layer gradually decreased over time, as the layer depth and density difference increased. The rate of entrainment across the interface appeared to be proportional to Ri_0^{-1}, similarly with (Turner, 1968).

Ruddick et al. (1989) found that layers form only in a salt (and not sugar) stratification stirred weakly by vertical rods. For sufficiently high stirring period, the layers begin to smooth out as a consequence of the high rate of mixing. Layers smooth out even at very low stirring period, meaning that a minimum of supply energy is required to produce and maintained the layered structure. The thickness of the layer increases with time, most likely due to merging of thinner layer as a result of the mechanisms discussed by Phillips (1972); Posmentier (1977).

Park et al. (1994) ran similar experiments on a linear stratified fluid horizontally stirred by a rod. For small overall Richardson number, Ri_0, defined on the basis of the speed u and diameter d of the rod, two homogeneous layers formed at the top and bottom boundaries and constantly advanced into the interior. As the mixing efficiency, the density difference between the two final mixed layers decreased progressively over time, until they met at the centre of the tank. If the initial Ri_0 was greater than a critical value, Ri_c, the middle stratified layer broke into a series of uniform layers. The interface between two subsequent layers eventually decayed and the two layers merged. In equilibrium, the height h_l of the layers seems to follow the form

$$h_l \propto \frac{u}{N_0} + c, \tag{2.9}$$

where c is a constant, and therefore be independent of the geometry of the rod. During the formation of steps, if Ri_0 is not so large compared to

Ri_c, the mixing efficiency, hence R_f, decreases with the local Richardson number, Ri. On the other hand, the mixing efficiency sharply increases for $Ri_0 \gg Ri_c$. The mixing between the layers is so intense that the local Ri is reduced to a minimum value. In equilibrium, when the density profile does not change significantly over time, the mixing efficiency becomes constant, and suddenly decreases during the final stage, when the layers coarsen and the number of interfaces decreases to a single large density interface in the middle of the tank.

According to Balmforth et al. (1998), in addition to the weak stratification condition, when turbulence mix everything up and the initial weak density gradient decays to homogeneous state, and intermediate stratification condition, when layering occur in the interior and edge layers form at the boundaries, there is a third condition, non yet experimentally verified. In this case, the initial linear stratification is so strong that no layers develop but only layers form at the edges because of the no-flux condition. These edge layers also expand self-similarly, with height $h(t) \sim t^{1/2}$.

(Holford and Linden, 1999) found that the critical value Ri_c below which the layering behaviour does not occur is 1.5 in a fluid stirred by a grid of vertical rods. In addition to the similar findings on the characteristic layer height due to Park et al. (1994), Holford and Linden (1999) also studied the dependance of the buoyancy flux on Ri_0, defined on a velocity scale $u = U(1 - d/M)$ and a length scale $d = \sqrt{DM}$, where U and D are the velocity and diameter of the rod and M the mesh spacing. At low Ri_0, the buoyancy flux is an increasing function of N^2. The eddy diffusivity is constant below a critical value of the buoyancy frequency, and increases with Ri_0 beyond. At high Ri_0, the buoyancy flux sharply increases only during the first stage, when interfaces are developing. When interfaces are well-established, N^2 increases but the buoyancy flux is reduced.

The critical value is of Ri_c is 1.0 for Rehmann and Koseff (2004), who found that for weaker salt, temperature or salt-temperature stratifications, $Ri_f \propto Ri_0^{1/2}$ and reaches a constant values for higher values of stratification, in the limit of their experimental range $0 < Ri_0 < 10$.

2.3 The Taylor-Couette apparatus

Stirring a grid of horizontal bars or vertical rods to mix a stratified fluid, as in the experiments described above, influences the dynamic of the flow by imposing a length and velocity scale associated with the geometry and mechanical oscillations of the grid.

A Taylor-Couette tank was used to generate non invasive turbulence at high Reynolds number by different authors (Guyez et al., 2007; Woods et al., 2010; Oglethorpe et al., 2013). In this section we are going to review their most important results, which have inspired the present work, about mixing in a fluid commencing with either a two-layer stratification or linear stratification.

The Taylor-Couette tank consists of a cylindrical annulus of inner radius R_1 and outer radius R_2. The gap width is $\Delta R = R_2 - R_1$. Shear can be applied to the fluid by rotating either the inner or the outer cylinder, or both, along the vertical axis. On the basis of the angular velocity of the rotating cylinder, Ω, the geometrical parameters and the kinematic viscosity of the fluid ν, a Reynolds number can be defined as

$$Re = \frac{\Omega R_1 \Delta R}{\nu}, \tag{2.10}$$

where ΩR_1 is a velocity scale and ΔR a length-scale, and a Taylor number as

$$Ta = \frac{2R_1^2}{R_2^2 - R_1^2} \frac{\Omega^2 \Delta R^4}{\nu^2} = \frac{2\Delta R^2}{R_2^2 - R_1^2} Re^2 \tag{2.11}$$

which represents the ratio between centrifugal to intertial forces due to rotation of fluid about an axis (Koschmieder, 1993). The definitions of Re and Ta may vary upon a correct scaling of the length and velocity of the flow, the definitions in equations 2.10 and 2.11 are taken from Roberts (1965).

When Ta exceeds a critical value Ta_c, intertial instabilities set it and the flow gets in a turbulent state. These instabilities are often called "Taylor instabilities" as they involve the presence of Taylor vortices with a toroidal structure, firstly discovered by Taylor (1923), up to a Ta much greater than Ta_c.

Different regimes have been observed by Boubnov et al. (1995) in a circular Couette flow with $R_1/R_2 = 0.784$. The stratification of the fluid, N, acts as a stabilizing parameter so the critical value of rotation rate increases with N. For this reason, the Froude number, Fr, proves more helpful in setting the boundaries for the different regimes rather than Re. If fluid is well mixed, $N = 0$, the size of the Taylor vortices equals the gap width and the critical Reynolds number is very low $Re \approx 90$. For $N > 0.4$ and $\Omega > \Omega(N)$ the layers equal half the gap width. For larger Ω the vortices begin to act in pairs and have a size of twice the gap width. More complex regimes arise for further increasing Ω. The density layers still follow the form $h \propto \Omega d/N_0$, with a minimum value that decreases with an increase of

the gap width (Boubnov et al., 1996). Boubnov et al. (1995) suggested that the scaling for the height of the layers can derive form a balance between the work done by the centrifugal force $\Phi \propto R_1\Omega^2$ against radial pressure gradient to move a parcel of fluid at a distance ΔR, and the work necessary to raise the fluid at a distance h in a linearly stratified fluid of buoyancy frequency N_0. Therefore

$$R_1\Omega^2\Delta R \propto N_0^2h^2 \Longrightarrow h \propto \sqrt{R_1\Delta R}\frac{\Omega}{N_0}. \tag{2.12}$$

In the experiments in Koschmieder (1993) the transition to turbulence occurs at around $100\,T_c$, when the vortex length scales lose their dependance on Ta. These length-scales are greater than the laminar Taylor vortices and are equal to $1.7\,\Delta R$ for $R_1/R_2 = 0.896$, and $1.2\,\Delta R$ for $R_1/R_2 = 0.727$. At approximately $700\,Ta_c$ the flow is statistically axisymmetric.

Lewis and Swinney (1999) found a transition in the coherent structures and azimuthal traveling wave velocity at a Reynolds number $Re = 1.3\times10^4$, for a system with $R_1/R_2 = 0.724$.

In the direct numerical simulations DNS for the standard configuration by Dong (2007) and counter-rotating system by Dong (2008), the flow transition occur in the range $1000 < Re < 3000$.

2.3.1 Mixing experiments

The vertical salt flux across the interface per unit cross area must equal the rate of change in the salt content in the upper (or lower) layer. We can write

$$F(z,t) = \frac{\mathrm{d}}{\mathrm{d}t}\int_0^{H/2}\frac{\rho(z,t)-\rho_0}{\rho_0}\mathrm{d}z, \tag{2.13}$$

with $H/2$ being the depth of one layer and H the depth of the fluid. The salt flux can also be expressed in terms of the density difference $\Delta\rho(t)$ between the layers and the entrainment velocity $u_e(t)$,

$$F(z,t) = \Delta\rho(t)u_e(t). \tag{2.14}$$

Substituting equation 2.14 into equation 2.3, we can relate the flux Richardson number Ri_f to the salt flux F,

$$Ri_f = \frac{d}{u^3}F = \frac{F}{\mathcal{E}}, \tag{2.15}$$

where $\mathcal{E}$ is the rate of dissipation of kinetic energy, proportional to the cube of a velocity scale, u^3, and a length-scale, d. Guyez et al. (2007)

show that for fixed $Re = 3409$, the mixing efficiency increases with Ri_B and reaches a maximum of $15 - 30\%$, in accordance with previous results (Linden, 1979, 1980), then descends and increases again at large Ri_B (i.e. large density gradient). The mixing efficiency curve is not bell-shaped then, but N-shaped, opposing the previous results. This is addressed to the kinetic energy scale which is smaller than the turbulent eddy macro length scale, fixed by the gap width.

In contrast, Woods et al. (2010) found that the buoyancy flux does not depend on Ri_B, for large values of Ri_B and for $Re \propto 10^4 - 10^5$. The flux, and hence the rate of change of potential energy, is rather proportional to $F \propto u_{rms}^3 \propto \Omega^3$ (u_{rms} was found to be proportional to Ω). The higher range of Re in their experiments may better disregard the influence of molecular transport processes than the previous experiments, where Re was definitely low. Woods et al. (2010) also measured the time-averaged radial profile of mean angular momentum $\langle U_\theta r \rangle$ and the root-mean-square fluctuation of angular momentum $\langle u_{rms} r \rangle$ with Particle Image Velocimetry (PIV). The mean and fluctuating velocities follow then the forms

$$U_\theta = 0.91 \frac{\Omega R_1^2}{r}, \tag{2.16}$$

$$u_{rms} = 0.086 \frac{\Omega R_1^2}{r}. \tag{2.17}$$

However, the depth of the fluid and the inner and outer radii of the tank were kept constant in both the experiments of Woods et al. (2010) and Guyez et al. (2007), so they did not investigate the influence of these geometrical parameters on the flux and velocity laws.

Oglethorpe et al. (2013), using the same apparatus of Woods et al. (2010) but with three different values of R_1, found that the vertical flux across a density interface in a two-layer system is constant and independent on Ri_B, provided that

$$Ri_B = \frac{g \Delta \rho R_2}{\rho_0 \left(\Omega R_1\right)^2} > 4, \tag{2.18}$$

with ΩR_1 as velocity scale in accordance with Woods et al. (2010) and R_2 - the only constant imposed external length-scale - as the best length-scale that maximize the collapse of the data. In the range $0.5 \leq Ri_B \leq 4$, the vertical flux follows the power law $F \propto Ri_B^{-1/2}$, analogously to previous experiments (Turner, 1968; Zellouf et al., 2005). However, different power-laws better fit different rages of Ri_B, but none of them describes the complete behavior of F with Ri_B for $Ri_B > 0.5$. At $Ri_B \approx 0.5$, F reaches a maximum

and rapidly decreases to zero for lower Ri_B, when $\Delta\rho$ between the layers is low enough that the interface overturns and the fluid becomes well mixed.

Oglethorpe et al. (2013) also extended the study to an initially linear stratified (LS) or five layered fluid (5L). According with previous results, a linear stratification spontaneously evolved into long-lived layers, with internal layers coarsening when the density difference across their interface was low enough to overturn the interface. The layer depth $h \propto \sqrt{\Delta\overline{RR}_1}\,(\Omega/N_0)$, where N_0 is the initial buoyancy frequency. For both LS and 5L experiments, the density of the top and bottom layers evolved over time, but the density in the interior is rather unchanged, suggesting that the vertical flux is the same across each interface. The flux is also independent on the number and height of the layers and on the initial condition and follows a "universal flux law" at least in the range $2 \leq Ri_B \leq 20$.

Following the results of Woods et al. (2010); Oglethorpe et al. (2013), the present thesis tries to explore more details of the mixing processes when a buoyancy flux is imposed externally to the turbulent flow.

We also make sure that our flow is fully turbulent. Donnelly and Schwarz (1965) determined the critical Taylor number Ta_c at the onset of instability in the wide range of $R_1/R_2 = 0.975 - 0.200$. In our experiments, we use the same Taylor-Couette tank of Woods et al. (2010); Oglethorpe et al. (2013), with $R_1/R_2 = 0.40$ so the critical Taylor number $Ta_c \approx 4137$. We also use another Taylor-Couette tank, with $R_1/R_2 = 0.50$ so $Ta_c = 3099$. The choice of a range of rotation rate $\Omega = 1.00 - 2.75\,\mathrm{rad\,s^{-1}}$ for both tanks leads to Taylor numbers of $Ta = \mathcal{O}\big(10^8 - 10^9\big)$, so 4-5 order of magnitude greater than the respective critical values. The flow is then fully turbulent and far from the point of transition to turbulence.

Chapter 3

Experimental Set-Up

This chapter focuses on the experimental set-up and the all the equipment adopted for the experiments, and it is organized as follows: section 3.1 describes the apparatus of the experiments carried out at BP Institute for Multiphase Flow and Bullard Laboratories of University of Cambridge, while section 3.2 illustrates the apparatus of the experiments run at the Hydraulic Laboratory of University of Parma.

3.1 The Taylor-Couette Tank in Cambridge

The suite of experiments at BP Institute for Multiphase Flow and Bullard Laboratories were carried out is the same Taylor-Couette tank of Woods et al. (2010) and Oglethorpe et al. (2013): the stationary outer cylinder has an internal radius $R_2 = 25\,\text{cm}$, while the rotating inner cylinder has an external radius $R_1 = 10\,\text{cm}$. The gap width between the two cylinders is $\Delta R = R_2 - R_1 = 15\,\text{cm}$. This cylindrical annulus has a vertical axis and a fixed base, and is filled with fluid up to a depth of $H = 40\,\text{cm}$. The top surface of the fluid is a free surface.

The tested range of angular velocities is $\Omega = 1.00 - 2.50\,\text{rad}\,\text{s}^{-1}$ and this leads to Reynolds numbers $Re = \mathcal{O}(10^5)$, where $Re = \Omega(\Delta R)^2/\nu$, with $\nu = 1.2 \cdot 10^{-6}\,\text{m}^2\,\text{s}^{-1}$ being the kinematic viscosity of the fluid.

3.1.1 Sources of fluids

In the present work we simulate rainfall, river run-off and ice-melting by supplying a flux of fresh water to the top of the fluid and density currents released by ice formation flowing on the ocean floor by a flux of salty water at the bottom of the fluid.

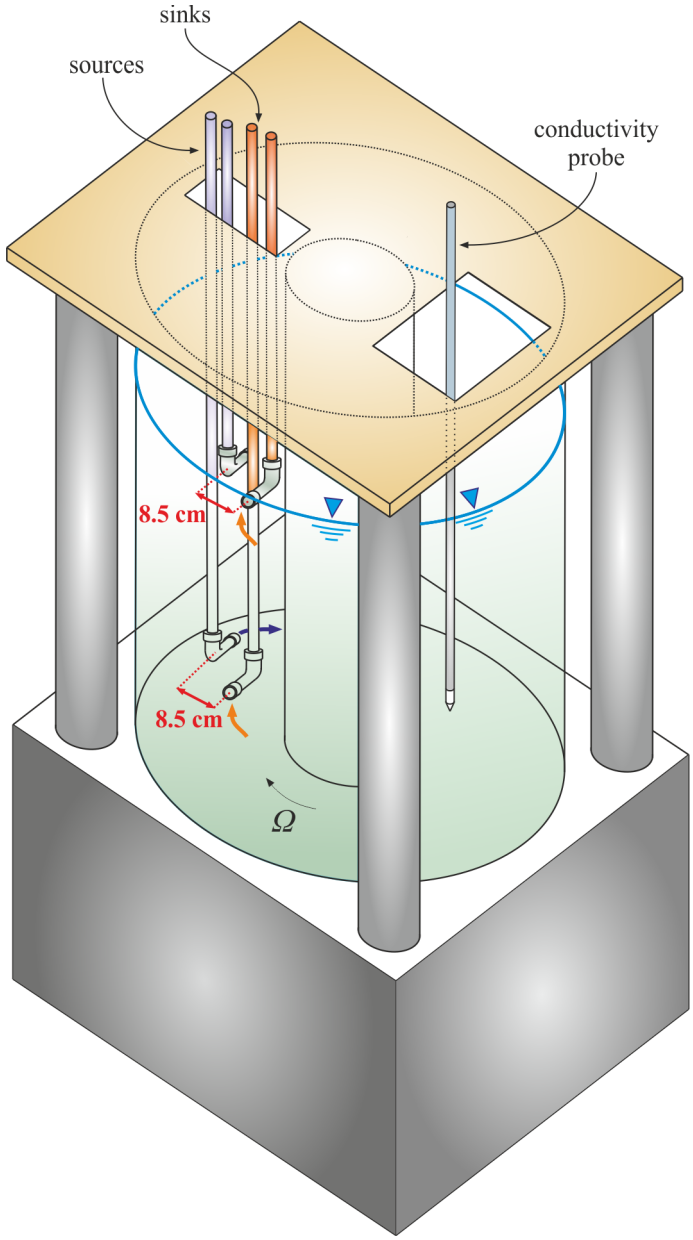

Figure 3.1: Position of the sources and sinks.

The density of the supplied fluids are constant during each experiment, but the salinity of the bottom source is varied from one experiment to

another. The saline fluid and fresh water are kept in separate 60 l containers and the saline fluid is continuously mixed by two submersible pumps. At the same depth of the two sources, we also introduce two sinks, which remove the same volume flux introduced to the system, in order to maintain the same volume of fluid inside the tank.

Both the sources and the sinks are located in the same vertical section of the tank, at 180° from where the conductivity probe profiles the fluid vertically, in order to minimize the disturbance and wakes registered by the probe. In addition, the sources and the sinks are at alternate position, with each source at a radial distance of 8.5 cm from the respective sink. The source supplying fluids are oriented downstream, in the azimuthal direction parallel to the rotation of the inner cylinder, while the two sinks are oriented upstream, in the opposite azimuthal direction, as shown in figure 3.1. In this way, the injected fluid moves with the current, dragged by the circular motion induced by the inner cylinder, and meets the opening of the sink downstream.

3.1.2 Conductivity Probe

During all the experiments, a 60 cm long conductivity probe, mounted on a traverse system above the tank, measures vertical density profiles continuously in time, at a mid radial distance between the two cylinders. The conductivity probe was home-made in D.A.M.T.P (Department of Applied Mathematics and Theoretical Physics, University of Cambridge, U.K.) and it is not commercially available. The complete set-up of the conductivy probe is illustrated in figure 3.2.

Although the conductivity probe provides intrusive measurements and may locally disturb the flow, to the best of our knowledge, it is most likely the most accurate and stable existing device for measuring density for long period at sufficiently high frequency rate. The operating principle relies on the possibility to infer the density of ionic solutions from their electrical properties. The probe is made of two concentric stainless steel electrodes, insulated from one another. At the top of the probe, a flexible narrow plastic tube is attached. By means of a small syringe connected to the end of this tube, it is possible to establish the siphon of the fluid from the the bottom tip hole of the probe, made of Araldite. The tip hole has a diameter of 0.6 mm and a length of 5.5 mm. This tiny geometry is dictated by the need of (i) confining the loss of potential within a small volume of sample fluid and so considering density data as local measurements, and (ii) avoiding signal distortions at higher values of conductivity (Hughes, 1996). The siphoning

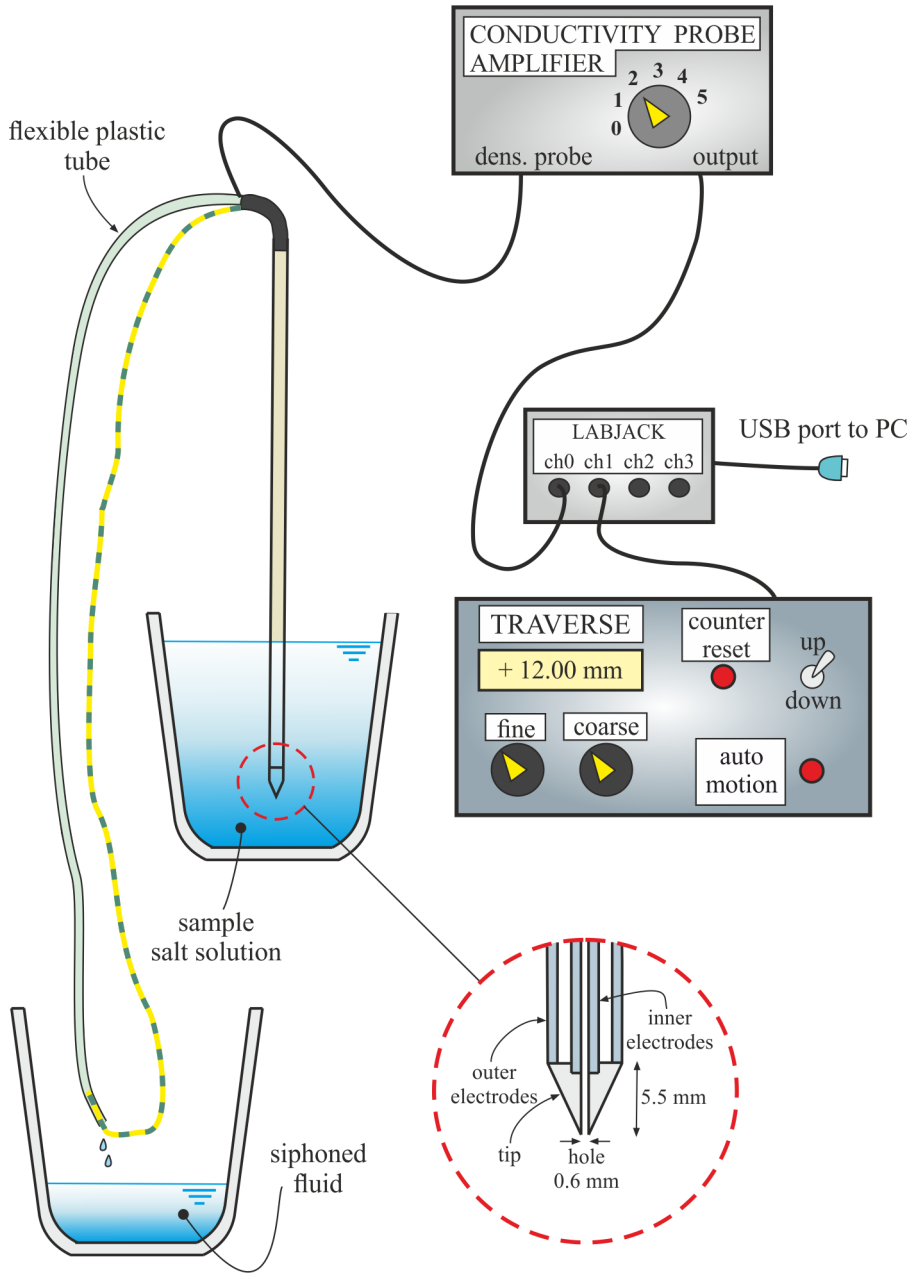

Figure 3.2: Conductivity probe, conductivity probe amplifier and traverse box.

rate is approximately $0.2\,\mathrm{ml\,s^{-1}}$ and the withdrawn fluid is collected in a recipe outside the tank. In this way, the electrodes situated at the tip of the probe are always in contact with new fluid. To ground the electronic circuit and avoid stray currents, a wire provides a solidly earthed neutral system if its tip is put inside the siphoning tube, as shown in figure 3.2. The volume loss of the fluid siphoned from the tank, approximately 0.7 l per hour, can be neglected in comparison with the initial volume of fluid in the annulus, $V = 70\,\mathrm{l}$ and the duration of the experiment ($1 - 4$ hours). Nevertheless, the inflow rate are slightly increased when the fluid depth decreases of ≈ 0.5 cm for a couple of minutes until the initial level is restored.

The probe profiles the fluid in the tank at a time scale of order of 30 s, which is a fair compromise between the fast rotation period of the cylinder, $T = 2.5 - 6.3\,\mathrm{s}$, and the relatively slow time scale of $5 - 30$ minutes over which the density of the fluid changes. Only the data of downward profiles are taken into account as measurements are affected by the probe's wake when the probe is moving upward, so we have approximately one profile per minute and we consider the density homogeneous in the radial direction.

The traversing mechanism consists of a frame positioned on the top lid of the tank. Onto the frame a stepper motor was mounted, attached to a vertical lead screw, and a clamp holding the conductivity probe, accurately aligned in the vertical direction. Two stops set the minimum and maximum height to reverse the motion of the probe. The movement of the stepper motor can be manually or automatically controlled by a traverse box, which counts the number of steps and transfers the signal to a personal computer. The position and density data are recorded every 0.1 s (at a frequency of 10 Hz) by the software DAQFactory® released by AzeoTech®, Inc.

3.1.3 Calibration of the conductivity probe

The probe is calibrated before each experiment, using 5 - 6 samples of different known salt contents. The calibration curve does not change significantly in time, proving a good repeatability and riproducibility of the measurements, as shown in figure 3.3*a*. The recorded signal can be amplified, switching from channel 0 to channel $1 - 5$ in order to operate in a shorter range of conductivities (i.e. densities), and optimize the density gain as shown in figure 3.3*b*. Attention must be paid because the amplifier box saturates at values $\geq 2.46\,\mathrm{V}$.

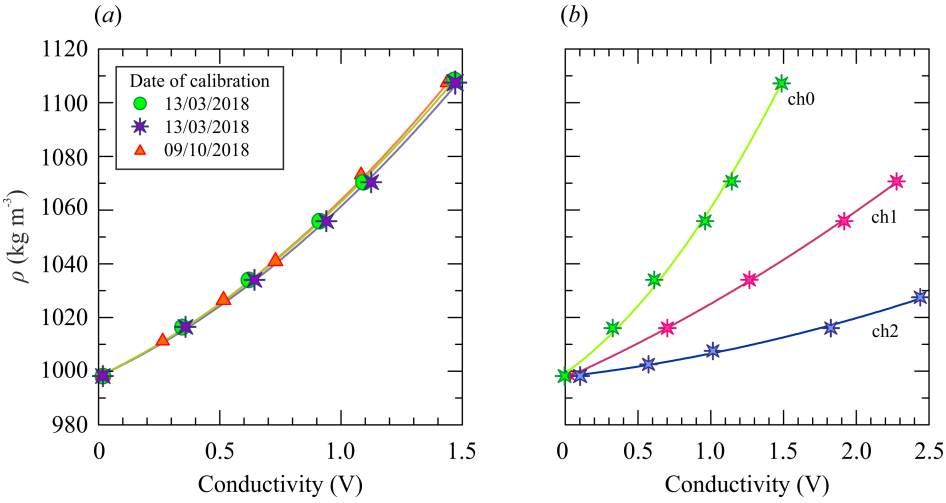

Figure 3.3: (a) Calibration curve repeated in the same day and after a period of 6 months; (b) Calibration curves for different signal amplifications.

To check the stability of the probe over a long time, we put the probe inside the tank filled with homogeneous fluid of known density. In figure 3.4a data were recorded over a period of 50 minutes in a fluid of density $\rho \approx 1034\,\mathrm{kg\,m^{-3}}$ and salinity $S = 5\%$ in both stationary condition (steady inner cylinder) and dynamic conditions (rotating inner cylinder at $\Omega = 2.00\,\mathrm{rad\,s^{-1}}$. In figure 3.4$b$ the same measurements were conducted on a fluid of greater density $\rho \approx 1071\,\mathrm{kg\,m^{-3}}$ and salinity $S = 10\%$. In both cases a slightly downward trend is registered when the inner cylinder is rotating. This density drop off is only less than 0.1% over an hour, therefore we envisage an excellent stability.

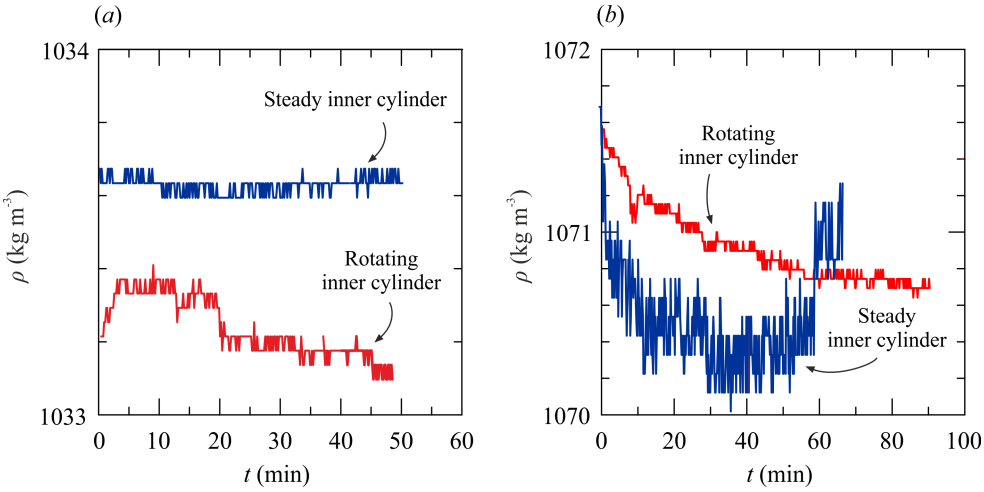

Figure 3.4: Density recorded in stationary and dynamic conditions for two homogeneous fluids with density (*a*) $\rho \approx 1034\,\mathrm{kg\,m^{-3}}$; (*b*) $\rho \approx 1071\,\mathrm{kg\,m^{-3}}$.

3.1.4 Calibration of the peristaltic pumps

Watson-Marlow $^{\mathrm{TM}}$ 520-Du and 530-Du peristaltic pumps are used to pump fluid in and out from the tank. Each pump is calibrated with fresh water by measuring the volume of pumped water (mass/density) in unit of time for different values of rounds per minute (r.p.m.). The calibration curves are shown in figure 3.5*a*. In order to check that the volume flux does not change significantly upon the density of the fluid, the pumps were also calibrated using salt water with 15% of salt content ($\rho = 1108.5\mathrm{kg\,m^{-3}}$). A comparison between two calibration curves is presented in figure 3.5*b*.

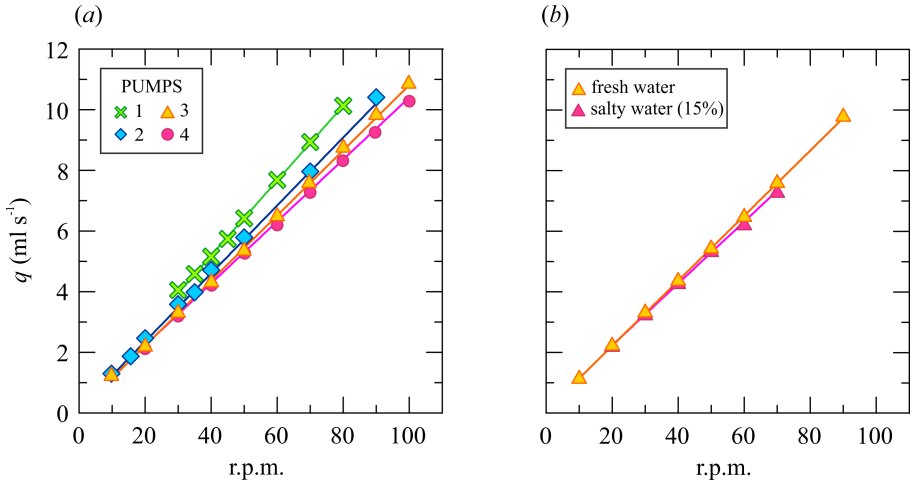

Figure 3.5: (a) Calibration curves for the four peristaltic pumps; (b) Comparison between the calibration curves for the same perisaltic pump, with fresh water and salty water (15% of salt content).

3.1.5 Measurements of the density of the outflows

The turbulent flow field is generated by rotating the inner cylinder and we monitor the density of the two outflows in time until a quasi-steady state is achieved (i.e. the density of the outflowing fluids do not vary over a period of 40-60 minutes). Using a volumetric pipette, samples of approximately 2 ml are collected from the outflowing fluids every 4-5 minutes and applied on the exposure area of the refractometer, sketched in figure 3.6. Each measurement is repeated twice or three times, if the first two samples give different results, and averaged.

The brix number, Bx, is converted into density ($\mathrm{kg\,m^{-3}}$) or salinity: S, mass of salt as a fraction of the total mass of the fluid (%), or C_s, mass of salt as a fraction of the volume of fresh water ($\mathrm{g\,l^{-1}}$).

$$S = 0.8766\,Bx - 0.1 \quad \text{if} \quad Bx \leq 3.0 \text{ or } Bx \geq 11.6 \tag{3.1}$$

$$S = 0.8766\,Bx - 0.2 \quad \text{if} \quad 3.1 \leq Bx \leq 11.5 \tag{3.2}$$

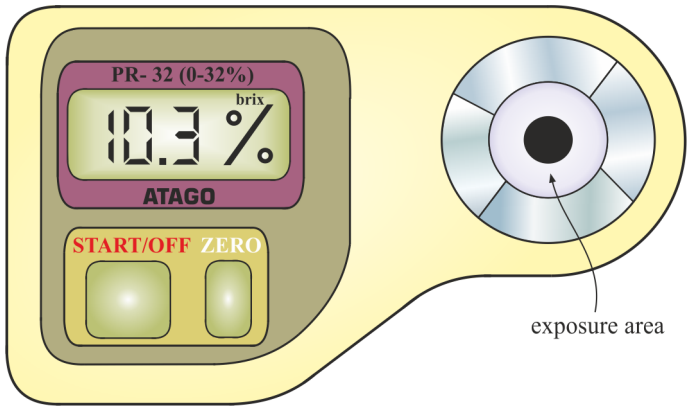

Figure 3.6: Digital refractometer PR-32 made by Atago^{TM}.

3.1.6 Experimental Set-Up

If the turbulence generated by the inner cylinder is intense enough to raise the centre of mass of the fluid and convert kinetic energy into potential energy, this will lead to a vertical salt flux through the tank. This flux can be associated to the vertical diapycnal mixing in the ocean and can be measured by the flux extracted at the top of the tank.

On the other hand, the fluid in excess which cannot be raised by the strength of the imposed turbulence, is collected by the sink at the base of the tank. This flux could be interpreted as the oceanic upwelling of deep water to the surface, although this flow may also be involved into some diapycnal mixing processes in the real situation.

The complete set-up of the experiments is shown in figure 3.7.

A first series of experiments is carried out keeping the flow rate of both the sources and the sinks constant, $q = 5.4\,\mathrm{ml\,s^{-1}}$.

In a second series of experiments, the fraction of fluid extracted at the top of the tank, Q_{to}, with respect to the total volume of fluid supplied to the system in unit of time Q_0, $\lambda = Q_{to}/Q_0$, is varied in the range $20 - 100\%$ (hence, the fraction of fluid taken out of the base is $1 - \lambda = 80 - 0\%$). In this case, the advective component is summed to the turbulent component, and they are both directed upwards if $\lambda > 0.5$, while they are directed in opposite directions if $\lambda < 0.5$.

In a third series of experiments, the salt content of the supplied fluids is kept constant (fresh water at the top and salty water, 15% of salinity, at the bottom) as well as the initial condition (two-layer stratification: 5% of salinity for top layer and 10% of salinity for bottom layer) and the position

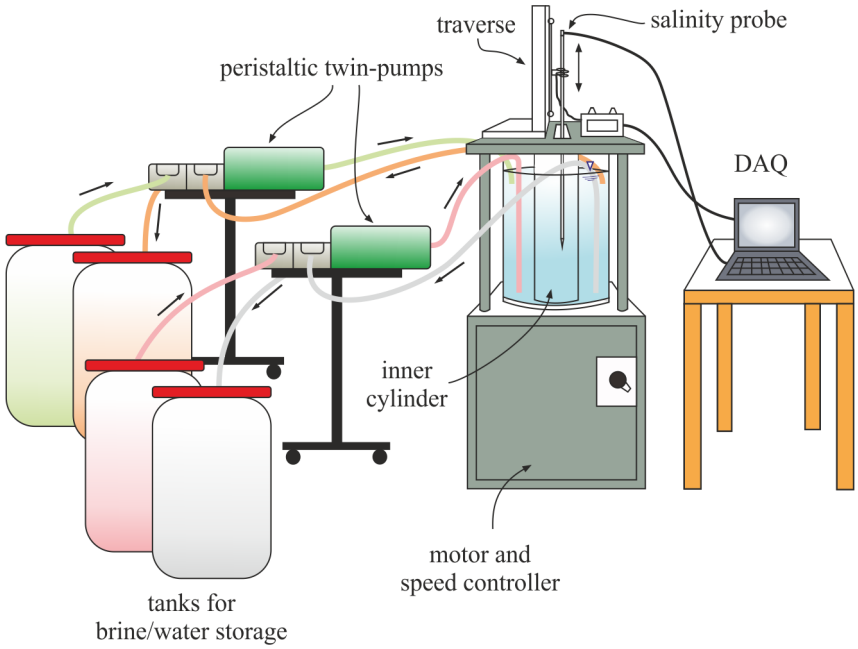

Figure 3.7: Set-up of the experiments at BP Institute for Multiphase Flow (University of Cambridge, U.K.).

of the sources and sink is varied along the vertical direction, as shown in figure (3.8).

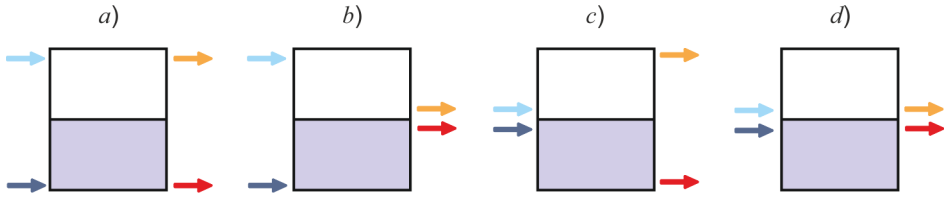

Figure 3.8: Position of the sources (dark and light blue arrows) and sinks (red and yellow arrows) in the third series of experiments.

These data will be presented and discussed in chapter 4.

3.2 The Taylor-Couette Tank in Parma

The experiments at the Hydraulic Laboratory of Parma were carried out in a Taylor-Couette tank similar to that at BP Institute. The tank is sketched in figure 3.9.

The radii of the rotating inner cylinder and steady outer cylinder are $R_1 = 8.5$ cm and $R_2 = 17.2$ cm respectively. The gap is $\Delta R = R_2 - R_1 = 8.7$ cm. The tank is filled with fluid up to a depth of $H = 25$ cm. The experiments were run in a range of angular velocities of $\Omega = 1.50 - 2.75\,\mathrm{ml\,s^{-1}}$, leading to Reynolds numbers of order $Re = \mathcal{O}10^4$, where Re is defined as in section 3.1. The motor of the spinner is stepper and is controlled by a Labview software.

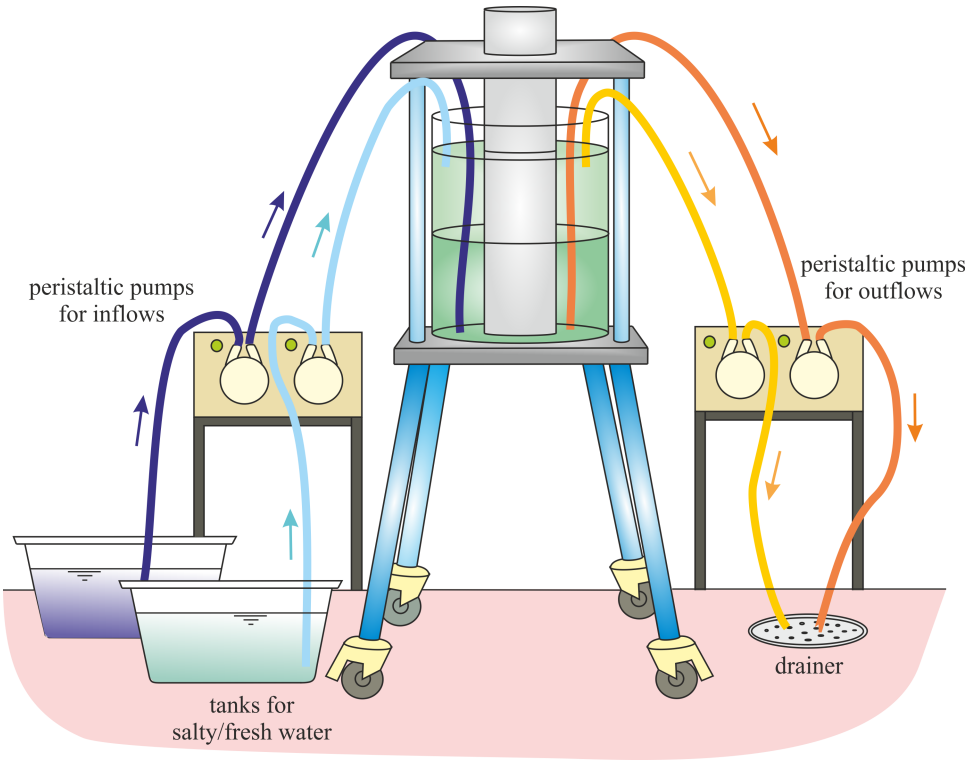

Figure 3.9: The Taylor-Couette tank at the Hydraulic Laboratory of Parma.

3.2.1 The Ultrasound Doppler Velocimetry Probes

To reconstruct the velocity field in the vertical, radial and azimuthal direction, 5 Ultrasound Velocity Profilers (UVPs, model DOP 2000 Signal Processing S.A, Switzerland, 2000), with a carrier frequency of 8 MHz, were arranged as sketched in figure 3.10. Seeding TiO_2 particles were injected into the fluid at the beginning of every experiment and before every data acquisition. The UVP probes emit bursts and receive echoes generated by reflection of particles or turbulent eddies, therefore the tip of the emitter/receiver must always be in contact with fluid. The positions (gates) of these targets is $x = c\Delta t/2$, where c is the celerity of ultrasounds in the fluid ($c = c_0 = 1500\,\mathrm{m\,s^{-1}}$ in fresh water) and Δt is the time interval between emission and receival of the echos. However, because c depends on the density ρ and temperature T of the fluid, the correct value for the gates, x_c was obtained as $\int_o^{x_c} \mathrm{d}x_c = (c(\rho, T)/c_0)\,\mathrm{d}x$, with $c(\rho, T)$ given by the formula suggested by Mackenzie (1981). One velocity profile along the axis of the ultrasonic cone, which diverges with a half angle of 1.2°, is computed by averaging a number of 128 burst emissions for the vertical probes and 256 burst emission for the radial and azimuthal probes. As the target position, the raw velocity profiles u were corrected as $u_c = u\,c(\rho, T)/c_0$. The correct alignment of the probe along the three principal dimensions was obtained when the echo of the tank wall (the bottom of the tank the vertical probes and the inner cylinder for the radial probe) hits the highest energy value at the expected distance from the tip of the UVP probe.

Probes A and B of figure 3.10 profile the vertical component of fluid velocity along the total depth of the fluid. The tip of the probes are positioned at 0.5 cm below the fluid free surface. Probe A is always at a fixed position $r_A = 5.0$ cm from R_2 (hence 3.5 cm from R_1). On the other hand, probe B can be moved along the radial direction: a series of measurement were carried out placing probe B at a distance $r = 0.5, 1.3, 2, 3, 4, 5, 6, 7$ and 8 cm from R_1.

Probe C is aligned along the radial direction and points inward. The probe C is "ultra-short", 1.2 cm long, and acquires data for a distance less than 7 cm from R_1, for all the depth of the fluid.

Eventually, the probe D and E measure the azimuthal and vertical components respectively. Probes D and E are "short", 2 cm long, and jointed to the conductivity probe at 2 cm above the electrodes, while probe C follows the position of the conductivity probe in time thanks to the supporting bar connected to the screw of the motor stepper.

Table 3.2.1 lists the number of profiles recorded by each probe, the pulse

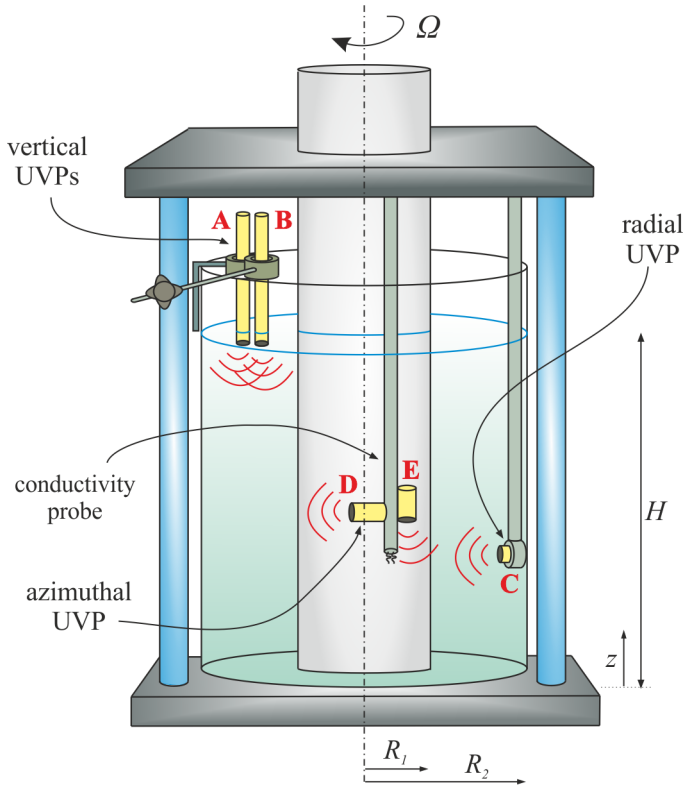

Figure 3.10: The Taylor-Couette tank at the Hydraulic Laboratory of DIA.

repetition frequency (P.R.F.), the spatial resolution along the probe axis in water, the minimum and maximum depths of the data recorded along the probe axis in fresh water, the frequency f representing the number of profiles recorded per second, and the accuracy of the velocity measurements. The minimum depth is due to a so high energy content in the region close to the tip of the emitter that the data are darkened.

Four multiplexer configurations are set on the software.

The first sequence of data (Configuration 1) is composed of 6000 profiles of probes B, C and D, for a total of 18 000 profiles, and it is repeated 9 times for the 9 radial positions of probe B. This means that, along the discrete radial grid, an amount of 6000 vertical velocity profiles are stored. Regarding probe C and D, during each of the nine sequences, they move along the vertical direction together with the conductivity probe, with probe D pointing downstream. The 6000 profiles of probe C are taken in approximately 400 seconds and correspond to a whole number of approximately 11 vertical

Probe	N° profiles	P.R.F. (Hz)	Spatial resolution (mm)	min depth (mm)	max depth (mm)	f (Hz)	accuracy (mm s^{-1})
			Configuration 1				
B	6000	3086	0.75	6.75	230.25	20	1.13
C	6000	4032	0.75	4.5	78.75	15	1.47
D	6000	7407	0.75	4.5	85.50	27	2.70
			Configuration 2				
E	2000	3086	0.56	5.25	50.0	21	1.13
			Configuration 3				
A	2000	3086	0.75	6.75	230.25	21	1.13
B	2000	3086	0.75	6.75	230.25	21	1.13
			Configuration 4				
D (2)	16000	4000	0.75	6.00	50.00	27	1.47

Table 3.1: Settings of the multiplexer configurations of the UVP probes.

excursions. On the other side, the 6000 profiles of probe D are cataloged in approximately 200 seconds, corresponding to a number of 5-6 total vertical excursions.

In the second configuration (Configuration 2), the only probe E is active and registers vertical velocity data for approximately 2 minutes at fixed heights, 1 cm spaced, in the range of $z = 2.5 - 23.5$ cm from the free surface. The correlation between the synchronized velocity and density data will be studied.

The third configuration (Configuration 3) alternates vertical velocity profiles from probe A and probe B 2000 times, with probe B positioned at 5 cm from R_2. The azimuthal distance between the two UVP probes is 4 cm. These data will be convenient when we analyze the temporal correlation between density waves.

Finally, in the last configuration (Configuration 4), probe D is arranged pointing upstream, with the axis forming an angle of $\alpha = 70°$ with the radial direction (see figure 3.11). Azimuthal velocity component is recorded at the gate 3.9 ± 0.2 cm distant from the conductivity probe and 2.7 cm from R_I. 16 000 profiles are recorded in approximately 10 minutes twice in a raw, for a total amount of 32 000 profiles in 20 minutes, which correspond

to 22 total vertical excursions. The split of the recordings is necessary for a faster data transcription on a text file.

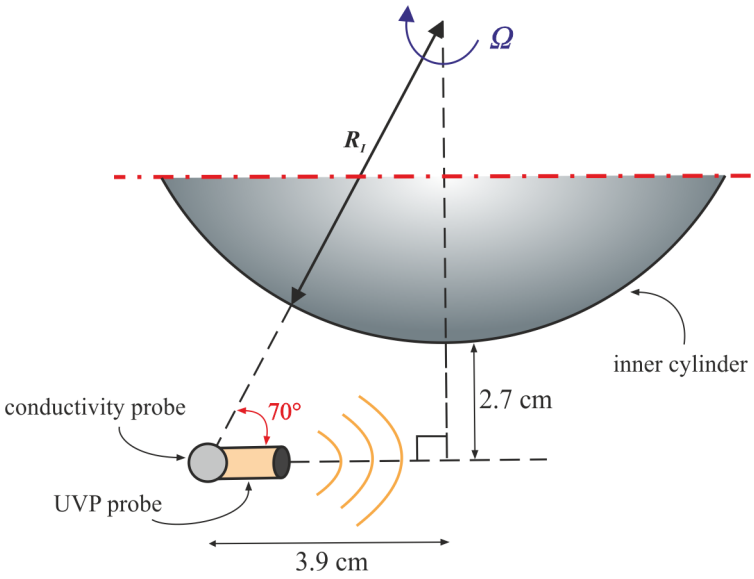

Figure 3.11: Configuration 4 of UVP probes.

3.2.2 Calibration of the conductivity probe

The conductivity probe used at Parma has two pins of micro USB type B connectors as electrodes, which are 5 mm long, 0.25 mm wide and 0.6 mm spaced out. The probe is plugged into a credit-card shaped platform, a four channel voltage stimulator and sampler composed of the Arduino and Conduino boards described in Carminati and Luzzatto-Fegiz (2017). Data are transmitted to a personal computer and controlled by a Matlab script after downloading a specific firmware. The standard sampling frequency is approximately 20 Hz (the time interval between two subsequent samples is $\mathrm{d}t = 48$ ms). In order to ground the Conduino electric circuit, a stainless steel bar is always plunged in the fluid.

Although the signal seems to be influenced by the presence of metallic compounds in contact with the fluid inside the tank, the positive feature of this device is that no fluid needs to be withdrawn from the tank. Because of the smaller geometry of this tank, the effects of the siphoning become significant.

In figure 3.12 five calibration curves are presented. The orange and

red curves are obtained in the total absence of metallic objects in the fluid with the exception of the grounding stainless steel bar. The last three calibration curves, the purple, light blue and green ones, are obtained after having attached three UVP probes to the conductivity probe. A downward shift is evident, but the calibration appears fairly enough stable in time.

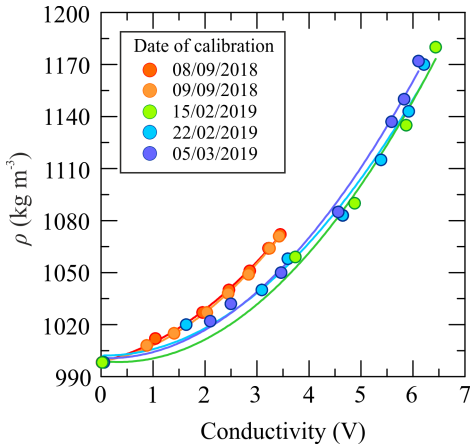

Figure 3.12: Calibration curve of the conductivity probe used at Parma.

Because salt ions move faster at higher temperatures, density measurements usually depend on the temperature. To quantify this dependence, we measure the conductivity of seven samples with different known salt contents in a range of temperature $T = 18 - 26°C$. The temperature is controlled by a thermostatic water bath. Figure 3.13 shows how the conductivity evolves with temperature for seven values of density, $\rho = 998.2, 1010, 1020, 1030, 1045, 1060, 1070\ \mathrm{kg\,m^{-3}}$, while figure 3.14 represents a contour plot, where conductivity is the x-axis, temperature is the y-axis and density is the false color.

The temperature dependence increases with the fluid density, as expected. For a given salt content, the conductivity, v, can be expressed as a function of temperature, T, in the form of

$$v = v_{ref}\left[1 + \alpha\left(T - T_{ref}\right)\right], \tag{3.3}$$

where v_{ref} is a reference value of conductivity at the temperature T_{ref}. According to our data, the coefficient of temperature dependance is $\alpha = 0.017 \pm 0.002$. However, the laboratory room temperature is almost constant during the experiments, taking care of not opening the windows to reduce temperature fluctuations, and calibrating the probe in the same temperature condition of the experiments.

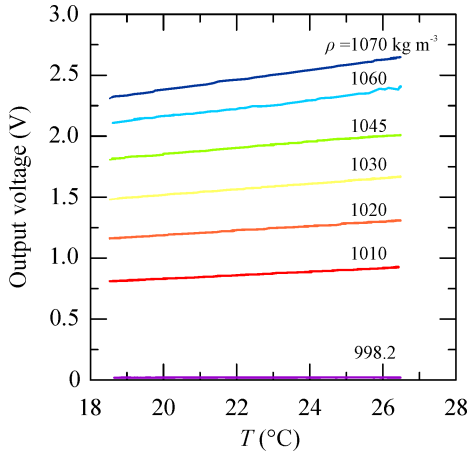

Figure 3.13: Output voltage dependence on temperature, for seven samples of known density at the nominal temperature of 22°C.

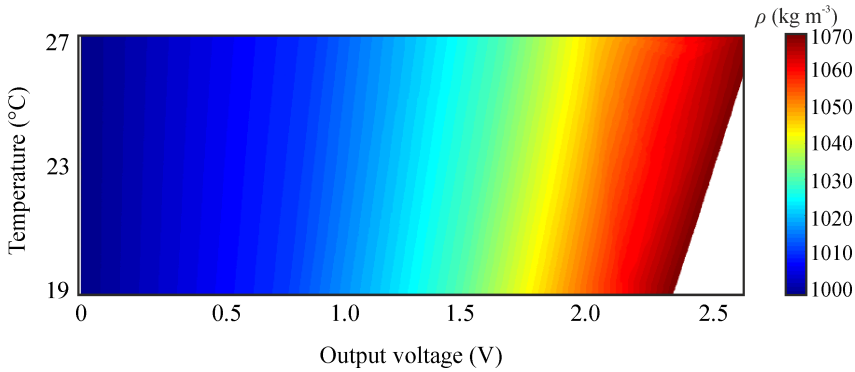

Figure 3.14: Color map of the output voltage dependence on temperature.

The conductivity probe is mounted on a home-made stepper motor with two stops setting the minimum and maximum height and the reverse of the motion. The position data are recorded using a position transducer but, because of the non-linearity at the tails, a pulley is used to reduce the excursion in order to be in the linear range of the transducer. The speed of the motor is set at maximum for the probe to profile the total depth of the fluid in 33 s.

In addition, in order to track the density and velocity waves traveling across the density jump, we made a larger twin-wire conductivity probe similar to the one used by Wessels and Hutter (1996). This probe is composed

of two stainless steel $\phi 1$ mm bars, 1 cm spaced, exposed to the fluid for a length of 1.8 cm, and insulated along the remainder of the length, as drawn in figure 3.15.

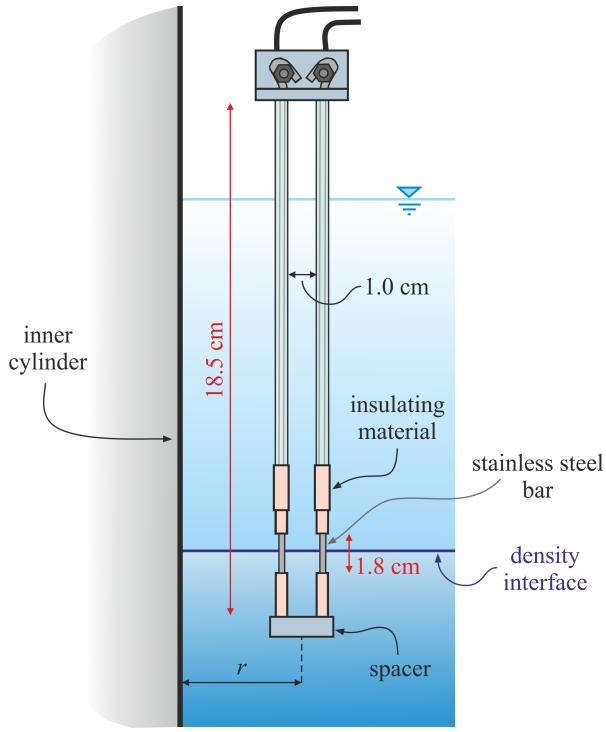

Figure 3.15: Home-made twin-wire conductivity probe.

The bars are electronically connected to a USB cable plugged onto one of the four available ports of the Conduino. The signal recorded is a mean of the conductivity of the bars over the exposure area. The conductivity is converted into height by using a 5^{th}-order fitting polynomial curve obtained by positioning the probe at known distances from the interface.

The y-axis of figure 3.16 represents the height of the interface with respect to the level of the probe during the experiment. The calibration points are collected inside a quiescent fluid, for each value of r, at the end of every experiment.

During the experiments, the probe remains in the same fixed position, with the mid-section of the exposed area of the bars at the same level of the density interface. The distance r between the probe and the inner cylinder can be varied manually and set at $r = 2, 4, 6$ cm. At each of the three values of r, the signal is recorded for 20 minutes at a frequency of approximately

20 Hz for $\Omega = 1.50 - 2.75\,\mathrm{rad\,s^{-1}}$.

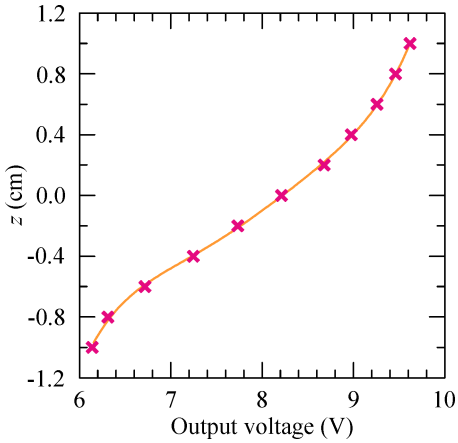

Figure 3.16: Typical calibration curve of the home-made twin-wire probe.

3.2.3 Calibration of the peristaltic pumps

The inflow and outflow rates are monitored by four 12 V DC dosing peristaltic pumps, each one connected to a electronic voltage stabilizer. The four pumps are calibrated with fresh water in the same conditions of the experiments, measuring the volume (mass/density) injected/extracted from the tank over time and the rounds per minutes (r.p.m.) using a digital tachometer, for a discrete voltage set range. The flow rate was double-checked during all the experiments and the expected and measured values always matched within an error of $\pm 4\%$. The four calibration curves are presented in figure 3.17*a*-*b*, where the voltage is associated with volume flux and r.p.m. respectively.

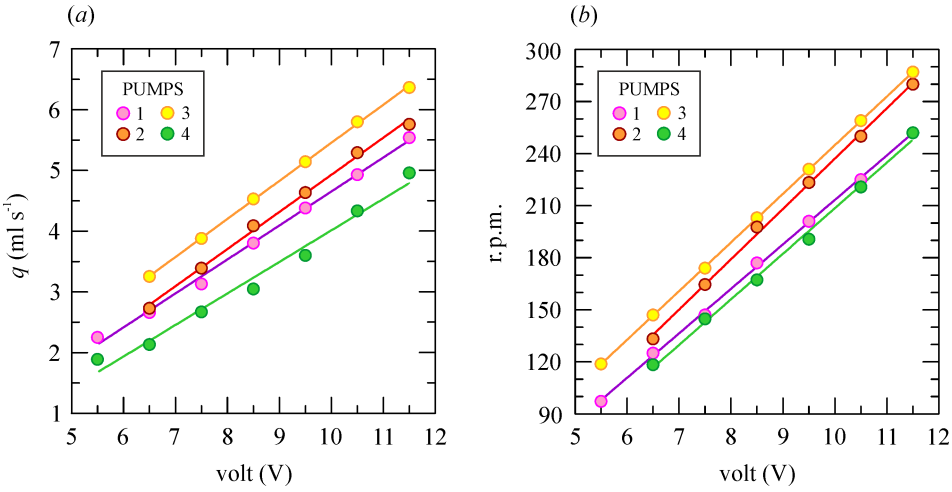

Figure 3.17: (a) Volume flux and (a) r.p.m. as functions of voltage for the four pumps.

3.2.4 Measurements of the density of the outflows

The density of the source solutions and the outflowing fluid are measured by a hydrometer, with accuracy of $1\,\mathrm{kg\,m^{-3}}$.

If the density is $\rho < 1070\,\mathrm{kg\,m^{-3}}$, the density is also checked by a refractomer, with accuracy of $3\mathrm{kg\,m^{-3}}$, sketched in figure 3.18. After placing one fluid drop onto the prism glass and covering it, it is possible to measure the density looking through the eyepiece at an internal scale, where the refractometer focuses the bended (blue filtered) light passing through the prism.

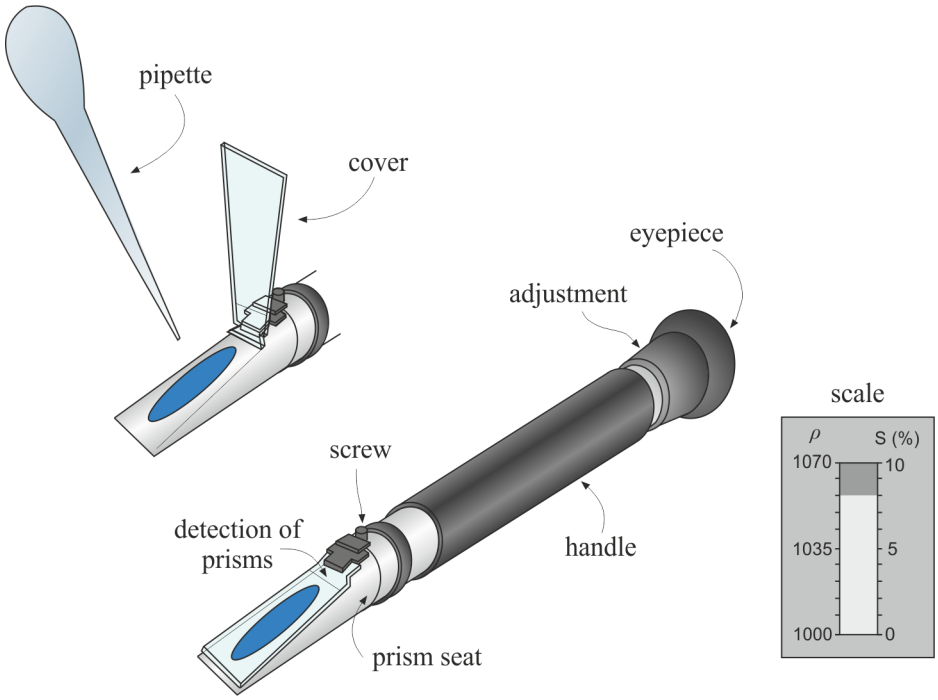

Figure 3.18: The digital refractomer.

Chapter 4

Results part I

In this chapter we present the data of the experiments carried out in the Taylor-Couette tank at BP Institute for Multiphase Flow, University of Cambridge This study has been published in Petrolo and Woods (2019).

The annulus is filled with fluid with different initial stratification. A source of fresh water and saline water are added at the top and bottom of the tank respectively. The turbulence generated by the rotation of the inner cylinder leads to a vertical transport of salt which will be extracted by the sink at the top of the tank. On the other hand, the fluid removed at the bottom is a measure of the remainder of the input salt flux.

The chapter is organized as follows. Section 4.1 deals with the measurement of the partitioning between the vertical buoyancy flux and upwelling flux in a turbulent flow in quasi steady state condition, for different values of rotation rate Ω and salinity of the bottom source fluid S_0. We also analyze how the vertical buoyancy flux and the mixing efficiency are related to the buoyancy frequency and discuss the implications for the salt and heat transport in the ocean. In section 4.2 we unbalance the outflowing flow rates to study the partitioning between turbulent and advective flux. We also propose a model for the salt diffusivity. Section 4.5 investigates the influence of the position of the sources and sinks on the stratification of the fluid in steady state, for fixed initial condition of the fluid in the tank and salinity of the supplied solutions to the system.

4.1 Measurement of the turbulent vertical flux

In these experiments we fill the gap of the Taylor-Couette tank with fluid up to a depth of $H = 40$ cm. We supply a continuous source of fresh water

at the top of the fluid and a source of saline solution at the bottom. In order to maintain a fixed volume in the tank, we extract the same volume flux as supplied, by two sinks located at the same depth of the respective sources. The flow rates of each source/sink is the same, so there is no advection due to net vertical fluid transport. The vertical buoyancy flux, if present, will be extracted by the sink at the top of the tank and will have a density greater than the fluid injected at the top (i.e. fresh water in our experiments). We consider the system as sketched in figure 4.1 and draw a horizontal plane at a generic depth dividing the fluid in two parts. The vertical turbulent buoyancy flux, $B_{vertical}$ is the flux crossing this plane.

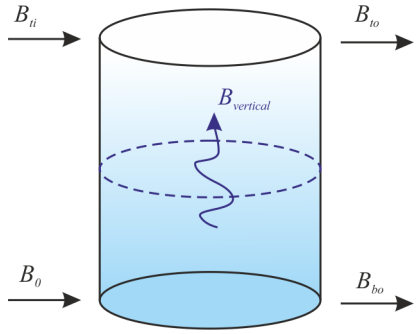

Figure 4.1: Sketch of the buoyancy fluxes supplied to or removed from the system and the vertical buoyancy flux through the system.

If we take into account the lower and upper portion of the fluid separately, in steady state we can write:

$$B_0 = B_{bo} + B_{vertical}, \tag{4.1}$$

$$B_{vertical} + B_{ti} = B_{to}. \tag{4.2}$$

where B_0, B_{bo} and B_{to} are the buoyancy flux of the bottom inflowing, bottom outflowing and top outflowing fluids respectively. As the salt injected at the top is always null ($B_{ti} \equiv 0$), $B_{vertical}$ must then equal B_{to}. In addition, because of the arbitrary choice of the depth of the horizontal plane, the vertical transport is the same at all depths of the fluid.

We can estimate the salt flux in two ways, according to the definition of salinity we take into account.

If salinity is the fraction of salt mass over the water mass of the solution ($\mathrm{g_{NaCl}\,kg_{H_20}}^{-1}$):

$$S_1 = \frac{m_{\mathrm{NaCl}}}{m_{\mathrm{H_2O}}} \tag{4.3}$$

the total mass of the solution is

$$\rho V = m_{\mathrm{NaCl}} + m_{\mathrm{H_2O}}, \tag{4.4}$$

where ρ and V are the density and volume of the solution. We can then express:

$$\begin{aligned} \rho V = m_{\mathrm{NaCl}} \left(1 + \frac{m_{\mathrm{H_2O}}}{m_{\mathrm{NaCl}}}\right) &= m_{\mathrm{NaCl}} \left(1 + \frac{1}{S_1}\right) \\ &= m_{\mathrm{NaCl}} \left(\frac{1 + S_1}{S_1}\right). \end{aligned} \tag{4.5}$$

The salt flux per unit area, F, is defined as the salt mass flowing in a unit of time, t, so

$$F = \frac{m_{\mathrm{NaCl}}}{t} = \rho\, Q\, \frac{S_1}{1 + S_1}. \tag{4.6}$$

Likewise, if salinity is the amount of salt mass dissolved in the total body of solution (%, or parts per thousands, ppt, if divided by a factor of 10),

$$S_2 = \frac{m_{\mathrm{NaCl}}}{m_{\mathrm{H_20+NaCl}}}, \tag{4.7}$$

the total mass of the solution is

$$\rho V = m_{\mathrm{NaCl}} + m_{\mathrm{H_2O}} = \frac{m_{\mathrm{NaCl}}}{S_2}. \tag{4.8}$$

In this case the salt flux per unit area is:

$$F = \frac{m_{\mathrm{NaCl}}}{t} = \rho\, Q\, S_2. \tag{4.9}$$

By comparing the two equations 4.6 and 4.9, we can find the relation between the two definitions of salinity:

$$S_2 = \frac{S_1}{1 + S_1}. \tag{4.10}$$

We use table 4.1 to convert the brix number, Bx, given by the refractometer, into density ρ and salinity S_1 (or S_2). Note that in table 4.1 the value of S_1 is given in $\mathrm{g\,l^{-1}}$ terms, but it is non dimensional considering the equivalence 1 l = 1 kg of water at ambient temperature, and considering the definition reported in equation 4.3.

Bx	ρ $\left(\mathrm{g\,cm^{-3}}\right)$	S_1 $\left(\mathrm{g\,l^{-1}}\right)$	S_2 (%)	Bx	ρ $\left(\mathrm{g\,cm^{-3}}\right)$	S_1 $\left(\mathrm{g\,l^{-1}}\right)$	S_2 (%)
0.0	0.9982	0.0	0.0	5.7	1.0326	50.4	4.8
0.1	0.9989	1.0	0.1	5.8	1.0333	51.5	4.9
0.3	0.9997	2.0	0.2	6.0	1.0340	52.6	5.0
0.4	1.0004	3.0	0.3	6.2	1.0355	54.9	5.2
0.5	1.0011	4.0	0.4	6.4	1.0369	57.1	5.4
0.6	1.0018	5.0	0.5	6.7	1.0384	59.3	5.6
0.8	1.0025	6.0	0.6	6.9	1.0398	61.6	5.8
0.9	1.0032	7.0	0.7	7.1	1.0413	63.8	6.0
1.0	1.0039	8.1	0.8	7.3	1.0427	66.1	6.2
1.1	1.0046	9.1	0.9	7.6	1.0442	68.4	6.4
1.2	1.0053	10.1	1.0	7.8	1.0456	70.7	6.6
1.4	1.0060	11.1	1.1	8.0	1.0471	73.0	6.8
1.5	1.0068	12.1	1.2	8.3	1.0486	75.3	7.0
1.6	1.0075	13.2	1.3	8.5	1.0500	77.6	7.2
1.7	1.0082	14.2	1.4	8.7	1.0515	79.9	7.4
1.8	1.0089	15.2	1.5	8.9	1.0530	82.3	7.6
2.0	1.0096	16.3	1.6	9.2	1.0544	84.6	7.8
2.1	1.0103	17.3	1.7	9.4	1.0559	87.0	8.0
2.2	1.0110	18.3	1.8	9.6	1.0574	89.3	8.2
2.3	1.0110	19.4	1.9	9.8	1.0588	91.7	8.4
2.4	1.0125	20.4	2.0	10.1	1.0603	94.1	8.6
2.6	1.0132	21.5	2.1	10.3	1.0618	96.5	8.8
2.7	1.0139	22.5	2.2	10.5	1.0633	98.9	9.0
2.8	1.0146	23.5	2.3	10.7	1.0647	101.3	9.2
2.9	1.0153	24.6	2.4	11.0	1.0662	103.8	9.4
3.0	1.0160	25.6	2.5	11.2	1.0677	106.2	9.6
3.2	1.0168	26.7	2.6	11.4	1.0692	108.6	9.8
3.3	1.0175	27.7	2.7	11.6	1.0707	111.1	10.0
3.4	1.0182	28.8	2.8	12.2	1.0744	117.3	10.5
3.5	1.0189	29.9	2.9	12.7	1.0781	123.6	11.0
3.6	1.0196	30.9	3.0	13.3	1.0819	129.9	11.5
3.7	1.0203	32.0	3.1	13.9	1.0857	136.4	12.0
3.9	1.0211	33.1	3.2	14.4	1.0894	142.9	12.5
4.0	1.0218	34.1	3.3	15.0	1.0932	149.4	13.0
4.1	1.0225	35.2	3.4	15.5	1.097	156.1	13.5
4.2	1.0232	36.3	3.5	16.1	1.1008	162.8	14.0
4.3	1.0239	37.3	3.6	16.6	1.1047	169.6	14.5

Table 4.1: For caption see next page.

Table 4.1: (Continued)

4.4	1.0246	38.4	3.7	17.1	1.1085	176.5	15.0
4.6	1.0254	39.5	3.8	18.2	1.1162	190.5	16.0
4.7	1.0261	40.6	3.9	19.3	1.1240	204.8	17.0
4.8	1.0268	41.7	4.0	20.4	1.1319	219.5	18.0
4.9	1.0275	42.8	4.1	21.5	1.1398	234.6	19.0
5.0	1.0282	43.8	4.2	22.5	1.1478	250.0	20.0
5.2	1.0290	44.9	4.3	23.6	1.1558	265.8	21.0
5.3	1.0297	46.0	4.4	24.7	1.1640	282.1	22.0
5.4	1.0304	47.1	4.5	25.7	0.1721	298.7	23.0
5.5	1.0311	48.2	4.6	26.8	1.1804	315.8	24.0
5.6	1.0318	49.3	4.7	27.9	1.1887	333.3	25.0

Table 4.1: Conversion table of Bx into density ρ and salinity S_1 or S_2.

4.1.1 Uncertainty of the measured fluxes

The uncertainty of the measurement of the volume flux, $Q = V/t = (m/\rho)\,t$, is

$$\frac{\mathrm{d}Q}{Q} = \frac{\mathrm{d}m}{m} + \frac{\mathrm{d}t}{t} + \frac{\mathrm{d}\rho}{\rho} \approx 9.24 \times 10^{-3}, \tag{4.11}$$

where $\mathrm{d}m = 0.1\,\mathrm{g}$, $\mathrm{d}t = 1\,\mathrm{s}$ and $\mathrm{d}\rho = 0.8\,\mathrm{kg\,m^{-3}}$. Consequently:

$$\frac{\mathrm{d}F}{F} = \frac{\mathrm{d}S_2}{S_2} + \frac{\mathrm{d}\rho}{\rho} + \frac{\mathrm{d}Q}{Q} \approx 0.01, \tag{4.12}$$

where $\mathrm{d}S_2 = 0.1\%$.

4.1.2 Experimental data

After an early transient regime, the system reaches an equilibrium and a steady-state condition. In steady state, the total mass in the system remains constant, therefore the salt flux supplied to the tank equals the salt flux removed from the tank. We deem the system to be in steady state if salinity of the two outflowing fluids do not change over a period of ≈ 60 minutes. Hereafter we will refer to salinity as the fraction of salt over the total mass of solution, as expressed by equation 4.7.

The salt fluxes of the sources and sinks are given by equation 4.9:

$$F_{ti} = Q\rho_{ti}S_{ti} \equiv 0, \tag{4.13}$$
$$F_0 = Q\rho_0 S_0, \tag{4.14}$$
$$F_{to} = Q\rho_{to}S_{to}, \tag{4.15}$$
$$F_{bo} = Q\rho_{bo}S_{bo}, \tag{4.16}$$

where the subscript "*ti*" refers to the top inflowing, "0" to the bottom inflowing, "*to*" to the top outflowing and "*bo*" tot he bottom outflowing fluid. However, it is convenient to show the results in terms of buoyancy fluxes, respectively defined as:

$$B_0 = gQ\frac{(\rho_0 S_0 - \rho_{ti}S_{ti})}{\rho_0}, \tag{4.17}$$
$$B_{to} = gQ\frac{(\rho_{to}S_{to} - \rho_{ti}S_{ti})}{\rho_0}, \tag{4.18}$$
$$B_{bo} = gQ\frac{(\rho_{bo}S_{bo} - \rho_{ti}S_{ti})}{\rho_0}, \tag{4.19}$$

where g is the gravity acceleration and $\rho_0 = 998.2\,\mathrm{kg\,m^{-3}}$ a density reference. The buoyancy flux supplied to the system at the top, B_{ti}, is null.

The suite of experiments and the main parameters are summarized in the table 4.2, where we report the rotation rate, Ω, the salinity of the bottom inflow S_0, the salinity of the top outflow S_{to} and bottom outflow S_{bo} in the steady-state, and the respective buoyancy fluxes B_0, B_{to} and B_{bo}. For all the experiments, the volume flux $Q = 5.45\,\mathrm{ml\,s^{-1}}$.

test	Ω	S_0	S_{to}	S_{bo}	B_0	B_{to}	B_{bo}
					$(\times 10^{-6})$	$(\times 10^{-6})$	$(\times 10^{-6})$
	$(\mathrm{rad\,s^{-1}})$	(%)	(%)	(%)	$(\mathrm{m^4\,s^{-3}})$	$(\mathrm{m^4\,s^{-3}})$	$(\mathrm{m^4\,s^{-3}})$
1	2.50	20.0	6.4	15.2	12.18	3.54	8.64
2	2.50	19.0	6.6	14.2	11.59	3.69	8.35
3	2.50	18.0	6.3	12.5	10.90	3.54	7.17
4	2.50	17.0	6.6	11.1	10.12	3.73	6.39
5	2.50	16.0	6.2	10.6	9.53	3.44	6.09
6	2.50	15.0	6.4	9.2	8.94	3.63	5.21
7	2.50	14.0	6.2	8.7	8.25	3.44	4.91
8	2.50	13.0	6.1	7.4	7.66	3.44	4.22
9	2.50	12.0	5.3	6.7	6.97	2.95	3.73

Table 4.2: For caption see next page.

Table 4.2: (Continued)

10	2.50	10.0	4.7	5.7	5.70	2.55	3.14
11	2.50	8.0	3.9	4.4	4.52	2.14	2.42
12	2.50	7.0	3.3	3.8	3.93	1.77	2.06
13	2.50	6.0	2.9	3.2	3.34	1.57	1.77
14	2.50	4.0	1.9	2.0	2.16	1.03	1.08
15	2.50	2.0	1.0	1.0	1.08	0.56	0.56
16	2.38	17.0	5.1	12.5	10.22	2.85	7.27
17	2.38	15.0	5.0	10.5	8.90	2.85	5.99
18	2.38	12.0	5.0	7.3	6.97	2.75	4.13
19	2.38	10.0	4.5	6.0	5.80	2.46	3.34
20	2.38	4.0	2.1	2.2	2.16	1.08	1.18
21	2.25	17.0	4.2	12.9	10.22	2.31	7.56
22	2.25	15.0	4.0	10.9	8.90	2.26	6.29
23	2.25	10.0	4.3	6.4	5.80	2.36	3.54
24	2.25	8.0	3.4	4.7	4.52	1.87	2.55
25	2.25	4.0	2.0	2.1	2.16	1.08	1.18
26	2.00	17.0	3.4	14.6	10.22	1.87	8.55
27	2.00	15.0	3.4	12.1	8.94	1.87	7.07
28	2.00	10.0	3.4	7.1	5.80	1.87	4.03
29	2.00	8.0	3.1	5.0	4.52	1.72	2.75
30	2.00	4.0	1.9	2.3	2.16	0.98	1.28
31	1.75	15.0	2.1	13.4	8.90	1.13	7.86
32	1.75	10.0	2.0	8.4	5.80	1.08	4.72
33	1.75	8.0	2.1	6.6	4.52	1.13	3.63
34	1.75	4.0	1.8	2.4	2.16	0.98	1.28
35	1.50	15.0	0.8	14.0	8.94	0.49	8.25
36	1.50	10.0	0.8	9.2	5.80	0.43	5.26
37	1.50	8.0	0.9	6.8	4.52	0.39	3.83
38	1.50	4.0	1.3	2.8	2.16	0.69	1.57
39	1.00	15.0	0.3	14.6	8.94	0.20	8.64
40	1.00	10.0	0.2	9.9	5.80	0.11	5.55
41	1.00	8.0	0.2	7.7	4.52	0.11	4.32
42	1.00	4.0	0.3	3.8	2.16	0.11	2.06

Table 4.2: Parameters of the experiments: the rotation rate Ω, the salinity of the bottom inflow S_0, top outflow S_{to} and bottom outflow S_{bo}, the buoyancy flux of the bottom inflow B_0, top outflow B_{to} and bottom outflow B_{bo}.

Figure 4.2 illustrates the vertical buoyancy flux, B_{to}, as a function of the buoyancy supplied at the base, for seven values of the rotation rate, in the range $\Omega = 1.00 - 2.50\,\mathrm{rad\,s^{-1}}$. For the highest values of Ω (i.e. $\Omega = 2.00 - 2.50\,\mathrm{rad\,s^{-1}}$), we observe that B_{to} increases linearly as the bottom source salinity is increased from zero, and eventually it reaches a maximum. This upper limit is maintained with any further increase in the source buoyancy flux, and the numerical value grows with Ω. On the other side, for the lowest values of rotation rate, $\Omega = 1.00 - 1.75\,\mathrm{rad\,s^{-1}}$, B_{to} is almost constant: we reckon that this constant value is already the maximum beyond which the vertical buoyancy flux does not increase anymore.

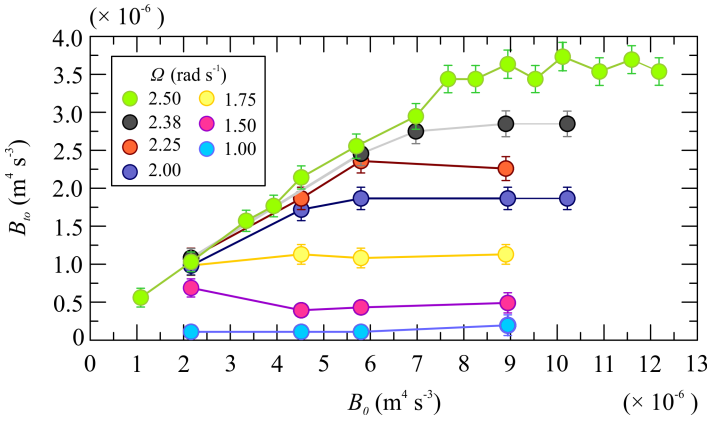

Figure 4.2: Variation of the vertical flux, B_{to}, with the bottom supplied buoyancy flux, B_0, for seven values of the rotation rate, Ω.

We then divide both the axis of figure 4.2 by the maximum value $B_{to,max}$, we can observe that the data collapse onto a single curve, as shown in figure 4.3. We then infer that, for small supplied buoyancy flux (i.e. small source salinity), the vertical buoyancy flux is supply limited. We will refer to this case as the *unsaturated* regime, and use empty circles to represent the data. On the other side, for larger supplied buoyancy flux (i.e. larger source salinity), the vertical transport is limited by turbulence. We will refer to this case as the *saturated* regime and use full circles as data symbols.

We notice that in the *unsaturated* regime, the vertical buoyancy flux B_{to} reaches the maximum value $B_{to,max}$ when the bottom source flux is approximately twice $B_{to,max}$. The slope 1:2 means that in this regime, the vertical buoyancy flux collected at the top of the tank is almost the same as the one removed at the bottom. As B_0 is boosted, the vertical flux cannot

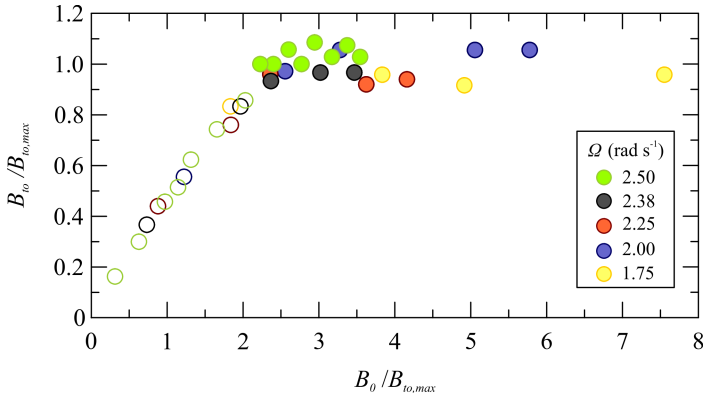

Figure 4.3: Variation of the normalized vertical salt flux, $B_{to}/B_{to,max}$, as a function of the non-dimensional bottom supplied salt flux, $B_0/B_{to,max}$, for $\Omega = 1.75 - 2.50\,\mathrm{rad\,s^{-1}}$.

grow any further as turbulence plays a limiting role and the remainder salinity remains at the bottom of tank, increasing B_{bo}.

To explore the partition between the diapycnal mixing B_{to} and the upwelling B_{bo} further, in figure 4.4*a-b* B_{to} and B_{bo} are expressed a fraction of the bottom source buoyancy flux and as a function of $B_0/B_{to,max}$.

In the *unsaturated* case, when $B_0/B_{to,max} \to 10^{-1}$, both B_{to} and B_{bo} approach $0.5B_0$. The consequence is that, in the steady state, ρ_{to} does not significantly differ from ρ_{bo} and the system becomes well-mixed. With the increase of the source salinity, the vertical buoyancy flux becomes a gradually smaller fraction of the total source buoancy flux, approaching $F_{to}/F_0 \to 0$ at low rotation rates, while the counterpart B_{bo} grows progressively to $B_{to}/B_0 \to 1$ at low rotation rates. The latter case corresponds to the system being strongly stratified, because of the larger density difference between the top and bottom outflows.

Because the upper limit of salt transport shows a dependence on Ω, we therefore compare the maximum values of $B_{to,max}$ for the seven rotation rates with the earlier findings of Woods et al. (2010) (hereafter W10). W10 stated that, for high enough density difference $\Delta\rho$ between two layers of equal depth H, the vertical transport of salt across the density interface does not depend on the density difference but on the time rate of change of the kinetic energy into potential energy. They found a law for the the transport of salt per unit area of the form:

$$f_s = (1.15 \pm 0.15) Ri^{-1}\, u_{rms}\, \Delta S\, \mathscr{A}\,(H/\Delta R)\,, \tag{4.20}$$

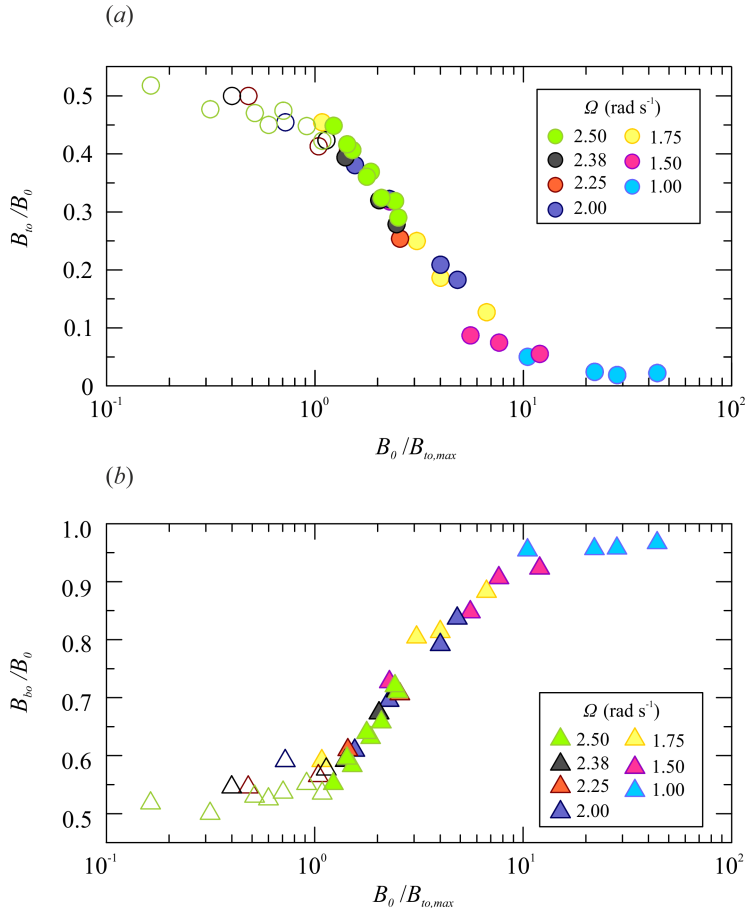

Figure 4.4: (a) Evolution of the vertical salt flux as a fraction of the supplied salt flux and (b) the upwelling salt flux as a fraction of the supplied salt flux, as a function of the supply buoyancy flux divided by the maximum turbulent transport.

where u_{rms} is the root mean square of the turbulent velocity fluctuations, Ri is the Richardson number defined as $Ri = g\,\Delta\rho\,H/\left(\rho_0\,u_{rms}^2\right)$, with ΔS the salinity contrast between two layers, and $\mathscr{A}\,(H/\Delta R)$ a non dimensional function of the ratio between the layer depth and the gap width ΔR, set to be unity.

W10 also analyzed the velocity field using the Particle Image Velocimetry (PIV) and found that

$$u_{rms} = 0.086\frac{\Omega R_1^2}{r}, \tag{4.21}$$

where r is the radial distance from the center of the inner cylinder R_1. Considering the following linear relation between density and salinity

$$\rho = \rho_0 \left(1 + \beta S\right), \tag{4.22}$$

where β is the dimensionless haline contraction coefficient $\beta \approx 0.727$, we can write the density contrast between two layers in terms of salinity contrast

$$\frac{\Delta\rho}{\rho_0} = \beta \Delta S. \tag{4.23}$$

Considering that $\mathscr{A}\left(H/\Delta R\right) = 1$, we can then substitute equations 4.21 and 4.23 into equation 4.20 to obtain:

$$\begin{aligned} f_s &= (1.15 \pm 0.15) \frac{\rho_0\, u_{rms}^2}{g\, \Delta\rho\, H}\, u_{rms}\, \Delta S \\ &= (1.15 \pm 0.15) \frac{u_{rms}^3}{g\, \beta\, H}, \\ &= (7.31 \pm 0.13) \times 10^{-4}\, \frac{\left(\Omega R_1^2\right)^3}{g\, \beta\, H}\, \frac{1}{r^3} \end{aligned} \tag{4.24}$$

If we integrate equation 4.24 over the area $\mathrm{d}A = 2\pi r\, \mathrm{d}r$,

$$\begin{aligned} F_s &= (7.31 \pm 0.13) \times 10^{-4}\, \frac{\left(\Omega R_1^2\right)^3}{g\, \beta\, H} \int_{R_1}^{R_2} \frac{2\pi r}{r^3}\, \mathrm{d}r \\ &= (4.60 \pm 0.82) \times 10^{-4}\, \frac{\left(\Omega R_1^2\right)^3}{g\, \beta\, H} \left(\frac{1}{R_1} - \frac{1}{R_2}\right), \end{aligned} \tag{4.25}$$

which gives the salt flux in terms of $[\mathrm{L}]^3\, [\mathrm{T}]^{-1}$. We shall multiply equation 4.25 by the salt density $\rho_{\mathrm{NaCl}} = 2160\, \mathrm{kg\, m^{-3}}$ to obtain the salt mass flux in $[\mathrm{M}]\, [\mathrm{T}]^{-1}$.

In figure 4.5 we compare the buoyancy flux of W10, $B_{W10} = gF_s/\rho_0$, with the maximum values of the *saturated* regime of the present study, as a function of $R_1^2 \Omega^3 \pi \left(R_2^2 - R_1^2\right)$. We find that the present data (green dots) are proportional to the cube of the rotation rate, Ω^3, and approximate the earlier findings of W10 (blue dots), provided that the vertical turbulent salt flux is expressed as:

$$F_{to,max} = \alpha R_1^2 \Omega^3 \pi \left(R_2^2 - R_1^2\right), \tag{4.26}$$

and the coefficient $\alpha = 1.30 \pm 0.05 \times 10^{-4}$.

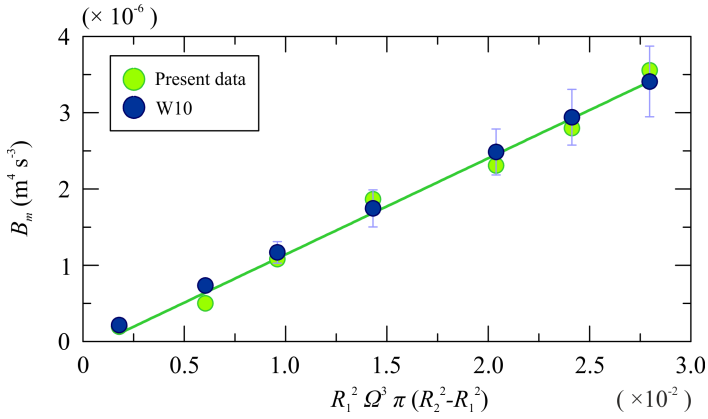

Figure 4.5: Maximum or *saturated* value of the vertical buoyancy flux B_{to} as a function of $R_1^2\Omega^3\pi\left(R_2^2 - R_1^2\right)$ for the present study (green dots) and W10 (blue dots).

4.1.3 Stability of the conductivity probe

The density field in the vertical direction is measured by the conductivity probe continuously in time. The accuracy and stability of the probe signal is checked before processing the data. Firstly, we calculate the total mass of salt at a time t, $M(t)$, by integration of the density profile along the total depth of the fluid, H:

$$M(t) = \int_0^H \rho(z,t)\, A\, dz, \tag{4.27}$$

where $A = \pi(R_2^2 - R_1^2)$ is the cross area of the tank. We have considered the density constant in the radial direction. Secondly, we compare this result with the total mass of salt evaluated by means of the the mass balance between external (inflowing-outflowing) fluxes and the rate of change of salt mass inside the tank:

$$\frac{\mathrm{d}M(t)}{\mathrm{d}t} = (F_0 + F_{ti}) - (F_{to} + F_{bo})\,. \tag{4.28}$$

Differentiating equation 4.28 yields:

$$M(t) = M_0 + \frac{dM(t)}{dt}dt \tag{4.29}$$

where M_0 is the initial salt content of the fluid in the tank. In figure 4.6 we report four typical examples which refer to experiments 4, 5, 24 and 36

of table 4.2. In all cases, neglecting some early time small discrepancies, we note a good agreement between the signal of the probe (gray line) and the density of external flows measured by the refractometer (red dots). The difference between the signals is always less than 1%. The constant salt mass in the last $\approx$ 60 minutes marks the achievement of the steady-state condition.

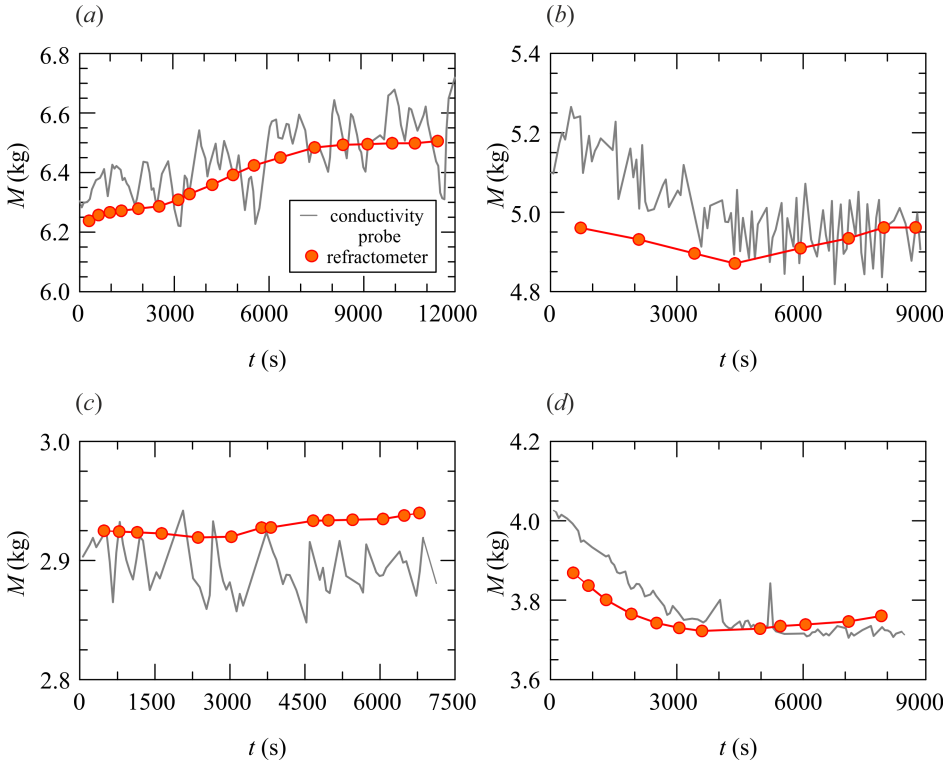

Figure 4.6: Time variation of the salt mass in the fluid, estimated using a conductivity probe and a refractometer, for test (a) n° 4, (b) 5, (c) 24, and (d) 36 of table 4.2.

4.1.4 Steady state density profile: stratified or well mixed

In this paragraph we are going to present the time evolution of the density field for some of the experiments listed in table 4.2. In figures 4.7-4.11 we show the superposition of instant final profiles (gray lines) and the time averaged density profiles (coloured lines) for different values rotation rate and source salinity. The time average is computed over the quasi steady

state period, of approximately 60 minutes. The number in the upper right corner indicates the salinity of the bottom source fluid S_0. The density evolution from a specific initial condition (well mixed, two-layer or linear stratification) towards a steady-state distribution is then shown in a panel underneath, with density at each depth shown in false colour as a function of depth and time.

In figure 4.7, experiments 15, 12, 10, 9, 7, 5, 3 and 1 of table 4.2 are represented, with increasing salinity of the source bottom fluid from 2% up to 20%, for fixed rotation rate $\Omega = 2.50\,\mathrm{rad\,s^{-1}}$. Figure 4.7*a*-*b* shows four experiments in the *unsaturated* regime, while figure 4.7*a*-*b* shows four experiments in the *saturated* regime.

In the case of really low bottom source salinity (i.e. $S_0 = 2 - 7\%$), the system commences as a well-mixed initial system, but only for $S_0 = 2\%$ the fluid remains in a homogenous state with $\rho \approx 1007\,\mathrm{kg\,m^{-3}}$. As S_0 is increased to 7%, the fluid becomes weakly stratified with a small density difference between the free surface and the bottom of the fluid, $\Delta\rho \approx 3\,\mathrm{kg\,m^{-3}}$.

When S_0 approaches $10-12\%$, the density gradient increases. The initial two-layer fluid goes through an early adjustment which gradually erodes the density interface in the middle of the tank. This transition involves a series of layers migrating upwards and leads to a linear stratification. These layers are more visible in the *saturated* regime, when $S_0 = 14 - 20\%$. The fresh water supplied at the top of the tank drives the formation of layers of low buoyancy which mix with the surrounding fluid, becoming progressively more dense and propagating downwards.

As the salinity of the lower source increases, the continuous stratification in the center of the tank increases in strength. With a further increase in S_0 to a value of $S_0 = 18 - 20\%$, a region of high salinity develops at the base of the system, separated by a sharp interface from the more weakly stratified upper layer. The excess salinity, which cannot be vertically transported by turbulence, leads to larger salt fluxes being removed from the sink at the bottom of the tank.

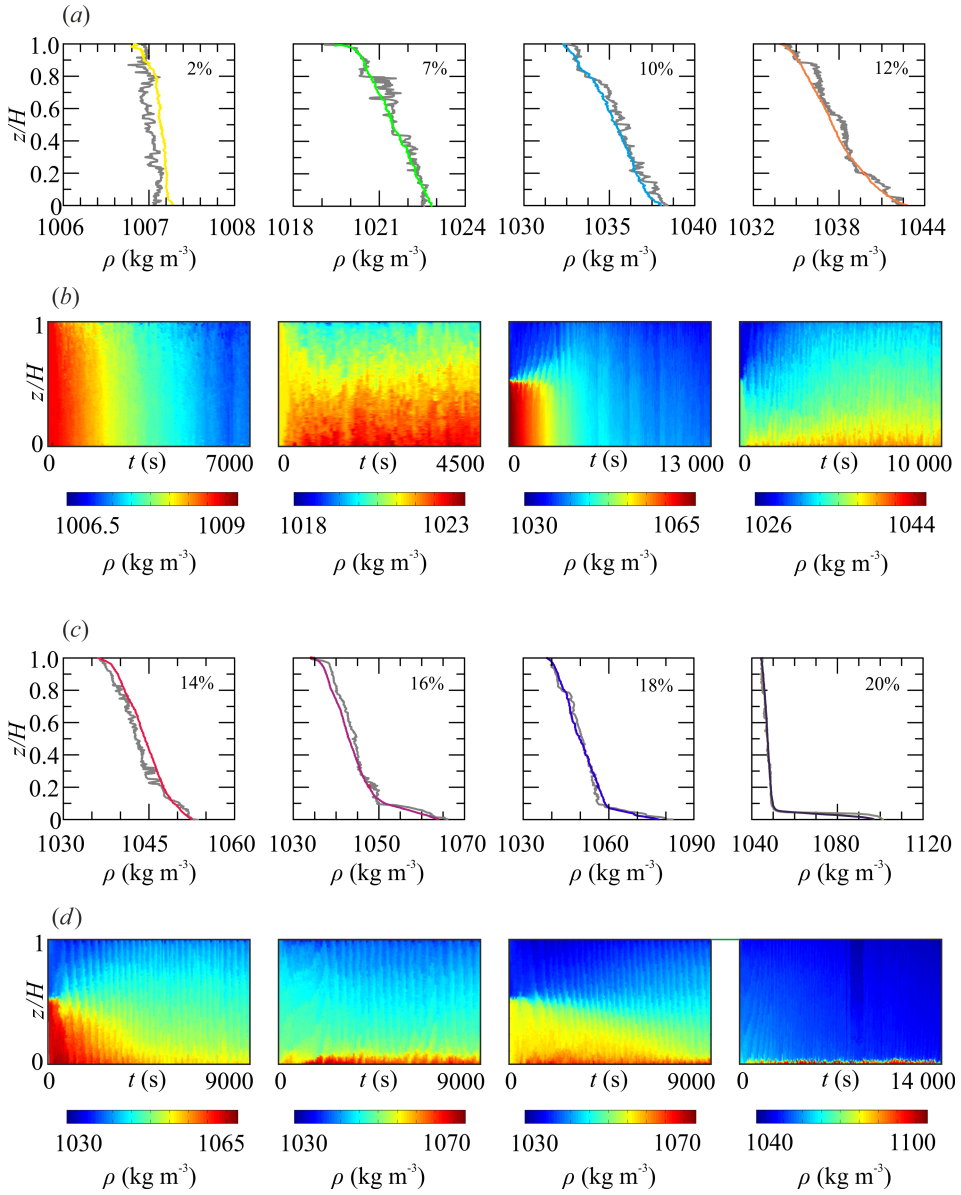

Figure 4.7: (*a*) Instant (gray lines) and time averaged (coloured lines) density profiles for test n° 15, 12, 10 and 9; (*b*) time series of density profiles for each experiment of panel *a*; (*c*) instant (gray lines) and time averaged (coloured lines) density profiles for test n° 7, 5, 3 and 1; (*d*) time series of density profiles for each experiment of panel (*c*)

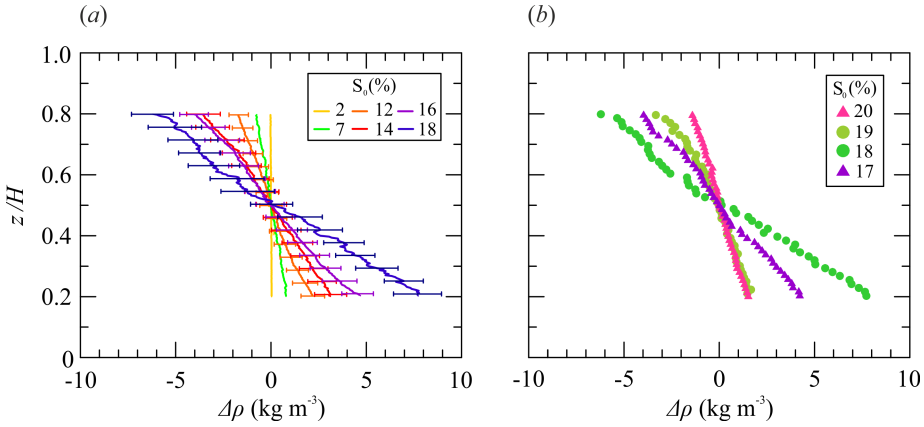

Figure 4.8: (a) Density gradients of six experiments with increasing source salinity and $\Omega = 2.50\,\mathrm{rad\,s^{-1}}$; ($b$) density gradients of two experiments with an initial two-layer stratification ($S_0 = 17 - 18\%$), and two experiments with an initial linear stratification ($S_0 = 19 - 20\%$).

In figure 4.8a we report the time averaged density gradients of six experiments introduced in figure 4.7, with error bars corresponding to two standard deviations. The data are horizontally shifted so that the density profiles meet at zero point in the middle of the tank. We can observe that the gradient becomes steeper as the source salinity is increased. However, the steepness of the gradient does not increase linearly with S_0 in the *saturated* regime. In figure 4.8b the tests with $S_0 = 20\%$ and $S_0 = 19\%$ commence with a linear stratification and are immediately ran after tests with $S_0 = 17\%$ and $S_0 = 18\%$ respectively, which started with a two-layer stratification. As a consequence, it appears that the density gradient depends on the initial condition if the vertical flux is limited by turbulence.

In figure 4.9, experiments 20, 19, 18, 17, and 16 of table 4.2 are represented, with increasing salinity of the source bottom fluid up to 17%, for fixed rotation rate $\Omega = 2.38\,\mathrm{rad\,s^{-1}}$. Again, we envisage larger density gradients with the increasing of the bottom source salinity, but it is interesting to note that the initial density difference may control the steady state condition. Figure 4.9c-d shows two experiments in the *saturated* regime: for the experiment in the left panel the input salinity is $S_0 = 15\%$ and the initial density difference $\Delta\rho_0 \approx 20\,\mathrm{kg\,m^{-3}}$, while in the right panel $S_0 = 17\%$ and the initial density difference $\Delta\rho_0 \approx 35\,\mathrm{kg\,m^{-3}}$. In the first case, a series of layers develop at the top and migrate downwards, mixing in the tank, and the initial density interface disappears leading to a continuous linear

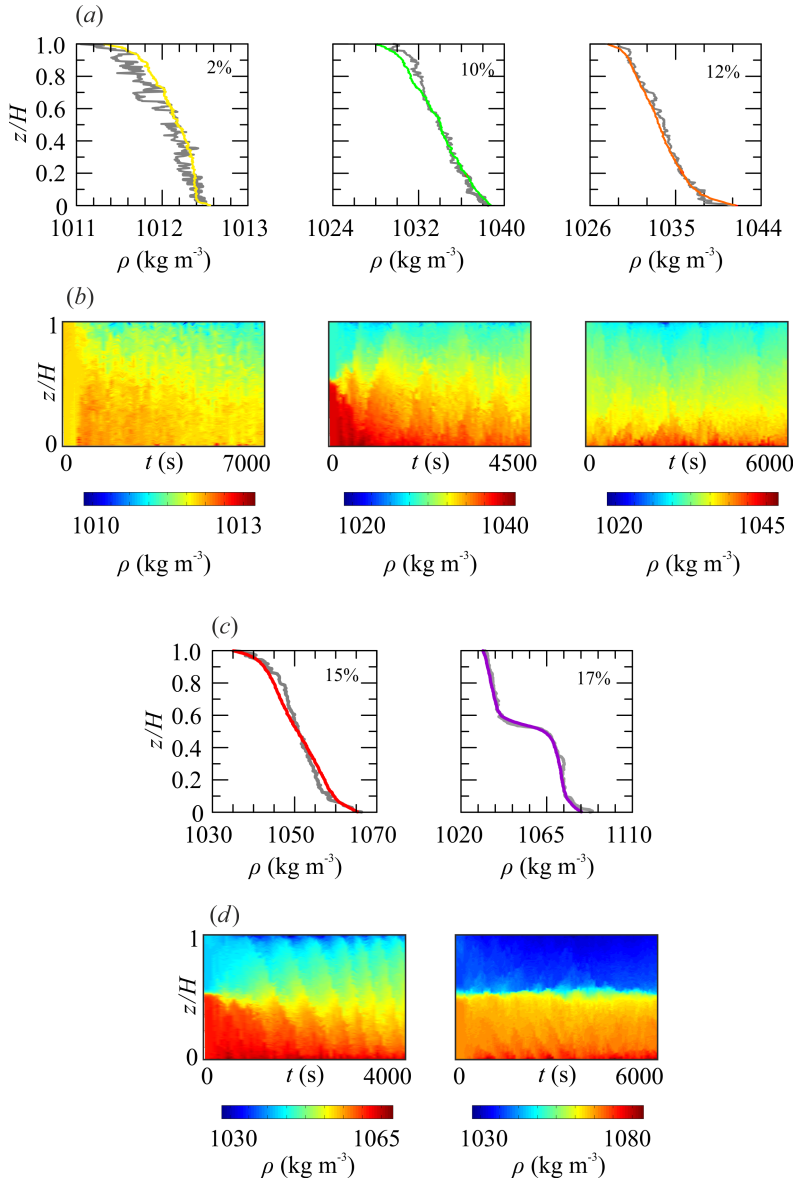

Figure 4.9: (*a*) Instant (gray lines) and time averaged (coloured lines) density profiles for test n° 20, 19, and 18; (*b*) time series of density profiles for each experiment of panel *a*; (*c*) instant (gray lines) and time averaged (coloured lines) density profiles for test n° 17, and 16; (*d*) time series of density profiles for each experiment of panel *c*.

density gradient. In the second case, the layers seem to form at the interface and migrate towards the top and bottom boundary layers. The turbulent transport tends to reduce the density difference between the two layers, but the initial density difference seems to be so large that the top and bottom inflows mix with the top and bottom layer, respectively, keeping the density contrast almost constant in time. The density interface is not so sharp, and spans from $0.4H$ to $0.6H$.

Figure 4.10 shows the time series evolutions and density gradients of experiments of 34, 33, 32 and 31 of table 4.2, with increasing salinity of the source bottom fluid up to 15%, for fixed rotation rate $\Omega = 1.75\,\mathrm{rad\,s^{-1}}$. For $S_0 = 4\%$ the fluid evolves in a linear stratification, but with increasing S_0 a boundary layer forms at the bottom of the tank. The growth of a boundary layer at the top of the tank depends on the initial density profile. If the initial density contrast at the interface, or initial density gradient, are sufficiently weak, and with a mean value of density not so much grater than ρ_0, the fluid will mix with the source of fresh water at the top without generating a discontinuity.

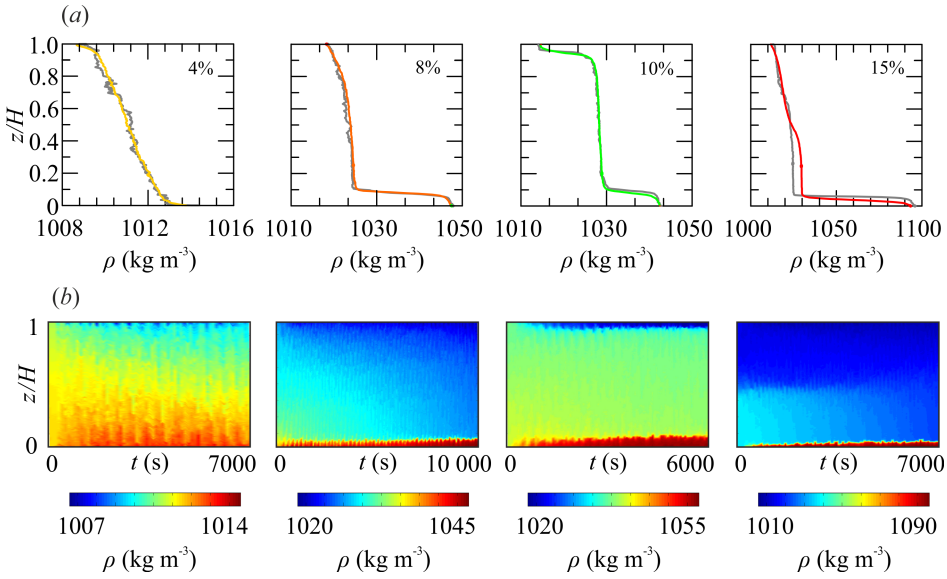

Figure 4.10: (a) Instant (gray lines) and time averaged (coloured lines) density profiles for test n° 34, 33, 32 and 31; (b) time series of density profiles for each experiment of panel a.

If Ω drops to $\Omega = 1.00\,\mathrm{rad\,s^{-1}}$, a salinity contrast between the top and bottom sources of just 4% is already too high to mix the fluid completely

and two boundary layers separated by sharp interfaces develop at top and bottom of the fluid. Figure 4.11 illustrate experiments 42, 41, 40, and 39 of table 4.2.

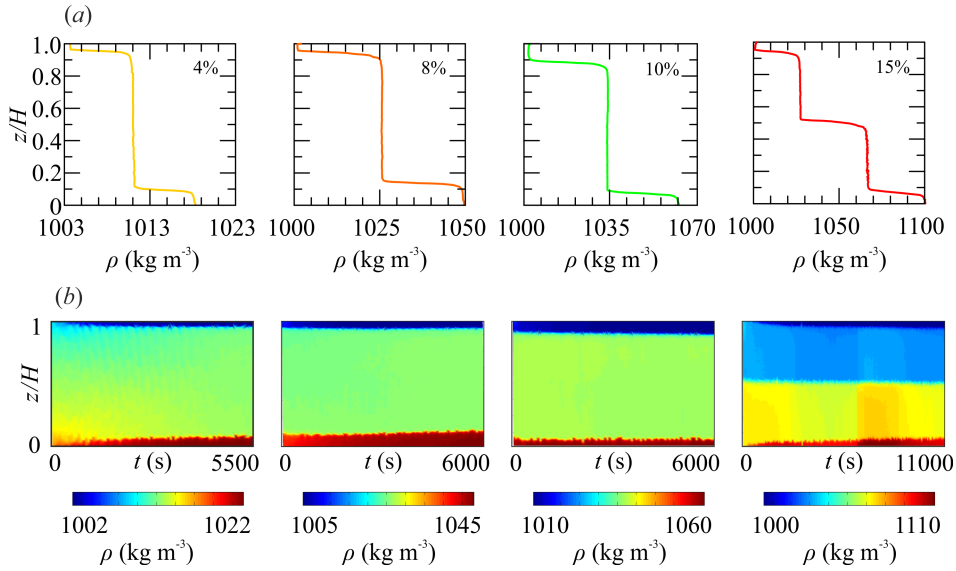

Figure 4.11: (*a*) instant (gray lines) and time averaged (coulored lines) density profiles for test n° 42, 41, 40, and 39; (*b*) time series of density profiles for each experiment of panel *a*.

4.1.5 Measurement of the buoyancy frequency N

The buoyancy frequency, N, is given by

$$N = \sqrt{-\frac{g}{\rho_0}\frac{\partial \rho}{\partial z}}, \tag{4.30}$$

and it is the maximum frequency of the oscillations of displaced parcels (or internal waves) supported by a stable stratification (when the density gradient $\partial\rho/\partial z < 0$, with z being positive upwards, N is a real number). The value of N is also a measure for the local density stratification.

test	Ω (rad s^{-1})	S_0 (%)	N^2 (s^{-2})	Initial Condition	test	Ω (rad s^{-1})	S_0 (%)	N^2 (s^{-2})	Initial Condition
1	2.50	20.0	0.164	LS	22	2.25	15.0	0.229	LS
2	2.50	19.0	0.205	LS	23	2.25	10.0	0.184	2L
3	2.50	18.0	0.450	2L	24	2.25	8.0	0.143	2L
4	2.50	17.0	0.348	2L	25	2.25	4.0	0.023	WM
5	2.50	16.0	0.327	LS	26	2.00	17.0	0.246	2L
6	2.50	15.0	0.327	2L	27	2.00	15.0	0.172	2L
7	2.50	14.0	0.266	2L	28	2.00	10.0	0.246	LS
8	2.50	13.0	0.184	2L	29	2.00	8.0	0.213	LS
9	2.50	12.0	0.160	2L	30	2.00	4.0	0.049	WM
10	2.50	10.0	0.106	2L	31	1.75	15.0	0.491	2L
11	2.50	8.0	0.057	2L	32	1.75	10.0	0.082	LS
12	2.50	7.0	0.044	2L	33	1.75	8.0	0.086	LS
13	2.50	6.0	0.025	WM	34	1.75	4.0	0.074	WM
14	2.50	4.0	0.012	WM	35	1.50	15.0	-	2L
15	2.50	2.0	0.002	WM	36	1.50	10.0	-	2L
16	2.38	17.0	0.553	2L	37	1.50	8.0	0.061	2L
17	2.38	15.0	0.491	2L	38	1.50	4.0	0.131	LS
18	2.38	12.0	0.192	LS	39	1.00	15.0	-	2L
19	2.38	10.0	0.205	2L	40	1.00	10.0	-	3L
20	2.38	4.0	0.020	WM	41	1.00	8.0		3L
21	2.25	17.0	0.196	2L	42	1.00	4.0	-	WM

Table 4.3: Parameters of the experiments: the rotation rate, Ω, the bottom source salinity, S_0, the buoyancy frequency, N^2 and the initial condition of the experiment (LS is linear stratification, 2L is two-layer, 3L is three layer, WM is well-mixed).

In our experiments, we consider the density ad a function of only z, so $\partial\rho/\partial z = \mathrm{d}\rho/\mathrm{d}z$. The density gradient is evaluated in the range $z = (0.2 - 0.8)\,H$, which appears to be less influenced by the boundary layers. In case of a final two-layer configuration, we evaluate $\mathrm{d}\rho/\mathrm{d}z$ separately for the upper layer, in the range $z = (0.6 - 0.8)\,H$, and lower layer in the range $z = (0.2 - 0.4)\,H$, obtaining approximately the same value. The density gradient is time averaged over the period of quasi steady-state.

In table 4.3 we report the value of the buoyancy frequency and the initial condition of the experiments already listed in table 4.2. We also rewrite the rotation rate Ω and the salinity of the bottom source S_0. The initial condition is indicated by the following abbreviations: LS for a linear stratification, 2L for a two-layer stratification, 3L for a three-layer stratification and WM for a well-mixed fluid.

In figure 4.12*a* the vertical buoyancy flux, normalized with the maximum value given by equation 4.26 is shown as a function N, while in figure 4.12b we rescale the buoyancy frequency with Ω. We note that this rescaling of the data leads to a single relationship between the buoyancy flux as a fraction of the maximum vertical transport, and the scaled stratification. For relatively weak source buoyancy fluxes, it follows that the salinity flux does depend on the vertical stratification. This is analogous to the conditions close to overturn as reported by Woods et al. (2010) and Oglethorpe et al. (2013), where the vertical flux increase as the initial buoyancy frequency N_0 and Ri decreases, in the limit $N_0 < 2\,\mathrm{s}^{-1}$ and $2 < Ri < 4$. However, in the present case, in the supply limited regime the system reaches a steady state and the flux decreases monotonically with decreasing vertical stratification. On the other side, for higher source buoyancy fluxes, the vertical transport does not depend on the stratification in steady state condition anymore. As we can see from table 4.3, in the turbulence limited regime, the value of N could depend on the initial stratification, as it appears to be smaller if the initial system is linear stratified (i.e. experiments 1 and 2 in case of $\Omega = 2.50\,\mathrm{rad\,s}^{-1}$, or experiment 18 in case of $\Omega = 2.38\,\mathrm{rad\,s}^{-1}$).

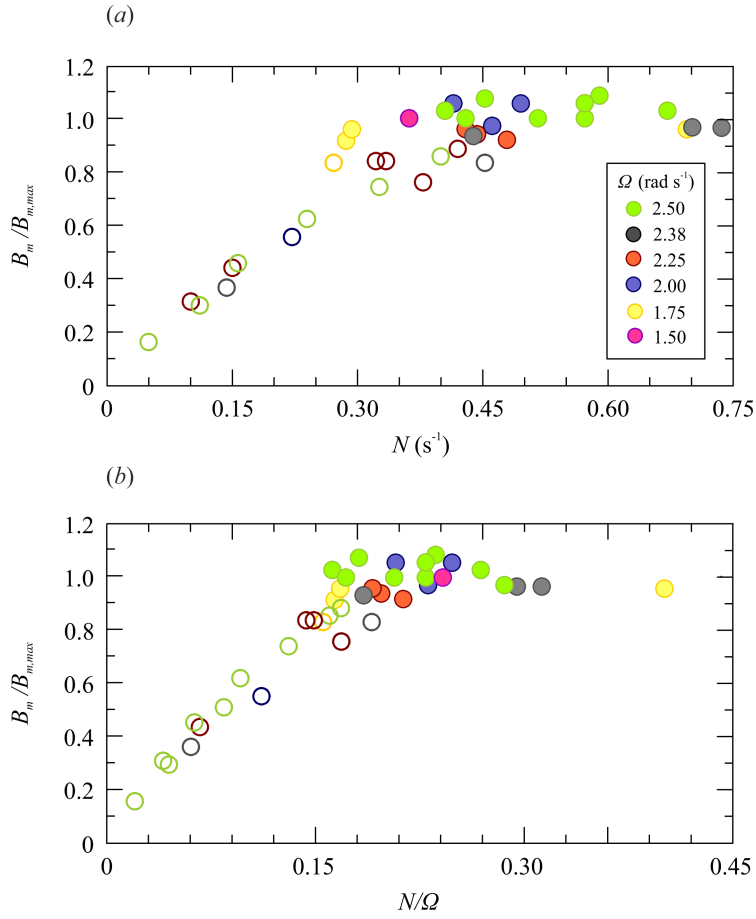

Figure 4.12: The normalized vertical buoyancy flux $B_{to}/B_{to,max}$ as a function of (a) the buoyancy frequency N and (b) the normalized buoyancy frequency N/Ω.

4.1.6 The influence on the initial condition

We repeated some experiments with a different initial condition of the fluid to explore how this could affect the steady state stratification. We report the new experiments in table 4.4, together with the reference experiments of table 4.2. The new experiments are denoted with an extra "bis" and all started with a well mixed system, except for experiment 15bis which commenced with a two-layer stratification.

test	Ω ($\mathrm{rad\,s^{-1}}$)	S_0 (%)	N^2 ($\mathrm{rad^2\,s^{-2}}$)	Initial Condition
5	2.50	16.0	0.327 ± 0.082	LS
5bis	2.50	16.0	0.491 ± 0.164	WM
7	2.50	14.0	0.266 ± 0.082	2L
7bis	2.50	14.0	0.450 ± 0.164	WM
9	2.50	12.0	0.160 ± 0.082	2L
9bis	2.50	12.0	0.295 ± 0.098	WM
13	2.50	2.0	0.025 ± 0.021	WM
13bis	2.50	2.0	0.04 ± 0.021	2L
21	2.25	17.0	0.196 ± 0.082	2L
21bis	2.25	17.0	0.239 ± 0.137	WM
23	2.25	10.0	0.184 ± 0.036	2L
23bis	2.25	10.0	0.287 ± 0.082	WM
24	2.25	8.0	0.143 ± 0.028	2L
24bis	2.25	8.0	0.102 ± 0.028	WM

Table 4.4: Parameters of the experiments: the rotation rate, Ω, the bottom source salinity, S_0, the buoyancy frequency, N^2 and the initial condition of the experiment (LS is linear stratification, 2L is two-layer, 3L is three layer, WM is well-mixed.

In figure 4.13 we illustrate the comparison between the steady state density profiles of the initially stratified fluid (S) (purple line) and initially well-mixed (WM) fluid (orange line) for the experiments at $\Omega = 2.50\mathrm{rad\,s^{-1}}$, with error bars corresponding to one standard deviation. In the top right corner we display the source bottom salinity. In all cases the density profiles collapse fairly well, meaning that the stratification does not depend significantly on the initial condition of the fluid. The colour maps represent the time series of the density field for the initially stratified and well mixed systems.

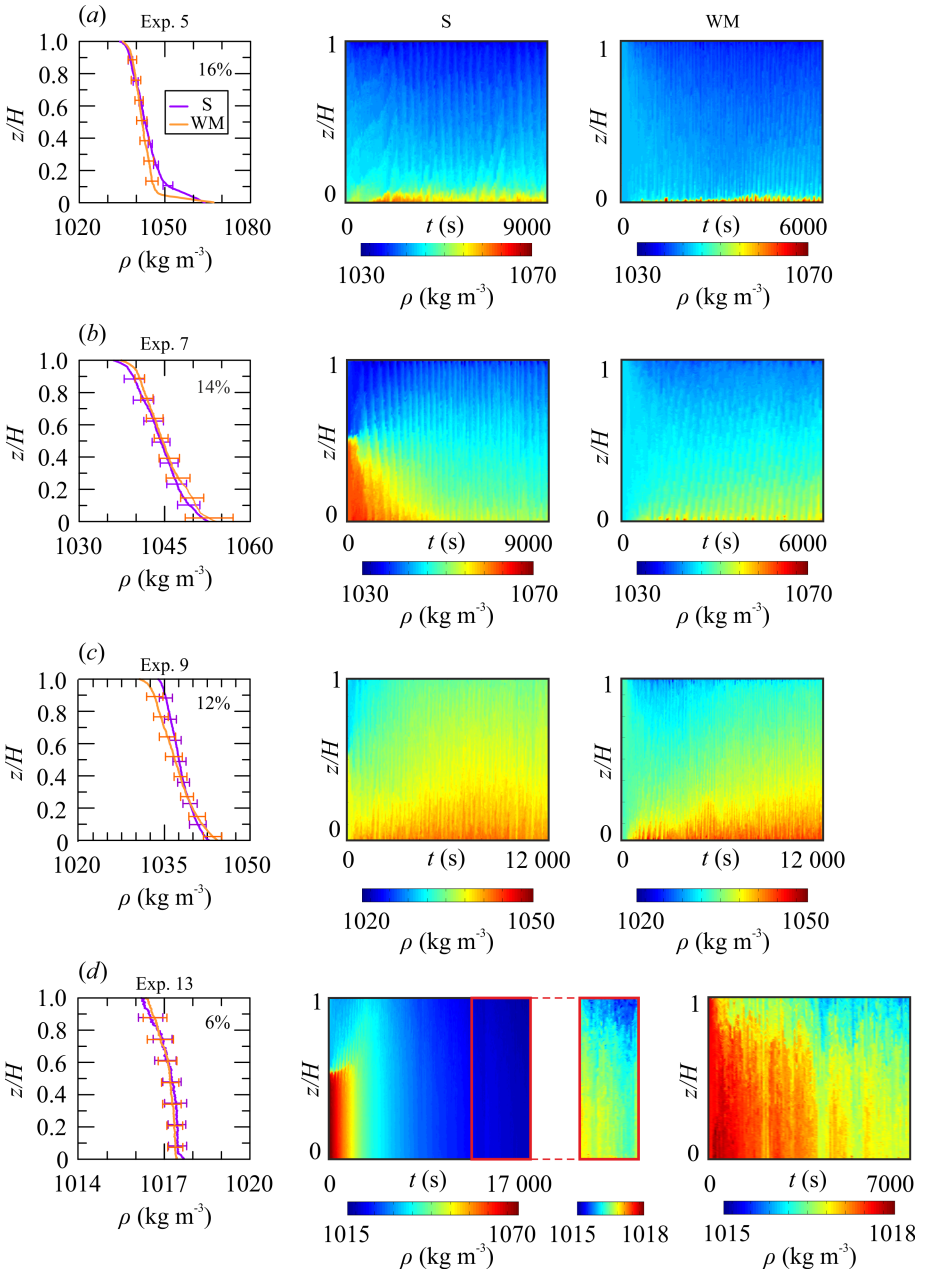

Figure 4.13: Steady state density profiles of an initial WM fluid (orange line) and stratified (S) fluid (purple line), time series density profiles as a function of height with density shown in false colour for (*a*) experiment 5, (*b*) experiment 7, (*c*) experiment 9, and (*d*) experiment 13 of table 4.4.

It is interesting to discuss the case of experiment 13bis (figure 4.13*d*), which starts with a two-layer stratification. The initial top layer has a salt content of 5% (i.e. $\rho \approx 1070\,\mathrm{kg\,m^{-3}}$) while the initial bottom layer has a salt content of 10% (i.e. $\rho \approx 1035\,\mathrm{kg\,m^{-3}}$). The vertical transport of salt gradually reduces the density difference between the two layers until the density of the system is equal to the initial top layer, $\rho \approx 1035\,\mathrm{kg\,m^{-3}}$ (green stripe on the left contour plot of figure 4.13*d*). Afterward, the density continuously decays to a value of $\rho \approx 1017\,\mathrm{kg\,m^{-3}}$, which is approximately half the density of the bottom source fluid $\rho_{bo} \approx 1041\,\mathrm{kg\,m^{-3}}$. As the initial stratification is very far from the equilibrium, the experiment takes almost 5 hours to reach the steady state condition. The false colour in the enlarged picture of the last 60 minutes of the experiment show a colour bar fairly similar to the experiment commenced with a well mixed fluid, shown in the right contour plot of figure 4.13*d*.

In figure 4.14 we represent the comparison between the steady state density profiles of the initially stratified fluid (S) (purple line) and initially well-mixed (WM) fluid (orange line) for the experiments at $\Omega = 2.25\mathrm{rad\,s^{-1}}$, with error bars corresponding to one standard deviation. While figure 4.14*b*-*c* refer to two experiments in the supply limited regime and exhibit a similar time evolution of the density field, figure 4.14*a* deserves greater attention. In case of initial two-layer stratification, the fresh water source at the top and the saline source at the base tend to mix with the top and bottom layer respectively, increasing the density contrast at the interface. The density interface at the center of the tank will last forever if no other perturbations affect the flow field. On the contrary, the initial well mixed fluid becomes linearly stratified and a dense boundary layer develops at the bottom of the tank. If we compare the density profiles in the top half portion of the tank, we find a very good superposition. Again, the buoyancy frequency does not show a significant dependence on the initial condition, even if density discontinuities persist or appear on the basis of the initial stratification.

Therefore we conclude that the initial stratification does not influence the buoyancy frequency at the equilibrium. The discrepancies between the mean values of N obtained from an initially stratified or well-mixed fluid fall within the error bars.

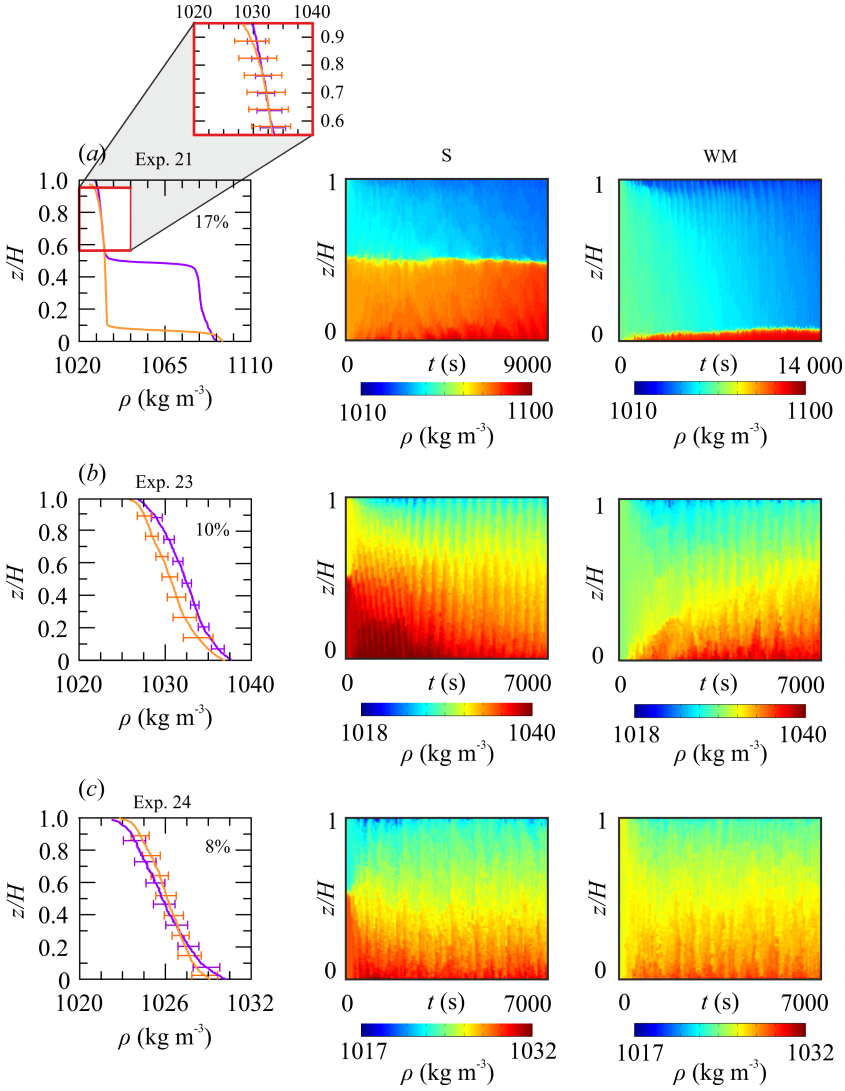

Figure 4.14: Steady state density profiles of an initial well-mixed WM fluid (orange line) and stratified (S) fluid (purple line); time series density profiles as a function of height with density shown in false colour for (a) experiment 21, (b) experiment 23 and (c) experiment 24 of table 4.4.

4.1.7 The influence of the sources and sinks position

In order to check the influence of the sources and sinks position, we ran some experiments switching the position of the source and sink of the fluids

flowing out of the tank, as shown in figure 4.15. Now the top source and top sink are close to each other in the middle of the gap, while the bottom source and sink are far apart, close to the outer and inner cylinder, respectively.

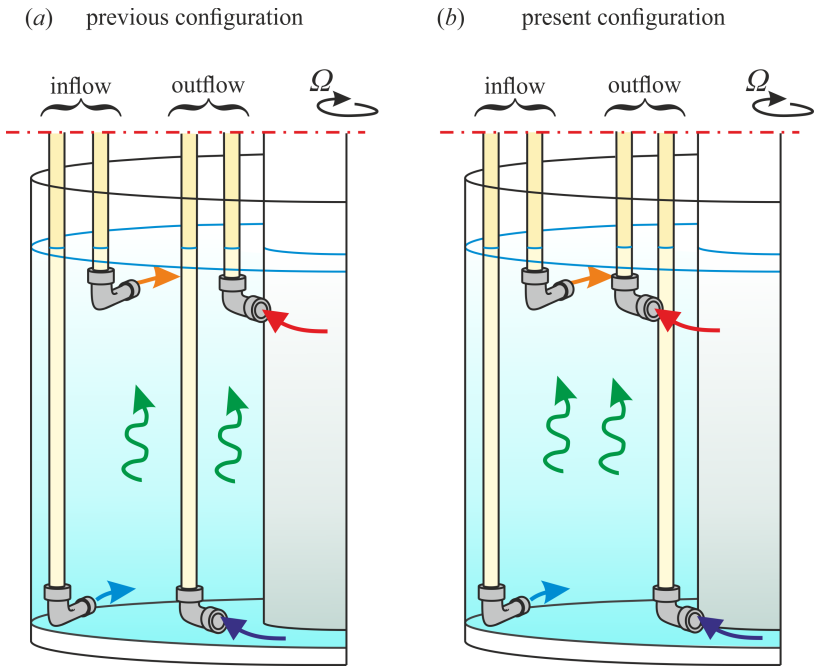

Figure 4.15: (*a*) Previous and (*b*) present radial positions of the sources and sinks of buoyancy.

The suite of these additional experiments is listed in table 4.5.

The results obtained with the new set-up are represented with pink dots in figure 4.16 and compared with the previous results which are reported with grey gots. Figure 4.16*a* shows the evolution of the vertical buoyancy flux as a fraction of the *saturated* value with respect to the supply buoyancy flux, scaled with the *saturated* value. In the inset of figure 4.16*a*, an enlargement of the region close to origin exhibits a decrease of the vertical salt transport in the supply limited regime for the new set-up. This reduction amounts to $13 \pm 6\%$. Unfortunately we carried out only one experiment in the turbulence limited regime, and repeated twice. The reduction of the vertical flux in this case appears to be even larger and approximately equal to 30%. It would be interesting to have more data in the *saturated* regime.

test	Ω	S_0	S_{to}	S_{bo}	B_0	B_{to}	B_{bo}	$\Delta B_{bo}/B_{max}$	N^2
					$(\times 10^{-6})$	$(\times 10^{-6})$	$(\times 10^{-6})$		
	$(\mathrm{rad\,s^{-1}})$	(%)	(%)	(%)	$(\mathrm{m^4\,s^{-3}})$	$(\mathrm{m^4\,s^{-3}})$	$(\mathrm{m^4\,s^{-3}})$	(%)	$(\mathrm{s^{-2}})$
A	2.50	15.0	4.1	11.2	8.94	2.26	6.48	-33	0.479
B	2.50	15.0	4.4	10.8	8.94	2.55	6.19	-24	0.420
C	2.50	7.0	2.8	4.3	3.93	1.57	2.36	-12	0.172
D	2.50	6.0	2.3	3.8	3.34	1.28	2.06	-18	-
E	2.50	4.0	1.8	2.2	2.36	0.98	1.18	-5	0.009
F	2.38	3.0	1.3	1.7	1.67	0.69	0.98	-16	0.007
G	2.25	7.0	2.6	4.4	3.93	1.47	2.46	-12	0.049
H	2.25	6.0	2.2	3.8	3.34	1.28	2.06	-14	0.049
I	2.25	3.0	1.3	1.7	1.67	0.69	0.98	-16	0.010
J	2.25	2.3	1.2	1.4	1.28	0.59	0.79	-5	0.010
K	2.00	3.0	1.2	1.8	1.67	0.69	0.98	-7	0.015
L	2.00	2.3	1.1	1.5	1.28	0.59	0.79	0	0.013
M	1.75	3	1.1	1.9	1.67	0.59	1.08	-20	0.023
N	1.75	2.3	1.1	1.6	1.28	0.59	0.88	0	0.020

Table 4.5: Parameters of the experiments: the rotation rate Ω, the salinity of the bottom inflow S_0, top outflow S_{to} and bottom outflow S_{bo}, the buoyancy flux of the bottom inflow B_0, top outflow B_{to} and bottom outflow B_{bo}, the reduction in the vertical transport $\Delta B_{bo}/B_{max}$, the buoyancy frequency N^2.

As a consequence of the reduced vertical transport, the flux subtracted at the base is greater, leading to an increase of the buoyancy frequency, N. Figure 4.16b shows the scaled vertical buoyancy flux with the maximum vertical transport as a function of the scaled buoyancy frequency, N/Ω. The data in the new set-up are subjected to an horizontal and vertical shift with respect to the previous set-up.

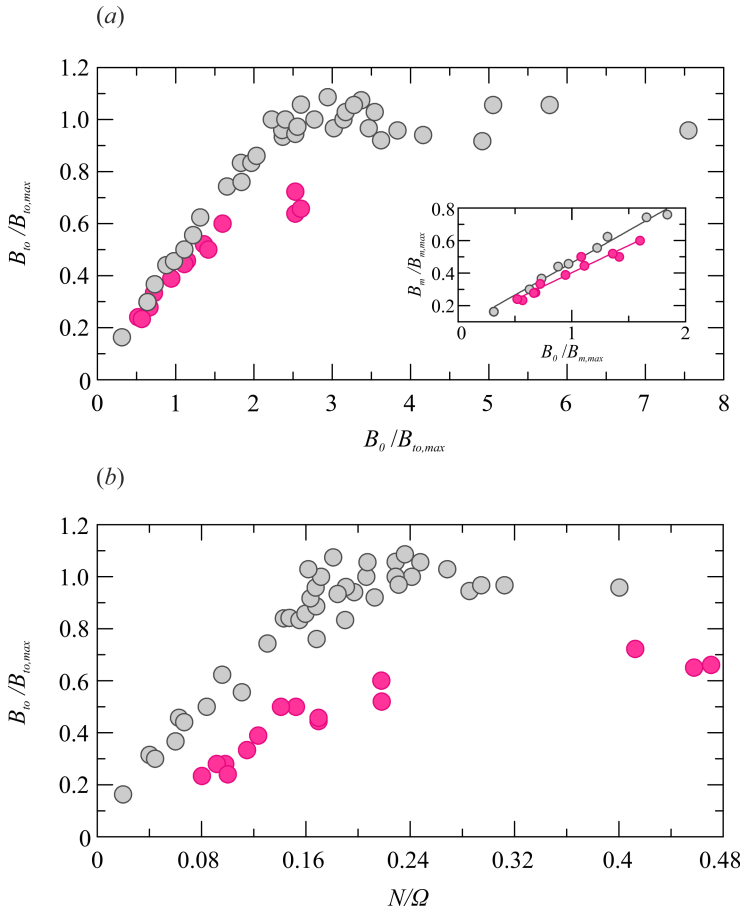

Figure 4.16: The normalized vertical buoyancy flux $B_{to}/B_{to,max}$ as a function of (a) the the supplied buoyancy flux as a fraction of the maximum vertical transport $B_0/B_{to,max}$ and (b) the normalized buoyancy frequency N/Ω.

The position of the source and sinks of buoyancy seems to play then a significant role in the mixing process. The reduced distance between the top source and sink may prevent fresh water from completely mixing with

the fluid inside the tank. A possible reason is that the fresh buoyancy may suffer the effects of the outflowing process as soon as it is injected. On the other hand, the increased distance between the bottom source and sink dense water may allow the dense solution to mix long before it is removed from the system. As a consequence, the bottom source salinity flux appears to be dominant on the top fresh water flux.

The arrangement of this set-up could simulate an imbalanced contribution between the fresh water flux and saline flux.

4.1.8 Mixing efficiency

The mixing efficiency Γ could be estimated by $\Gamma = b_{to}/\mathcal{E}$, where b_{to} is the vertical flux of buoyancy per unit area and $\mathcal{E}$ is the rate of dissipation of turbulent kinetic energy per unit area. $\mathcal{E}$ is defined as the ratio of the radial average of the root mean square velocity fluctuations, $\langle u_{rms}^3 \rangle$, and the eddy length-scale, L:

$$\mathcal{E} = \frac{1}{L} \frac{\int_{R_1}^{R_2} u_{rms}^3 2\pi r \mathrm{d}r}{\int_{R_1}^{R_2} 2\pi r \mathrm{d}r}. \tag{4.31}$$

The PIV measurements reported in Woods et al. (2010) have shown that $u_{rms}(r) = 0.086\, \Omega\, R_1^2/r$, and if we use this turbulent field as an approximate description of the present flow, we can express $\mathcal{E}$ as

$$\mathcal{E} = \frac{1}{L} \left(0.086\, \Omega\, R_1^2\right)^3 \frac{2\,(R_2 - R_1)}{R_1 R_2\,(R_2 + R_1)}. \tag{4.32}$$

By substituting $R_1 = 0.10$ m and $R_2 = 0.25$ m, yields

$$\mathcal{E} = \frac{1.45 \times 10^{-4}\, \Omega^3 R_1^3}{L}. \tag{4.33}$$

The eddy length-scales appear to have order of $L = 2-4$ cm, as observed by dispersion and mixing of dye streaks in the flow. A picture of the dye streak taken by a camera placed on the top of tank is shown in figure 4.17.

In the *saturated* regime, where the vertical flux is controlled by turbulence, we find that the horizontally averaged vertical buoyancy flux per unit area is

$$b_{to,max} = 1.30 \times 10^{-4} \Omega^3 R_1^2, \tag{4.34}$$

suggesting a constant value for the mixing efficiency

$$\Gamma_{max} = \frac{b_{to,max}}{\mathcal{E}} = 0.18 - 0.36. \tag{4.35}$$

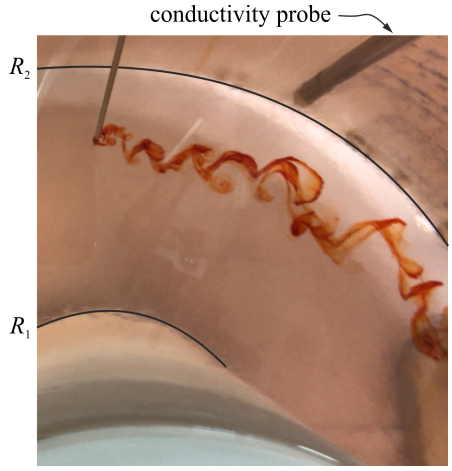

Figure 4.17: Dye dreaks within the flow.

The order of Γ_{max} is consistent with the often quoted value of $\Gamma = 0.2$, originally estimated by Osborn (1980).

If we define the Froude number as $Fr = u_{rms}/(NL)$, and considering that $u_{rms} \propto \Omega$, we notice that $Fr \propto (N/\Omega)^{-1}$. Therefore, in the turbulence limited regime, the vertical buoyancy flux (i.e. the mixing efficiency) should not depend on the inverse of Fr.

On the other hand, as the source flux decreases, the vertical buoyancy flux seems to be limited by the source supply rather than the turbulence, and it depends linearly on the scaled stratification N/Ω, so it should depend linearly also on the inverse of Fr. We can write then the following law for buoyancy flux b:

$$b_{to} = b_{to,max} \frac{Fr_c}{Fr}, \tag{4.36}$$

and for the mixing efficiency, Γ:

$$\Gamma = \Gamma_m \frac{Fr_c}{Fr}, \tag{4.37}$$

in the limit of $0.1 < 1/Fr < 1/Fr_c$ or $Fr_c < Fr < 10$.

According to equation 4.37 the mixing efficiency decreases with increasing Froude number in the range $0.1 < Fr < 10$.

The vertical buoyancy flux does not depend on the stratification any further if the Froude number is below the critical value $Fr_c = 1.0 \pm 0.3$.

Γ_m is shown as a function of the inverse of the Froude number in figure 4.18. On top of the plot, an additional blue x-axis indicates the value of Fr.

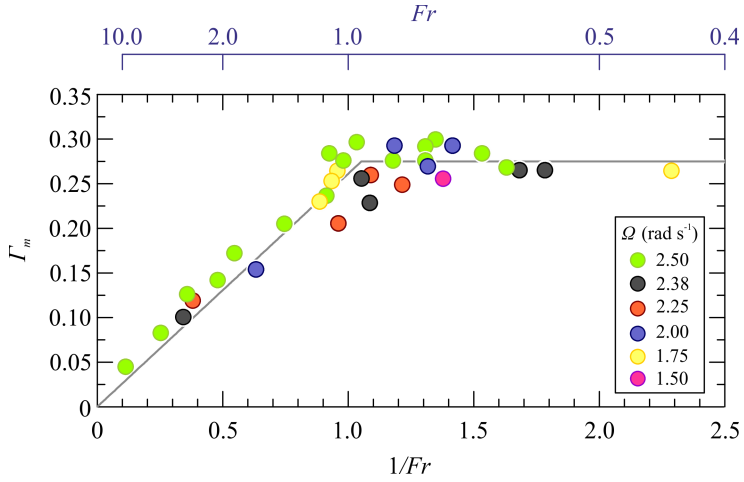

Figure 4.18: The mixing efficiency Γ_m as a function of the inverse of the Froude number.

Maffioli et al. (2016) also found a constant value of $\Gamma \approx 0.33$ for low values of Fr, although it reaches a maximum of $\Gamma \approx 0.50$ at $Fr = 0.3$. In their calculations, the mixing efficiency appears to decrease with Fr^{-1} in the range $0.3 < Fr < 1.5$, although there are only four data available, approaching a value of $\Gamma \approx 0.10$ at $Fr \approx 1.5$. For $Fr > 1.5$, Γ is smaller than 0.05 and follows a Fr^{-2} scaling. This latter behavior cannot be tested by our apparatus, as the system becomes well mixed for values of Fr larger than 10, when the the mixing efficiency is expected to be $\Gamma < 0.05$.

4.2 Turbulence plus advection

A series of experiments were carried out keeping the same total flow rate injected in the tank as in section 4.1, $Q_0 = 10.9\,\mathrm{ml\,s^{-1}}$, but changing $\lambda = Q_{to}/Q_0$, the fraction of volume flux extracted at the top of the tank Q_{to} with respect to Q_0. The buoyancy imposed at the top of the tank is always null, while the rotation rate is kept fixed to $\Omega = 2.50\,\mathrm{rad\,s^{-1}}$. We also varied the salinity of the bottom source of fluid, S_0.

In case of a complete balance between the two outflowing fluids as in section 4.1, no advection is present and λ is equal to 0.5.

We list the main parameters of the new experiments in table 4.6.

test	λ	S_0 (%)	S_{to} (%)	S_{bo} (%)	B_{to} ($\times 10^{-6}$) ($m^4\ s^{-3}$)	B_{bo} ($\times 10^{-6}$) ($m^4\ s^{-3}$)	N^2 (s^{-2})
1	0.2	17	6.7	10.8	1.45	10.05	0.430
2	0.2	15	6.3	9.7	1.36	8.86	0.295
3	0.2	13	5.8	8.2	1.24	7.41	0.221
4	0.2	10	4.6	6.0	0.98	5.34	0.143
5	0.2	8	3.9	4.6	0.83	4.05	0.053
6	0.2	6	3.0	3.2	0.60	2.79	0.018
7	0.4	17	6.7	11.4	2.89	7.87	0.450
8	0.4	15	6.6	10.0	2.85	6.84	0.368
9	0.4	13	6.0	8.2	2.58	5.54	0.270
10	0.4	10	4.9	5.9	2.09	3.80	0.123
11	0.4	8	3.9	4.6	1.65	3.03	0.057
12	0.4	6	3.1	3.2	1.31	2.09	0.020
13	0.6	17	6.6	12.0	4.41	5.50	0.737
14	0.6	15	6.6	10.0	4.34	4.52	0.348
15	0.6	13	6.4	8.6	4.33	3.85	0.327
16	0.6	12	5.6	7.4	3.74	3.29	0.225
17	0.6	10	4.9	6.0	3.28	2.64	0.143
18	0.6	8	3.8	4.7	2.53	2.05	0.115
19	0.6	6	2.9	3.2	1.83	1.38	0.029
20	0.7	17	7.2	12.0	5.57	4.22	0.532
21	0.7	15	7.0	10.2	5.48	3.60	0.315
22	0.7	13	6.5	8.2	5.07	2.85	0.196
23	0.7	10	4.9	6.0	3.68	2.03	0.143
24	0.7	8	4.0	4.5	3.03	1.52	0.053
25	0.7	6	3.1	3.2	2.30	1.06	0.027
26	0.8	17	6.8	12.6	6.07	2.83	0.737
27	0.8	15	7.0	10.0	6.05	2.21	0.287
28	0.8	13	6.4	8.6	5.71	1.97	0.287
29	0.8	12	5.7	7.4	5.06	1.61	0.184
30	0.8	10	4.9	6.0	4.33	1.29	0.143
31	0.8	8	3.8	4.7	3.29	1.00	0.106
32	0.8	6	2.8	3.2	2.38	0.71	0.049
33	1	17	8.2	0.0	9.28	0	0.450
34	1	15	7.7	0.0	8.45	0	0.307
35	1	13	6.5	0.0	7.27	0	0.221

Table 4.6: For caption see next page.

Table 4.6: (Continued)

36	1	12	5.9	0.0	6.57	0	0.205
37	1	10	5.0	0.0	5.54	0	0.160
38	1	8	4.0	0.0	4.40	0	0.131
39	1	6	3.1	0.0	3.39	0	0.037

Table 4.6: Parameters of the experiments: the fraction of the volume flux extracted at the top of the tank, λ, the salinity of the bottom inflow S_0, top outflow S_{to} and bottom outflow S_{bo}, the buoyancy flux of the top outflow B_{to} and bottom outflow B_{bo}, the square of the buoyancy frequency N^2.

Figure 4.19*a* shows the total vertical buoyancy flux B_{to} as a function of the buoyancy supplied at the base, for different values of λ. We also report the experiments with $\lambda = 0.5$ and $\Omega = 2.50\,\mathrm{rad\,s^{-1}}$ (gray dots), already discusses in section 4.1, as a reference for the zero-advection condition. Empty circles refer to the *unsaturated* regime, whereas full circles refer to the *saturated* regime.

The experiments with $\lambda < 0.5$ are characterized by a negative (downward) advection and as a consequence, a smaller total vertical buoyancy flux. On the other hand, the experiments with $\lambda > 0.5$ indicate a positive (upward) advection and a larger total vertical buoyancy flux. All the curves present a linear dependence of the vertical flux on the supplied flux for $B_0 < 7.6\,\mathrm{m^4\,s^{-3}}$, and reach a plateau for greater values of B_0. When $\lambda = 1.0$, all the injected fluid is extracted at the top of the tank, so the vertical buoyancy flux is only limited by the salinity of the supplied fluid.

Figure 4.19*b* illustrates B_{to} as a function of λ, for different salinity S_0 of the bottom source of fluid. The general trend is an increase of the vertical transport of salt for fixed buoyancy supplied at the base. In the range $0.2 < \lambda < 0.8$, B_{to} increases with S_0 up to the value $S_0 = 13\%$ and remains constant for $S > 13\%$.

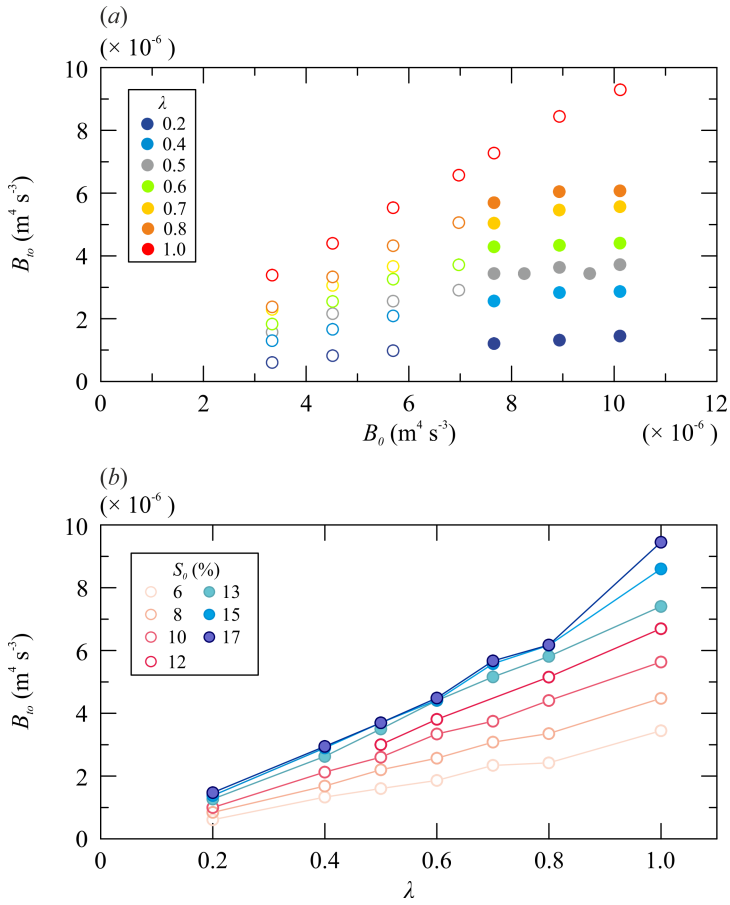

Figure 4.19: (a) The vertical buoyancy flux B_{to} as a function of the buoyancy flux supplied at the base of the tank, for different values of λ; (b) The vertical buoyancy flux B_{to} as a function of λ, for different values of the supplied buoyancy flux.

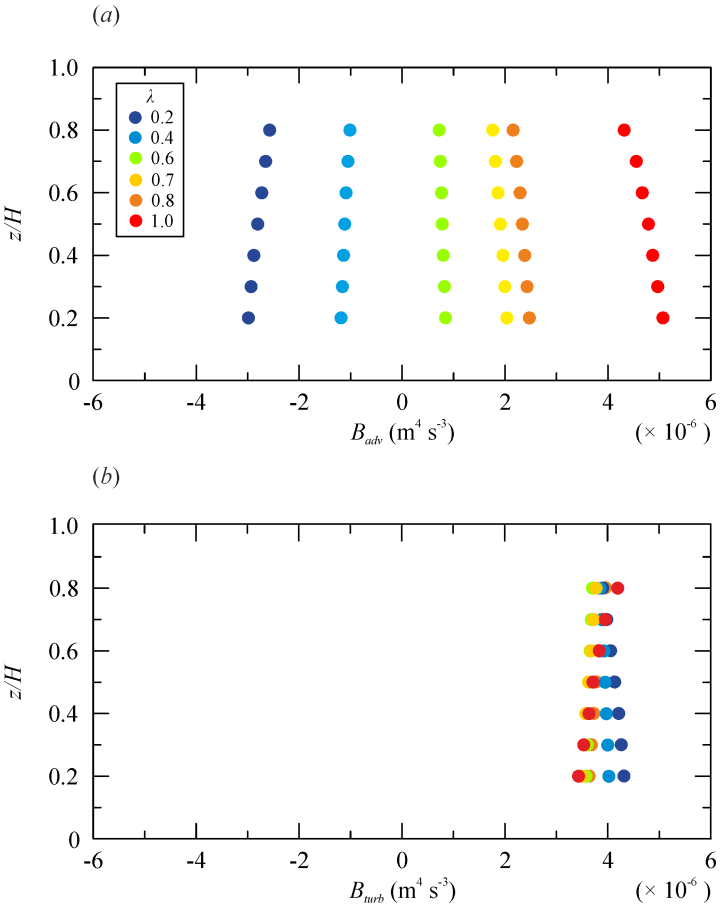

Figure 4.20: (a) Advective flux B_{adv} and (b) turbulent flux B_{turb} as a function of height, for different values of λ and fixed input salinity $S_0 = 15\%$.

In figure 4.20a we report the advective flux B_{adv} as a function of depth, for fixed supplied buoyancy, $B_0 = 8.94 \times 10^{-6}\ \mathrm{m^4\,s^{-3}}$ corresponding to a fluid with 15% of salinity, and different values of λ. At each height in the range $0.2 < z/H < 0.8$, hence far from the boundary layers, B_{adv} has been evaluated as

$$B_{adv,z/H} = (Q_{to} - Q_{ti})\,\rho_{z/H} S_{z/H}, \tag{4.38}$$

where $Q_{to} - Q_{ti}$ is the net top outflowing volume flux, $\rho_{z/H}$ and $S_{z/H}$ are the density and salinity as functions of depth.

Considering that $Q_{to} = \lambda Q_0 = 2\,\lambda\,Q_{ti}$, equation 4.38 results in a positive advection if $Q_{to} - Q_{ti} > 0$ or $\lambda > 0.5$, and a negative advection if $Q_{to} - Q_{ti} < 0$ or $\lambda < 0.5$. B_{adv} varies slightly linearly with depth as

a result of the linear density gradient of the fluid in steady state condition. As the variation of B_{adv} along the vertical is $\leq 10\%$, we can consider the advective flux constant with depth.

The turbulent flux B_{turb} in figure 4.20*b* is evaluated as the difference between the total buoyancy flux measured at the top of the tank, B_{to}, and the advective flux given by equation 4.38 and it is always posivite (upward). The linear density gradient seems to be in contrast with the hypothesis of Munk (1966) who supposed that salinity and temperature follow an exponential law, on the basis of the 2nd order differential diffusion-advection equations. If we average B_{turb} over depth, we find that it is approximately equal to the turbulent flux measured in case of no advection. The data for $\lambda = 0.5$, discussed in section 4.1, are shown in gray dots in figure 4.21. In the *saturated* regime, the turbulent component appears to be slightly higher than the one at $\lambda = 0.5$ if the advection is downward, and lower if the advection is upward. We address this difference to experimental errors.

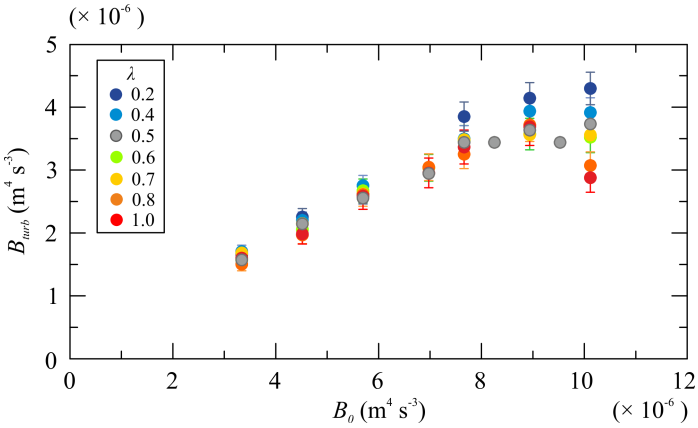

Figure 4.21: Turbulent component of the total vertical buoyancy flux as a function of the buoyancy supplied at the base, for different values of λ.

In figure 4.22 we show the turbulent ad advective fractions of the total vertical buoyancy flux as functions of the input buoyancy flux, for upward advection (panel *a*) and downward advection (panel *b*). Both fractions do not vary with the input buoyancy.

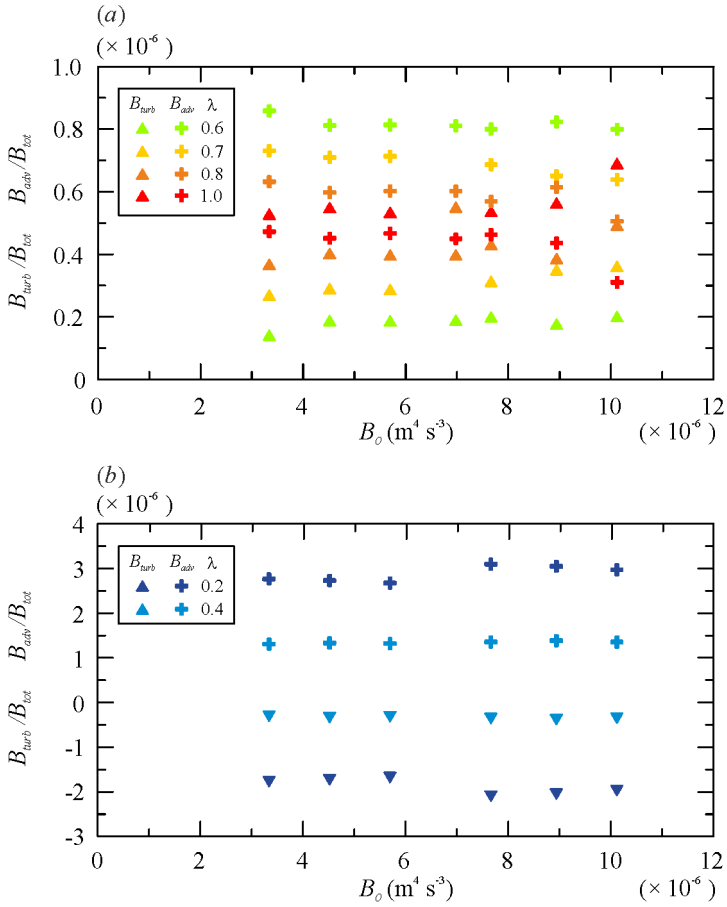

Figure 4.22: Turbulent and advective fractions of the total vertical buoyancy flux as functions of the input buoyancy for upward advection (a) and downward advection (b).

Therefore, if we take an average value, we can see that the turbulent component decreases with λ, while the advective component increases, until they become equivalent at $\lambda = 1.0$. The two curves are symmetric with respect to $B/B_{tot} = 0.5$.

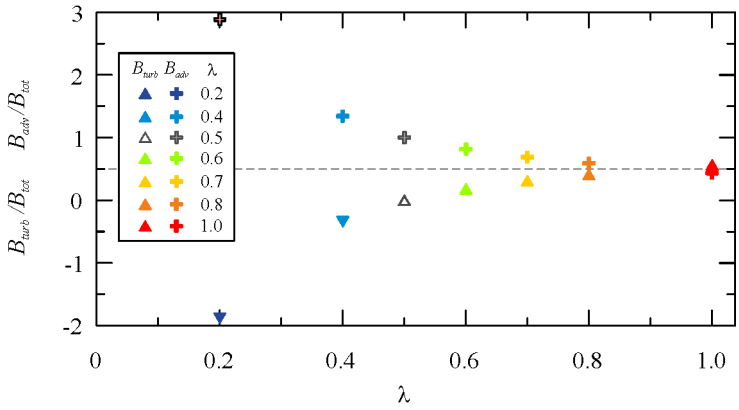

Figure 4.23: Turbulent and advective components as functions of λ.

4.3 Diffusivity

As a first measure, we assume that the salinity expressed as the salt mass fraction of the total mass of the solutions is almost equivalent to the ratio of the salt mass over the volume of the solution:

$$S = \frac{\mathrm{g_{NaCl}}}{\mathrm{g_{tot}}} \approx S' = \frac{\mathrm{g_{NaCl}}}{\mathrm{ml_{tot}}}. \tag{4.39}$$

The we can simplify the expression for the buoyancy flux:

$$\frac{g}{\rho_0} Q \rho S \approx \frac{g}{\rho_0} Q S'. \tag{4.40}$$

In our experiments, the maximum salinity of the top outflow is 6.5%, therefore the error we make in the approximation from equation 4.40 is always less than 4.3%.

The advection-diffusion equation for the total vertical buoyancy flux, B_{to}, which is the sum of the turbulent and advective components, can be written as:

$$A\mathcal{D}\frac{g}{\rho_0}\frac{\mathrm{d}S}{\mathrm{d}z} + \frac{g}{\rho_0}\left(Q_{to} - Q_{ti}\right) S_{z/H} = \frac{g}{\rho_0} Q_{to} S_{to}, \tag{4.41}$$

where A is the cross area of the tank, $\mathcal{D}$ is the salt diffusivity, $\mathrm{d}S/\mathrm{d}z$ is the salinity gradient, Q_{to} and S_{to} are the volume flux and salinity of the top outflow, Q_{ti} is the volume flux of the top inflowing fluid and $S_{z/H}$ is the salinity at depth z/H.

Figure 4.24 shows the vertical turbulent buoyancy flux, adimensionalized with the maximum turbulent flux (equation 4.26), as a function of N/Ω.

Dots refer to the experiments of table 4.2, with $\lambda = 0.5$ and $\Omega = 1.00 - 2.50\,\mathrm{rad\,s^{-1}}$, while stars correspond to the experiments of table 4.6, with $\Omega = 2.50\,\mathrm{rad\,s^{-1}}$ and $\lambda = 0.2 - 1.0$.

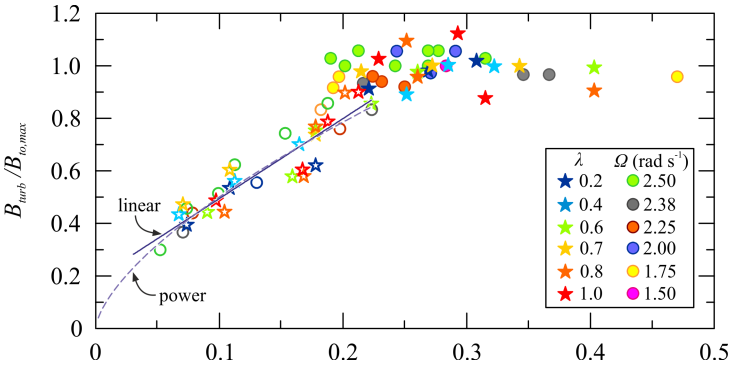

Figure 4.24: The vertical turbulent buoyancy flux, adimensionalized with the maximum vertical flux for the same Ω, $B_{turb}/B_{turb,max}$, as a function of N/Ω. Dots refer to the experiments with $\lambda = 0.5$ and $\Omega = 1.00{-}2.50\mathrm{rad\,s^{-1}}$, while stars correspond to the experiments run with $\Omega = 2.50\,\mathrm{rad\,s^{-1}}$ and $\lambda = 0.2 - 1.0$.

In the *saturated* regime, for $N/\Omega > 0.2$, the turbulent vertical transport of salt can be parametrized according to equation 4.26 as $B_{turb,max} = \alpha\, R_1^2\, \Omega^3 A$, with $\alpha = 1.30 \times 10^{-4}$. Following the study of Oglethorpe et al. (2013), who used three different inner radii to adimensionalize the vertical flux and find a "universal flux law", we can also express the maximum turbulent flux as $B_{turb,max} = \alpha'\ (\Omega\, R_1)^3\, A/\Delta R$, provided that $\alpha' = 1.96{\times}10^{-4}$. We can then substitute the latter expression in equation 4.41 and introduce $N^2 = (g/\rho_0)\mathrm{d}S'/\mathrm{d}z$ to obtain

$$A\mathcal{D}N^2 = \alpha' \frac{R_1^3}{\Delta R} A\, \Omega^3. \tag{4.42}$$

Then the diffusivity depends on the scaled buoyancy frequency N/Ω

$$\frac{\mathcal{D}}{N} = \alpha' \frac{R_1^3}{\Delta R} \left(\frac{\Omega}{N}\right)^3 = 0.013 \left(\frac{\Omega}{N}\right)^3. \tag{4.43}$$

with R_1 and ΔR expressed in cm and D in $\mathrm{cm^2\,s^{-1}}$. If we choose Ω as a time scale

$$\frac{\mathcal{D}}{\Omega} = \alpha' \frac{R_1^3}{\Delta R} \left(\frac{\Omega}{N}\right)^2 = 0.013 \left(\frac{\Omega}{N}\right)^2. \tag{4.44}$$

The choice of N or Ω as a time scale implies a dependence of D on N/Ω to the power of 3 or 2, but equations 4.43 and 4.44 are equivalent.

In the *unsaturated* regime, for $N/\Omega < 0.2$, the experimental data seem to follow either a linear or power-law dependence on N/Ω of the form $B_{turb}/B_{turb,max} \propto (N/\Omega)^n$, with $n = 0.65$. Further data are needed in the range $B_{turb}/B_{max} < 0.3$, but as mentioned before, we struggle in measuring the density gradient when the fluid evolves toward a well-mixed steady state. If we assume that $B_{turb} = 2.24\, B_{max}\, (N/\Omega)^{0.65}$ and substitute it in equation 4.41, yields

$$A\mathcal{D}N^2 = \alpha' \frac{R_1^3}{\Delta R} A\, \Omega^3 \left(\frac{N}{\Omega}\right)^{0.65}, \tag{4.45}$$

which implies that

$$\frac{\mathcal{D}}{N} = \alpha' \frac{R_1^3}{\Delta R} \left(\frac{N}{\Omega}\right)^{2.4} = 0.030 \left(\frac{N}{\Omega}\right)^{2.4}, \tag{4.46}$$

with R_1 and ΔR expressed again in cm and $\mathcal{D}$ in $\mathrm{cm^2\,s^{-1}}$.

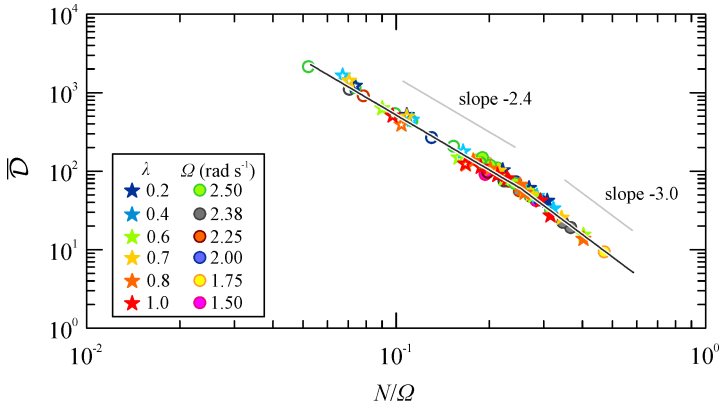

Figure 4.25: The adimensionalized diffusivity $\overline{D}$ as a function of N/Ω. For legend, see figure 4.24.

Figure 4.25 shows the adimensionalized diffusivity, $\overline{D}$, given by

$$\overline{\mathcal{D}} = \frac{\mathcal{D}}{\alpha' \dfrac{R_1^3}{\Delta R} N}, \tag{4.47}$$

as a function of N/Ω in a log-log plot. The coefficients of the two best-fit curves match the theoretical values (equations 4.43 and 4.46).

In figure 4.26 we illustrate the mean value of the diffusivity, $\mathcal{D}_m$, in the *saturated* regime, for different values of λ, with error bars corresponding to one standard deviation. The diffusivity assumes a nearly constant value of $0.46\,\mathrm{cm}^2\,\mathrm{s}^{-1}$, independent on λ.

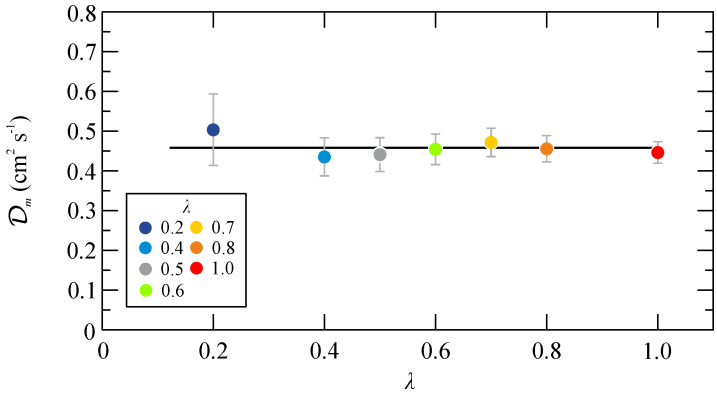

Figure 4.26: Mean value of D in the *saturated* regime as a function of λ.

4.4 Dye dispersion

During some of the experiments with $\lambda \neq 0.5$, when the fluid reached the steady state condition, some dye was added to the bottom source fluid in order to see how it disperses in the turbulent flow.

Figure 4.27*a* shows a time series of a vertical line of pixels for experiment 7 of table 4.6, $\lambda = 0.4$ and $S_0 = 17\%$. The time $t = 0$ corresponds to the start of the recording. As the dye is injected in the fluid, it seems to be transported upwards by a series of artificial layers which originate periodically at the bottom of the tank. The period of these structures is of approximately 22 s. The dye seems to spiral across the inner cylinder, as it spreads horizontally and upwards and after a period of revolution, it appears at a higher level than the previous rotation cycle. The blank zones correspond to times when the dye is at the back of the recording station, hidden by the inner cylinder. At $t \approx 700$ s, when the dye seems to have diffused in the whole water column, the layers propagating upwards appear to meet in the middle of the tank other layers propagating downwards with the same frequency. Figure 4.27*b* shows the iso-contour lines corresponding to constant dye concentrations (constant light intensity in the blue channel), as a function of time. The slope of the iso-contour lines appears to vary with time, as it is steeper at early times and becomes more gentle at late times.

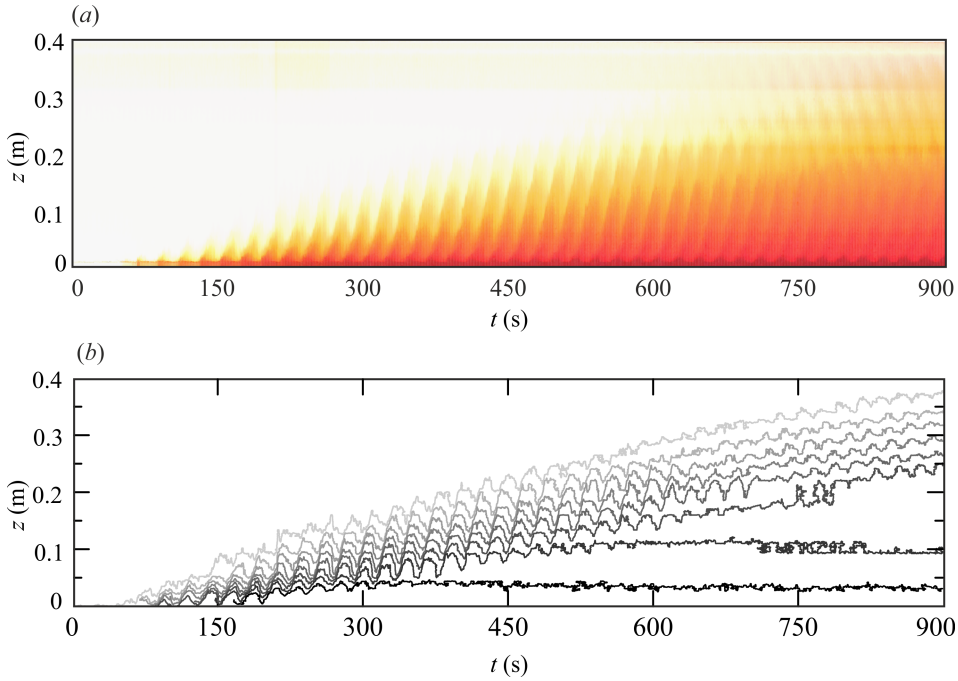

Figure 4.27: Experiment 7. (a) Time series of a vertical line of pixels showing the diffusion of dye injected at the bottom of the tank; (b) iso dye concentration lines shown as a function of time; (c) iso dye concentration lines shown as a function of the square root of time.

We are still working on these data in order to understand the behavior of this passive tracer.

Another example is shown in figure 4.28, where we illustrate experiment 20 of table 4.6, with $\lambda = 0.7$ and $S_0 = 17\%$ i. In this experiment, while the dye is diffusing upwards, the layers carrying information about density waves are propagating only downwards, with a period similar of experiment 7, $T \approx 20$ s. The iso-concentration lines again have a slope that varies with time.

The layered structures are clearly visible in a strongly stratified flow. As a matter of fact, for low supplied buoyancy flux the fluid evolves to a weakly stratified condition and the dye rapidly diffuses in the water column. Figure 4.29 shows the time sequence of the vertical line of pixels showing the dye spreading in the turbulent flow, for experiment 25 of table 4.6, $\lambda = 0.7$ and $S_0 = 6\%$.

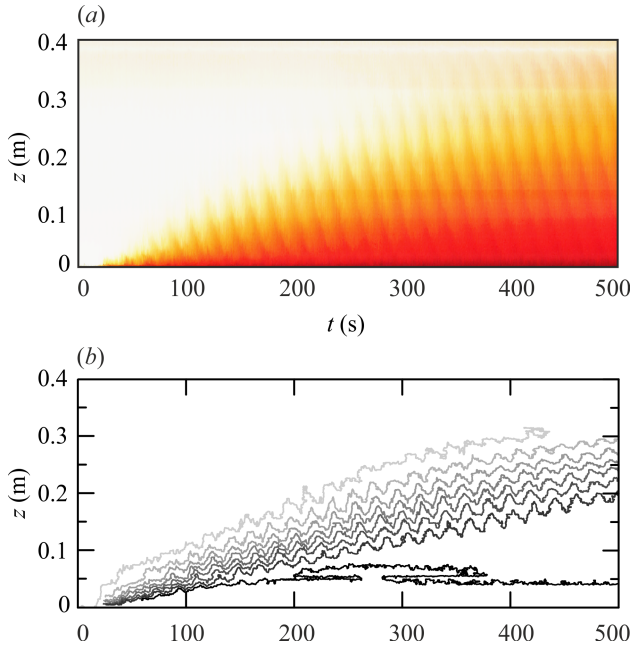

Figure 4.28: Experiment 20. For caption, see figure 4.27.

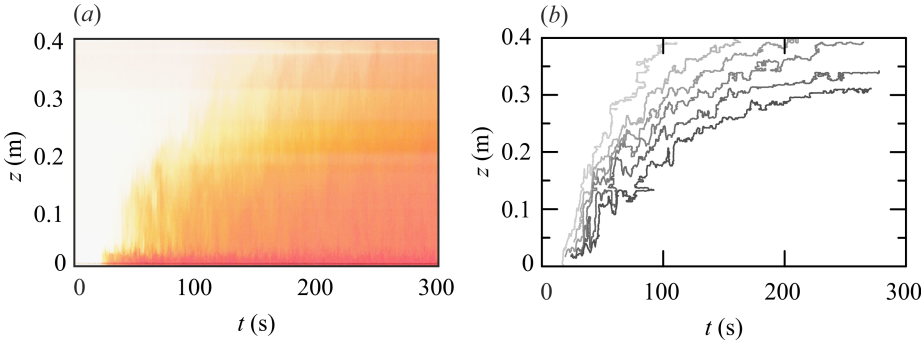

Figure 4.29: Experiment 25. For caption, see figure 4.27.

4.5 The influence of the depth of the sources/sinks

In this section we are going to discuss the influence of the depth of the sources and sinks on the steady state density profile of the fluid.

For this purpose, we run a set of experiments fixing the initial condition as a two-layer stratification, with the top layer of density $\rho_{TL} = 1034\,\mathrm{kg\,m^{-3}}$ and salinity $S_{TL} = 5\%$ and the bottom layer of density $\rho_{BL} = 1071\,\mathrm{kg\,m^{-3}}$ and salinity $S_{BL} = 10\%$. We also fix the buoyancy supplied ad the bottom of the tank, $B_0 = 8.94\,\mathrm{rad\,}s^{-1}$, corresponding to a fluid with $\rho_0 = 1109\,\mathrm{kg\,m^{-3}}$ and $S_0 = 15\%$.

We arranged the sources and sinks according to the four configurations sketched in figure 4.30. Set-up 1 is similar to that adopted in all the experiments discussed in section 4.1, with the upper source and sink located below the free surface and the lower source and sink at the bottom of the tank. In set-up 2 the two sources are moved just above and below the density interface in middle of the tank. Set-up 3 is asymmetric with respect to configuration 2, as the two sinks are close to the interface, while the two sources are at the top and bottom of the tank. In set-up 4 we inject and extract fluid in the middle of the tank.

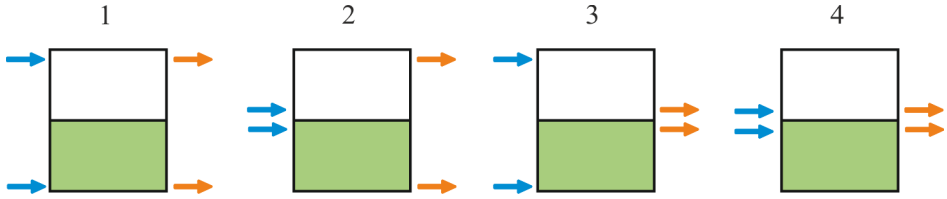

Figure 4.30: Four set-ups with different points of injection/extraction of fluid in/from the tank.

The suite of the experiments is listed in table 4.7, where we report the rotation rate Ω, the number of the set-up of the sources and sinks, the flow rate q, the steady-state salinity of the upper and lower withdrawn fluids S_{to} and S_{bo}, and their respective buoyancy flux B_{to} and B_{bo}. In the last column we report the stratification of the fluid in steady state.

test	Ω ($\mathrm{rad\,s^{-1}}$)	set-up	Q ($\mathrm{ml\,s^{-1}}$)	S_{to} (%)	S_{bo} (%)	B_{to} ($\times 10^{-6}$) ($\mathrm{m^4\,s^{-3}}$)	B_{bo} ($\times 10^{-6}$) ($\mathrm{m^4\,s^{-3}}$)	Final Condition
1	2.50	1	5.4	6.6	10.6	3.661	6.045	WM
2	2.00	1	5.4	2.9	12.0	1.567	6.913	2L
3	1.00	1	5.4	0.2	14.7	0.106	8.625	4L
4	2.50	1	14.2	3.0	12.4	4.267	18.837	WM
5	1.00	1	14.2	0.2	14.1	0.279	21.665	2L
6	2.50	2	5.5	7.2	8.0	4.085	4.564	WM
7	2.25	2	5.5	4.9	10.3	2.736	5.971	2L
8	2.00	2	5.5	2.9	12.3	1.596	7.231	2L
9	1.00	2	5.5	1.0	14.0	0.543	8.328	2L
10	2.50	2	14.2	3.0	12.5	4.267	18.937	2L
11	2.50	3	5.5	7.0	8.6	3.966	4.925	WM
12	2.25	3	5.5	4.9	10.6	2.736	6.157	2L
13	2.00	3	5.5	3.2	12.3	1.765	7.231	2L
14	1.00	3	5.5	0.2	14.6	0.108	8.717	2L
15	2.50	3	14.2	2.6	12.4	3.688	18.837	2L
16	2.50	4	5.5	7.8	8.1	4.444	4.626	WM
17	2.50	4	14.2	3.2	12.3	4.558	18.668	2L

Table 4.7: Parameters of the experiments: the rotation rate Ω, the number of the set-up of sources and sinks, the flow rate Q, the salinity of the top outflow S_{to} and bottom outflow S_{bo}, the buoyancy flux of the top outflow B_{to} and bottom outflow B_{bo}, the stratification of the fluid in steady state. WM is well-mixed, 2L is two-layer, 4L is four-layer.

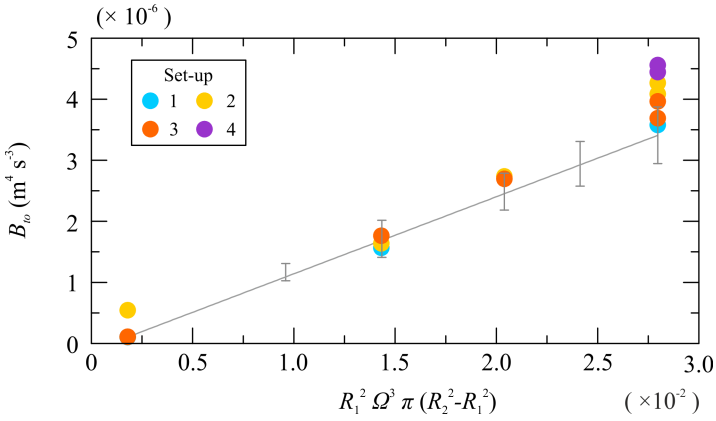

Figure 4.31: Buoyancy flux extracted by the top sink for the four set-ups.

In figure 4.31 we report the vertical buoyancy flux B_{to}, measured by the upper sink, for the different set-up conditions. B_{to} does not seem to change significantly upon the vertical positions of sources and sinks, with the exception for $\Omega = 2.50\,\mathrm{rad\,s^{-1}}$, where we register an increment in the vertical transport if the sources are located close to the interface.

The conductivity probe is not grounded when these experiments are being carried out. Sometimes during the experiments, instantaneous voltage jumps are registered, probably due to extra electrical charge around the electrodes. To overcome this issue, a wire is added before running the experiments discussed in section 4.1, connecting the electrodes to the siphoned fluid.

Therefore, for these experiments the density profiles may not be quantitatively reliable, but they give sufficient information about the qualitative evolution of density with depth over time, which is the key point of this section.

4.5.1 Set-up 1: external inflows and external outflows

Figure 4.32 shows the time evolution of the density profiles of experiments 1-5 of table 4.7. Figure 4.32*a-c* refer to three experiments run with the same flow rate $Q = 5.5\,\mathrm{ml\,s^{-1}}$, but decreasing rotation rate, Ω. If Ω is sufficiently high (i.e. case *a*, $\Omega = 2.50\,\mathrm{rad}\,s^{-1}$), turbulence is strong enough to erode the density interface and the fluid evolves towards a linear stratification. For lower value of rotation rate (i.e. case *b*, $\Omega = 2.00\,\mathrm{rad}\,s^{-1}$), the initial density difference does not disappear. The density difference between the layers increases as the fresh water mixes with the top layer and the saline solutions mixed with the bottom layer. At very low rotation rate (i.e. case *c*, $\Omega = 1.00\,\mathrm{rad}\,s^{-1}$), the two sources form two boundary layers at the top and bottom of the tank and the mixing efficiency is very low.

If we increase the inflow rate up to $Q = 14.2\,\mathrm{ml\,s^{-1}}$ for the highest and lowest value of flow rate (case d and e), the final density profile is not much altered, but the gradient in case d seems larger than that in case a. In fact, for the highest flow rate, the fluid removed at the top has a lower salinity, while the fluid removed at the bottom has a higher salinity.

Figure 4.33*a-b* illustrates the supply and outflow buoyancy fluxes as a function of time, for $Q = 5.5\,\mathrm{ml\,s^{-1}}$ and $Q = 14.2\,\mathrm{ml\,s^{-1}}$ respectively. The difference between the salinity of the outflowing fluids decreases with Ω and increases with Q.

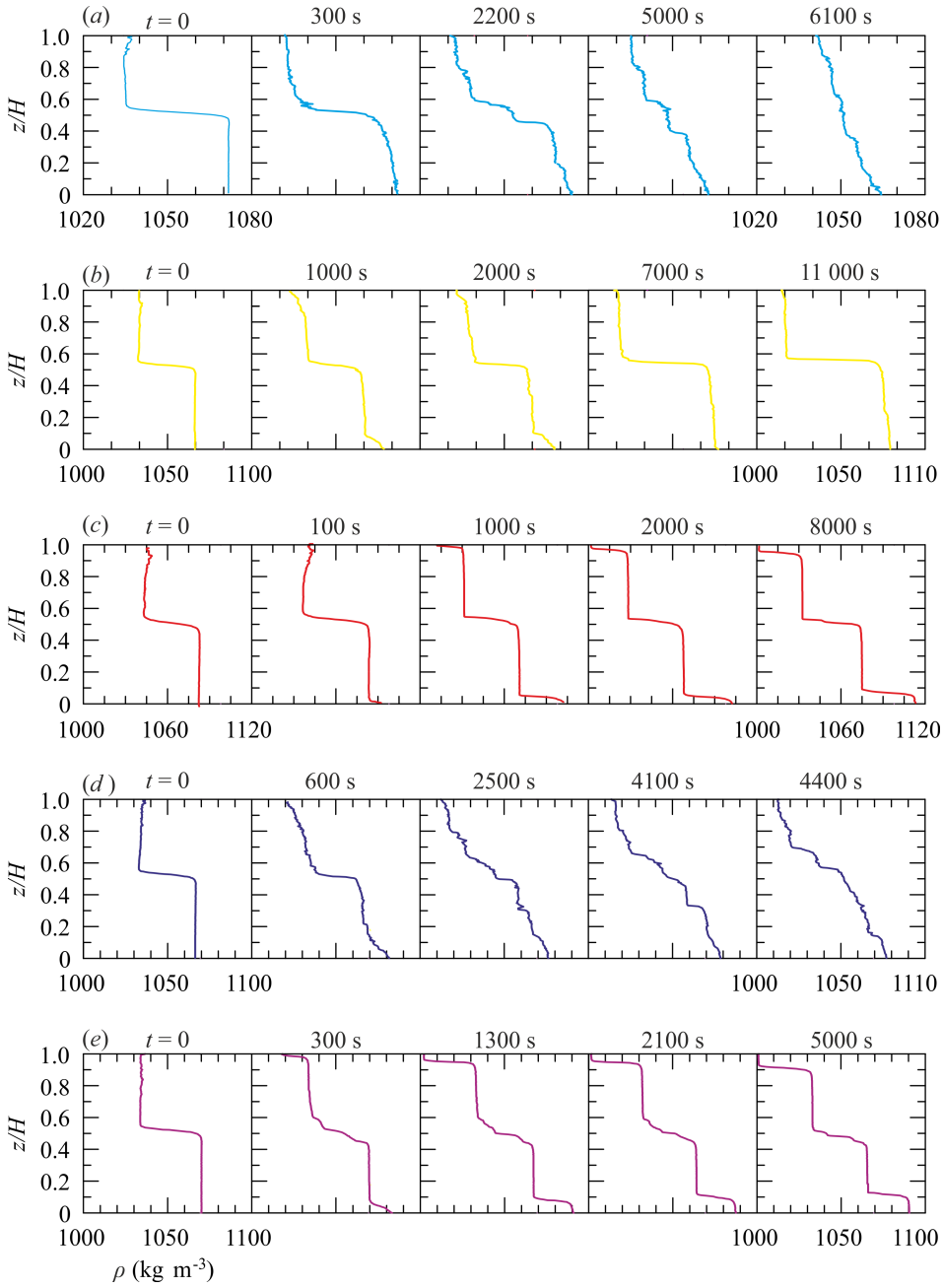

Figure 4.32: (a)-(e) Five instantaneous density profiles for experiments 1-5 of table 4.7. Set-up 1: sources and sinks far from the density interface.

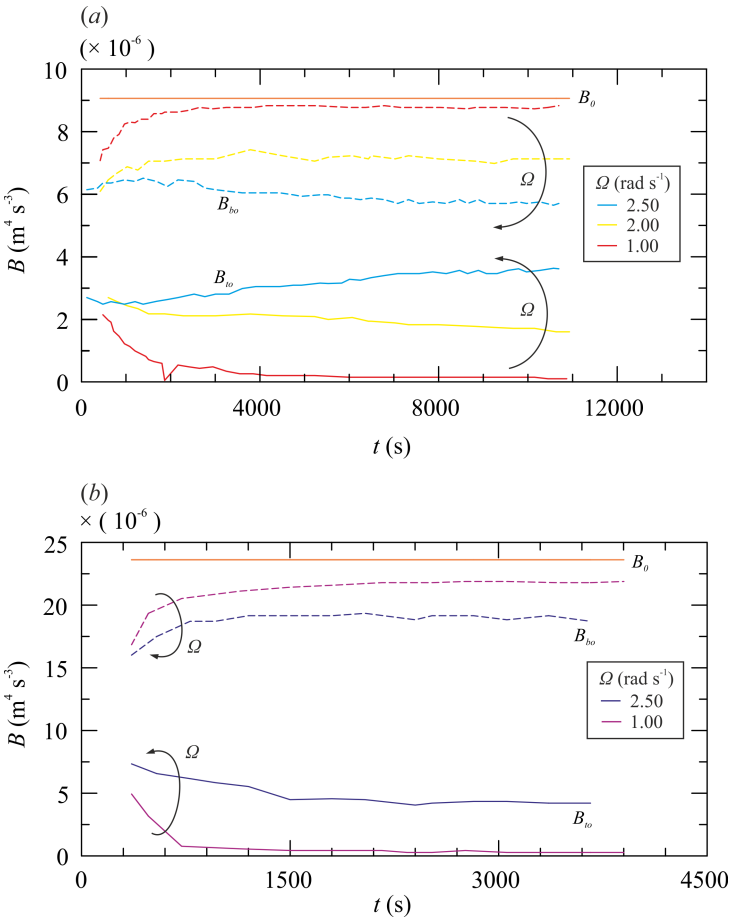

Figure 4.33: Supply and outflow buoyancy fluxes as a function of time, for (a) $Q = 5.5\,\mathrm{ml\,s^{-1}}$ and (b) $Q = 14.2\,\mathrm{ml\,s^{-1}}$. Set-up 1: sources and sinks far from the density interface.

4.5.2 Set-up 2: internal inflows and external outflows

Figure 4.34 shows the time evolution of the density profiles of experiments 6 - 10 of table 4.7. Figure 4.34*a-d* refers to four experiments run with the low flow rate $Q = 5.5\,\mathrm{ml\,s^{-1}}$, but decreasing rotation rate, Ω. If Ω is sufficiently high (i.e. case *a*, $\Omega = 2.50\,\mathrm{rad\,}s^{-1}$), the density difference between the two layers decreases in time. Each layer seems to be homogenous until the fluid becomes well-mixed, similarly to the experiments described by Woods et al. (2010). Some transient layers seem to form at the interface and migrate upward in the same way of the layers in the experiments described in this work. For any lower value of rotation rate tested (i.e. case *b-c-d*, $\Omega = 2.25 - 2.00 - 1.00\,\mathrm{rad\,}s^{-1}$), the initial density interface between the layers persists in time but the density contrast increases in time. The density contrast in steady state is also larger for lower rotation rate.

In case e we increased the inflow rate up to $Q = 14.2\,\mathrm{ml\,s^{-1}}$, with $\Omega = 2.50\,\mathrm{rad\,}s^{-1}$. The final density profile is not well mixed anymore as in case a but it is similar to the steady state condition registered at lower rotation rates and lower Q. Hence, a reduction of the level of turbulence has the same effects of an increase in the sources/sinks flow rate and they both reduce the mixing efficiency.

Figure 4.35 illustrates the supply and outflow buoyancy fluxes as a function of time, for $Q = 5.5\,\mathrm{ml\,s^{-1}}$ and $Q = 14.2\,\mathrm{ml\,s^{-1}}$ respectively. The difference between the salinity of the outflowing fluids decreases with Ω.

Figure 4.36*a-b* show the comparison of the supply and outflow buoyancy fluxes, for same rotation rate $\Omega = 2.50\,\mathrm{rad\,}s^{-1}$ an increasing flow rate. If Q is sufficiently low, the fluid tends to become homogenous and the buoyancy fluxes removed by the two sinks approach the same value. As Q increases, the two layers continue to be separated by a sharp interface with increase of the density contrast between them.

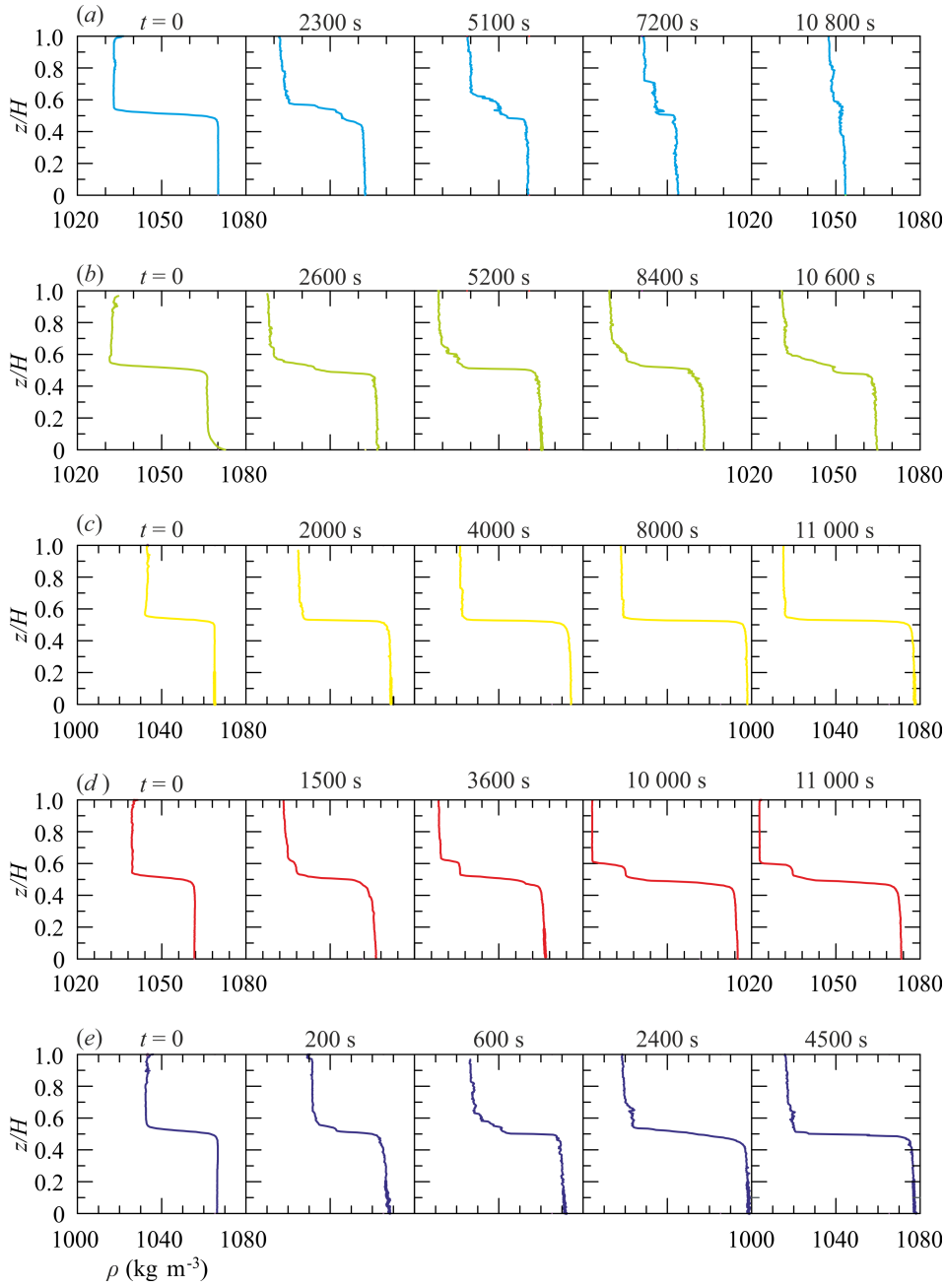

Figure 4.34: (a)-(e) Five instantaneous density profiles for experiments 6 - 10 of table 4.7. Set-up 2: sources close to the density interface, sinks far from the density interface.

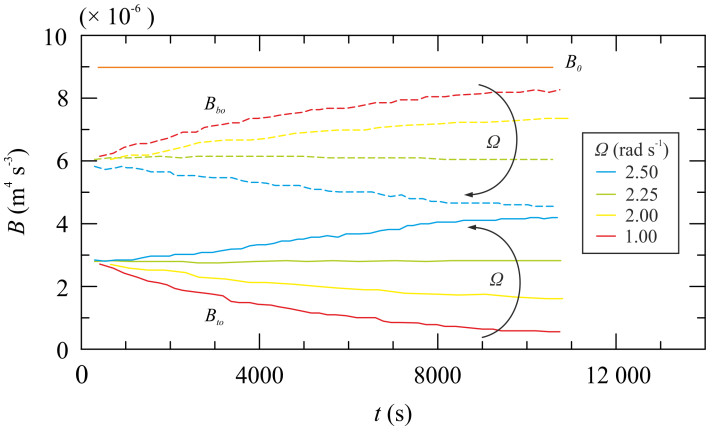

Figure 4.35: Supply and outflow buoyancy fluxes as a function of time for $Q = 5.5\,\mathrm{ml\,s^{-1}}$ and $\Omega = 2.50 - 1.00\,\mathrm{rad\,s^{-1}}$. Set-up 2: sources close to the density interface, sinks far from the density interface.

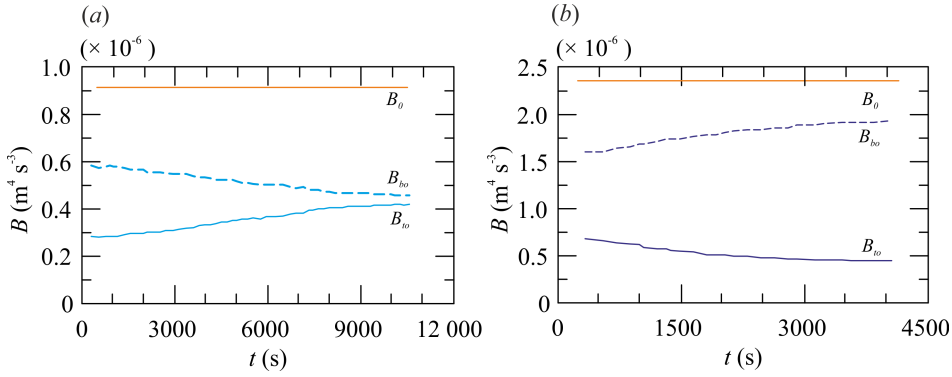

Figure 4.36: Supply and outflow buoyancy fluxes as a function of time for $\Omega = 2.50\,\mathrm{rad\,s^{-1}}$ and (a) $Q = 5.5\,\mathrm{ml\,s^{-1}}$ and (b) $Q = 14.2\,\mathrm{ml\,s^{-1}}$. Set-up 2: sources close to the density interface, sinks far from the density interface.

4.5.3 Set-up 3: external inflows and internal outflows

Figure 4.37 shows the time evolution of the density profiles of experiments 11-15 of table 4.7. Figure 4.34*a-d* refer to four experiments run with the same flow rate $Q = 5.5\,\mathrm{ml\,s^{-1}}$, but decreasing rotation rate, Ω. The results are generally similar to those presented in section 4.5.2. For sufficiently high rotation rate, (i.e. case *a* $\Omega = 2.50\,\mathrm{rad\,s^{-1}}$), the top and bottom layers

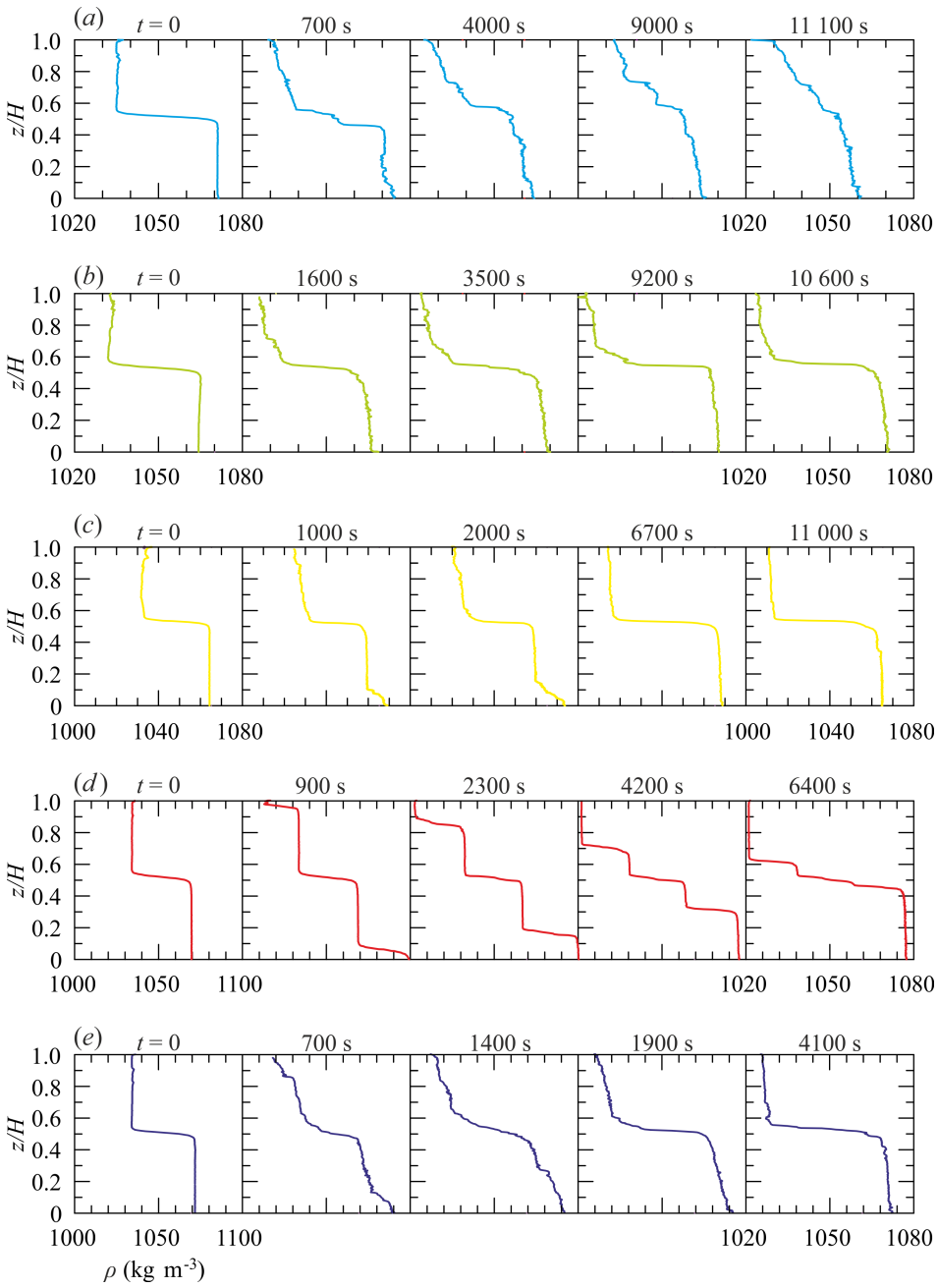

Figure 4.37: (a)-(e) Five instantaneous density profiles for experiments 11 - 15 of table 4.7. Set-up 3: sources far from the density interface, sinks close to the density interface.

become linearly stratified and they progressively merge at the middle of the tank. The final density gradient seems to be discontinuous with depth, it appears steeper in the bottom half of the fluid. For intermediate value of rotation rate, (i.e . case *b*-*c* $\Omega = 2.25 - 2.00\,\mathrm{rad\,s^{-1}}$), the density difference between the two layers increases in time. Both layers appear well mixed and the fluid remains two-layer stratified. At the lowest value of tested rotation rate (i.e. case *d*, $\Omega = 1.00\,\mathrm{rad\,s^{-1}}$), the initial two layers are gradually removed by the sinks at the interface and replaced by the new source fluids. The steps registered in the final profile close to the interface are due to the positions of the sinks, which were not vertically aligned with the interface.

In case e we increased the inflow rate up to $Q = 14.2\,\mathrm{ml\,s^{-1}}$, at $\Omega = 2.50$ $\mathrm{rad\,s^{-1}}$. In a first transient regime, the two initial layers become linearly stratified but eventually become well-mixed, separated by a sharp density interface.

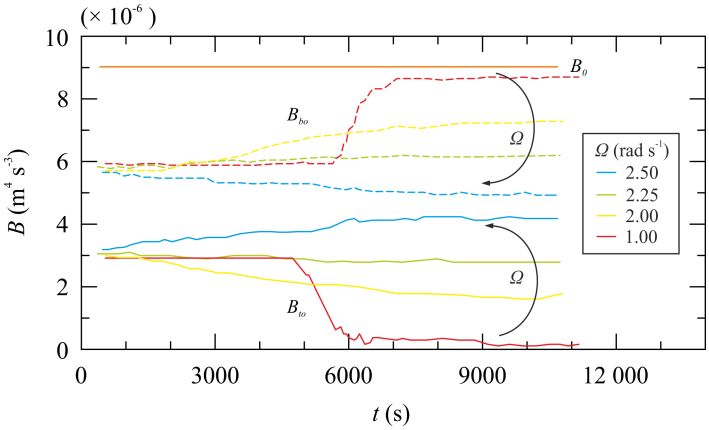

Figure 4.38: Supply and outflow buoyancy fluxes as a function of time for $\Omega = 2.50 - 1.00\,\mathrm{rad\,s^{-1}}$ and $Q = 5.5\,\mathrm{ml\,s^{-1}}$. Set-up 3: sources far from the density interface, sinks close to the density interface.

Figure 4.38 illustrates the supply and outflow buoyancy fluxes as a function of time, for $Q = 5.5\,\mathrm{ml\,s^{-1}}$, while figure 4.39*a*-*b* shows the comparison between the outflow buoyancy fluxes of case *a* and case *e*, for same $\Omega = 2.50\,\mathrm{rad\,s^{-1}}$ but different flow rate.

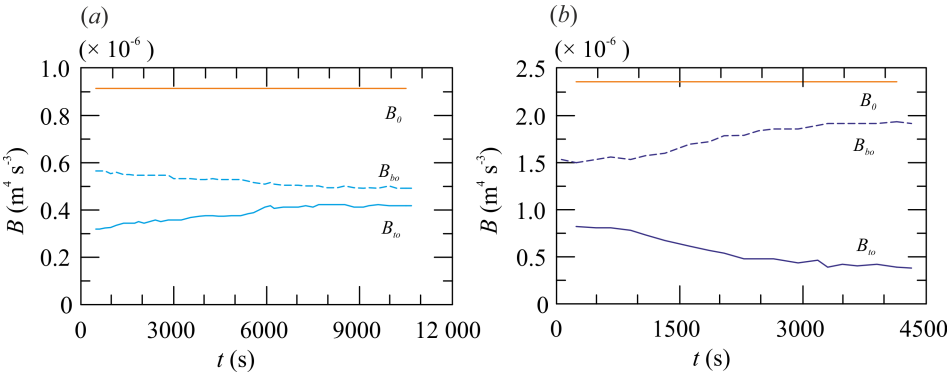

Figure 4.39: Supply and outflow buoyancy fluxes as a function of time for $\Omega = 2.50\,\mathrm{rad\,s^{-1}}$ and (a) $Q = 5.5\,\mathrm{ml\,s^{-1}}$ and (b) $Q = 14.2\,\mathrm{ml\,s^{-1}}$. Set-up 3: sources far from the density interface, sinks close to the density interface.

4.5.4 Set-up 4: internal inflows and internal outflows

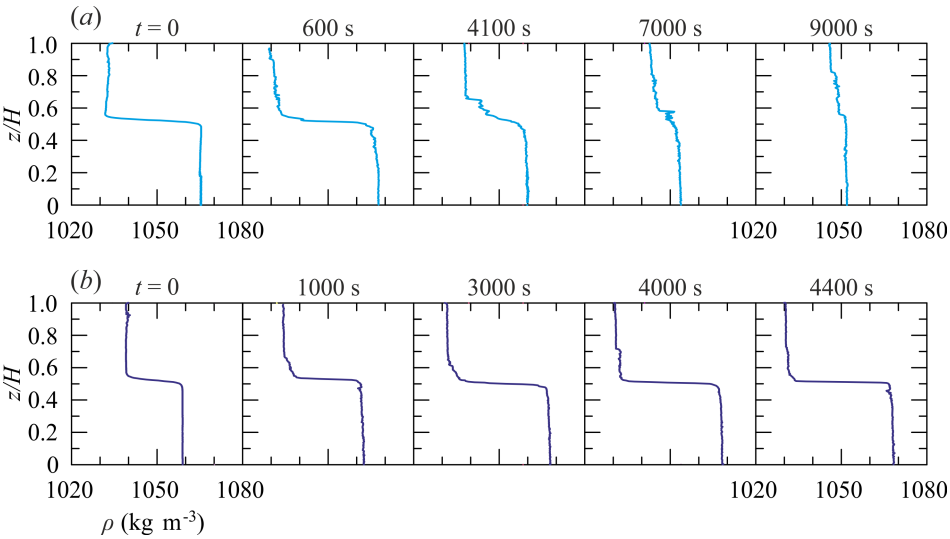

Figure 4.40: (a)-(e) Five instantaneous density profiles for experiments 16 - 17 of table 4.7. Set-up 4: sources and sinks close to the density interface.

Figure 4.37 shows the time evolution of the density profiles of experiments 16-17 of table 4.7, with $\Omega = 2.50\,\mathrm{rad\,}s^{-1}$ but different flow rate, $Q = 5.5\,\mathrm{ml\,s^{-1}}$ for case a and $Q = 14.2\,\mathrm{ml\,s^{-1}}$ for case b. The results are

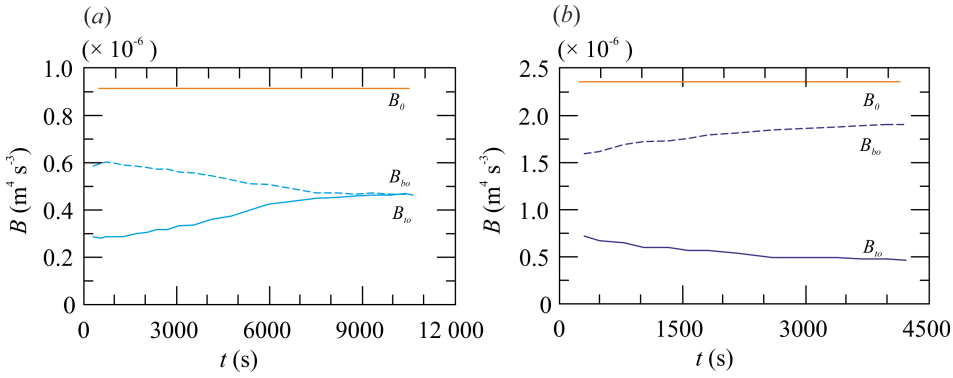

Figure 4.41: Supply and outflow buoyancy fluxes as a function of time for $\Omega = 2.50\,\mathrm{rad\,s^{-1}}$ and (a) $Q = 5.5\,\mathrm{ml\,s^{-1}}$ and (b) $Q = 14.2\,\mathrm{ml\,s^{-1}}$. Set-up 4: sources and sinks close to the density interface.

very similar to those presented in section 4.5.2. For low inflow rate, both layers remain well-mixed but the density difference decreases in time until the layers meet in the middle of the tank. In steady state condition, the buoyancies extracted by the sinks positioned above and below the initial density interface approach the same value, as shown in figure 4.41 *a*. In contrast, for higher inflow rate, the density difference increases in time, and the buoyancy fluxes withdrawn from the tank diverge, as shown in figure 4.41 *b*.

4.6 Conclusions

We have conducted experiments in a Taylor-Couette flow, supplying fresh water at the top and dense water at the bottom of the tank in order to find out how the vertical buoyancy flux B_{to} varies with the rotation rate of the inner cylinder Ω and the buoyancy supplied at the base B_0. In order to have a constant volume of fluid in the tank, we removed the same volume flux as the supplied with two sinks located at the same depth of the respective sources.

In a first study, where the inflow and outflow rates are balanced, we found that, for low values of B_0 (source-limited regime or *unsaturated* regime), the scaled vertical transport of salt $B_{to}/B_{to,max}$ increases linearly with B_0 until it reaches the maximum value of 1. In this regime, the vertical salt flux is also linear dependent on the buoyancy frequency N, and the mixing efficiency Γ increases linearly with the inverse of the Froude number $Fr = u_{rms}/(NL)$. For high values of B_0 (mixing-limited regime or *saturated*

regime), the vertical buoyancy flux is constant and equal to the maximum value $B_{to,max}$ and independent on the stratification. We also found that $B_{to,max}$ varies as the cube of rotation rate, approximating the vertical flux through a density interface in a two-layer fluid (Woods et al., 2010) and in a multi-layer or linear stratified fluid (Oglethorpe et al., 2013), in the absence of external fluxes. In the *saturated* regime, the mixing efficiency is constant $\Gamma = 0.18 - 0.35$, consistently with the results of Osborn (1980), and independent on $1/Fr$. In our experiments, the critical Froude number is $Fr_c = 1.0 \pm 0.3$.

In the deep ocean, the typical velocity scale for currents is of the order of $0.1 - 1.0\,\mathrm{m\,s^{-1}}$, while the largest length-scale for turbulent eddies is of order of 100 m (Sheen et al., 2009; Falder et al., 2016). The buoyancy frequency has values in the range $N^2 \sim 10^{-4} - 10^{-5}\,\mathrm{s^{-2}}$, so the expected Froude number is $Fr = 0.1 - 10.0$. This suggests that in the deep ocean there could be regions where the mixing may be either controlled by the local turbulent intensity with a constant mixing efficiency, or by the source buoyancy flux with a mixing efficiency that linearly depends on $1/Fr$.

Our experiments also show that in both the *saturated* and *unsaturated* regimes, the steady state density profile does not seem to be affected by the initial stratification. The vertical buoyancy flux is reduced, if the radial distance between the top source and sink is less than the one between the bottom source and sink, but it is approximately invariant with the vertical position of both sources and sinks.

In a second study we introduced advection by unbalancing the flow rate extracted by the top and bottom sinks. The total vertical buoyancy flux is increased in case of upward advection, and decreased in case of downward advection. While the turbulent component of the total salt flux is always directed upwards, the advective components can change sign according to the direction of advection.

We also modeled the non-dimensional salt diffusivity $\overline{D}$. The best-fit power law is $\overline{D} \propto (N/\Omega)^{-3}$ in the *saturated* regime and $\overline{D} \propto (N/\Omega)^{-2.4}$ in the *unsaturated* regime. In steady state, we added some dye to the bottom source fluid in order to study the dye dispersion in the turbulent Taylor-Couette flow. We are still working on these data in order to understand the behavior of this passive tracer.

Chapter 5

Results part II

This chapter focuses on the data of the experiments carried out in the Taylor-Couette tank at the Hydraulic Laboratory of Parma. These data are reported in a paper which is currently under review.

The annulus of the tank is filled with a two-layer fluid. During the rotation of the inner cylinder, the density interface is stabilized with a source of fresh water at the top of the upper layer and a source of saline water at the bottom of the lower layer. The same amount of fluid is removed from two sinks in order to have a constant volume in the tank. In steady state, we measure the density and velocity field in the vertical, radial and azimuthal direction and investigate the mechanisms that lead to mixing at the interface.

The chapter is organized as follows. In section 5.1 we compare the vertical buoyancy flux in the two Taylor-Couette tanks and verify that the adimensionalization of the vertical salt flux is consistent. In sections 5.2 and 5.3 we present the velocity field and the turbulent kinetic energy, in section 5.4 we estimate the macro (integral) and micro (Taylor) length scales. Then we move to section 5.5 where we discuss the density and velocity fluctuation in a limited region across the interface and the waves propagating along the density discontinuity. In section 5.6 we report some video and image analysis of the mixing mechanisms at the interface and to this end we inject some dye at three different radial distance from the inner cylinder. Then we consider a simple theoretical model for the salt transport across the interface in section 5.7 and, finally, we draw our conclusions in section 5.8.

5.1 Vertical buoyancy flux

The vertical buoyancy flux measured at the top of the tank,

$$B_{to} = \frac{g\,Q\,(\rho_{to} S_{to} - \rho_{ti} S_{ti})}{\rho_0}, \tag{5.1}$$

is determined for six values of rotation rate $\Omega = 1.50 - 2.75\,\mathrm{rad\,s^{-1}}$, in the *saturated* (mixing limited) regime. In equation 5.1, ρ_{to} and S_{to} are the density and salinity of the top outflowing fluid, while ρ_{ti} and S_{ti} are the density and salinity of the top inflowing fluid, in steady state condition. The series of experiments and the main parameters are listed in table 5.1. In the experiments 1 - 9, the bottom source fluid has a constant density $\rho_{bi} \approx 1187\,\mathrm{kg\,m^{-3}}$ and salinity $S = 25\%$ (the maximum concentration of NaCl in water at ambient temperature). B_{bo} is the buoyancy flux extracted at the bottom of the tank. We also report the Reynolds number defined as $Re = \Omega R_1^2/\nu$, with R_1 the inner cylinder and ν the kinematic viscosity, and the Richardson number $Ri = g\,(\Delta\rho/\rho_0)\,H/\left(\Omega\,R_1^2\right)$, with H the depth of a single layer and $\Delta\rho$ the density difference between the two layers in steady state. Six additional experiments (experiments 10 - 15) are conducted in fresh water in order to build reference for comparison of the velocity field. In these experiments, the pumped circulation is maintained by injecting and removing fresh water from the tank.

n° test	Ω (rad s^{-1})	ρ_{to} (kg m^{-3})	ρ_{bo} (kg m^{-3})	S_{to} (%)	S_{bo} (%)	B_{to} $\times 10^{-6}$ (m^4 s^{-3})	B_{bo} $\times 10^{-6}$ (m^4 s^{-3})	Re $\times 10^4$	Ri
			two-layer						
1	2.75	1040	1150	5.8	20.2	1.47 ± 0.04	5.71 ± 0.04	1.66	2.5
2	2.50	1027	1161	4.0	21.7	1.00 ± 0.04	6.20 ± 0.04	1.51	3.6
3	2.50	1028	1158	4.1	21.3	1.03 ± 0.04	6.07 ± 0.04	1.51	3.5
4	2.25	1020	1165	3.0	22.2	0.75 ± 0.03	6.35 ± 0.03	1.35	4.9
5	2.25	1021	1163	3.2	21.9	0.81 ± 0.03	6.26 ± 0.03	1.35	4.8
6	2.00	1012	1170	1.9	22.8	0.47 ± 0.03	6.55 ± 0.03	1.20	6.7
7	2.00	1013	1171	2.0	22.9	0.51 ± 0.03	6.59 ± 0.03	1.20	6.7
8	1.75	1008	1175	1.4	23.3	0.35 ± 0.03	6.73 ± 0.03	1.05	9.3
9	1.50	1006	1182	1.1	23.3	0.27 ± 0.03	6.77 ± 0.03	0.90	13.3
			water						
10	2.75	998.2	998.2	0	0	0	0	1.66	0
11	2.50							1.51	
12	2.25							1.35	
13	2.00							1.20	
14	1.75							1.05	
15	1.50							0.90	

Table 5.1: Parameters of the experiments: Ω is the rotation rate, ρ_{to} and ρ_{bo} are the density, S_{to} and S_{bo} the salinity, B_{to} and B_{bo} the buoyancy flux of the top and bottom outflowing fluids respectively. $Re = \Omega R_1^2/\nu$ is the Reynolds number and $Ri = g\,(\Delta\rho/\rho_0)\,H/\left(\Omega\,R_1^2\right)$ is the Richardson number.

In figure 5.1*a*, the vertical buoyancy flux B_{to} (blue dots) is shown as a function of Ω^3 and it follows a linear trend similarly to the data collected in Cambridge and discussed in chapter 4 (red dots), although it is reduced. This reduction can be addressed to the smaller geometry of the tank. In fact, the two curves collapse if B_{to} is expressed in terms of $R_1^2\Omega^3\pi\left(R_2^2 - R_1^2\right)$, with a linear non dimensional coefficient $\alpha = 1.33 \pm 0.13$, see figure 5.1*b*.

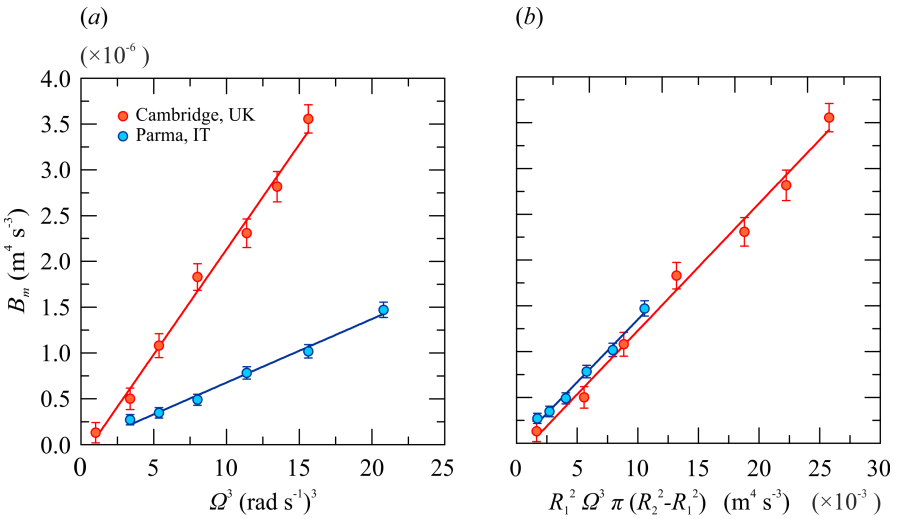

Figure 5.1: (*a*) The vertical buoyancy flux B_{to} as a function of Ω^3. Blue dots refer to the experiments carried out at Parma, red dots to those at Cambridge; (*b*) the vertical buoyancy flux B_{to} as a function of $R_1^2\Omega^3\pi(R_2^2 - R_1^2)$.

5.2 Velocity field

The velocity field was reconstructed in the $z - r$ plane, where z is the vertical axis ($z = 0$ is set at the interface), while r is the radial axis (it points outward from the inner cylinder, where $r = 0$). The time averaged vertical velocity, $\overline{w}$, and radial velocity, $\overline{u_r}$, are

$$\overline{w(z)} = \frac{1}{T}\int_0^T w(z,t)\,\mathrm{d}t, \quad \overline{u_r(z)} = \frac{1}{T}\int_0^T u_r(z,t)\,\mathrm{d}t, \tag{5.2}$$

where w and u_r are instant velocity components, and T is the duration of acquisition. $\overline{w}$ is measured by a "long" UVP probe, vertically aligned

and with the head immersed approximately 0.5 cm from the free surface, at a distance $r = 0.5, 1.3, 2, 3, 4, 5, 6, 7$ and 8 cm from R_1. For every radial position, $\overline{w}$ is averaged over 6000 velocity profiles (≈ 5 minutes). On the other hand, $\overline{u_r}$ is measured by a "mini-short" UVP probe, which is radially aligned and pointing inward through the inner cylinder and moving jointly with the conductivity probe along the vertical direction. The head of this probe is at the same level of the electrodes of the conductivity probe. $\overline{u_r}$ is computed over a number of 54 000 velocity profiles, which correspond to a whole number of ≈ 100 vertical excursions of the conductivity probe and the radial UVP, and a time $T \approx 50$ minutes.

Figure 5.2*a* and figure 5.3*a* illustrate the time series of the density profile during the steady state, for the highest rotation rate $\Omega = 2.75\ \mathrm{rad\,s^{-1}}$ (experiment 1 of table 5.1) and the lowest rotation rate $\Omega = 1.50\ \mathrm{rad\,s^{-1}}$ (experiment 9 of table 5.1) respectively. The density contrast between the two layers increases with decreasing Ω. During the experiments, the position of the interface does not significantly migrate in the vertical direction, as a consequence of the fairly good balance between the peristaltic pumps.

Figure 5.2*b*-*c* and figure 5.3*b*-*c* show two typical examples of colour maps of $\overline{w}$ and $\overline{u_r}$ for the same rotation rate of panels a. Positive values of $\overline{w}$ refer to upward vertical velocity and positive values of $\overline{u_r}$ to outward radial velocity. The vectors represent the fluid velocity in the $z - r$ plane. Blank zones at $r > 7$ cm in the radial colour maps are due to the radial UVP hindrance, while blank zones at the top and bottom of the fluid are a consequence of unavailability of velocity data.

In figure 5.2*b*, the $\overline{w}$ colour map exhibits a generally positive value, with a strong exchange of vertical flux at the interface. A red spot of upward flux is registered close to the inner cylinder, just below the interface, while a downward flux occurs above. A net upward flux is clearly visible at the bottom of the tank, close to the inner cylinder. This is a secondary inward radial flow driven by the centrifugally imbalanced pressure gradient at the bottom boundary, where a no-slip condition holds (Burin et al., 2006), and it is a characteristic feature of the apparatus for all Ω. This secondary flow would also occur symmetrically at the top surface if there was a fix lid in contact with the fluid.

The radial velocity field in figure 5.2*c* presents a vortex circulation, with three persistent main patches of velocity directed toward the outer cylinder, two of them are in the top and bottom layer respectively and the last one crosses the density interface.

For lower Ω, upward values of $\overline{w}$ tend to be confined along the inner cylinder in the bottom layer, while radial spots are still detected but they

appear faded (see figure 5.3*b*). The $\overline{u_r}$ component are significantly reduced (see figure 5.3*c*).

Figure 5.2*d* and figure 5.3*d* report the instantaneous colour map of radial velocity for the highest and lowest rotation rates respectively. Instantly, the radial velocity spans over a wider range and more recirculation cells are present than the averaged velocity map.

Figure 5.4 and 5.5 illustrate the colour maps of $\overline{w}$ and $\overline{u_r}$ in panels a-b and the colour map of the istantaneous u_r in panel c, for fresh water at $\Omega = 2.75$ and $1.50\,\mathrm{rad\,s^{-1}}$ (experiments 10 and 15 of table 5.1). The averaged velocity field appears different, especially in the vertical, where the fluid undertakes a 8-shaped path. The parcels moves up along the inner cylinder from the bottom of the tank, reaching almost the mid-height of the fluid where they diverge towards the outer cylinder, continuing to move upward. At the free surface, the motion is inverted and parcels start falling along the inner radius for mid-height and deviate to the outer radius.

The averaged radial velocity field looks similar to the stratified case, except for the number and size of the vortexes: two main vortex paths evolve in a deeper portion of the domain, fading more gradually in space at lower Ω. On the other hand, the recirculation cells in the instantaneous velocity field are not quite visible.

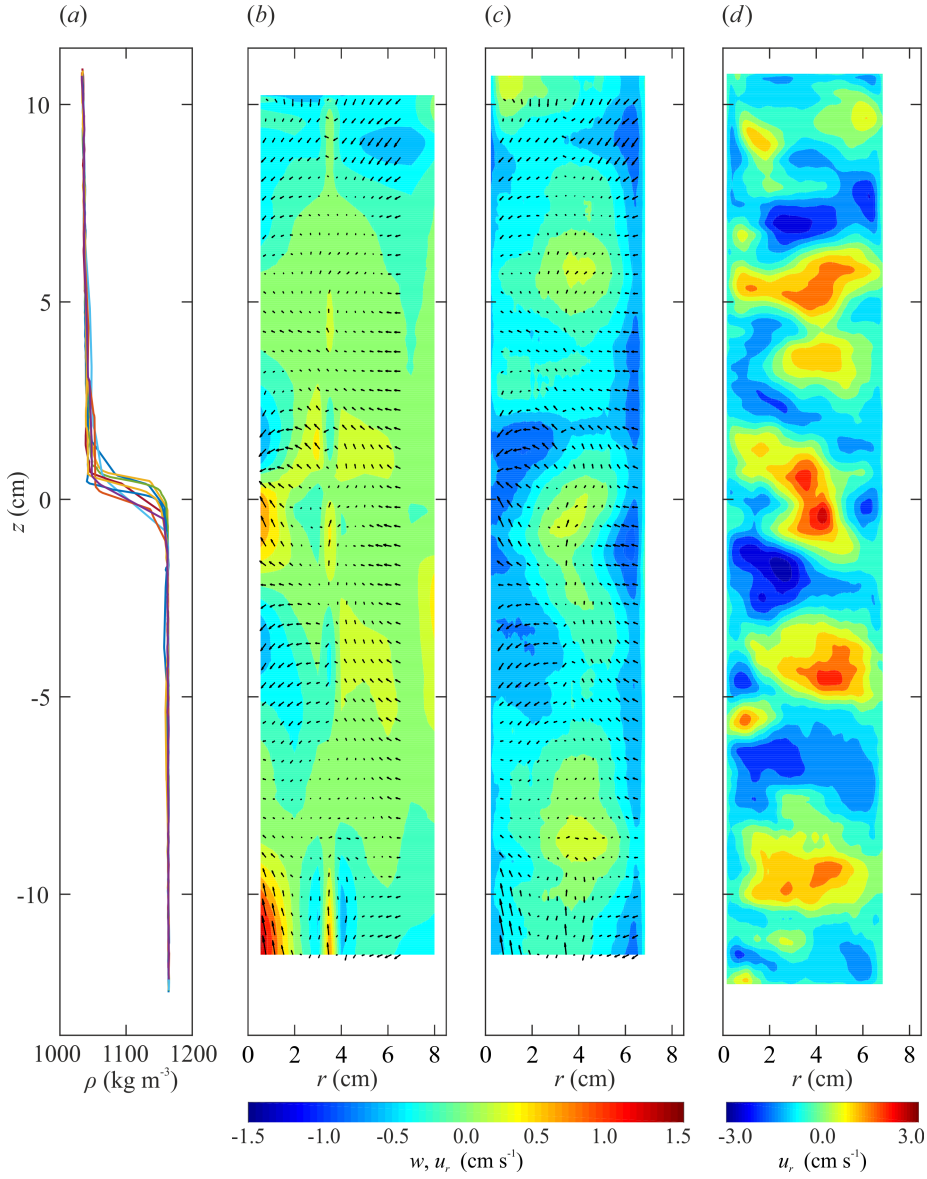

Figure 5.2: (a) Time series of density profiles during the steady state; colour maps of (b) the time averaged vertical velocity component, $\overline{w}$, (c) the time averaged radial velocity component, $\overline{u_r}$, (d) the instantaneous radial velocity component, u_r, reconstructed by UVP signal from experiment 1, $\Omega = 2.75\,\mathrm{rad\,s^{-1}}$.

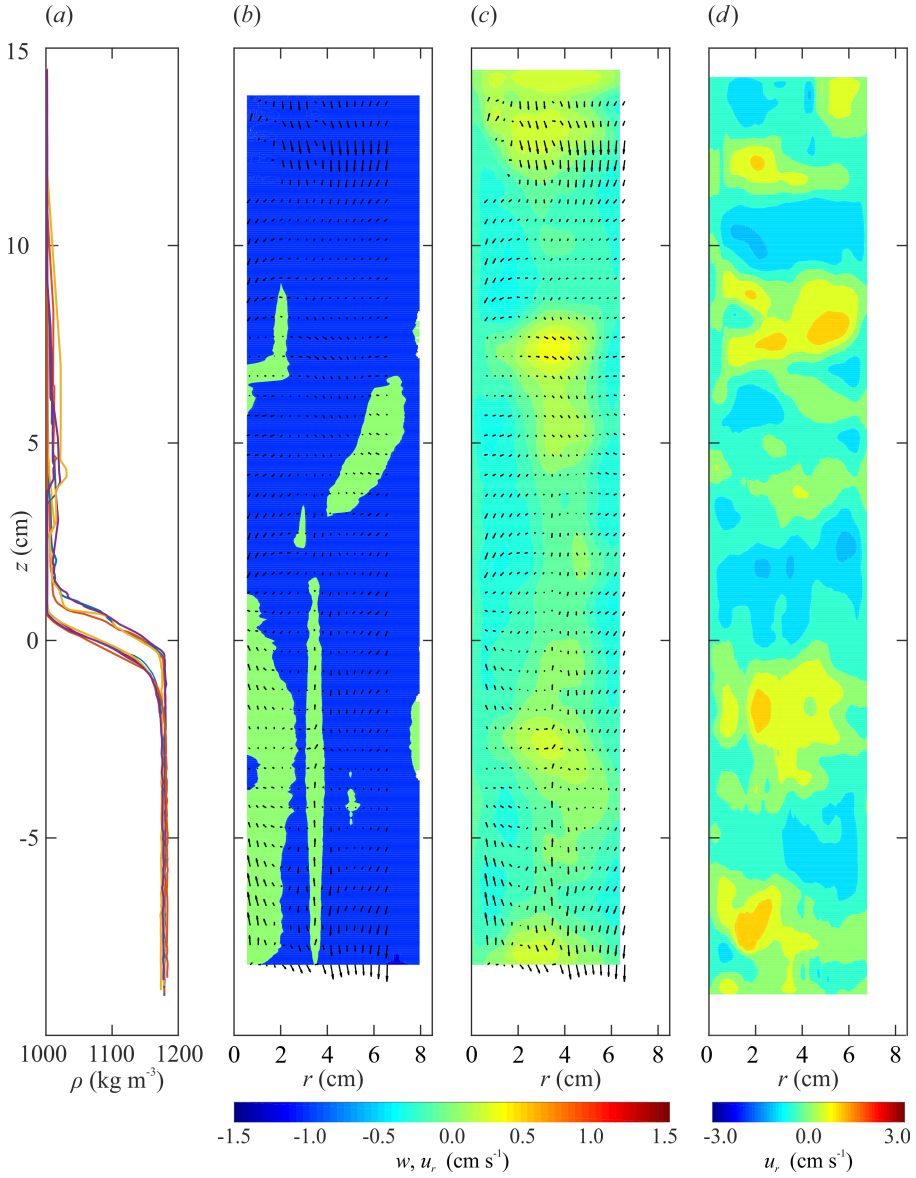

Figure 5.3: (a) Time series of density profiles during the steady state; colour maps of (b) the time averaged vertical velocity component, $\overline{w}$, (c) the time averaged radial velocity component, $\overline{u_r}$, (d) the instantaneous radial velocity component, u_r, reconstructed by UVP signal from experiment 1, $\Omega = 1.50\,\mathrm{rad\,s^{-1}}$.

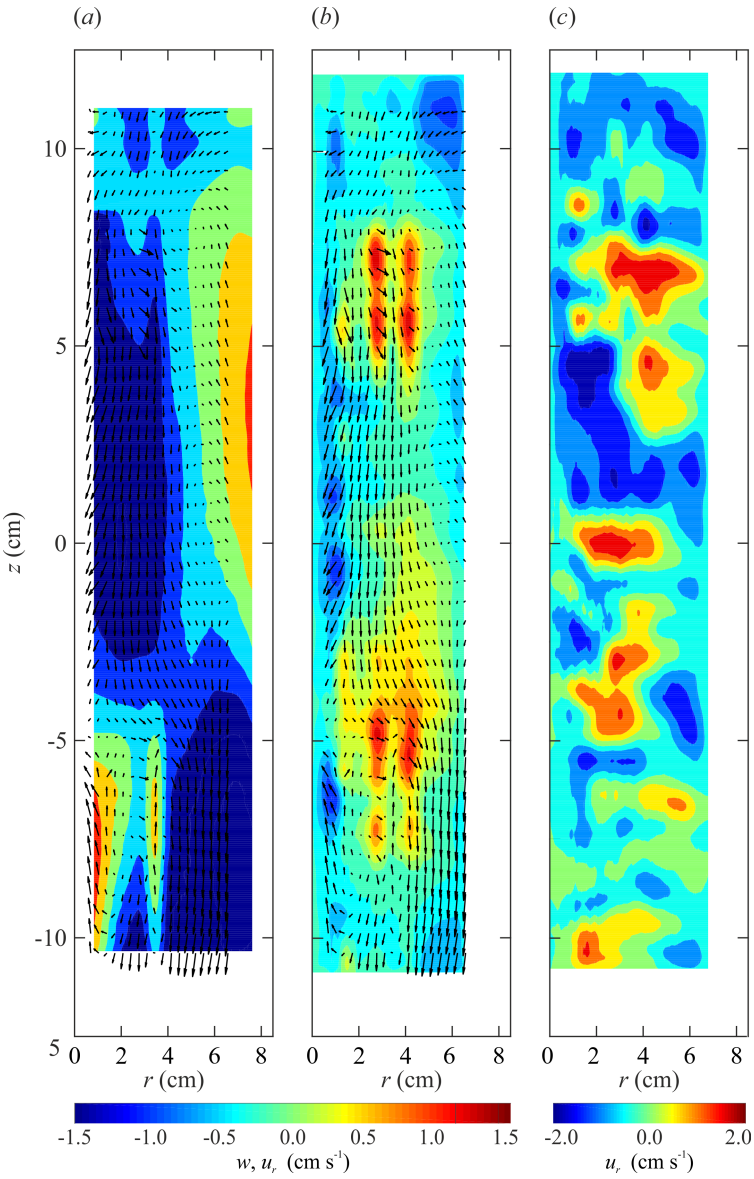

Figure 5.4: Colour maps of (a) the time averaged vertical velocity component, $\overline{w}$, (b) the time averaged radial velocity component, $\overline{u_r}$, (c) of the instantaneous radial velocity component, u_r, in fresh water, reconstructed by UVP signal from experiment 10, $\Omega = 2.75\,\mathrm{rad\,s^{-1}}$.

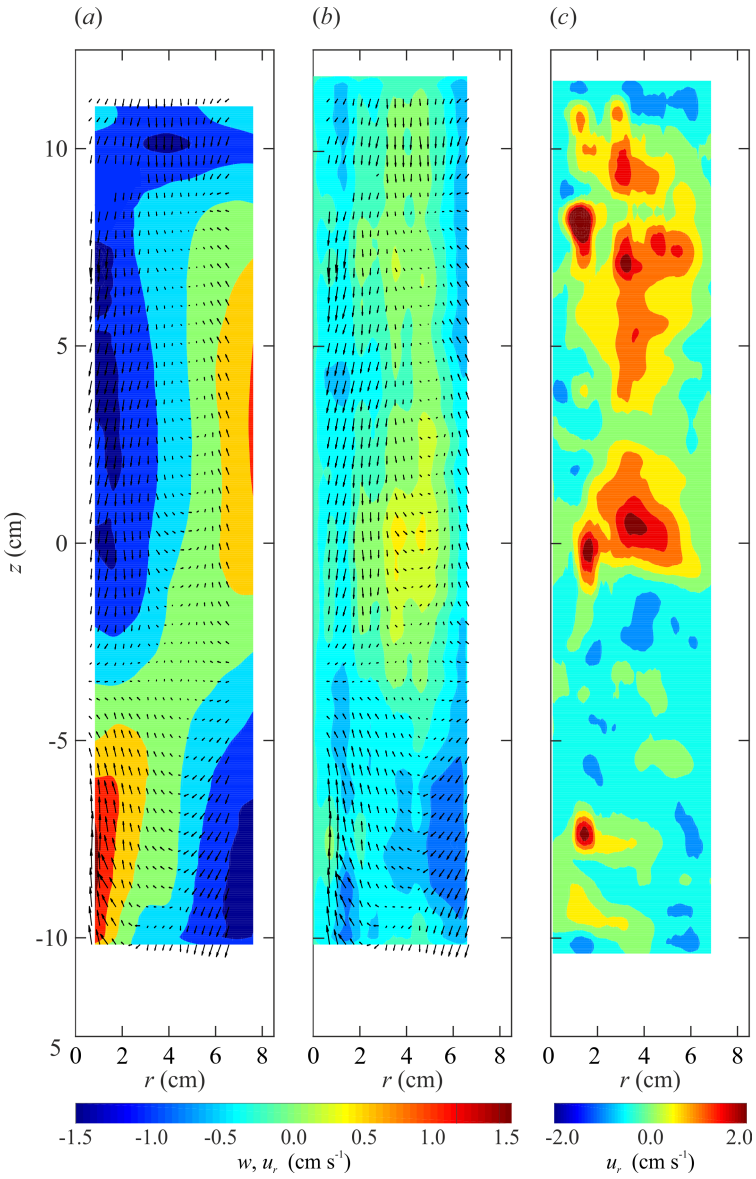

Figure 5.5: Colour maps of (a) the time averaged vertical velocity component, $\overline{w}$, (b) the time averaged radial velocity component, $\overline{u_r}$, (c) of the instantaneous radial velocity component, u_r, in fresh water, reconstructed by UVP signal from experiment 15, $\Omega = 1.50\,\mathrm{rad\,s^{-1}}$.

5.3 Turbulence field

5.3.1 Turbulence fluctuations

Considering the instantaneous vertical velocity profile, $w(z)$, as the sum of a time averaged velocity, $\overline{w(z)}$ and a fluctuating turbulent component $w'(z)$, we can compute the root mean squared (r.m.s.) vertical velocity fluctuation as

$$w_{rms}(z) = \sqrt{\Big(w(z) - \overline{w(z)}\Big)^2}, \tag{5.3}$$

which is positive definite, at different distances r from the inner cylinder. After that, $\overline{w_{rms}}$ is spatially averaged along the interior of the two layers, without including the thickness of the interface so far. We introduce the angle brackets $< ... >$ whenever we compute a spatial average. In figure 5.6*a*, $< \overline{w_{rms}} >$ is represented as a function of Re, at radial distance $r = 0.5, 1.3, 2, 3, 4, 5, 6, 7$ and 8 cm from R_1. The vertical turbulent fluctuations linearly increase with Ω, as $Re \propto \Omega$, and decrease with r. As expected, the highest fluctuations are very close to the rotating inner cylinder, with a more irregular trend throughout the considered range of Re.

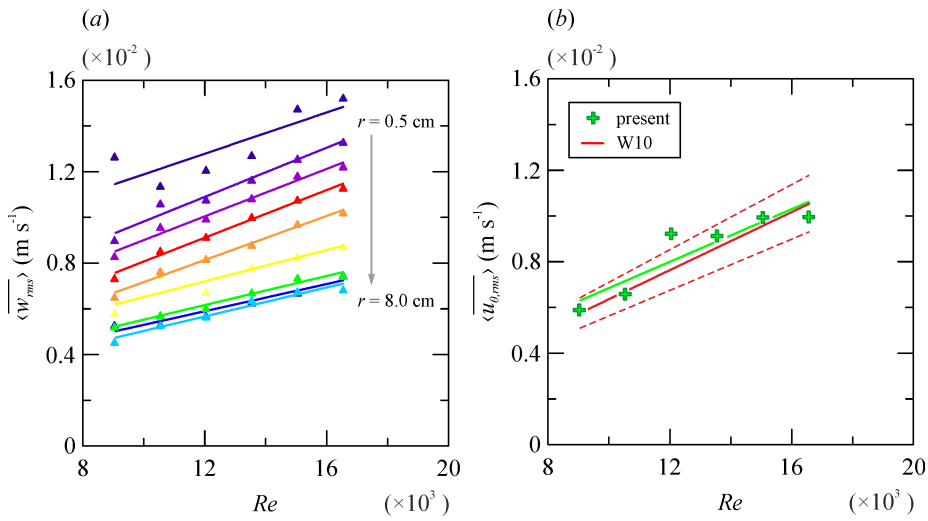

Figure 5.6: (*a*) Radial and time average of the r.m.s. vertical turbulent velocity, $\langle\overline{w_{rms}}\rangle$, as a function of Re at different distance r from R_1; (*b*) comparison between the space and time average of the azimuthal turbulent velocity, $\langle\overline{u_{\theta,rms}}\rangle$, of the present study (green crosses and green solid line) with the empirical relationship of Woods et al. (2010) (W10, red solid line).

Regarding the fluctuating azimuthal velocity, figure 5.6*b* shows $\langle\overline{u_{\theta,rms}}\rangle$, averaged in time and depth of the fluid, measured at a distance $r = 2.7$ cm from the inner cylinder by a "short" azimuthal UVP probe pointing upstream. The experimental data of the present work are compared with the PIV (particle image velocimetry) results of Woods et al. (2010), who used the same tank as the one described in chapter 4 (the inner radius $R_1 = 10$ cm, the outer radius $R_2 = 25$ cm and the depth of a single layer $H = 19.5$ cm) and found that

$$\langle u_{\theta,rms} r\rangle = (0.086 \pm 0.01)\, \Omega R_1^2. \tag{5.4}$$

Gap averaging equation 5.4, and introducing Re defined in section 5.1, yields

$$\langle u_{\theta,rms}\rangle = \frac{0.086 \pm 0.01}{R_2 - R_1} \ln\left(\frac{R_2}{R_1}\right) \nu Re = (6.3 \pm 0.7) \times 10^{-7} Re, \tag{5.5}$$

which is the red curve in figure 5.6b. The fairly good superposition of the results indicates the scalability of the Taylor-Couette cell as a generator of turbulence.

In figure 5.7*a*-*b* the absolute value of the time averaged vertical velocity, $|\overline{w'}|$, and density fluctuations, $|\overline{\rho'}|$, are illustrated as a function of depth z, with respect to the interface, and the correlation $\overline{\rho' w'}$ in figure 5.7*c*, for the two-layer experiments 1-9 of table 5.1. Density and velocity data were recorded simultaneously for approximately 2 minutes by the conductivity and a "short" vertical UVP probe at fixed depths, with a vertical space lag of 1 cm in the range $z \approx \pm 12.5$ cm. Both $|\overline{w'}|$ and $|\overline{\rho'}|$ are affected by the presence of the density interface at $z = 0$. In the interior of the top and bottom layers, the vertical velocity fluctuations present a mean value of $|\overline{w'}| = 0.5\ \mathrm{cm\,s^{-1}}$ that reduces by a factor of 60% at the interface. In contrast, density fluctuations reach a peak of $5 - 8\ \mathrm{kg\,m^{-3}}$ at the interface and decrease rapidly above and below the interface to a value that decreases itself with Ω. The overall trend of the correlation, shown in figure 5.7*c* follows a trend similar to the density fluctuations.

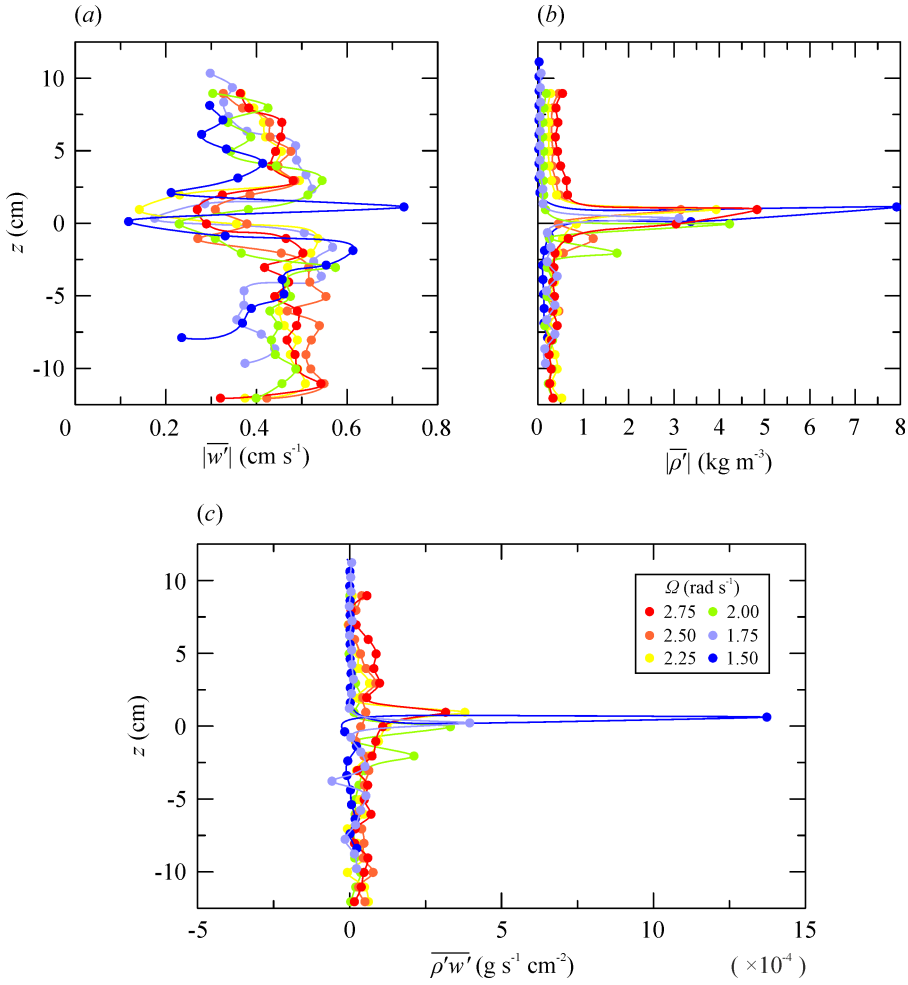

Figure 5.7: (a) Absolute value of the time average of the vertical velocity fluctuations, $\left|\overline{w'}\right|$; (b) absolute value of the time average of the density fluctuations, $\left|\overline{\rho'}\right|$; (c) time average correlation, $\overline{\rho' w'}$, as a functions of z (the interface is at $z = 0$).

5.3.2 Turbulent kinetic energy

In figure 5.8*a*-*b* we compare the mean turbulent kinetic energy (TKE) of the vertical and radial fluctuating velocity, averaged along the total depth of the fluid, H_{tot}, and per unit volume of fluid, at different r from R_1. Data for the azimuthal kinetic energy are available only at $r = 2.7$ cm from R_1

and are reported in figure 5.8*c*. The mean TKE is evaluated as

$$\mathrm{TKE} = \frac{1}{2}\frac{1}{H_{tot}}\int_0^{H_{tot}} \rho u'^2 \mathrm{d}h, \tag{5.6}$$

with $u' = w', u'_r$, or u'_θ.

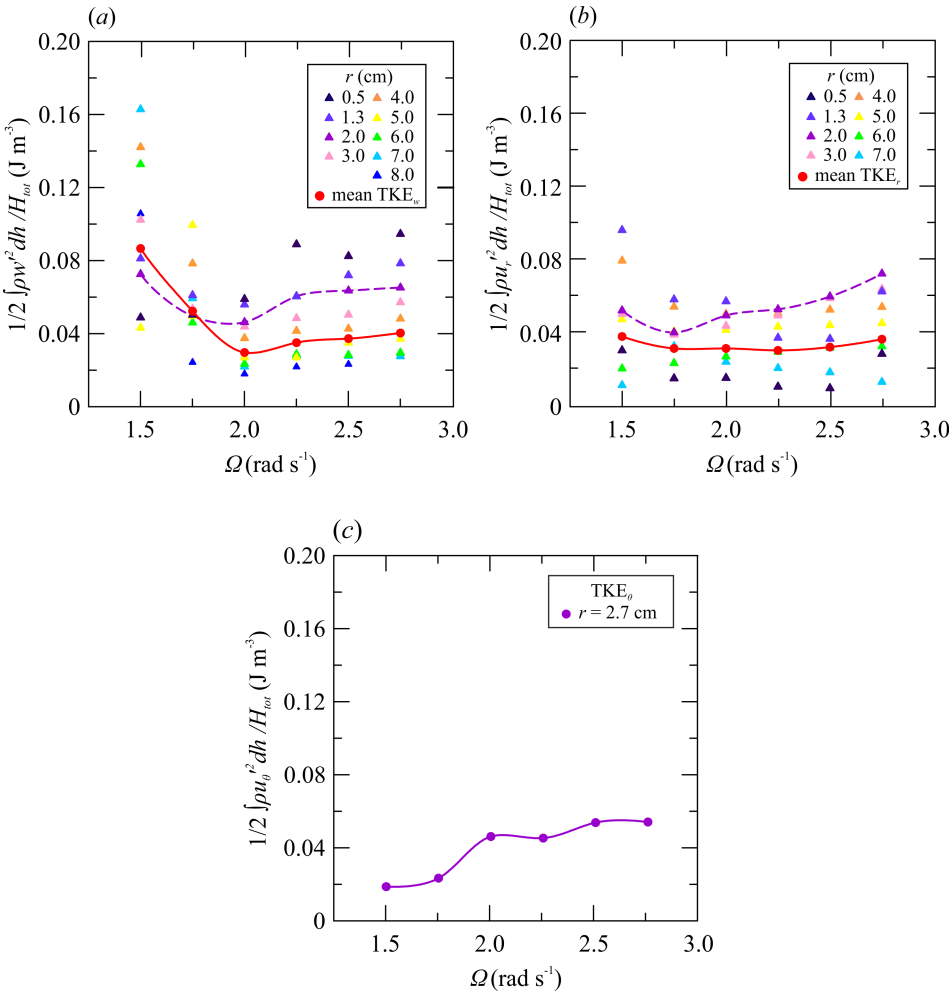

Figure 5.8: (*a*) Vertical turbulent kinetic energy, TKE_w; (*b*) radial turbulent kinetic energy, TKE_r; (*c*) azimuthal turbulent kinetic energy, TKE_θ, as functions of Ω.

The gap averaged vertical (TKE_w) and radial (TKE_r) turbulent kinetic energy are represented with red dots and red solid line. TKE_w and TKE_r

at $r = 2$ and 3 cm are highlighted with dashed purple lines, for an easily comparison with the azimuthal turbulent kinetic energy, TKE_θ, measured at $r = 2.7$ cm from R_1. The TKE generally decreases with r and it increases with increasing source of turbulence (i.e. Ω), reaching a nearly constant value around $0.06\,\mathrm{Jm}^{-3}$ for $r = 2 - 3$ cm in all the principal directions.

It is interesting to compare the three contributions to the total TKE at a fixed radial distance, i.e. $r \approx 2$ cm. In figure 5.9 we can observe that at low Ω, the vertical component dominates while the azimuthal is very small. The difference between the three contributions decreases with Ω and at $\Omega = 2.00\,\mathrm{rad\,s}^{-1}$ the turbulent field appears totally isotropic. At higher rotation rate, the isotropy fades gradually but the three components remain almost equivalent. The total TKE hits the lowest point at $\Omega = 1.75\,\mathrm{rad\,s}^{-1}$ and tends to increase with Ω. The kink at low Ω still remains unexplained.

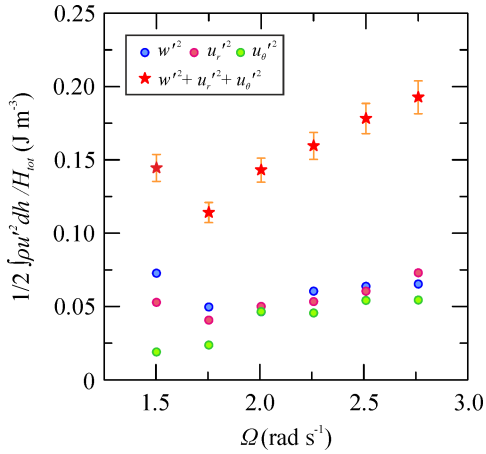

Figure 5.9: TKE_w (blue dots), TKE_r (pink dots), TKE_θ (green dots) and total TKE (red stars) at $r \approx 2$ cm.

Two typical examples of the TKE_w and TKE_r contour plots are shown in figure 5.10*a*-*b* for $\Omega = 2.75\,\mathrm{rad\,s}^{-1}$ (experiment 1 of table 5.1) and figure 5.10*c*-*d* for $\Omega = 2.00\,\mathrm{rad\,s}^{-1}$ (experiment 4 of table 5.1). TKE_w reaches a peak at the inner cylinder and in the central region of top and bottom layers, and gradually tends to zero towards the outer cylinder. The whole density interface ($z = 0$) is characterized by a null TKE_w. TKE_r is highest at around $r = 2$ cm, and decreases radially towards the lateral borders. These features are common for all the rotation rates in our experimental range.

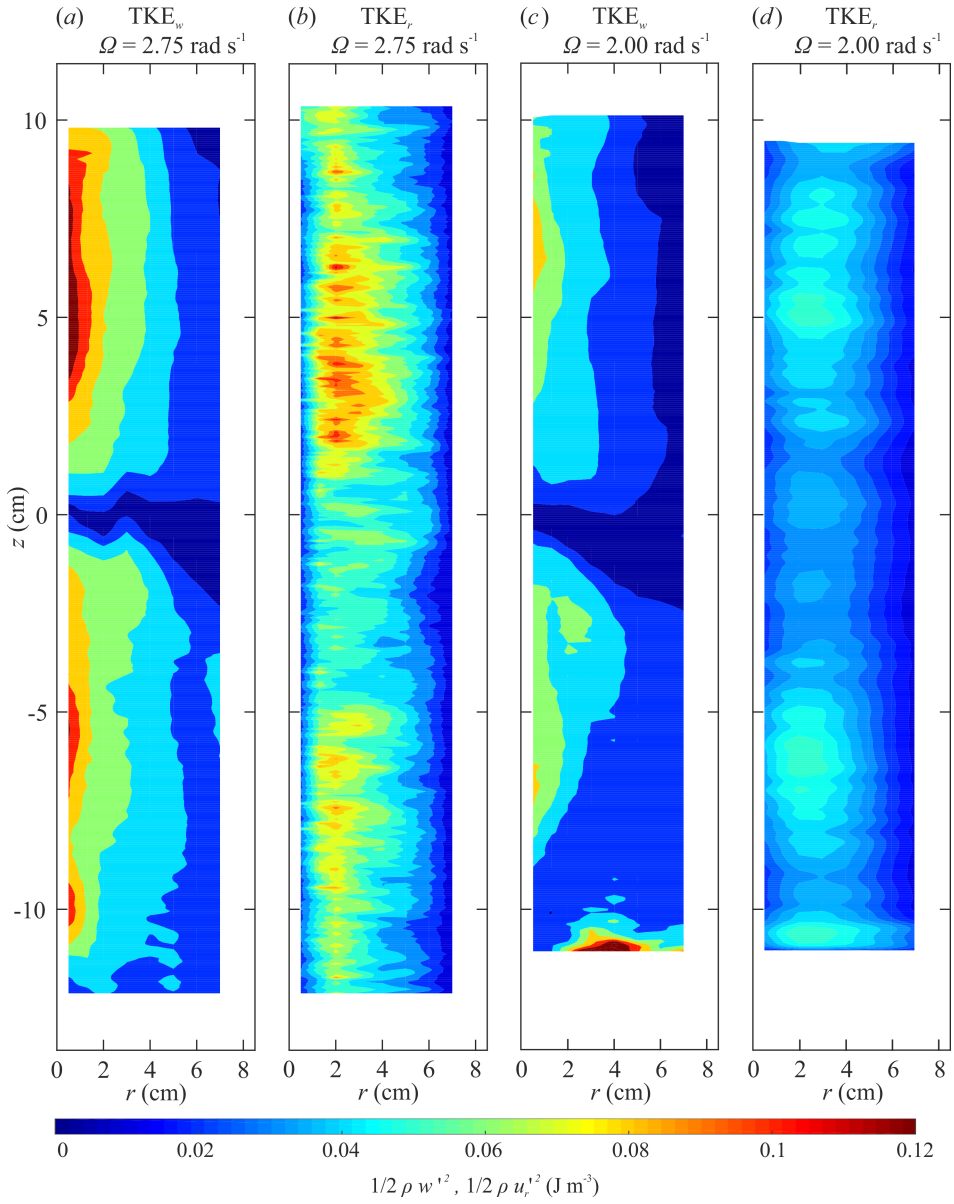

Figure 5.10: (a) Vertical turbulent kinetic energy, TKE_w and (b) radial turbulent kinetic energy, TKE_r for $\Omega = 2.75\,\mathrm{rad\,s^{-1}}$; (c) TKE_w and (d) TKE_r for $\Omega = 2.00\,\mathrm{rad\,s^{-1}}$.

5.4 Macro and micro length scales

The integral, Λ_i, and micro, λ_i, length scales of the flow field along the three principal directions can be evaluated by means of the normalized auto-correlation function of the fluctuating velocity component

$$\chi_i(z,\zeta) = \frac{u'(z,y)u'(z,y+\zeta)}{u'^2}, \tag{5.7}$$

with $u' = w', u'_r$ or u'_θ, and ζ the space lag.

We define the integral length scale as:

$$\Lambda_i(z) = \int_0^{\overline{\zeta}} \chi_i(z,\zeta)\mathrm{d}\zeta, \tag{5.8}$$

where $\overline{\zeta}$ is the length over which the auto-correlation function is positive, while the Taylor micro length scale is related to the auto-correlation coefficient at the origin, see Tennekes and Lumley (1972). We approximate the correlation function with a symmetric parabola passing through the origin $(\zeta, \chi(z,\zeta)) = (0,1)$ and $(\zeta, \chi(z,\zeta)) = (\mathrm{d}\zeta, \chi(z,\mathrm{d}\zeta))$, so

$$\lambda(z) = \mathrm{d}\zeta\sqrt{\frac{1}{1-\chi(z,\mathrm{d}\zeta)}}, \tag{5.9}$$

where $\mathrm{d}\zeta$ is the space accuracy of the probe. A typical example of normalized auto-correlation function is shown with a blue solid line in figure 5.11, while the symmetric parabola passing through the origin is shown with a red solid line.

The integral length-scale is representative of the size of the coherent macro structures of the flow field (large eddies), while the Taylor microscale is associated with the small scale eddies and gives a convenient estimation for the fluctuating strain rate field. In the present analysis we deal with Eulerian length scales, since we are considering correlations between fluctuating velocities measured at fixed points in a fixed frame of reference.

Time series of vertical velocity data are recorded by the "short" vertical UVP probe every 1 cm along the vertical, in the range $z = \pm 12.5$ cm, for approximately 2 minutes. Because of the linearity of the average and integral operators, the time averaged vertical macro length scales of the auto-correlation function of instant vertical velocity fluctuations are equal to the vertical lenght-scales of the time-averaged auto-correlation function:

$$\overline{\Lambda_w(z)} = \overline{\int_0^{\overline{\zeta}} \chi_w(z,\zeta)\mathrm{d}\zeta} \equiv \int_0^{\overline{\zeta}} \overline{\chi_w(z,\zeta)}\mathrm{d}\zeta. \tag{5.10}$$

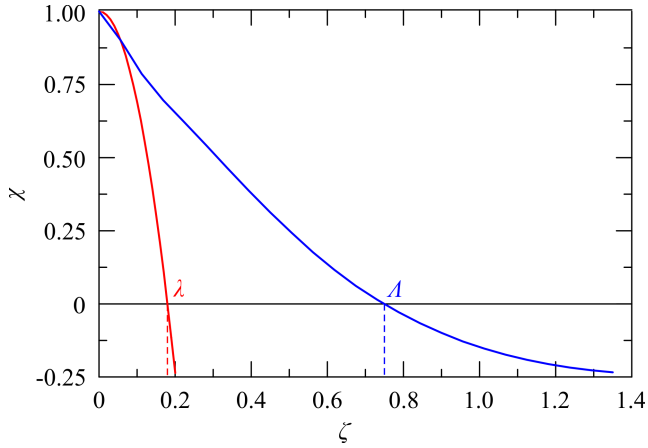

Figure 5.11: Auto-correlation function χ (blue line) and parabola passing through the origin (red curve). Their respective x-axis intersections determine the integral length scale Λ and Taylor length scale λ.

An instant vertical micro length scale is associated to every instant auto-correlation function. We average to obtain the mean value.

On the other hand, radial and azimuthal velocity data are recorded by the "mini-short" UVP probe moving jointly with the conductivity probe. After approximately 11 vertical excursions of radial velocity, 5 vertical excursions of azimuthal velocity are immediately recorded and this sequence is repeated 9 times. We follow different paths to calculate the radial and azimuthal length scales:

(i) we firstly evaluate the mean velocity at every realization, spatially averaged over ± 1 cm across discrete vertical depths. Then we calculate the auto-correlation function of the mean velocity and the length scales. We finally time average the length scales over 11×9 realizations of radial velocity and 5×9 realizations of azimuthal velocity;

(ii) we extract instantaneous velocity data at discrete vertical depths from each of the 11×9 realization for the radial velocity and 5×9 realizations for the azimuthal velocity, and evaluate the time averaged auto-correlation function of the overall sample data and the length scales;

(iii) the auto-correlation function and length scales are firstly determined from every single realization and then time averaged over the whole number of realizations.

Although the trend of the Taylor micro length scale does not depend significantly on the the chosen strategy, the first two procedures lead to smaller values of Λ_r and Λ_θ than procedure (iii). Nevertheless, we assume that procedure (iii) is more similar to the method adopted for the vertical length scale evaluation.

In figure 5.12 we illustrate the vertical micro and macro length scales λ_w and Λ_w, in figure 5.13 the micro and macro radial length scales λ_r and Λ_r and in figure 5.14 the micro and macro azimuthal length scales λ_θ and Λ_θ, in a two-layer fluid (coloured plots) and in fresh water (gray-scale plots), with error bands corresponding to one standard deviation.

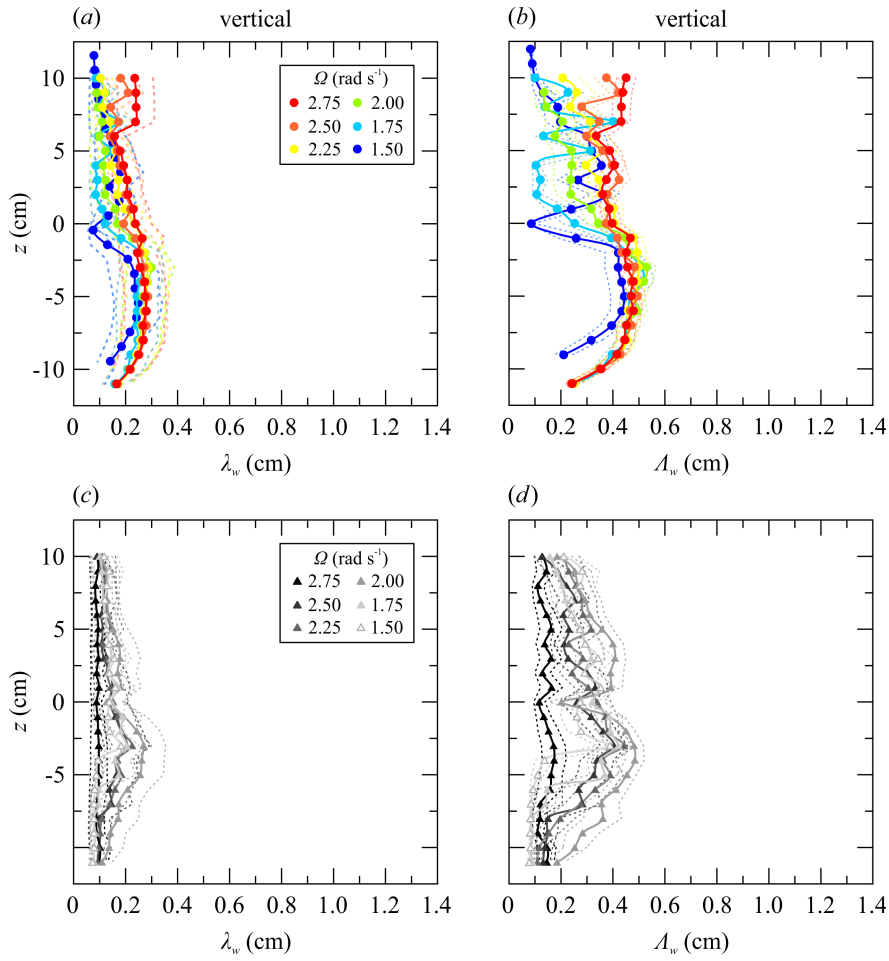

Figure 5.12: (a) λ_w in a two-layer fluid; (b) Λ_w in a two-layer fluid; (c) λ_w in fresh water; (d) Λ_w in fresh water.

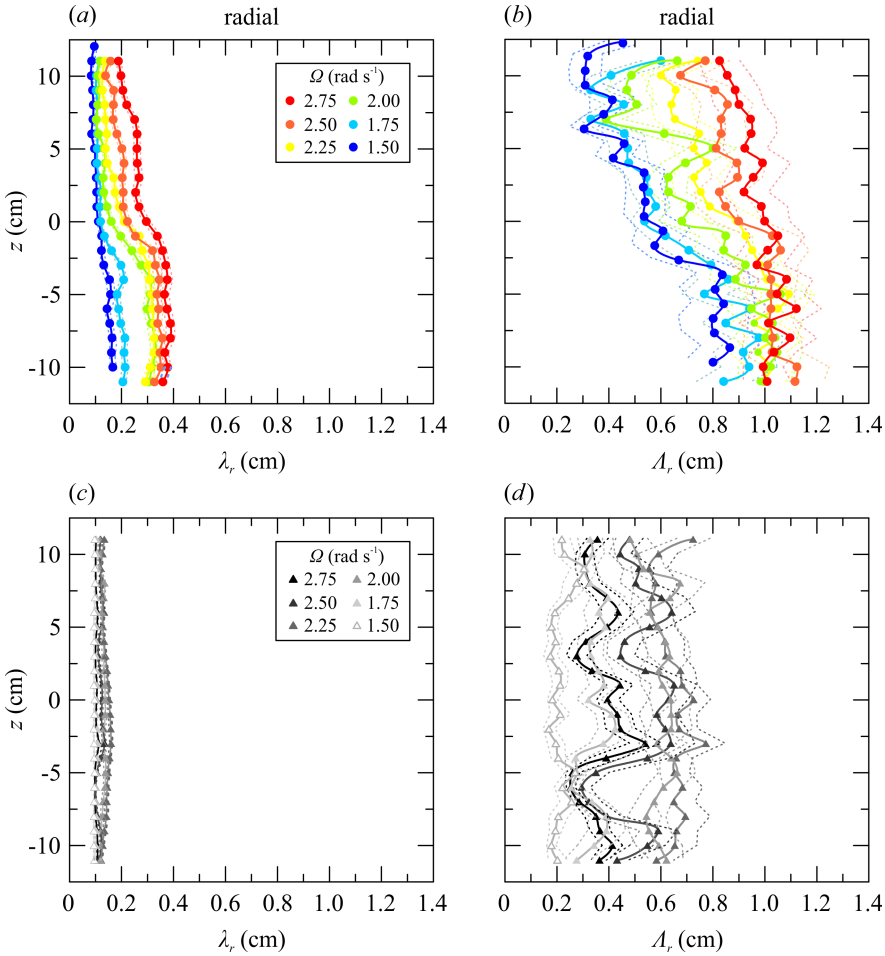

Figure 5.13: (a) λ_r in a two-layer fluid; (b) Λ_r in a two-layer fluid; (c) λ_r in fresh water; (d) Λ_r in fresh water.

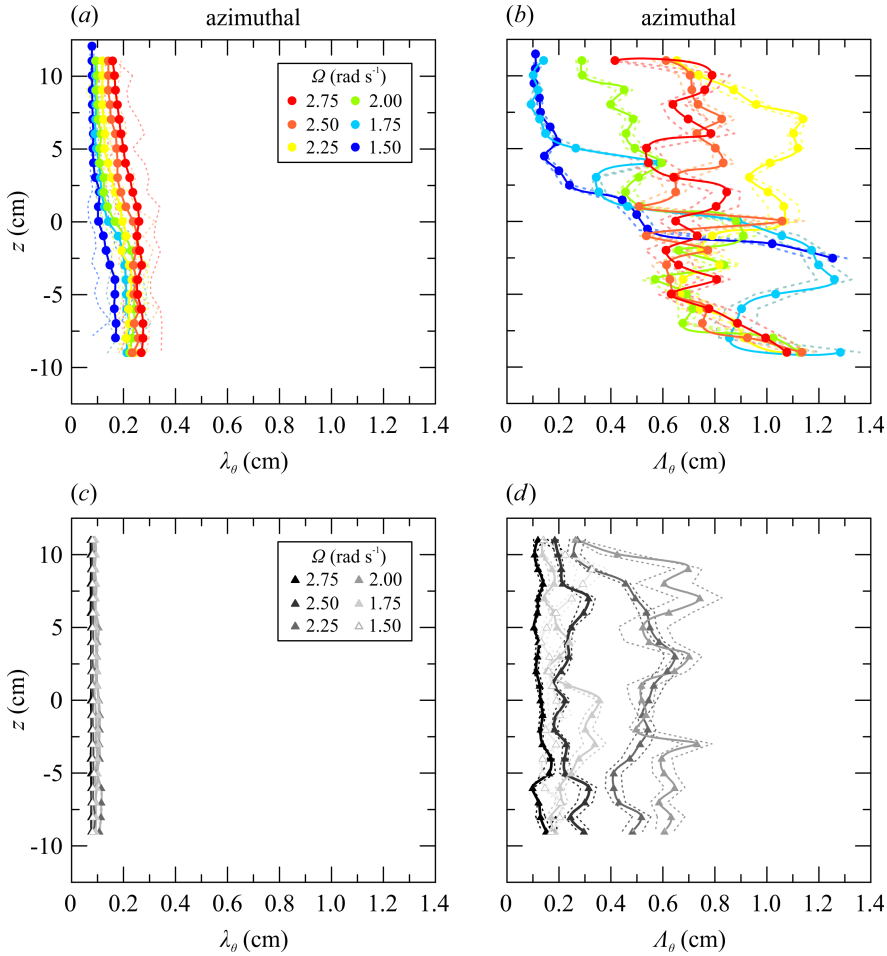

Figure 5.14: (a) λ_θ in a two-layer fluid; (b) Λ_θ in a two-layer fluid; (c) λ_θ in fresh water; (d) Λ_θ in fresh water.

Regarding the stratified system, the general trend is of an increment of the scales with Ω and depth and a larger variability in the upper layer respect to the lower layer. The most relevant variations are observed for the vertical length scales, which drop near the interface at low Ω. It can be addressed to the interface, which, at large values of Ri, acts like a rigid boundary, flattening the turbulent eddies and transferring energy from the vertical to horizontal scales (Briggs et al., 1996; Hannoun et al., 1988).

As previously defined, the Richardson number is $Ri = g\,(\Delta\rho/\rho_0)\,H/\left(\Omega\,R_1^2\right)$, where g is the acceleration due to gravity, $\Delta\rho$

the density difference between the two layers, ρ_0 a reference for density, and H the height of the layer. With increasing Ω and same bottom source buoyancy flux, $\Delta\rho/\rho_0$ in steady state decreases with $\propto -\Omega^{5/2}$, as shown in figure 5.15*a*, even if for sufficiently low rotation rate $\Delta\rho/\rho_0$ seems to drop linearly with Ω. As a consequence, Ri decreases with Ω as shown in figure 5.15*b*, where Ri seems to follow a decreasing trend with $\propto \Omega^{-5/2}$ in our experimental range. A cubic-fit polynomial better interprets the rapid fall of Ri at $\Omega = 2.75 - 3.00\,\mathrm{rad\,s^{-1}}$. In our experiments, if $\Omega = 3.00\,\mathrm{rad\,s^{-1}}$, the density difference between the layers becomes low enough to overturn the density interface and the fluid becomes weakly linear stratified. The decrease of Ri involves a reduction of the vertical length scales, λ_w and Λ_w, in the top layer, but this does not correspond to an increase of horizontal length scales.

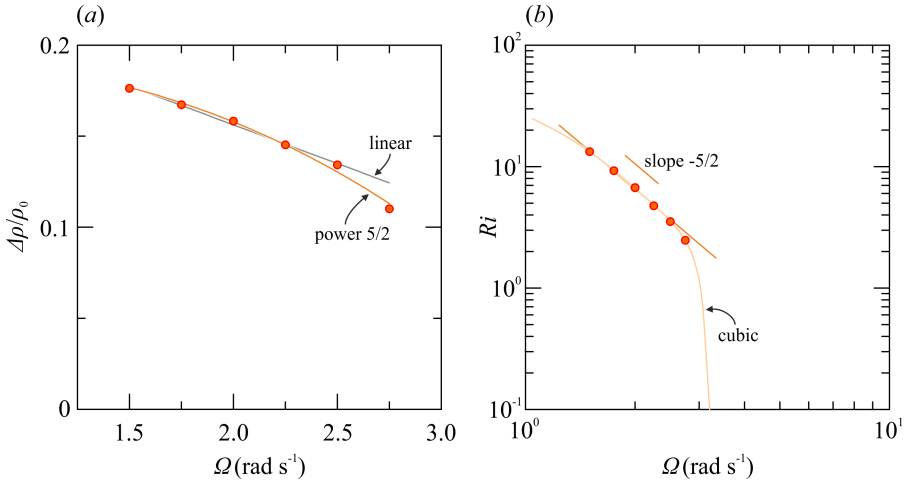

Figure 5.15: (*a*) $\Delta\rho/\rho_0$ and (*b*) Ri as functions of Ω.

On the other side, in fresh water, we can observe generally lower values and constant length scales along the vertical at high Ω.

The radial macro length scales Λ_r in figure 5.13 are greater than the vertical, and show a decreasing trend with height and Ω. In fresh water, Λ_r fluctuate along the vertical around a constant mean value but do not show a clear dependence on Ω. The azimuthal macro length scales Λ_θ in figure 5.14 show a more chaotic behavior in stratified fluid than in water where, again, we observe reduced values at higher Ω. As Λ_i represent how far the velocity is related in time along the i direction, a possible explanation may be the more intense instability of the flow.

5.5 Dynamics at the interface

5.5.1 Density and vertical velocity fluctuations

In order to gain a deeper insight of the mixing mechanisms in a two-layer fluid, in this section we look more closely at the interface. We record the density and vertical velocity every 2 mm in the vertical direction, for a time $t = 120$ s, along a 4 cm deep region across the density interface. The density is recorded by the conductivity probe, mounted on the traverse system and at a radial distance $r = 3.5$ cm from the inner radius. Velocity data are collected by a "short" ultrasonic UVP probe, glued to the conductivity probe, with the head at 2 cm above the electrodes. The UVP probe points downward and the velocity data are registered at the gate 2 cm far from the head of the UVP probe. Velocity and density data are then interpolated over the same time and correlated.

The time averaged density, $\overline{\rho}$, are shown as a function of distance from the interface at $z = 0$, in figure 5.16*a*, while the absolute value of the density fluctuations, $\left|\overline{\rho'}\right|$, are shown in figure 5.16*b*. Again we observe that the density difference $\Delta\rho$ between the layers in steady state decreases with Ω. In the interior of each layer, where the $\overline{\rho}$ is nearly homogeneous, the density fluctuations are very small but they rapidly increase towards the density discontinuity. The normalized cumulative area of the $\overline{\rho'}$ curves, A_ρ, are reported in figure 5.16*c*. The tails of the curves are generally confined in the top and bottom 10% of A_ρ, while the remainder 80% of A_ρ corresponds to a vertical depth of approximately 1 cm, which can be considered as a good measure of the thickness of the interface.

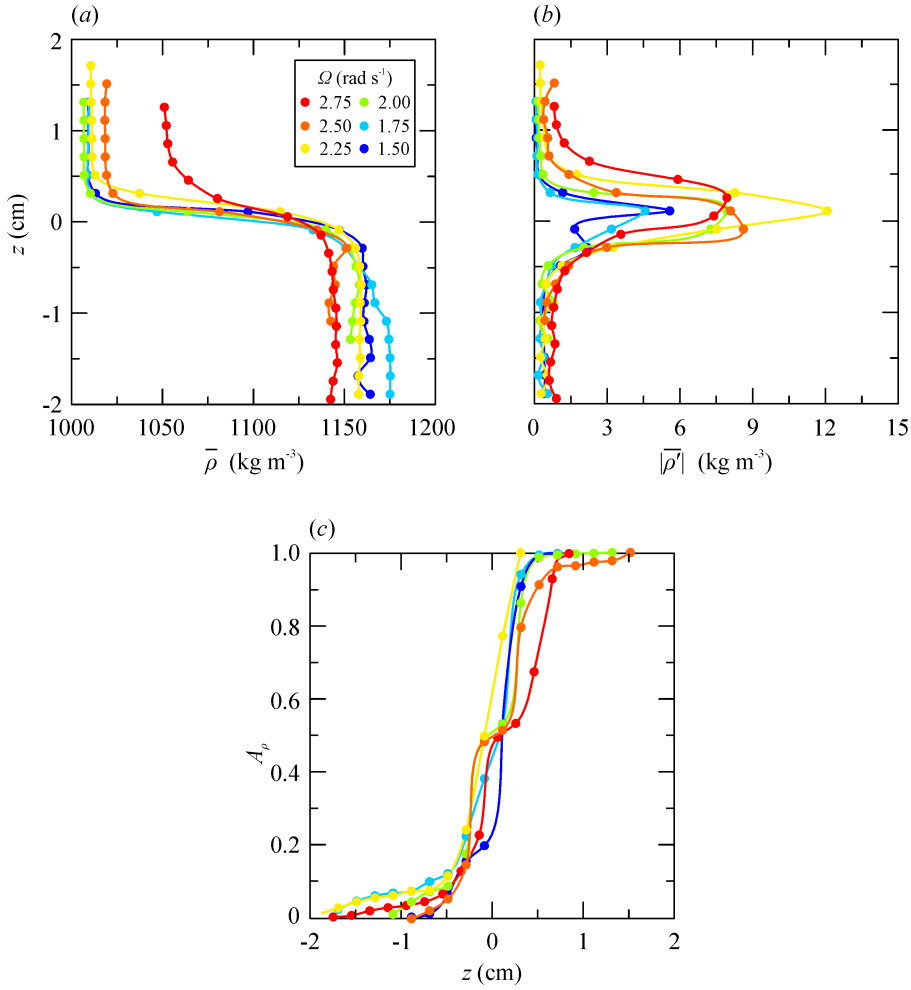

Figure 5.16: (a) Time averaged density; (b) time averaged density fluctuations; (c) cumulative area of the density fluctuations.

The time averaged vertical velocity $\overline{w}$, shown in figure 5.17a is negative (downward), with greater values at higher Ω and below the interface. The time averaged velocity fluctuations, $\left|\overline{w'}\right|$, illustrated in figure 5.17b, generally decrease to zero at the interface more gradually than the r.m.s. density fluctuations, and even more gently at low rotation rates. The drop of $\left|\overline{w'}\right|$ occurs over a depth of approximately 2 cm, or twice the thickness of the interface and as reported by the normalized cumulative area A_w in figure 5.17c, no tails can be observed within ± 2 cm from the interface. This

means that the density interface affects the velocity field much further than the density field.

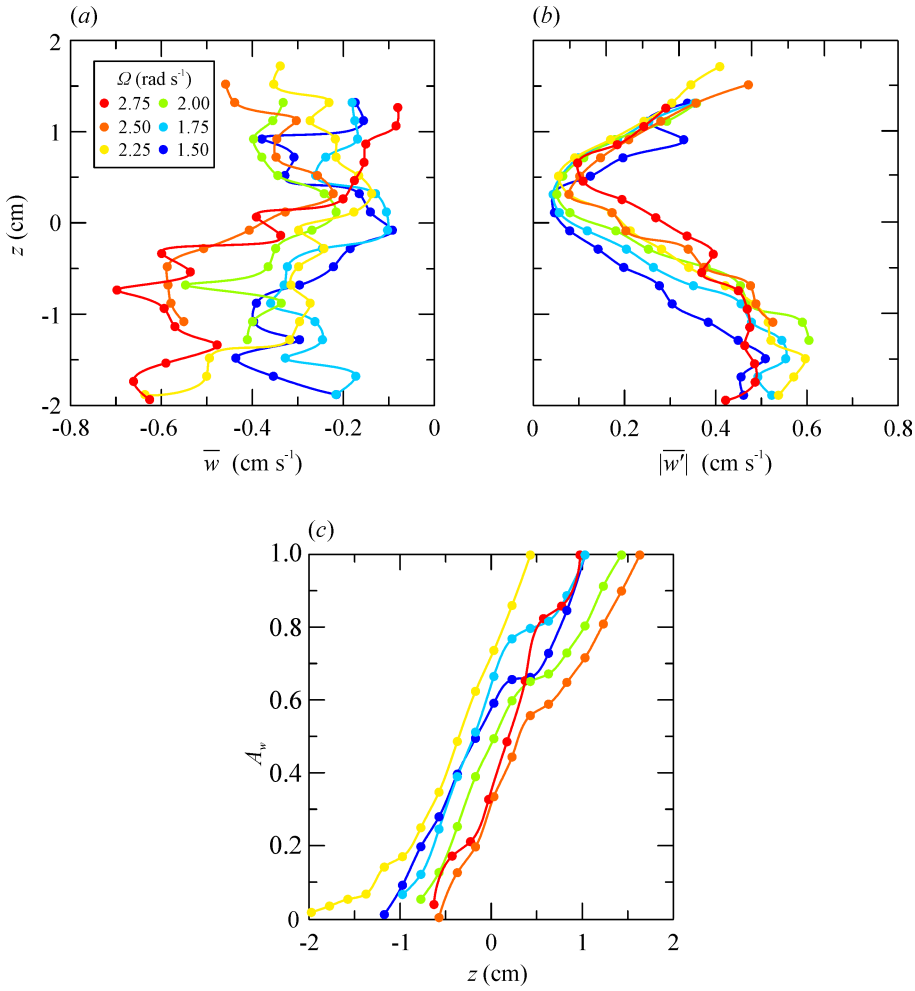

Figure 5.17: (*a*) Time averaged mean vertical velocity; (*b*) time averaged vertical velocity fluctuations; (*c*) cumulative area of vertical velocity fluctuations.

Figure 5.18*a* shows the steady state density profile for experiment 2 of of table 5.1 and the corresponding instantaneous vertical velocity fluctuations w' and density fluctuations ρ' shown as a function of time in figure 5.18*b* and figure 5.18*c* respectively, at single points marked with dots in the density profiles. The distance between two subsequent marks is equivalent to $1\,\mathrm{cm\,s^{-1}}$ in the vertical axis of w', and to $10\,\mathrm{kg\,m^{-3}}$ in the vertical axis of

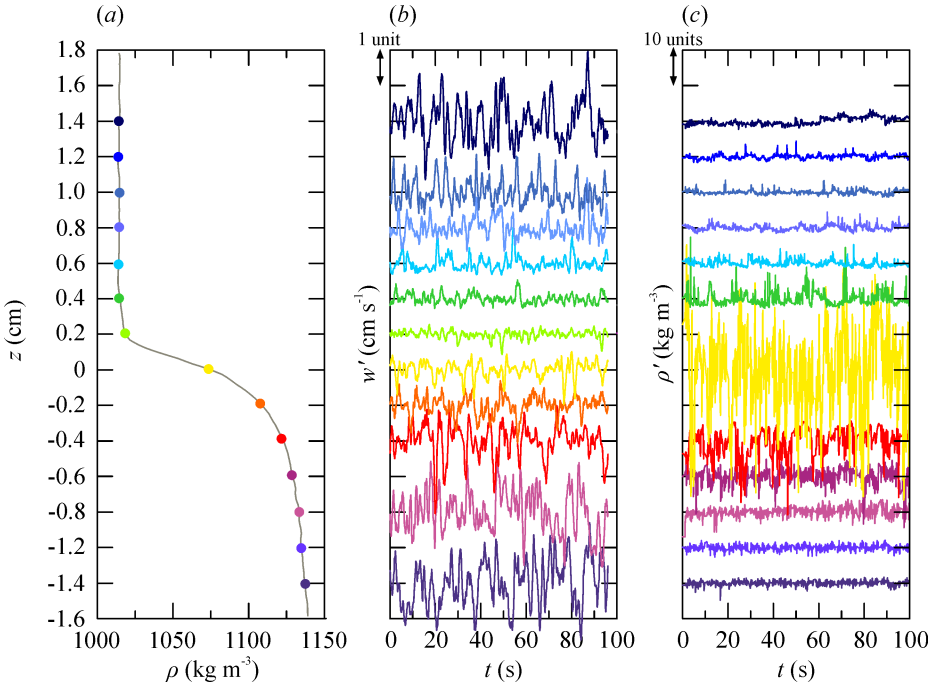

Figure 5.18: (a) Density profile; (b) instantaneous vertical velocity fluctuations w' as function of time; (c) instantaneous density fluctuations ρ', as function of time. Experiment 2 of table 5.1.

ρ'. We can easily notice how w' reduces and ρ' increases within $z = \pm 2$ cm from the interface, while far from the interface w' has a larger and ρ' a smaller amplitude. We also notice that both signals seem to be periodic and similar at each position. Similar results are obtained for all the values of Ω in our experimental range.

The correlation $\overline{\rho' w'}$ is illustrated in figure 5.19a and, because it is a measure of the vertical salt flux per unit area, we can estimate the vertical buoyancy flux as $B_{to} = g\overline{\rho' w'} A/\rho_0$, where $A = \pi \left(R_2^2 - R_1^2\right)$ is the cross area of the tank and ρ_0 a reference for density, here $\rho_0 = 998.2\,\mathrm{kg\,m^{-3}}$, coherently with previous definitions (see section 5.1). The results are reported in figure 5.19b, where we can see that the flux vanishes at low rotation rates.

If we average B_{to} with depth, in a vertical interval comprising 98% of the cumulated correlation across the interface, for the six values of Ω, we find that the salt flux crossing the density interface and modeled by $\overline{\rho' w'}$, is a fair approximation of the vertical salt transport across the water column. This implicates that all the principle mechanisms responsible for mixing

occur at the the interface.

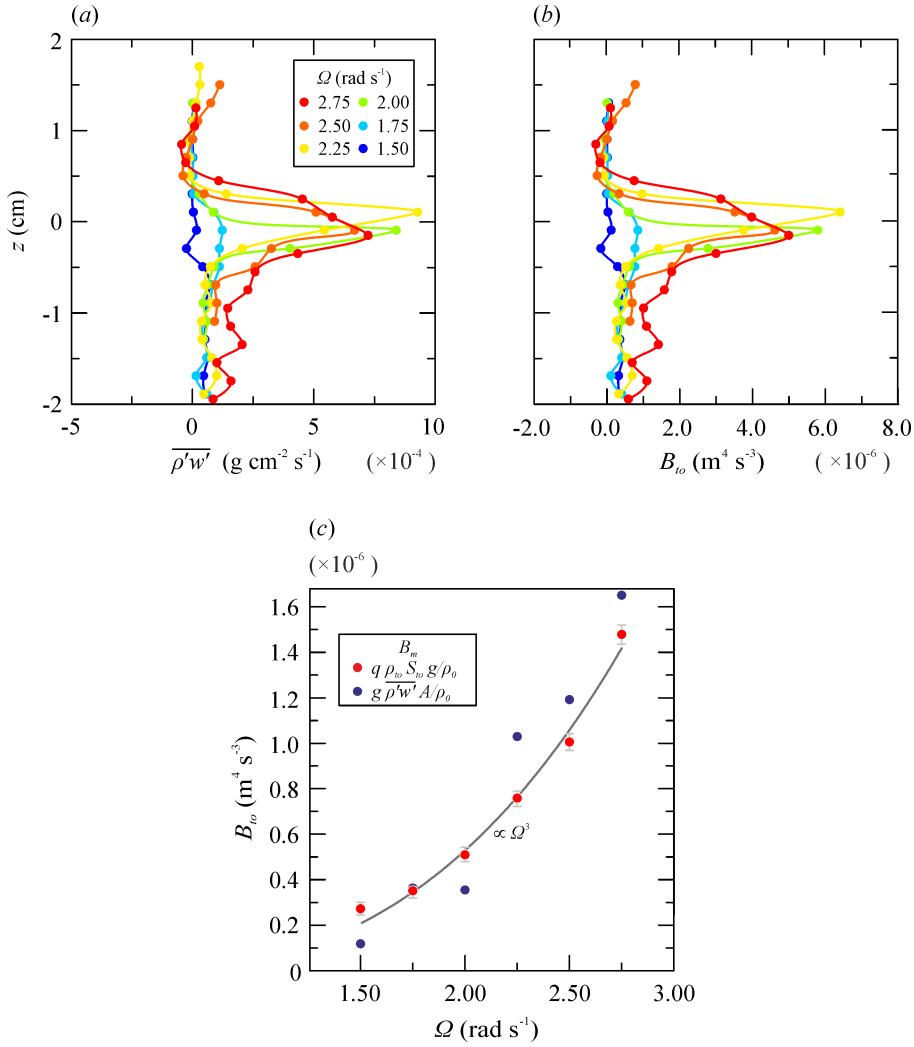

Figure 5.19: (a) Time averaged correlation between density and velocity fluctuations; (b) vertical buoyancy flux estimated as $g\overline{\rho' w'}A/\rho_0$; (c) comparison between the vertical buoyancy flux measured at the top of the tank and that exchanged at the density interface, expressed as a function of Ω. The flux vanishes at low rotation rates.

5.5.2 Quadrant Analysis

Let us consider a quadrant decomposition of density ρ' and vertical velocity fluctuations w' as shown in figure 5.20. The events may fall in one of the four quadrants according to the follow sampling conditions:

- quadrant Q1 if $\rho' > 0$ and $w' > 0$;
- quadrant Q2 if $\rho' > 0$ and $w' < 0$;
- quadrant Q3 if $\rho' < 0$ and $w' < 0$;
- quadrant Q4 if $\rho' < 0$ and $w' > 0$.

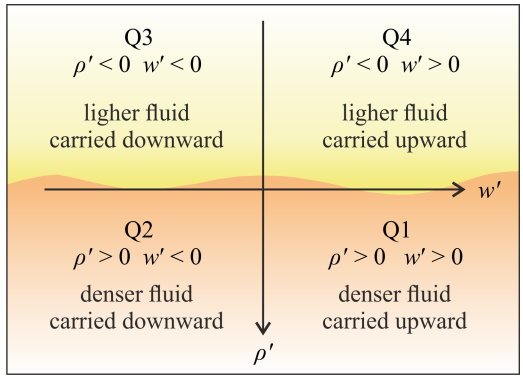

Figure 5.20: Sketch of the four quadrants.

Assuming that the vertical salt flux per unit area can be expressed as $\langle \overline{\rho' w'} \rangle = -\mathcal{D}\, \partial\rho/\partial z$ where $\mathcal{D}$ is the diffusivity, and considering that the background stratification is stable (i.e. the density gradient is negative), quadrants Q1 and Q3 contribute to the upward diffusive buoyancy flux, because the resulting correlation is positive, while Q2 and Q4 contribute to the downward diffusive buoyancy flux, because the resulting correlation is negative.

The event-averaged (phasic-averaged) correlation for the i-th quadrant is computed as:

$$\langle \overline{\rho' w'} \rangle_i = \frac{1}{N_i} \sum_{j=1}^{N_i} \left[\left(\rho' w' \right)_j \right]_i \quad \text{for } i = 1, 2, 3, 4, \tag{5.11}$$

where N_i is the number of events and j is the current sample number of the i-th quandrant. The time averaged correlation for the i-th quadrant is

computed as:

$$\left(\overline{\rho' w'}\right)_i = \frac{1}{N} \sum_{j=1}^{N_i} \left[\left(\rho' w'\right)_j \right]_i \quad \text{for } i = 1, 2, 3, 4, \tag{5.12}$$

where N is the total number of events. It follows that the total time averaged correlation is the sum of the time averaged contributions of the four quadrants:

$$\left(\overline{\rho' w'}\right) = \sum_{i=1}^{4} \left(\overline{\rho' w'}\right)_i = \sum_{i=1}^{4} \frac{N_i}{N} \left\langle \overline{\rho' w'}_i \right\rangle . \tag{5.13}$$

The ratio N_i/N represents the concentration (or permanence) of event in the i-th quadrant.

We can further analyze the values above fixed amplitude thresholds, which are defined as multiples β of the product of the root mean square of density and velocity fluctuations $\rho'_{rms} w'_{rms}$, so:

$$\left|\rho' w'\right| > \beta \rho'_{urms} w'_{rms}. \tag{5.14}$$

The $\beta = 0$ case corresponds to a null threshold. Figure 5.21 illustrates the concentration, the time and phasic averaged contributions of each quadrant for $\beta = 0$, normalized with respect to the overall time averaged correlation $\overline{\rho' w'}$ as a function of distance from the density interface, for $\Omega = 2.75\,\mathrm{rad\,s^{-1}}$ (experiment 1 of table 5.1). The gray dots represents the contributions from all quadrants. The concentration does not change dramatically from one quadrant to another and it falls in the range $0.2 - 0.3$. However, a slightly larger concentration is registered in quadrant Q1 ($\rho' > 0, w' > 0$), followed by Q3 ($\rho' < 0, w' < 0$). This means that the bursts of denser fluid displacing upward and burst of lighter fluid displacing downward are more frequent and intense. As previously forecast, positive time-averaged correlations coming from Q1 and Q3 contribute to the upward diffusive buoyancy flux, while negative correlations coming from Q2 and Q3 contribute to a downward contra-diffusive flux being approximately half the value of the upward. All the correlations hit a maximum value at the interface, $z = 0$. On the other hand, phasic averaged contributions are generally more balanced, as the events have a comparable intensity in all the quadrants.

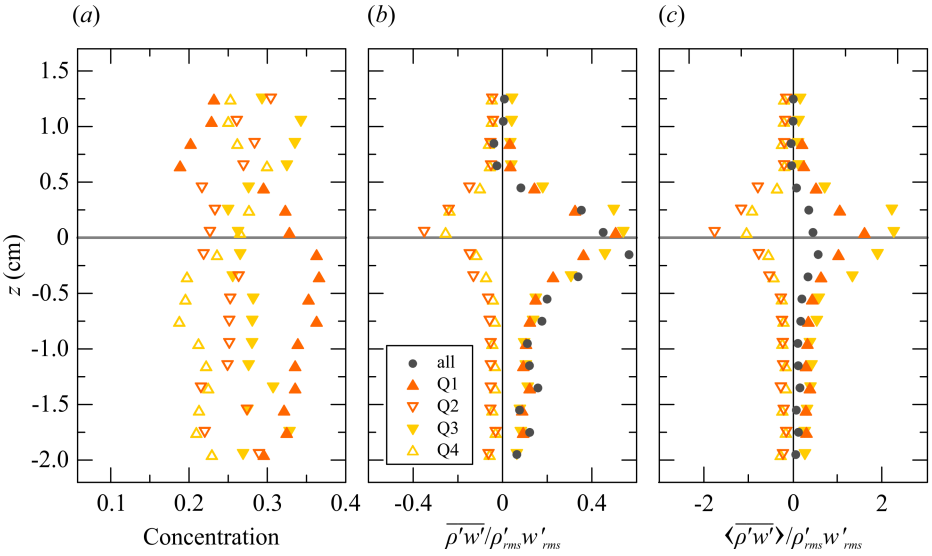

Figure 5.21: (a) Cross-correlation of fluctuating density and vertical velocity, for quadrants Q1 ($\rho' > 0, w' > 0$), Q2 ($\rho' > 0, w' < 0$), Q3 ($\rho' < 0, w' < 0$), Q4 ($\rho' < 0, w' > 0$), with no threshold ($\beta = 0$). (a)Concentration; (b) time average correlation; (c) phasic average correlation. Filled circles indicate the contribution from all quadrants. Data from Exp 1, $\Omega = 2.75\,\mathrm{rad\,s^{-1}}$.

Figure 5.22 illustrates the concentration, the time and phasic averaged contributions of each quadrant for $\beta = 2$, normalized again with respect to the overall $\overline{\rho' w'}$. The permanence of the events in each of the four quadrants is reduced to zero in the interior of both layers, where the correlation is nearly zero, and it grows rapidly to approximately 0.1 at the interface. The events have comparable intensity for all quadrants. The trend of the time averaged and phasic averaged contributions with depth does not seem to change from the $\beta = 0$ case. The phasic average correlation seems to be grater for Q3 ($\rho' < 0, w' < 0$), revealing that the bursts of lighter fluid parcels downward are intense and frequent. According to this scheme, the (diffusive) action generating salt flux is turbulence in the upper layer, with lighter fluid eddies scraping the interface from the top. If we compare the peak values of the time-average correlation in figures 5.21b and 5.22b, we can observe a reduction of 60% (from 0.6 to 0.4), so an amount of 60% of the flux is related to energetic events of Q1 and Q3. This analysis confirms that the buoyancy flux is an intermittent phenomenon also at the small scale,

with intense events occurring at the passage of the wavelike perturbation that will be described in sections **??** and 5.6.

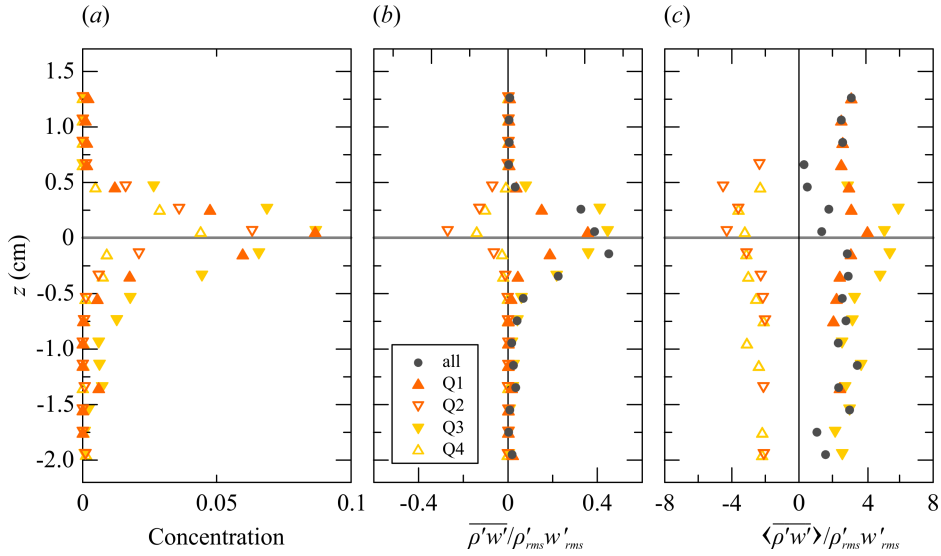

Figure 5.22: (*a*) Cross-correlation of fluctuating density and vertical velocity, with $\beta = 2$. For caption, see figure 5.21.

Figure 5.23 shows the joint probability density functions (pdf) for the events in each quadrant for the same experiment of figure 5.21 and 5.22, at four different levels $z = 0.85, 0.65, -0.35$ and -0.95 cm from the interface. If we firstly look at panel (b), above the interface for $z \leq 0.65$ cm, the velocity fluctuations are much reduced to values $w' \leq 0.5$ cm s^{-1}, and increase slightly with distance from the interface (as in panel (a) where $z = 0.85$ cm). In contrast, the density fluctuations are quite relevant, and increase to values $\rho' \approx 7$ g cm^{-3} just below the density interface, at $z \approx 0.35$ cm in panel c, where the pdf has a broader and wider area. Approaching the interior of the bottom layer (panel d), ρ' falls while w' rise and the pdf presents a much narrower extension along the ρ' axis.

Figure 5.24 shows the contributions of each quadrant to the total vertical buoyancy flux per unit area, for the same levels of figure 5.23. Above the interface, the main contribution comes from the quadrant Q3, so lighter fluid is displaced from the top layer downward, mixing with the bottom layer. Below the interface instead, the dominant role is played by quadrant Q1, hence by denser fluid displaced by the bottom layer upwards and mixing with the top layer.

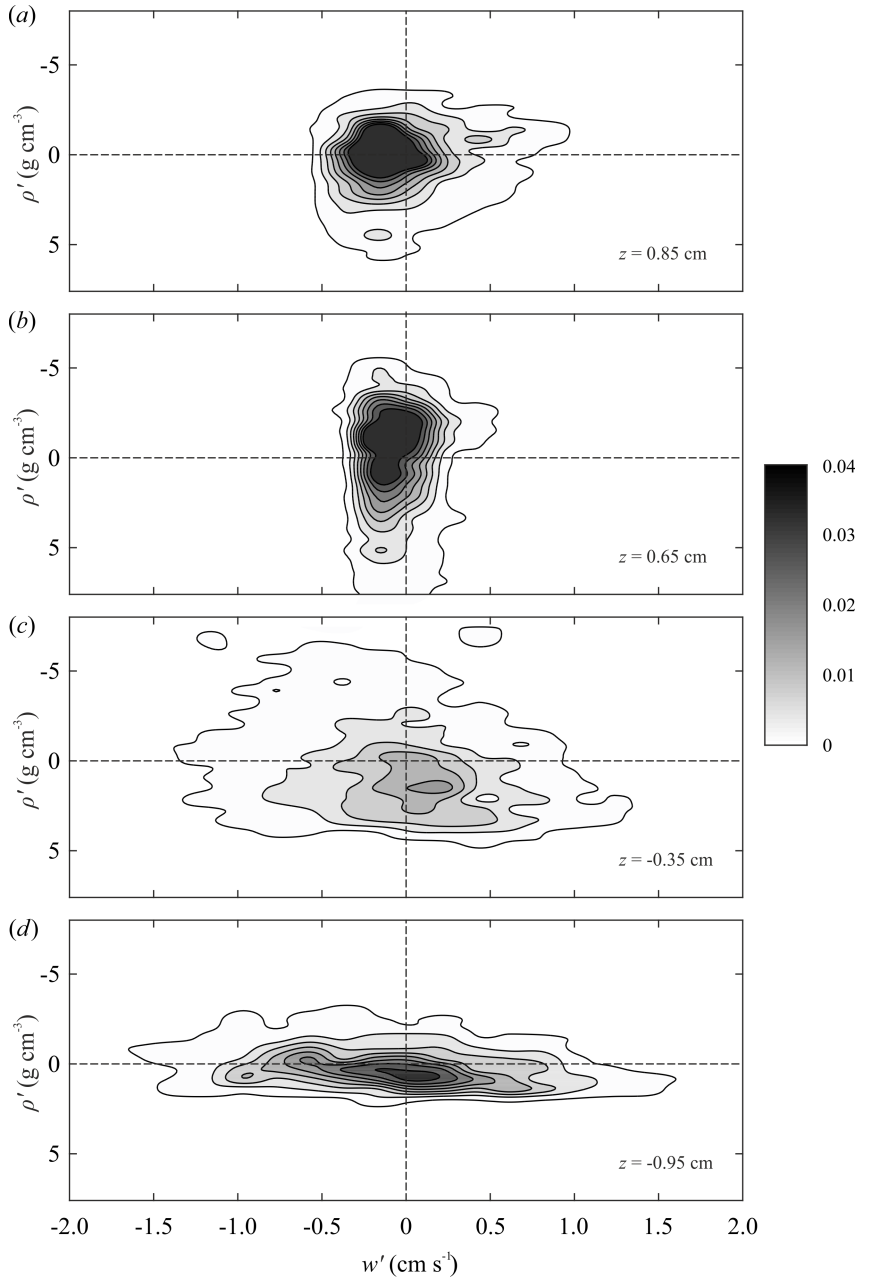

Figure 5.23: Joint p.d.f. of w' and ρ' at (a) $z = 0.85$ cm; (b) $z = 0.65$ cm; (c) $z = -0.35$ cm; (d) $z = -0.95$ cm, for $\Omega = 2.75\,\mathrm{rad\,s^{-1}}$.

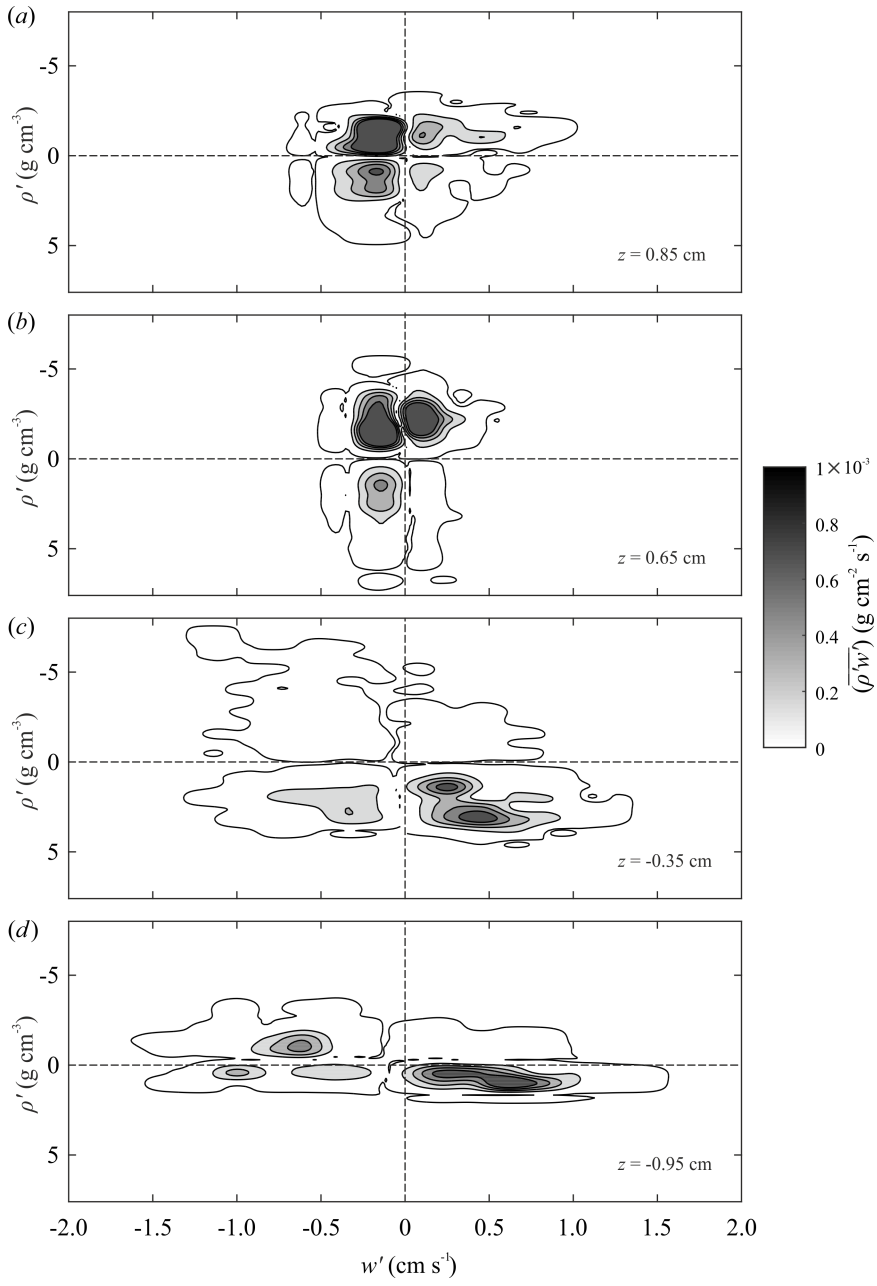

Figure 5.24: Frequency-weighted turbulent flux absolute value at (a) $z = 0.85$ cm; (b) $z = 0.65$ cm; (c) $z = -0.35$ cm; (d) $z = -0.95$ cm, for $\Omega = 2.75\,\mathrm{rad\,s^{-1}}$.

Figure 5.25 shows the contour maps of the time averaged normalized contributions from the four quadrants at increasing threshold coefficient β, and as a function of the vertical distance from the interface. The contour lines represent the iso-concentration lines at values of $0.05-0.10-0.15-0.20$.

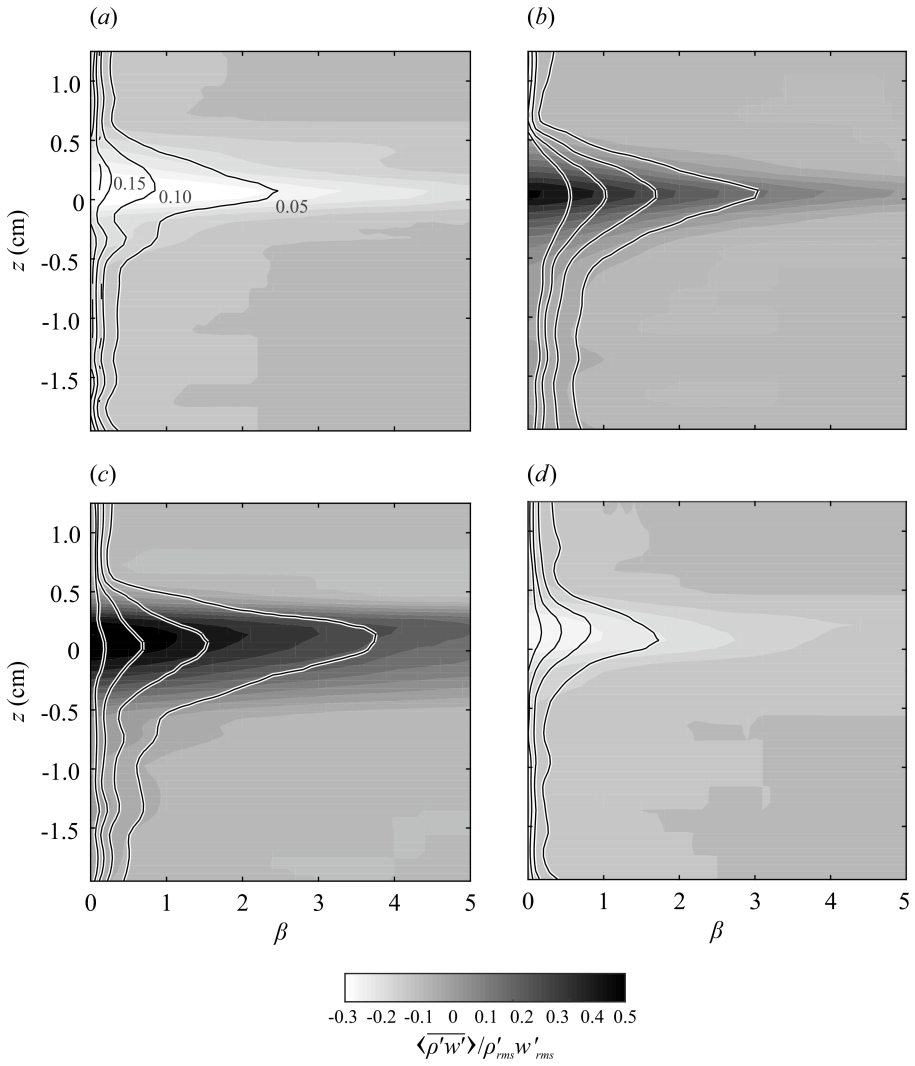

Figure 5.25: Contourf maps of the time averaged normalized contributions from (a) Q2, (b) Q1, (c) Q3 and (d) Q4, as a function of depth and threshold. The isolines are iso-concentration at the values $0.05-0.10-0.15-0.20$.

5.5.3 Height and frequency of the interfacial waves

The two-wires home-made probe is set at three different radial positions in the tank to record the equivalent level of the interface in time, and connected to the same electronics used to measure density. The home-made probe is extremely sensitive and stable, with an overall accuracy better than 0.1 mm and a frequency response of ≈ 20 Hz.

The two-wire probe is calibrated with fluid at rest. We move the wires in the vertical direction with a step of 2 mm and record the conductivity of the fluid for approximately 1 minute in the range $z = \pm 1$ cm from the interface. In this way it is possible to correlate the conductivity of the fluid the relative position of the interface.

On the contrary, during the experiments, the middle point of the exposed area of the two wires levels out the density interface and does not move vertically during the recording. In steady state condition, the mean density of the top and bottom layers are constant in time, but the salt flux is still transported vertically from the bottom to the top layer by the correlation of density and velocity fluctuations, as reported in paragraph 5.5.1. Therefore, the signal registered by the two-wires probe should record an increase (or decrease) in the conductivity of the fluid as a consequence of an upward (or downward) movement of the equivalent level of the density interface. We say "equivalent" because the interface may not be always very sharp or radially homogenous.

The list of the experiments is reported in table 5.5.3: Ω is the rotation rate, r is the distance between the probe and the inner cylinder, f_p and $T_p = 1/f_p$ are the frequency and the period of the interfacial waves related to the peak in the energy spectrum and $H_{1/3}$ is the one highest third wave height given by the zero-(up)crossing analysis.

n° test	Ω (rad s^{-1})	r (cm)	f_p (Hz)	T_p (s)	$H_{1/3}$ (mm)
1	2.75	2	0.0684	14.6	0.73
2	2.75	4	0.0750	13.3	0.63
3	2.75	6	0.0733	13.6	0.63
4	2.50	2	0.0674	14.8	0.46
5	2.50	4	0.0663	15.1	0.39
6	2.50	6	0.0666	15.0	0.83
7	2.25	2	0.0602	16.6	0.59
8	2.25	4	0.0624	16.0	0.39
9	2.25	6	0.0605	16.5	0.67
10	2.00	2	0.0482	20.7	0.36
11	2.00	4	0.0529	18.9	0.33
12	2.00	6	0.0531	18.8	0.60
13	1.75	2	0.1084	9.2	0.29
14	1.75	4	0.0460	21.7	0.15
15	1.75	6	-	-	0.21
16	1.50	2	0.0897	11.2	0.22
17	1.50	4	0.0405	24.7	0.31
18	1.50	6	0.0415	24.1	0.32

Table 5.2: Parameters of the experiments: Ω is the rotation rate, r is the distance from the inner cylinder, f_p and T_p are the frequency and the period of the waves, $H_{1/3}$ is the one highest third wave height.

An example of the signal recorded by the two-wire probe is shown with a gray line in figure 5.26. The signal seems to drift in time from zero up to a value of, generally speaking, approximately 1 mm. This could be due to small unbalances between the peristaltic pumps. Detrending is then applied to the signal by subtracting a running average evaluated over a sufficiently large window width, here set to 1000 points which correspond to 48 seconds. The running average is displayed with a red line.

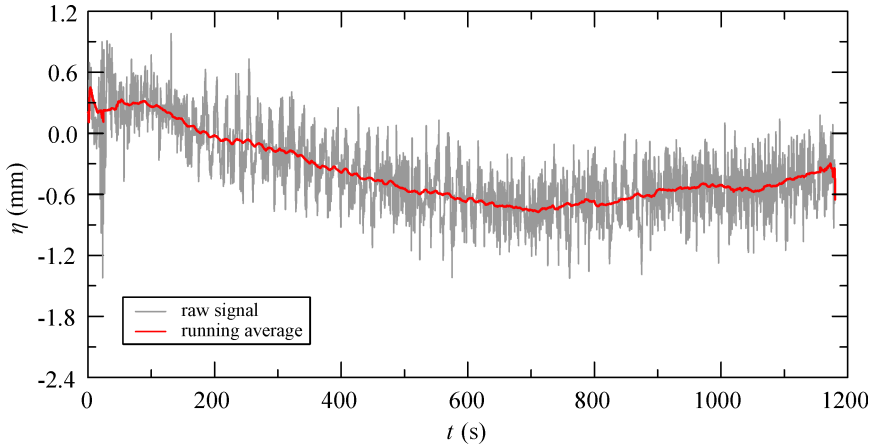

Figure 5.26: Raw signal recorded by the two-wire home-made probe (gray line) and running average over a time window width of 48 s (red line), for experiment 7 of table 5.5.3.

Figure 5.27*a* shows a time window of the equivalent interface position, η, for experiment 9 of table 5.5.3. Gray dots refer to the raw signal after detrending, while the red line is a moving average over a time window of ≈ 2.5 seconds. We can observe a wake-like signal that oscillates vertically around a mean value. We shall refer to these oscillations as a perturbation traveling periodically across the interface around the annulus. Before performing a zero-(up)crossing analysis, a 5^{th} order low-pass filter with a cut-off frequency of 0.15 Hz is applied to the detrended signal. Figure 5.27*b* shows the energy spectrum for the same experiment reported in panel *a*. The peak of the spectrum has a frequency of $f_p = 0.0\overline{6}\,\text{Hz}$ corresponding to a period of $T_p = 15\,\text{s}$, analogously to the time interval between two subsequent troughs (or crests) of the waves in figure 5.27*a*.

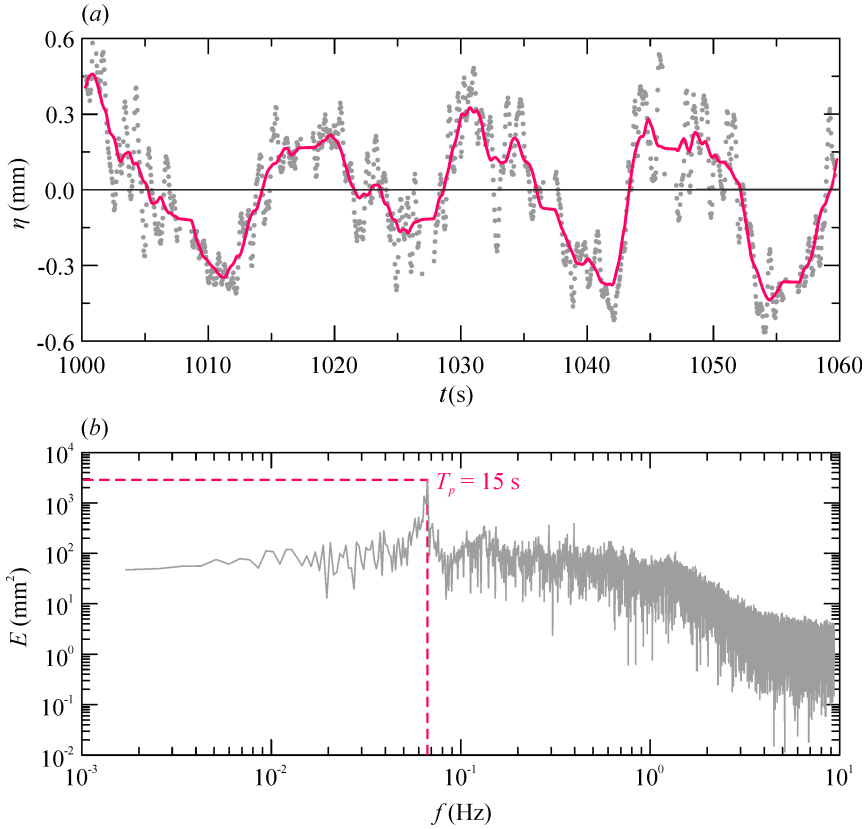

Figure 5.27: (*a*) Time window of the interface position for experiment 9 5.5.3. Raw signal after detrend (gray dots) and running average with a time window of ≈ 2.5 seconds (red solid line); (*b*) energy spectrum for the same experiment of panel (*a*).

We now show the time series of the interface position, η, for six values of rotation rate $\Omega = 1.50 - 2.75\,\mathrm{rad\,s^{-1}}$ at a distance $r = 4\,\mathrm{cm}$ from the inner cylinder in figure 5.28*a* and the energy spectrum in figure 5.28*b*. We can observe that the wave height decreases with Ω, and so does the frequency of the peak of the energy spectrum, f_p. For $\Omega = 2.75\,\mathrm{rad\,s^{-1}}$, the wave height reaches a value of approximately 0.8 cm in the time window considered, and the shape of the wave seems asymmetric, with wider troughs and slimmer crests. At low rotation rates, the wave height reduces to a values of a approximately 0.2-0.3 mm and the waves appear more symmetric with respect to the mean equivalent interface level.

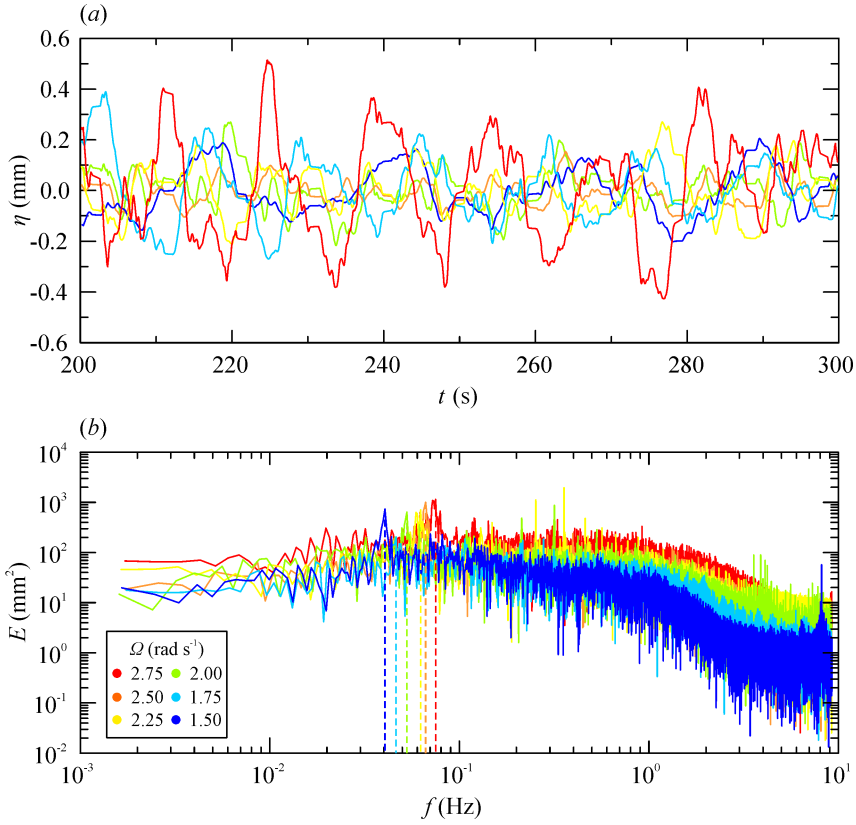

Figure 5.28: (*a*) Time windows of the interface position; (*b*) energy spectra for experiments 2, 5, 8, 11, 14, 17.

The frequency of the peak of the energy spectrum, f_p, linearly increases with Ω, so the period $T_p \sim \Omega^{-1}$ both at a distance $r = 4$ cm and $r = 6$ cm from the inner radius, as illustrated in figure 5.29. The empirical best-fit curve is $T_p = 12\pi/\Omega$. Oglethorpe (2014) suggested that

$$T = 4.82 \sqrt{\frac{R_2 - R_1}{R_1}} \frac{2\pi}{\Omega}, \tag{5.15}$$

which gives $T = 9.75\pi/\Omega$, a little smaller than our results.

If we focus on the region close to the inner cylinder, T_p at a distance $r = 2$ cm does not seem to follow a regular pattern with Ω: T_p decreases for low rotation rates but suddenly increases to $T_p \approx 21$ s at $\Omega = 2.00\,\mathrm{rad\,s^{-1}}$, and then follows the same $12\pi/\Omega$ trend for higher Ω. This could be address to the larger number to disturbancies occurring at the inner cylinder, where

interfacial waves seem to originate and propagate radially and azimuthally across the tank, analogously to the "fetch" for wind gravity waves. For $\Omega < 2.00\,\mathrm{rad\,s^{-1}}$, the waves coalesce with non-linear interactions close to the inner cylinder, then propagate radially with a double period, according to the regime configuration. For $\Omega > 2.00\,\mathrm{rad\,s^{-1}}$, the perturbations evolve faster and with a period equal to the regime configuration even at $r = 2$ cm, following a more organized wave pattern.

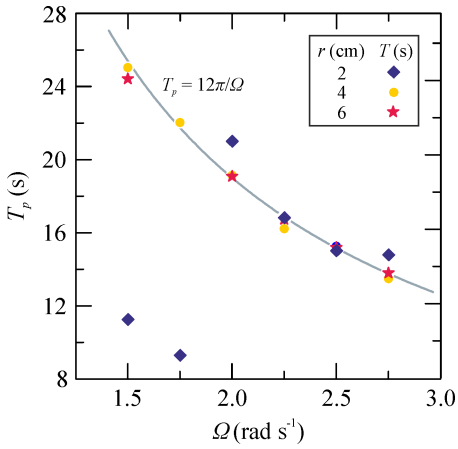

Figure 5.29: Peak period, T_p, at a distance $r = 2, 4, 6$ cm from the inner cylinder as a function of *Omega*.

The wave height was estimated by the zero-(up)crossing analysis of the detrended signal. The number of the waves counted over the recorded time $t = 120$ seconds stands in the range $70 - 90$. In figure 5.30*a* we illustrate the one highest third wave height $H_{1/3}$ as a function of rotation rate, at $r = 2, 4, 6$ cm from the inner radius. The wave height generally grows with both Ω and r. If we compare the crests with the troughs, we find that the waves appear symmetric at low rotation rates, as previously anticipated. On the opposite, the crest amplitude, $a_{sup,1/3}$, becomes smaller than the trough, $a_{inf,1/3}$, at higher rotation rates. Figure 5.30*b* shows only the data at $r = 2$ cm, but the trend is similar with further distance from R_1.

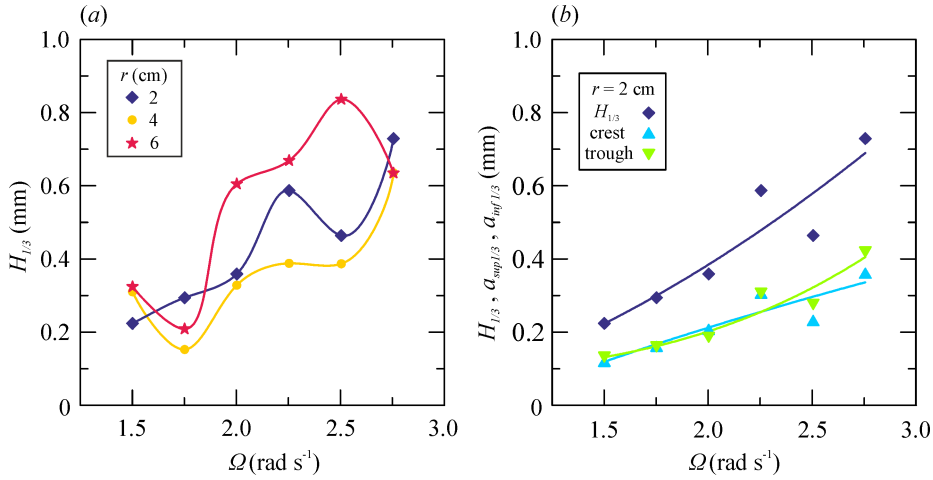

Figure 5.30: (a) $H_{1/3}$ as a function of Ω, at $r = 2, 4, 6$ cm from the inner radius; (b) total wave height $H_{1/3}$, crest amplitude, $a_{sup,1/3}$, and trough amplitude, $a_{inf,1/3}$, at $r = 2$ cm from R_1.

5.5.4 Wave energy at the interface

It is interesting to understand how these interfacial waves are generated. To this purpose, we firstly look at the vertical, radial and azimuthal TKE along the vertical:

$$\begin{aligned} \mathrm{TKE}_w(z) &= \frac{1}{2}\,\rho(z)\,w'(z)^2, \\ \mathrm{TKE}_r(z) &= \frac{1}{2}\,\rho(z)\,u_r'(z)^2, \\ \mathrm{TKE}_\theta(z) &= \frac{1}{2}\,\rho(z)\,u_\theta'(z)^2, \end{aligned}$$

where w', u_r' and u_θ' are respectively the vertical, radial and azimuthal velocity fluctuations.

Figure 5.31*a-b-c* shows TKE_w, TKE_r and TKE_θ, measured at a distance $r = 2$ cm from the inner cylinder, for $\Omega = 2.75\,\mathrm{rad\,s^{-1}}$. TKE_w tends to grow with height but nearly falls to zero in a narrow region across the density interface, where the vertical velocity fluctuations are small. On the other hand, even if TKE_r is also reduced along a wider region across the interface, TKE_r and TKE_θ appear more uniform with height, but more scattered. The three components contribute equivalently to the total TKE, TKE_T, shown in figure 5.31*d*. In the vertical range $z_1 - z_2$, the TKE_T profile presents

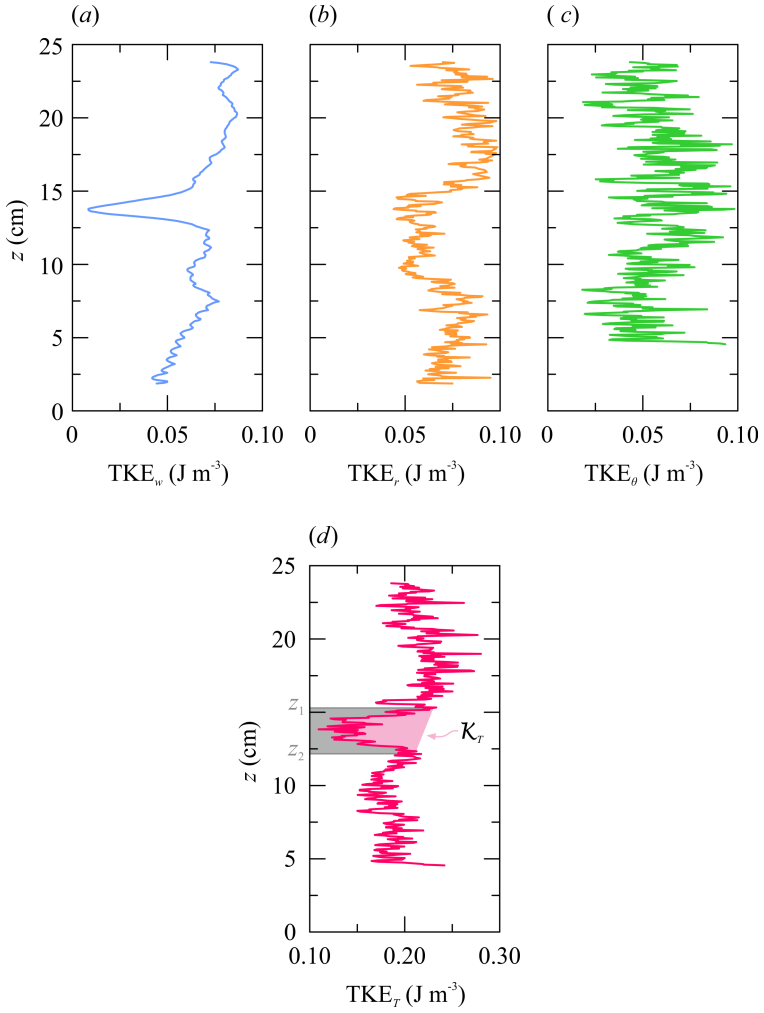

Figure 5.31: (a) TKE$_w$; (b)TKE$_r$; (c) TKE$_\theta$; (d) TKE$_T$ as functions of z, evaluated at a distance $r = 2$ cm from the inner cylinder, for $\Omega = 2.75\,\mathrm{rad\,s^{-1}}$.

a lack of energy, which is represented by the pink area, mainly due to the fall of vertical velocity fluctuations. We shall call this lack of energy as the "missing turbulent kinetic energy", $\mathcal{K}$, and it represents the difference between a well-mixed state and a two-layer fluid, or the TKE transformed into potential energy. We evaluate the total missing turbulent kinetic energy $\mathcal{K}_T$ as the difference between the trapezoidal area with height $z_1 - z_2$ and TKE$_T(z_1)$ and TKE$_T(z_2)$ as base-lines, and the area of the TKE$_T$ curve

in the same vertical range, which is the gray area in the background in figure 5.31*d*. We can decompose $\mathcal{K}_T$ into the three components that include the velocity fluctuations in the vertical (z-component), radial (r-component) and azimuthal direction (θ-component), as :

$$\mathcal{K}_w = \frac{1}{2}\left[\rho(z_1)w'(z_1)^2 + \rho(z_2)w'(z_2)^2\right] - \int_{z_2}^{z_1} \rho {w'}^2 \mathrm{d}z, \tag{5.16}$$

$$\mathcal{K}_r = \frac{1}{2}\left[\rho(z_1)u_r'(z_1)^2 + \rho(z_2)u_r'(z_2)^2\right] - \int_{z_2}^{z_1} \rho {u_r'}^2 \mathrm{d}z, \tag{5.17}$$

$$\mathcal{K}_\theta = \frac{1}{2}\left[\rho(z_1)u_\theta'(z_1)^2 + \rho(z_2)u'\theta(z_2)^2\right] - \int_{z_2}^{z_1} \rho {u_\theta'}^2 \mathrm{d}z, \tag{5.18}$$

$$\mathcal{K}_T = \mathcal{K}_w + \mathcal{K}_r + \mathcal{K}_\theta. \tag{5.19}$$

We can then compare $\mathcal{K}_T$ with the potential energy associated with the interfacial waves:

$$E_{pot}\left(H_{w,1/3}\right) = \frac{1}{16}\left(\rho_b - \rho_t\right) g H_{w,1/3}^2, \tag{5.20}$$

where ρ_b and ρ_t are the steady state density of the bottom and top layers respectively, g is the acceleration due to gravity and $H_{w,1/3}$ is the one highest third wave height at $r = 2$ cm shown in figure 5.30*a*.

This comparison is represented in figure 5.32. Three series of $\mathcal{K}$ are shown on the basis of the considered fluctuating velocity components. Blue dots refer to the only vertical velocity component (i.e. equation 5.16), while orange dots indicate the velocity fluctuations in the $r - z$ plane (i.e. equations 5.16 and 5.17). Green dots correspond to velocity fluctuations in all three directions (i.e. equation 5.19).

The results seem to infer that potential energy of the waves is only a few percent of $\mathcal{K}$. $\mathcal{K}_r$ and $\mathcal{K}_\theta$ generally increases with Ω until they reach a maximum. In the range $\Omega = 2.25 - 2.50\,\mathrm{rad\,s^{-1}}$ data show a turnaround in the wave potential energy, as $H_{w,1/3}$ slightly decreases from $\Omega = 2.25\mathrm{rad\,s^{-1}}$ to $\Omega = 2.50\,\mathrm{rad\,s^{-1}}$. Considering only the vertical velocity component, $\mathcal{K}_w$ exhibits an initially upward trend and then decreases at high rotation rate and disappears for $\Omega \geq 3.00\,\mathrm{rad\,s^{-1}}$. We performed some experiments with an initial two-layer stratification at $\Omega = 3.00\,\mathrm{rad\,s^{-1}}$ (not shown in this thesis), and the turbulent eddies were able to overturn the density interface and the two-layer stratification evolved into a linear stratification.

We now consider the potential energy due to the interface distortion $\eta(t)$ recorded close to the inner cylinder:

$$E_{pot}\left(\eta\right) = \frac{1}{2T}\left(\rho_b - \rho_t\right) g \int_0^T \eta(t)^2 \mathrm{d}t, \tag{5.21}$$

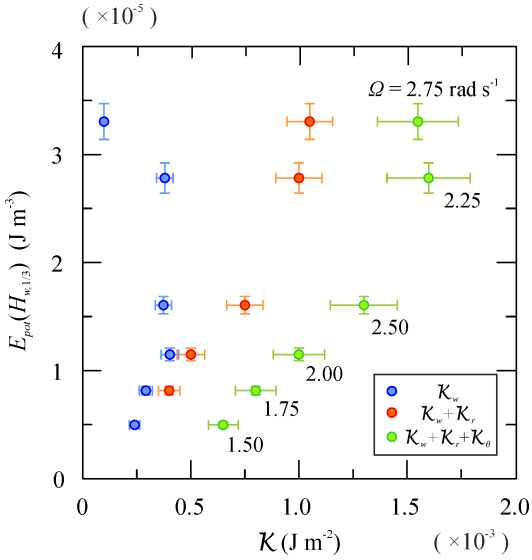

Figure 5.32: Potential energy associated to interfacial waves close to the inner cylinder as a function of $\mathcal{K}_w$ (blue dots), $\mathcal{K}_w + \mathcal{K}_r$ in the $r - z$ plane (orange dots), and $\mathcal{K}_T$ in the $r - z - \theta$ space (green dots).

where T is the length of each data set.

The interface potential energy, E_{pot}, is almost twice the wave potential energy, but still much smaller than $\mathcal{K}_T$, as reported in figure 5.33*a*. In addition, E_{pot} seems to be uniformly distributed in the radial direction, as shown in figure 5.33*b*.

Further analysis are required to explain the energy conversion of the remainder $\mathcal{K}_T$.

5.5.5 Celerity of the waves

In this section, we are going to compare the phase celerity of the coherent structures and of the interfacial disturbances.

The former is measured by two long UVP probes, aligned along the vertical direction, positioned at a distance $r = 3.5$ cm from the inner cylinder, and spaced out 3.5 cm in the azimuthal direction. A number of 2000 velocity profiles are alternately recorded by each probe at a frequency of ≈ 10 Hz. For all the experiments in the range $\Omega = 1.50 - 2.75\,\mathrm{rad\,s^{-1}}$, the cross-correlation between the two probes is computed (i) over the whole depth of the fluid, as shown in figure 5.34*a* for $\Omega = 2.50 - 2.75\,\mathrm{rad\,s^{-1}}$, and over a 5 cm deep region inside (ii) the top layer and (iii) bottom layer separately, as

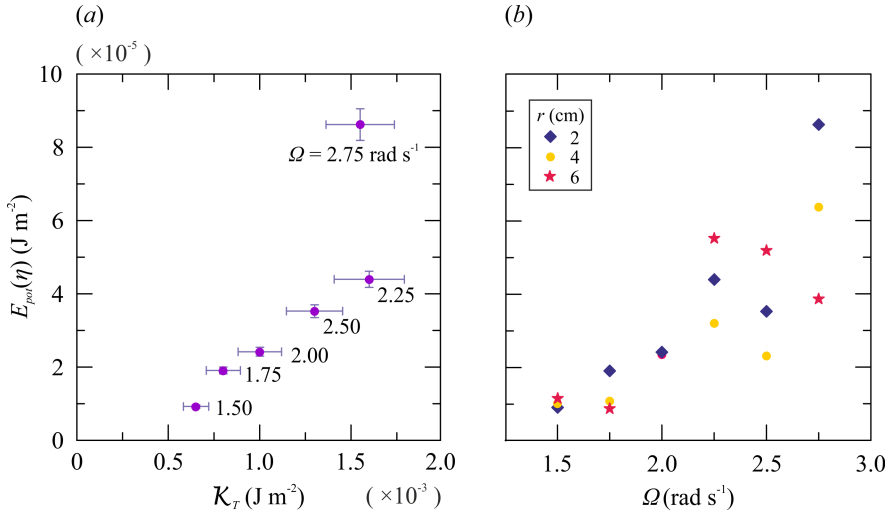

Figure 5.33: (a) Potential energy due to the interface distortion $E_{pot}(\eta)$ recorded at $r = 2$ cm, as a function of $\mathcal{K}_T$; (b) $E_{pot}(\eta)$ as a function of Ω, at $r = 2, 4, 6$ cm from R_1.

shown in figure 5.34b for the same experiment of panel a. The maximum time lag is denoted with a white asterisk. For $\Omega = 2.50\,\mathrm{rad\,s^{-1}}$ the absolute value is equal to $\mathrm{d}t = 0.46, 0.27$ and 0.48 s for (i), (ii), (iii) cases respectively.

Figure 5.35 illustrates the correlation pattern for the whole depth of the fluid at high rotation rate $\Omega = 2.75\,\mathrm{rad\,s^{-1}}$ and low rotation rate $\Omega = 1.75\,\mathrm{rad\,s^{-1}}$. The experiment with even lower Ω has peaks only in the top layer (not shown).

The peak of correlation is a measure of the time for coherent structures to travel the distance between the two UVP probes. As the peak has a limited variability along the vertical, we consider a time averaged value. We can then estimate the wave celerity as the ratio between the azimuthal distance between the two UVP probes (3.5 cm) and the averaged maximum time delay. The results of celerity of the coherent structures are reported with a blue solid line and triangles in figure 5.36 as a function of Ω.

On the other hand, the phase celerity of the interfacial perturbations is measured by two two-wire probes, very similar to the one adopted for detection of the interface distortion. We align the two two-wires probe vertically, set them at a distance $r = 3$ cm from the inner cylinder, and space them out 7 cm in the azimuthal direction. We then cross-correlate the conductivity recorded over a period of 10 minutes and estimate the wave celerity again as the ratio between the azimuthal distance between the two

probes (7 cm) and the maximum time delay. The results of celerity of the interfacial perturbations are reported with a green solid line and crosses in figure 5.36.

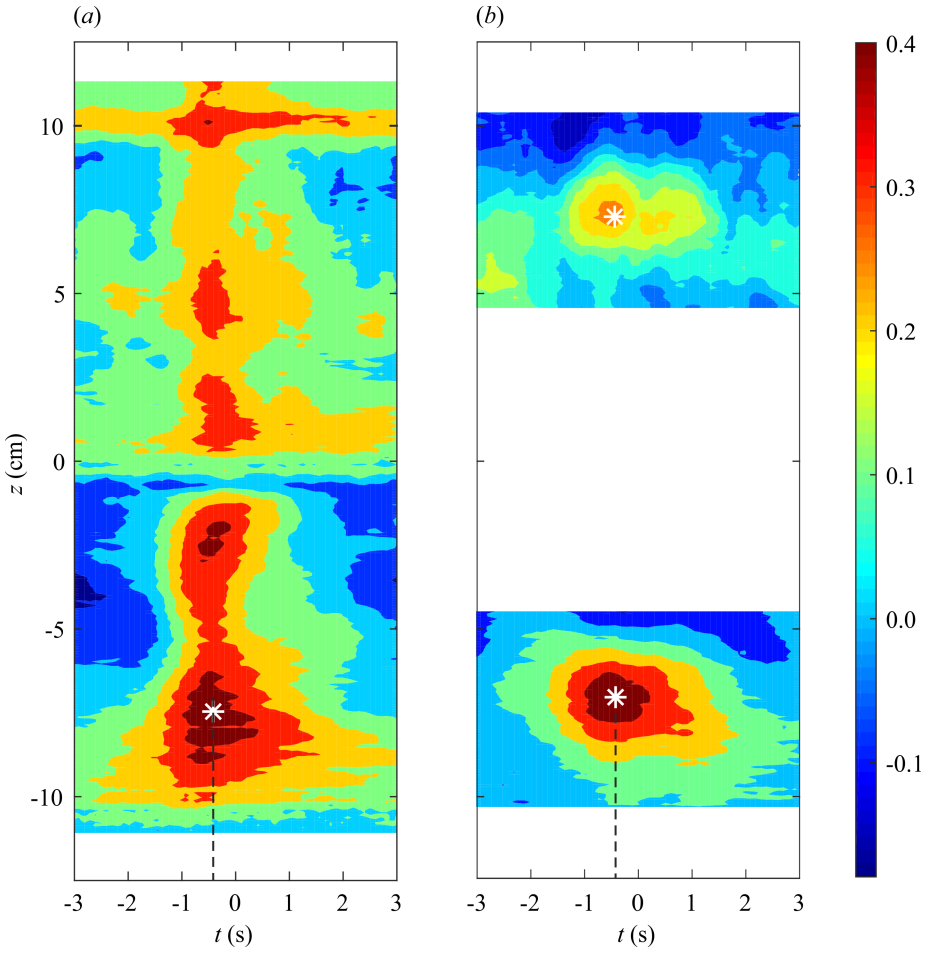

Figure 5.34: (a) Cross-correlation between two vertical UVP probes at $r = 3.5$ cm from R_1 and 3.5 cm spaced out in the azimuthal direction, evaluated over the whole depth of the fluid and (b) over two separate 5 cm regions in the interior of the top and bottom layers, for $\Omega = 2.50\,\mathrm{rad\,s^{-1}}$.

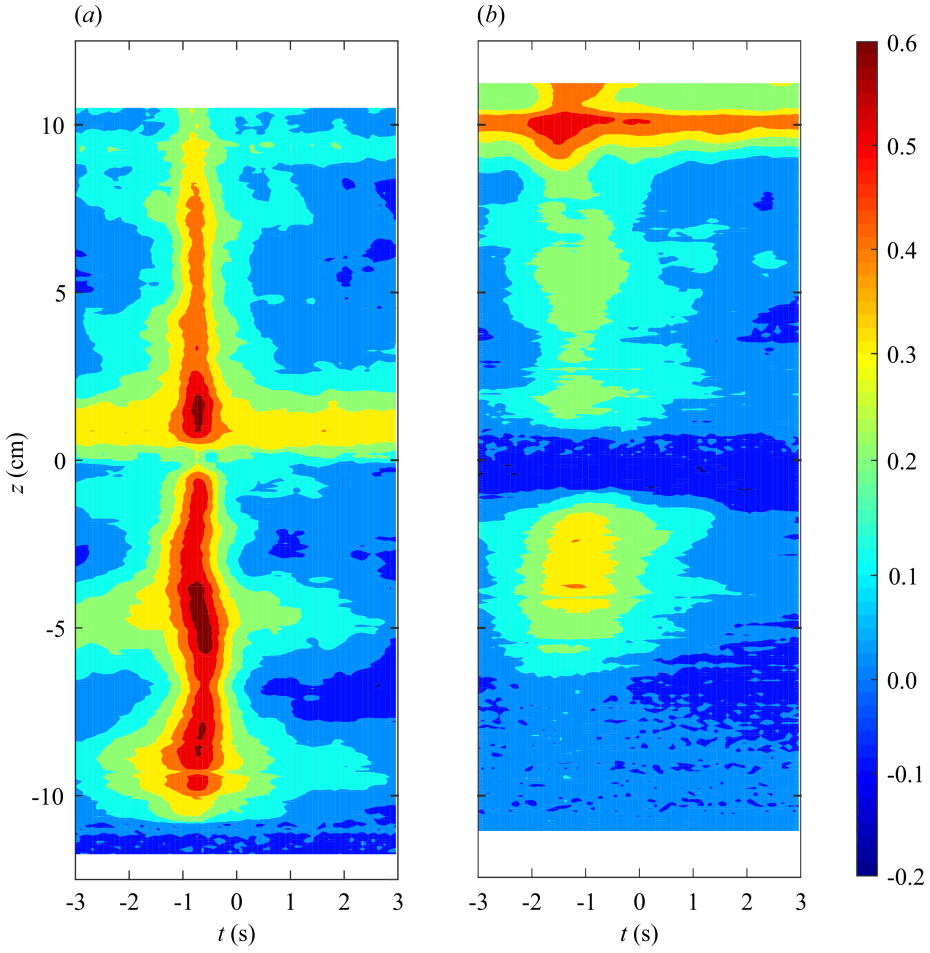

Figure 5.35: (a) Cross-correlation between two vertical UVP probes at $r =$ 3.5 cm from R_1 and 3.5 cm spaced out in the azimuthal direction, evaluated over the whole depth of the fluid and (b) over two separate 5 cm regions in the interior of the top and bottom layers, for $\Omega = 2.50\,\mathrm{rad\,s^{-1}}$.

The error bars include the error related to distance ($\Delta r \approx 0.5$ cm) and the error related to the time delay given by correlation $\sigma_p/\mu_p = 1/\sqrt{BT} \approx 0.013$, where $B = 1/(2\,\mathrm{d}t) \approx 42Hz$ is the Nyquist's frequency and T is the length of the data set, $T = 600$ s. Then the celerity error is computed as

$$\frac{\Delta c}{c} \approx \sqrt{\left(\frac{\Delta r}{r}\right)^2 + \left(\frac{\sigma_p}{\mu_p}\right)^2} \approx 3.7 - 4.5\%. \tag{5.22}$$

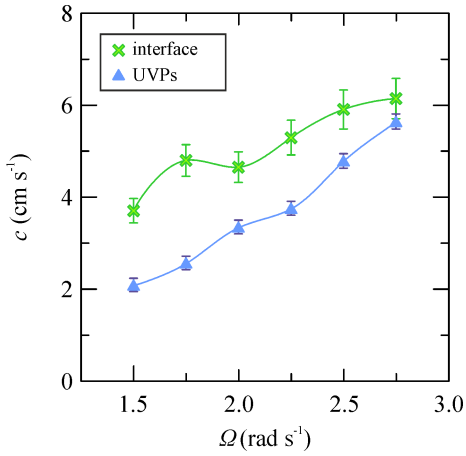

Figure 5.36: Wave celerity as function of Ω.

Both the waves at the interface and the coherent structures of the velocity field appear to travel faster with increasing Ω, but with different celerity. However, the difference in celerity decreases with Ω until it probably disappears at $\Omega \approx 3.00\,\mathrm{rad\,s^{-1}}$, when the interfacial perturbations and the coherent structures approach the same celerity and probably cause the fluid to resonate. As we know from section 4.1.8 and from the experiments performed in Parma at $\Omega \approx 3.00\,\mathrm{rad\,s^{-1}}$, mixing is enhanced at high Ω, and when the fluid hits the resonance, the interface is overturned and the two-layer stratification disintegrate into a linear stratification.

5.6 Dye spreading at the interface

In order to visualize the periodic signal at the interface, we inject some dyed solutions through three radially aligned sticks, 2 cm spaced out, with heads in contact with the density interface in the middle of the tank. The dyed fluids have an intermediate density between the top and bottom layer. They are dyed with red, blue and green water colours and are kept in three separate syringes, each one being regulated by a valve.

During the experiments, we record videos with three web-cams (two Logitech c310 web-cams and one Logitech c200 web-cam, 800×600 pixels) positioned at 120° and connected to three personal computers. Video are recorded by the Logitech Webcam Software at 15 frames per second (fps) for ≈ 6 minutes. This software does not cause troubles about low fps lag issues or fps constantly changing in time. We also record a lateral view of the density interface by a high-resolution video-camera (Canon Legria HF 20, 1920×1080 pixels). The set-up of the tank is sketched in figure 5.37.

At the bottom of the tank we glue a radial plastic grid with marks every 20°.

After filling the tank with a transparent two-layer stratification, we switch on the pumps and the spinner, slightly open the valves of the syringes and fluid gradually flows from the sticks. To check the synchronization of the web-cams, three leds controlled by a Labview software switch on and off every 2 seconds. The leds are arranged so that each web-cam could film at least one of them.

We run three experiments in a row with increasing rotation rate, $\Omega = 1.50 - 2.00 - 2.75\,\mathrm{rad\,s^{-1}}$. At the end the first experiments, we find that the dyed fluid has not diffused evidently in the top and bottom layers. The thin intermediate layers that formed in the middle of the tank is gently siphoned out of the tank before running the following experiment.

The three videos are edited together by Adobe Premiere Pro to reconstruct the whole tank. Figure 5.38 shows 12 snapshots extracted every 2 seconds from the experiment at $\Omega = 2.00\,\mathrm{rad\,s^{-1}}$. The time reported on the top of the first snapshot of the row indicates the time after the start of the recording.

It is interesting to notice that all the red coloured parcels accumulate and travel around until they adjust to a periodic wave-like structure, with given size and angular velocity. The red nose of this wave close to the outer cylinder is indicated with a red arrow. The wave travels across the tank, continuously mixing with the surrounding fluid and dye. In figure 5.38*j* the wave appears to reach the same position it has in figure 5.38*a*, so we roughly

can estimate that the period of this wake is $T = 18$ s.

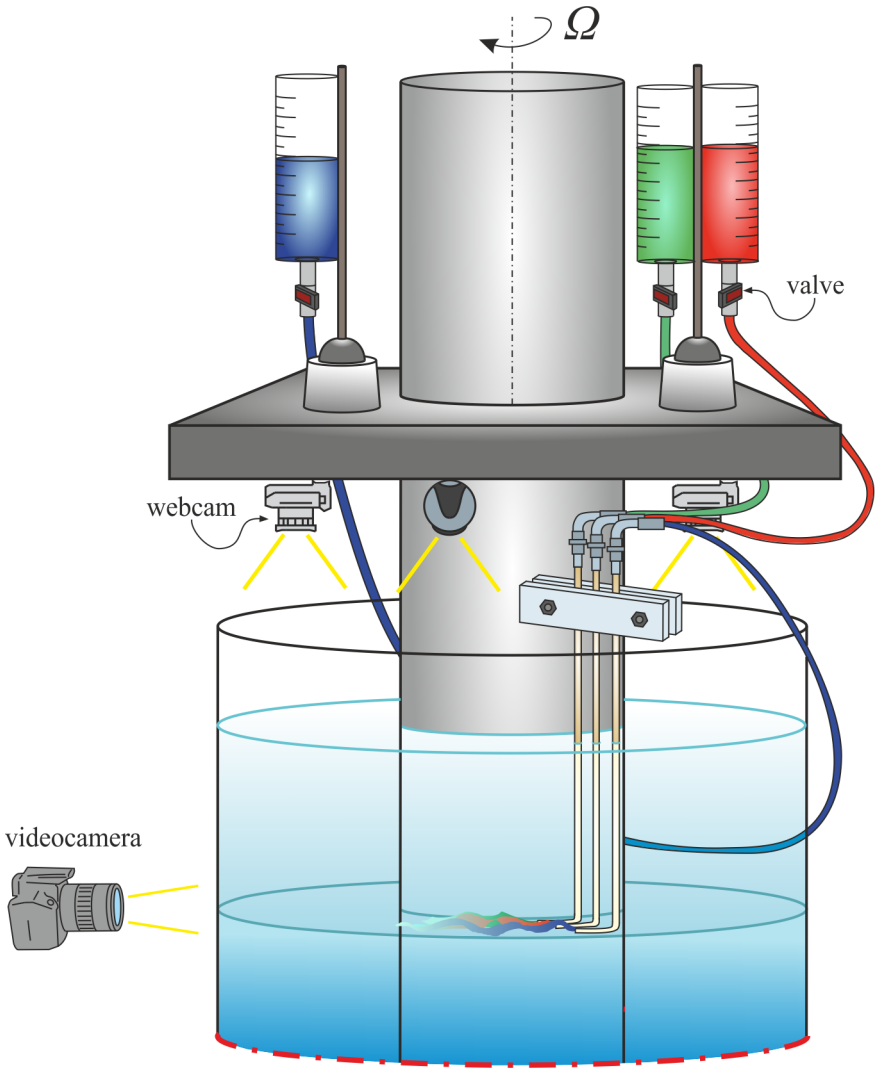

Figure 5.37: Set-up of the tank.

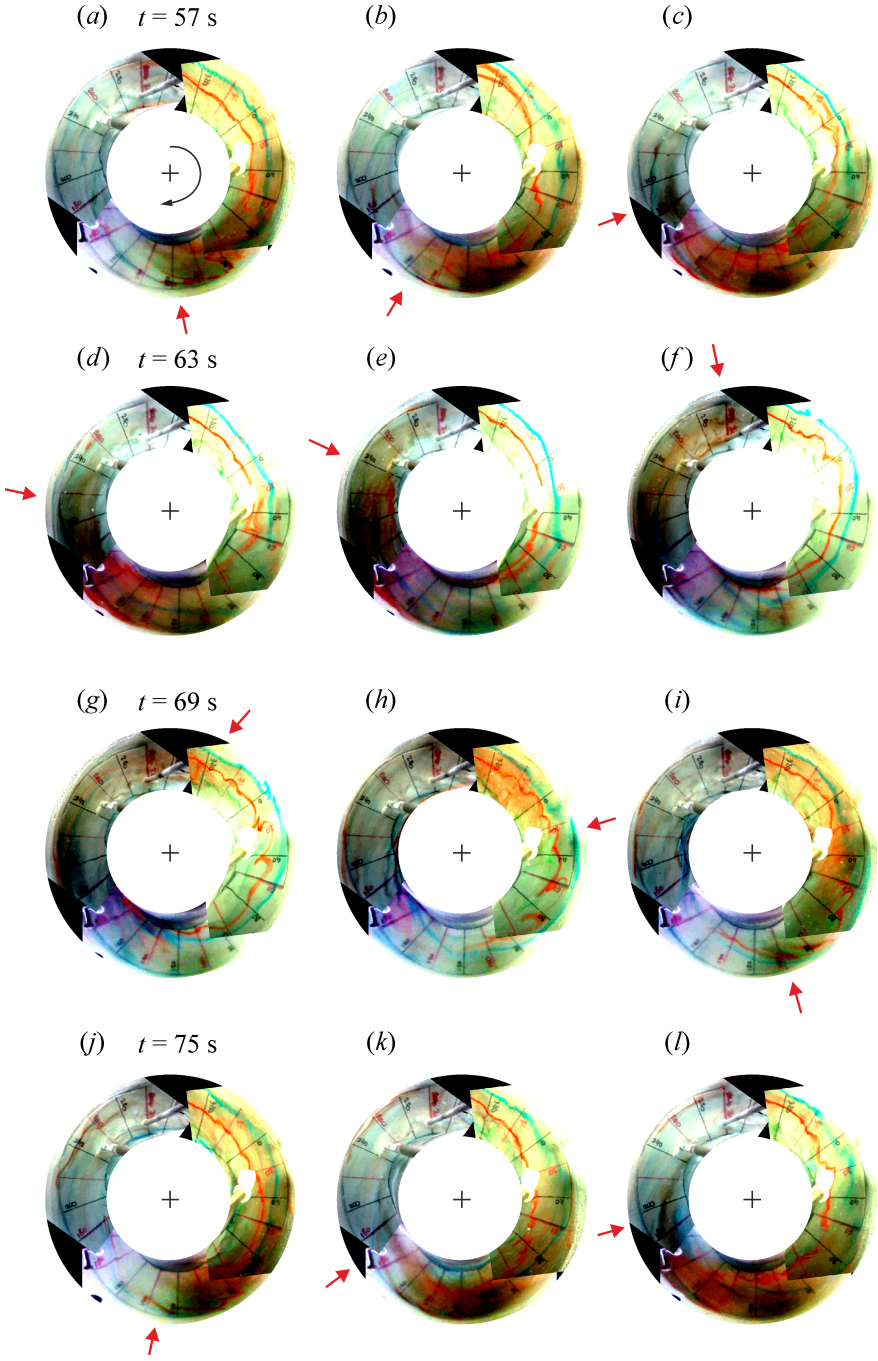

Figure 5.38: (a) - (l) Snapshots extracted every 2 seconds from the experiment at $\Omega = 2.00\,\mathrm{rad\,s^{-1}}$.

Figure 5.39*a*-*b*-*c* contains three time series images describing the evolution of a single radial line of pixels, 2 cm downstream from the dye injections, spanning from the inner radius R_1 and outer radius R_2, as a function of time, for $\Omega = 1.50, 2.50$ and $2.75 \mathrm{rad\,s^{-1}}$ respectively. The time $t = 0$ corresponds to the start of the recording. The green and red streaks are closer to the rotating cylinder and appear to fluctuate more wildly than the blue one which flows in the outer region of the tank.

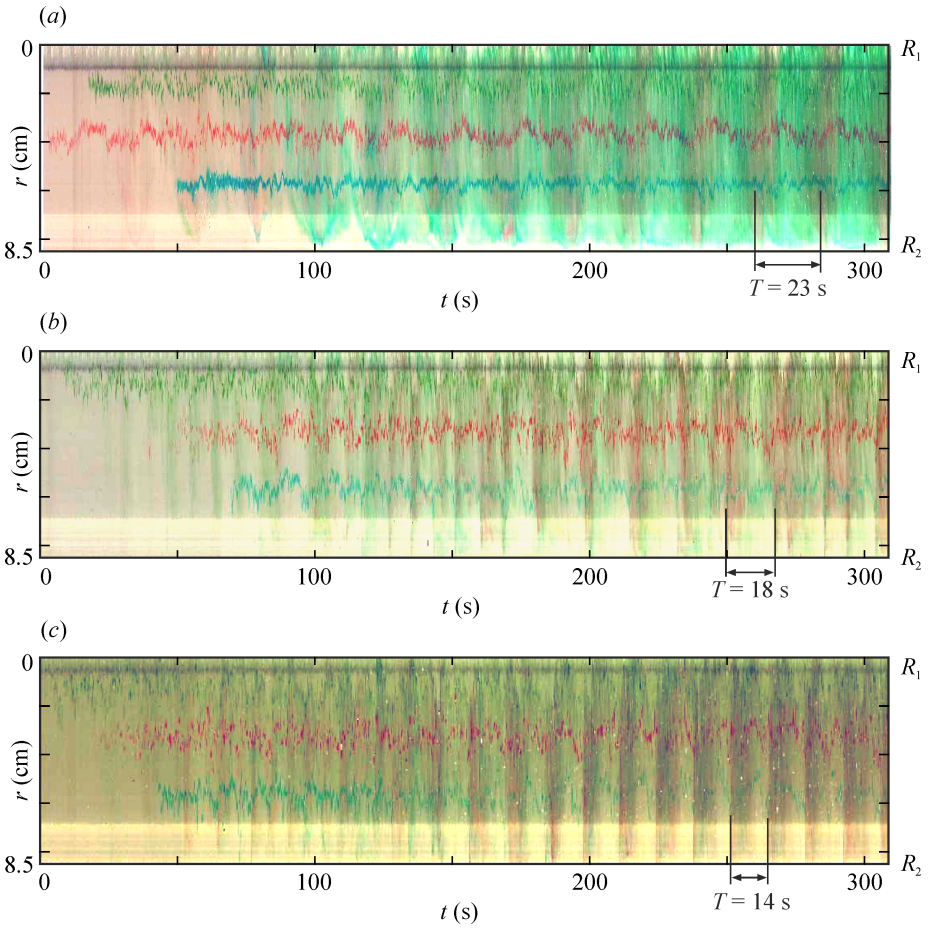

Figure 5.39: Time series of a single vertical line of pixels, through the gap of the tank for (*a*) $\Omega = 1.50 \mathrm{rad\,s^{-1}}$; (*b*) $\Omega = 2.00 \mathrm{rad\,s^{-1}}$ and $\Omega = 2.75 \mathrm{rad\,s^{-1}}$.

In figure 5.39*a*, by the time $t \approx 100$ s, the green dye has diffused through the whole gap of the tank. Red dye seems to accumulate behind the front of a wave with a constant period $T = 23$ s. These red waves appear slanted,

propagating toward the outer region of the gap in advance with respect of the inner region.

As the rotation rate increases, the frequency of the red waves increases and the period falls to $T = 18$ and 14 s for $\Omega = 2.00\,\mathrm{rad\,s^{-1}}$ in figure 5.39*b*, and $\Omega = 2.75\,\mathrm{rad\,s^{-1}}$ in figure 5.39*c* respectively.

We digitize the dye streaks as reported in figure 5.40 for $\Omega = 1.50\,\mathrm{rad\,s^{-1}}$ by extracting the highest iso-contour lines in RGB channels for the red, green and blue dye. We notice that the green and red streaks seem much more correlated than the blue one. This indicates that the wave is generated close to the rotating inner cylinder and propagates radially outwards, without apparently reaching the outer cylinder, at least for low values of rotation rate. At higher rotation rates, also the blue streak is more perturbed and the dynamic of the flow is generally more complex.

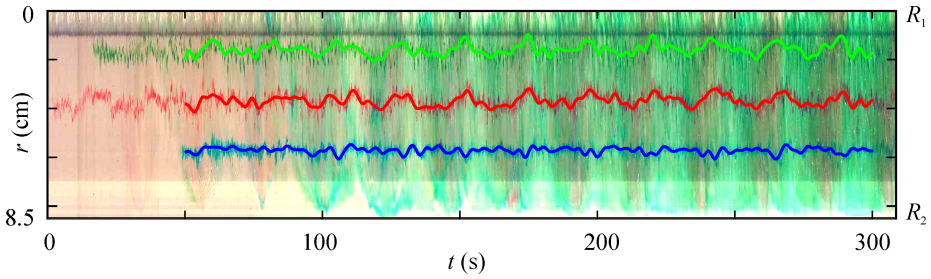

Figure 5.40: Digitized dye streaks for $\Omega = 1.50\,\mathrm{rad\,s^{-1}}$.

We can estimate the macro and micro time scales from the autocorrelation functions of the green, red and blue streaks locates at a distance $r = 2, 4$ and 6 cm from the inner radius. The time scales are reported in table 5.6.

Ω ($\mathrm{rad\,s^{-1}}$)	Λ_T (s) $r = 2 - 4 - 6$ cm			λ_T (s) $r = 2 - 4 - 6$ cm		
1.50	0.8	1.2	0.5	0.10	0.16	0.10
2.00	0.5	0.5	0.6	0.12	0.12	0.14
2.75	0.6	0.5	0.6	0.12	0.15	0.11

Table 5.3: Macro Λ_T and micro λ_T time-scales measured at $r = 2, 4, 6$ cm from the inner cylinder for $\Omega = 1.50 - 2.00 - 2.75\,\mathrm{rad\,s^{-1}}$.

The micro time-scales remain almost constant with Ω and distance r from the inner cylinder. This means that they are less affected by the dynamics of the flow than the macro time-scales, which tend to decrease with increasing Ω. In addition, the macro time-scales vary with r at low rotation rates, and reach a peak at $r = 4$ cm, far from the later walls of the tank. Similar information can be obtained from a lateral view of the density interface. In figures 5.41, 5.42 and 5.43 we illustrate times series of a vertical line of pixels through the density interface in the middle of the tank in real colour in the first and false colour in the second panel. In figure 5.41 the dye injected at the interface forms a intermediate layer between the top and bottom layers, at the vertical mixing at $\Omega = 1.50\,\mathrm{rad\,s^{-1}}$ is very weak. However, red spots appear to diffuse and migrate upwards while blue spots propagate downwards the interface. This different behavior can be due to different concentrations of the powder, leading to coloured solutions of slightly different density. The image in false colour allows us to easily determine the mean period between two subsequent vertical lines of red fluid of $T = 24$ s. The dye show a saw-tooth profile, as it slowly expands in the advancing perturbation and then diffuse upwards.

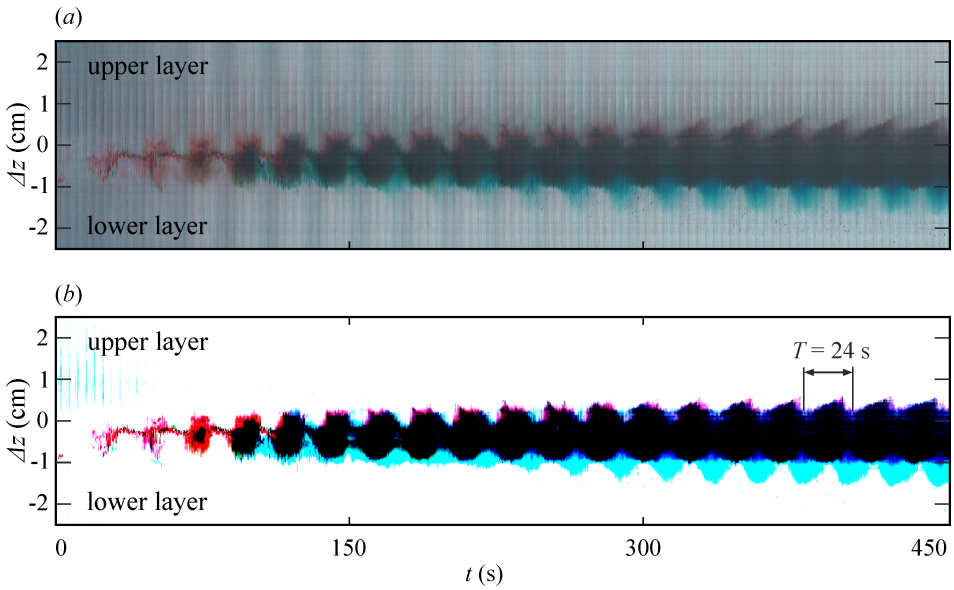

Figure 5.41: Times series of a vertical line of pixels in (a) real colour and (b) false colour, at $\Omega = 1.50\,\mathrm{rad\,s^{-1}}$.

Figure 5.42 refers to the experiment run at $\Omega = 2.00\,\mathrm{rad\,s^{-1}}$. Turbulence

is intense enough to dilute the dye, which forms a circular spot as soon as it is injected and mixes with the surrounding fluid after a period of $T = 19$ s.

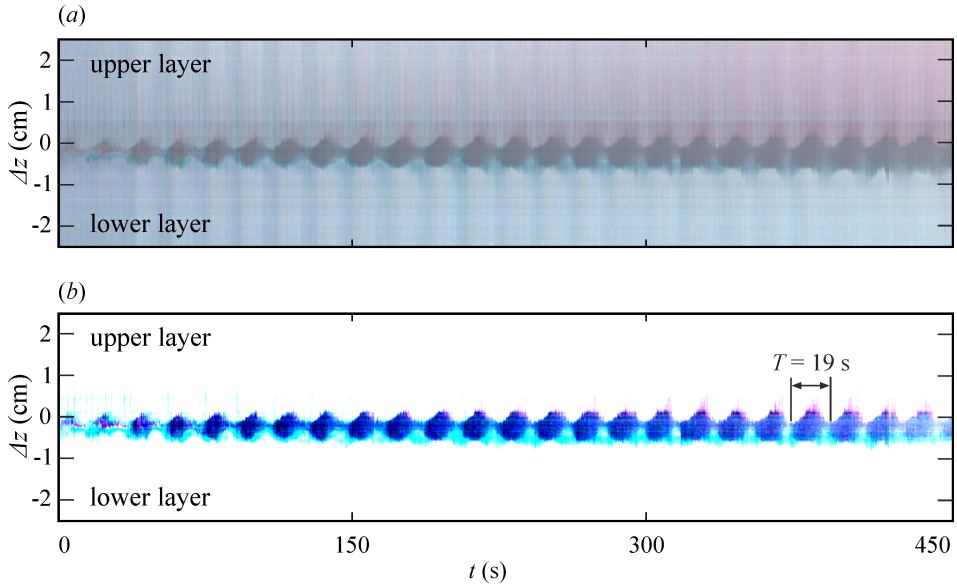

Figure 5.42: Times series of a vertical line of pixels in (a) real colour and (b) false colour, at $\Omega = 2.00\,\mathrm{rad\,s^{-1}}$.

Finally, figure 5.43 refers to the experiment run at $\Omega = 2.75\,\mathrm{rad\,s^{-1}}$. In this case it is quite hard to detect the period of the transient waves, by the only trace of dye at the interface. Therefore, we take into account the mean time interval between two subsequent blue vertical stripe of dye that propagate upwards in the top layer. The resulting period is $T = 14$ s.

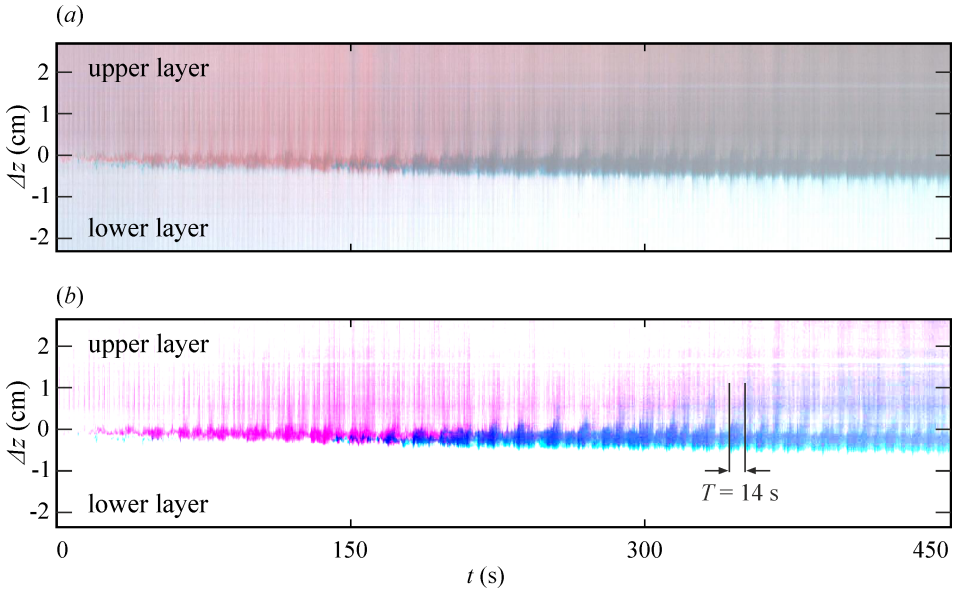

Figure 5.43: Times series of a vertical line of pixels in (a) real colour and (b) false colour, at $\Omega = 2.75\,\mathrm{rad\,s^{-1}}$.

We compare the period evaluated by the top and lateral view of the dye spreading at the interface with the best-fit of the period of the interface distortions for $r > 2$ cm, $12\pi/\Omega$, shown in figure 5.29. The results seem to be fairly consistent.

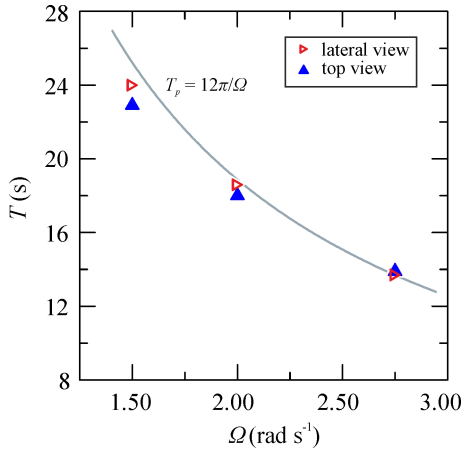

Figure 5.44: Period of the interfacial waves as function of Ω.

5.7 A model for salt transport across the density interface

Figure 5.45 shows a series of enlarged shadowgraph pictures of a restricted region across the density interface. The eight pictures are extracted with a time step of 0.2 s from a video of the experiment 7 of table 4.2, with $\Omega = 2.50\,\mathrm{rad\,s^{-1}}$ and $S_0 = 14\%$ and an initially two-layer stratification. The experiment was performed in Cambridge, using the tank in Bullard Laboratories. The shadow-graph technique is obtained by horizontally illuminating the tank with a Kodak carousel slide projector, positioned at a distance of approximately 2 m from the outer cylinder. Interfaces and any other density disturbances change the refractive index and project shadows onto the white surface of the inner cylinder.

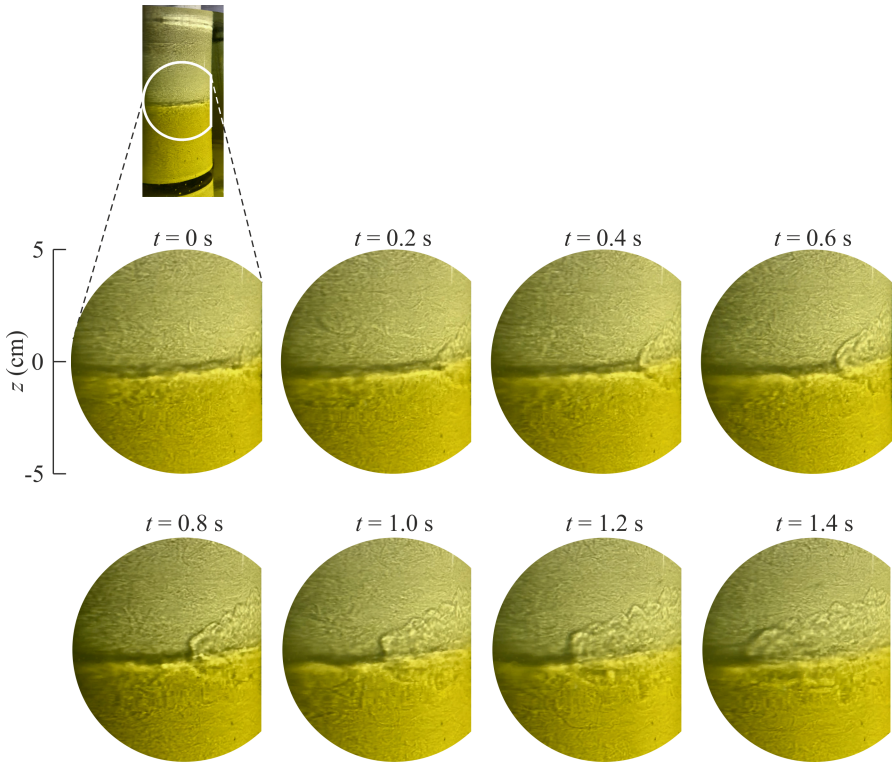

Figure 5.45: Shadowgraph pictures of a wake propagating at the density interface, taken at a time interval of 0.2 s, at $\Omega = 2.50\,\mathrm{rad\,s^{-1}}$.

From figure 5.45 we can clearly see a wave-like signal traveling clock-

wise, following the rotation of the inner cylinder, apparently propagating symmetrically in the top and bottom layers. As the wave passes by, the interface is disturbed and a strong mixing occurs between the two fronts of the wake, where shadows are thicker. This perturbation is similar to the wake following the breaking region just below the free surface, characterized by entrainment of lighter fluid (air) into denser fluid (water) (Peregrine and Svendsen, 1978; Battjes and Sakai, 1981). Similar structures were observed for the same Taylor-Couette tank by Oglethorpe (2014). We also observed these structures in the Taylor-Couette tank used in Parma and described in section 3.2, but the metallic inner cylinder reflected most of the light shed by the projector, making it difficult to obtain high-quality images.

A quite similar perspective can be gained in time domain, from a time series of a vertical line of pixels, shown in figure 5.46*a*. Figure 5.46 refers to the same experiment shown in figure 5.45. In figure 5.46*b* we highlight the linear expansion of the top and bottom fronts of the wake with dashed lines. The speed of the front expansion is $0.7\,\mathrm{cm\,s^{-1}}$. The thickness of the wake, $\delta(t)$, is defined as the distance between the two fronts and seems to linearly increase with time, analogously to the turbulent mixing layer growing between two fluids of different mass density and velocity described by (Brown and Roshko, 1974). Both the fronts are visible for the whole period T_p, when the wake has completed a cycle. After a period T_p, the top front appears to be reflected by the free surface or maybe interacts with density layers propagating from the top buoyancy source. The mixing region, which mainly contributes to the diffusion of salt, is characterized by a higher number of eddies and hence shadows, and lasts for a fraction of the period of the wave-like signal αT_p, with $\alpha \approx 0.4$. We define α as the time between the nose of the wake (which appears at 4 s in figure 5.46*a*) and the time at which the interface gets darker again after disruption (which happens at 12.4 s), as a fraction of the period T_p of the wake. Our result is similar to the value of $\alpha \approx 0.36$ found by Oglethorpe (2014). At the nose of the wake and within the mixing region, the shadow of the density interface also appears weaker, as a consequence of the diffusive mixing and small variation in light intensity. When the mixing event is over, the shadow of the interface becomes darker again. As also observed by Oglethorpe (2014), although turbulent eddies are not able to penetrate the stable density interface, they can scour partially mixed fluid from both sides of the interface.

The periodicity of the disturbances generates intermittency with a sequence of intense and low diffusion events. The wake can then be considered as a trigger for turbulence that spreads in both layers, just like a surface roller in coastal environments (Peregrine and Svendsen, 1978). As the pe-

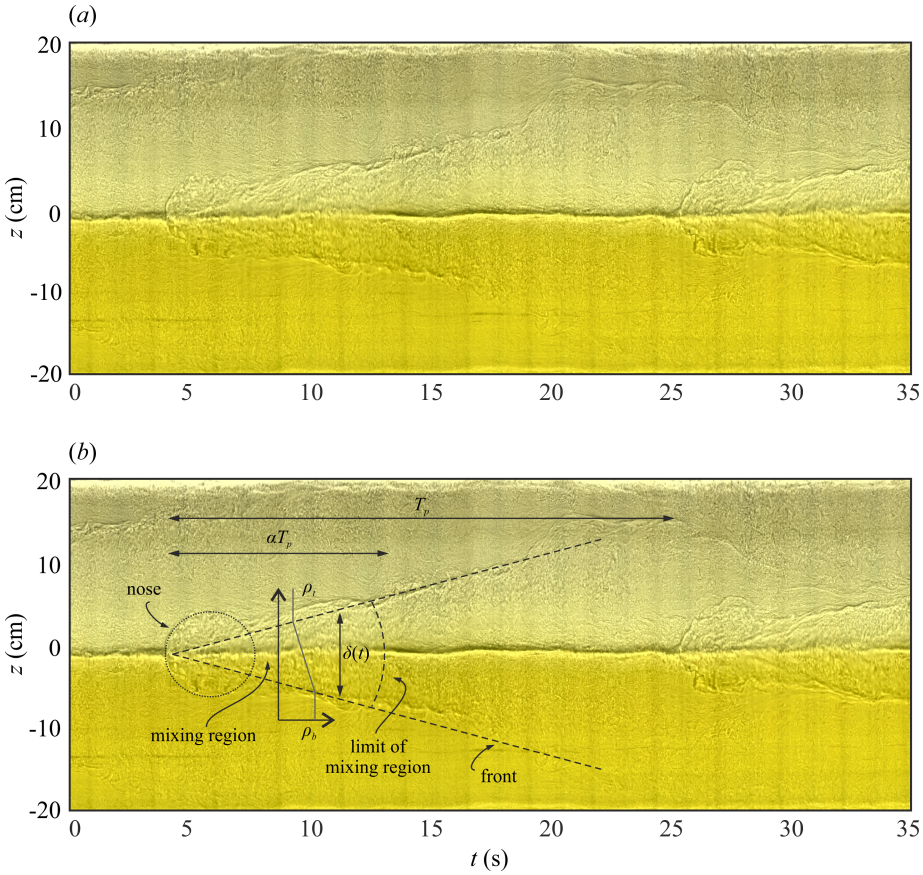

Figure 5.46: (*a*) Time series of a vertical line of pixels showing the evolution of the wake expanding from the interface; (*b*) sketch of the main features of the wake and schematic for the salt transport model. The slightly different colours indicate the two layers, the dark horizontal band is the interface as evidenced by refraction of the collimated light. Experiment at $\Omega = 2.50\ \mathrm{rad\,s^{-1}}$.

riod of the wake decreases (and the frequency increases) with rotation rate, the vertical transport of buoyancy also increases with rotation rate.

As the wake enhances mixing, we assume that the top and bottom layer are well-mixed far from the wake, while the fluid inside the mixing region has a linear density gradient equal to $(\rho_t - \rho_b)/\delta(t)$, with ρ_t and ρ_b the density of the top and bottom layer in steady state, see figure 5.46*b*. In the mixing region, the correlation between density and vertical velocity fluctuations can

then be expressed as a function of the salt diffusivity $\mathcal{D}(t)$:

$$\overline{\rho' w'}(t) = -\mathcal{D}(t)\frac{\rho_t - \rho_b}{\delta(t)}. \tag{5.23}$$

Considering that the mixing event lasts $\alpha\, T_p$, we can then estimate the time averaged vertical buoyancy flux over a cycle, per unit cross area, A:

$$\frac{1}{T_p}\int_{t_0}^{t_0+\alpha T_p} \frac{g}{\rho_0}\overline{\rho' w'}(t)\mathrm{d}t = -\frac{1}{T_p}\int_{t_0}^{t_0+\alpha T_p} \frac{g}{\rho_0}\mathcal{D}(t)\frac{\rho_t - \rho_b}{\delta(t)}\mathrm{d}t \equiv \frac{B_{to}}{A}. \tag{5.24}$$

We then model the diffusivity as the product of a length scale, equal to the thickness of the mixing region, $\delta(t)$, and a velocity scale, c, equal to the celerity of the waves at the interface, obtained by the cross-correlation of the interface distortions and already discusses in section 5.5.5:

$$\mathcal{D}(t) = k\delta(t)c, \tag{5.25}$$

where k is a non-dimensional coefficient that may include information about the aspect ratio and other geometrical parameters of the experimental set-up. We can then solve the integral of equation 5.24 to obtain

$$k\alpha = \frac{B_{to}\rho_0}{A\,(\rho_r - \rho_t)\,cg} = \frac{F_{to}}{A\,(\rho_r - \rho_t)\,c}, \tag{5.26}$$

where $F_{to} = B_{to}\rho_0/g$ is the salt flux collected by top sink, measured as salt mass per unit of time. The experimental value of $k\alpha$ is shown as a function of Ω in figure 5.47. Assuming that the fraction of the period interested by the mixing region α is constant with Ω, we find that also k does not depend on rotation rate and results $k = 3.5\times10^{-3}$. The Schmidt number, defined as $Sc = \nu_T/\mathcal{D}$, where ν_T is the momentum eddy diffusivity and $\mathcal{D}$ the density diffusivity, has a significant impact on the layer formation, diffusion and on the values of Ri_f (Leclercq et al., 2016a,b). When the spreading rate of density is greater than velocity, as it occurs in shear layers between helium and nitrogen, mass and momentum are diffused much differently and Sc is less than 1 (Brown and Roshko, 1974). In contrast, in water environments, where the molecular diffusivity $\mathcal{D}$ is small, Sc tends to be much greater than 1 (Variano and Cowen, 2013). If we assume $Sc = 1$ for simplicity, or not much different from unity, the empirical coefficient of proportionality for diffusion of momentum $k_T = k_\rho = 3.5\times10^{-3}$, slightly less than the Prandtl coefficient $k_{T,Prandtl} = 0.01$ (Prandtl, 1942), for plane mixing layers. The reason for this difference could stand in the choice of the velocity scale,

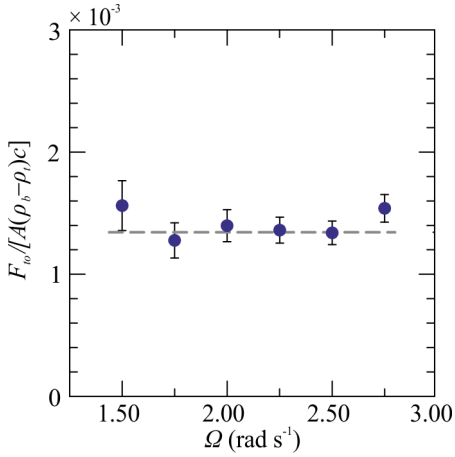

Figure 5.47: $k\alpha$ as a function of Ω.

which could be better represented by the defect of velocity in the mixing layer, than the celerity of the wake. We also have neglected the entrainment and the region of the nose, characterized by a more complex scenario. The wake could be also non homogeneous in the radial direction.

5.8 Conclusions

In this chapter we have looked at the density and velocity field in a two-layer turbulent Taylor-Couette flow. The density was measured by a conductivity probe continuously in time along the vertical direction, while the velocity in the vertical, radial and azimuthal direction was recorded by a series of UVP probes. As the density difference between the two layers would have reduced in time due to a vertical transport of salt (Woods et al., 2010; Petrolo and Woods, 2019), we stabilized the interface by a source of fresh water at the top and a source of saline water at the bottom of the tank and at the same time we withdrew the same volume flux as supplied by two sinks positioned at the same depth of the respective sources. All the measurements were made in the steady state condition. In this chapter we also looked in detail at the visible mechanisms that are responsible for mixing at the interface.

The time averaged radial velocity field shows some recirculation cells with a length scale equal to the gap of the cell and a mean value of $1.0\,\mathrm{cm\,s^{-1}}$, while instantaneously a larger number of the recirculation cells are present with velocity up to $3.0\,\mathrm{cm\,s^{-1}}$. On the other hand, the vertical velocity field shows an intense exchange of fluid close to the inner cylinder at the density

interface and a net upward flux at the bottom of the cell. The averaged TKE increases with Ω and the turbulent field becomes more isotropic. However, the TKE is non uniform in the radial direction and generally higher close to the rotating inner cylinder. At the density interface the TKE is abruptly damped.

We then focused our attention on the density interface, where different unique mechanisms are observed. Firstly, more detailed measurements of the vertical velocity and density field show a reduction of the vertical velocity fluctuations $\left|\overline{w'}\right|$ which is the cause of the decrease of the TKE at the interface, and an increase of density fluctuations $\left|\overline{\rho'}\right|$. The correlation $\overline{\rho' w'}$ is almost null in the interior of both layers and has a peak at the interface, and the vertically averaged value is a good approximation of the vertical buoyancy flux per unit area measured at the top of the tank. The quadrant analysis in the middle of the gap confirms that the main contributes to the total buoyancy flux are diffusive and comes from quadrant Q1 ($\rho' > 0$, $w' > 0$) below the interface and from quadrant Q3 ($\rho' < 0$, $w' < 0$) above the interface. Therefore, the mixing mechanisms at the interface involve the displacement of lighter fluid from the top layer downward and denser fluid from the bottom layer upward, as we have previously noticed in the time averaged vertical velocity field. By means of the autocorrelation function, we estimated the turbulent length scale, which are strongly reduced in the vertical, as already mentioned by other researchers. This is probably the consequence of the density interface which acts like a rigid boundary for the colliding turbulent eddies. However, the energy that is supposed to be transferred to the horizontal scales does not involve an increase in the radial and azimuthal length scales in our experiments.

We also used a twin-wire conductivity probe to measure the equivalent level of the density interface over time. We observed that the signal exhibits a periodicity and the zero-(up)crossing analysis reveals that the wave height increases with Ω up to $H \approx 0.8$ cm for $\Omega = 2.75\,\mathrm{rad\,s^{-1}}$, while the peak period follows the form $12\pi/\Omega$, slightly larger than the estimate $9.75\pi/\Omega$ by Oglethorpe (2014). The potential energy of the density interface distortions is only a few percent of the total missing kinetic energy $\mathcal{K}_T$ which represents the TKE that would have been in the absence of the density interface. Further analysis is needed to explain how the remainder $\mathcal{K}_T$ is converted (it may be transferred to the mean motion with an inverse cascade process, feeding coherent structures different from the analyzed one, see Pouquet et al. (2013)). In addition, we found that $\mathcal{K}_T$ disappears at $\Omega \approx 3.00\,\mathrm{rad\,s^{-1}}$, when the density difference between the two layers become so small that the interface is overturned by the turbulent eddies and the fluid evolves towards

a linear stratification. This could also be a consequence of a resonance between the coherent structures and the interfacial perturbations which seem to approach the same celerity at $\Omega \approx 3.00\,\mathrm{rad\,s^{-1}}$.

In order to visualize this periodic signal at the interface, we injected some dye and recorded some videos from the top and lateral view of the tank. We found that a single wave-like perturbation travels across the interface with a period that decreases with rotation rate, with a similar trend of the interface distortions measured by the twin-wire conductivity probe. Because for low Ω, the dye radial fluctuations close the steady outer cylinder appear smaller than the ones close to the rotating inner cylinder, we infer that the perturbation originates close to R_1, and then spreads radially and azimuthally. Oglethorpe (2014) suggests that the mixing across the high shear and speed region at the interface close to the inner cylinder creates a region of mixed fluid. Parcels accumulate in the mixed fluid and do work against the radial pressure gradient in order to move radially and organize in a single wave-like periodic structure similar to an intrusive gravity current. This wave spreads outward and splashes on the outer cylinder, where the radial momentum is converted into vertical and azimuthal momentum. The mixed fluid is finally homogenized with the layers by the large scale turbulent eddies.

From the lateral shadowgraph images, the perturbations appear wave-like, spreading symmetrically in both layers. When the wake passes by, a portion of the interface seems less sharp, probably due to the diffusive intermittent mixing events that transfer salt from the bottom to the top layer and viceversa. The diffusive interface creates a weak shadow and small variation in light intensity. When Ω increases, the frequency of the mixing events increases, as the period T decreases, and mixing is enhanced. The mixing events last for a time αT, with $\alpha \approx 0.4$, similarly to the value $\alpha \approx 0.36$ found by Oglethorpe (2014). We modeled the salt transport expresses by the correlation $\overline{\rho' w'}(t)$ as the product of the salt diffusivity $\mathcal{D}(t)$ and the linear density gradient across the thickness of the wake $\delta(t)$. If we express $\mathcal{D}(t) = k\delta(t)c$, where c is the celerity of the interfacial perturbations and k a non-dimensional coefficient, we found that $k\alpha$ is independent on Ω.

Chapter 6

Conclusions and future work

The aim of this thesis was to explore the steady-state vertical buoyancy flux in a stratified turbulent Taylor-Couette flow, in order to shed light about how mixing occurs in the deep ocean.

In our experimental activity, we modeled rainfall and ice melting by supplying fresh water at the top of the tank, and we modeled dense currents released by ice formation by supplying saline fluid at the base. At the same time we vented the same volume flux as the supply from two sinks at the top and bottom of the tank, in order to simulate the global overturning ocean circulation. The vertical buoyancy flux, or dyapicnal mixing, can be associated to the sink at the top of the tank, while the sink at the base could provide a measure of the upwelling flux. The real situation is more complex than the stylized experiments, as the upwelling can be also affected by mixing. Nevertheless, the goal of this thesis was to understand how the vertical buoyancy transport evolves upon a change in the salinity of the supplied fluid, or in the turbulence intensity generated by the rotating inner cylinder.

This thesis also provided insight about mixing mechanisms occurring specifically in a two-layer fluid. Much information about visible phenomena at the density interface was retained by image analysis and videos taken from the top and lateral view of the tank.

However, different questions remained unanswered and in this chapter we will look at some direction for future work.

6.1 A short summary of the main results

In a first series of experiments, we addressed the following fundamental questions: how the vertical buoyancy flux in the deep ocean, B_{to}, may vary during iterglacial periods and upon the local intensity of the turbulence, and how B_{to} and the mixing efficiency, Γ, are related to the buoyancy frequency, N. These experiments were discussed in chapter 4.

We observed that low values of the source buoyancy flux tend to rate-limit the vertical transport of salt, and the fluid in the tank approach a nearly well mixed condition. An increase in the source buoyancy flux, which may reproduce more intense deglaciations, implies an increase in the vertical salt transport, as well as the buoyancy frequency. On the other hand, we observed that, for higher values of the source buoyancy flux, the vertical buoyancy flux is rate-limited by turbulence, is proportional to Ω^3, and matches the equivalent flux across a density interface in a two-layer or multi-layer stratification, or crossing the layers spontaneously forming in a initial linear stratification, for sufficiently high initial buoyancy frequency (Woods et al., 2010; Oglethorpe et al., 2013). We interpreted this phenomenon as a transition from a source-limited (or *unsaturated*) regime, where the turbulent transport is limited by the salinity of the bottom source and depends linearly on the stratification, to a mixing-limited (or *saturated*) regime, where the vertical transport does not depend either on the source buoyancy flux, or the steady-state buoyancy frequency, but rather on the rotation rate Ω. When the fluid is stratified, the mixing mechanism involves a series of dense layer forming at the base, gradually becoming less dense and migrating upwards or, sometimes, a series of light layer forming at the top, gradually becoming more dense and migrating downwards.

We expressed the mixing efficiency $\Gamma = b_{to}/\mathcal{E}$ as the ratio between the vertical buoyancy flux per unit cross area of the tank, b_{to}, and the mean turbulent dissipation rate, $\mathcal{E}$. In the *saturated* regime, where the fluid is strongly stratified, Γ is constant and falls in the range $\Gamma = 0.18 - 0.36$, consistently with the estimates of Osborn (1980) and consequently, independent on the Froude number $Fr = u_{rms}/(NL)$, for $Fr < 1$. The vertical flux $b_{to,max}$ is proportional to $\Omega^3 R_1^2$, and u_{rms}^3/L, so the vertical diffusivity $\mathcal{D} = b_{to,max}/N^2$ is proportional to $u_{rms}^3/\left(N^2 L\right) \equiv u_{rms} L Fr^2$. On the other hand, in the *unsaturated* regime, where the fluid is well-mixed or weakly stratified, Γ depends linearly on $1/Fr$, at least in our experimental range $1 < Fr < 10$. In this case, the vertical buoyancy flux can be expressed as $b_{to} = b_{to,max} Fr_c/Fr$, so the diffusivity $\mathcal{D}$ becomes proportional to $u_{rms}^2/N \equiv u_{rms} L Fr$. The critical Froude number is $Fr_c = 1.0 \pm 0.3$ in

our experiments.

This transition from the source-limited regime to the mixing regime suggests that in the deep ocean, where the expected Froude number falls in the range $Fr = 0.1 - 10.0$, the vertical mixing could be either limited by the salinity of the deep water flux, or by the local intensity of turbulence, if turbulence varies in space.

Moreover, the future ocean stratification may depend on the salinity of the deep dense currents. In case of strong deglaciation, when a possible stop of ice formation would prevent the release of dense currents flowing over the ocean floor, the whole ocean interior would become well-mixed and the top and bottom boundary layers would disappear. In contrast, strong glacial events would increase the density gradient and probably new density interfaces would form wherever turbulence is not intense enough.

Eventually, we should consider the role played by advection, where present, because it would support the upwelling flux if the mean velocity of the deep currents is upward, or downwelling otherwise.

In a second series of experiments, we looked in more detail at the mixing mechanisms across a density interface, using a different Taylor-Couette tank but with similar aspect ratio (i.e. the ratio between the total depth of the fluid and the gap of the tank). To this purpose, we stabilized the initial density interface with a source of fresh water in the top layer and a source of dense water in the bottom layer. If the initial density difference between the two layers is sufficiently high and the rotation rate is sufficiently low, the turbulent eddies are not able to penetrate and overturn the stable interface. We conducted experiments where we measured both the density and the velocity field, using Ultrasound Velocity Profilers. These experiments were discussed in chapter 5.

From the time averaged vertical velocity map we observed an intense exchange of fluid at the density interface and close to the inner cylinder. More detailed information of the density and vertical velocity fluctuations suggests that the mean time averaged correlation $\overline{\rho' w'}$ over a restricted region across the interface is a good approximation of the vertical buoyancy flux per unit cross area. This means that the principle mixing mechanism is diffusive and is localized at the density discontinuity. From the quadrant analysis we found that the main contributes to the vertical buoyancy flux come from upward displacements of denser parcels and downward displacements of lighter parcels of fluid.

From the density measurements we observed interfacial perturbations traveling with a peak period that follows the trend $T_p = 12\pi/\Omega$ and through

visualization experiments we deduced that these perturbations originate close to the inner cylinder, where the radial fluctuations of the dye streaks are greater. From the top view of the tank, we inferred that the fluid parcels self-organize into a single wave that spreads out radially and azimuthally causing the interface level to rise and fall periodically. From the lateral shadowgraph images, this wave appears more like a wake, with trailing edges propagating symmetrically in the top and bottom layers. Close to the leading edge of the wake, the shadow projected by the density interface to the inner cylinder appears weaker for a time approximately equal to $\alpha = 40\%$ of the period of revolution and we described this portion of the interface as the mixing region. We therefore assumed that the mixing events are intermittent and linearize the density gradient between the tailing edges of the wake, within the mixing region. As the rotation rate increases, also the frequency of the mixing events increases and the buoyancy transport is enhanced. We modeled the correlation $\overline{\rho' w'}(t) = -\mathcal{D}(t)\Delta\rho/\delta(t)$, where $\mathcal{D}(t)$ is the diffusivity, $\Delta\rho$ the density difference between the layers in steady state and δ is the thickness of the mixing region. If we express $\mathcal{D} = k\delta(t)c$, with k a non-dimensional coefficient and c is the celerity of the interfacial perturbations, we found that the value of $k\alpha$ is independent on Ω.

For sufficiently low rotation rate, the density difference between the two layers can not be penetrated by the turbulent eddies, which bump against the interface and are immediately flattened. On the other hand, for sufficiently high rotation rate, the density difference at the interface becomes small enough to be overturned and the fluid evolves toward a linear stratification. We infer that this is a consequence of a possible resonance between coherent structures of the velocity field and interfacial perturbations which approach the same propagating speed (celerity).

When a density interface is present, we also register a defect of the total turbulent kinetic energy TKE right at the interface, but this missing TKE, $\mathcal{K}_T$, is two-order of magnitude grater than the potential energy of the periodic interfacial perturbations.

6.2 Directions for future work

In this thesis we detected the presence of a wake-like structure at the density interface, originating near the inner cylinder and spreading horizontally. However, the source of this wave remains unclear. Whether is it a self-organizing process, or a non-linear instability, further analysis are needed. According to Singh et al. (2018), they are first-mode interfacial internal gravity waves, similar to the gravity waves described by Mujica

and Lathrop (2006) that develop at the free surface close to the inner cylinder. Maybe more theoretical or numerical analysis could improve the overall understanding of turbulent mixing in a layered fluid.

We also found that the mixing mechanism in a two-layer fluid is localized at the interface and it is diffusive, as the averaged correlation $\overline{\rho' w'}$ approximates the vertical buoyancy flux. However, because $\overline{\rho' w'}$ is almost null in the interior of both layers, some other non-diffusive mixing mechanisms are responsible for the vertical salt transport inside the well-mixed regions of the fluid. We could argue that, once the parcels of intermediate density are lifted up to the top layer by the turbulent eddies, they are vertically transported by advection.

Another question that immediately arises is whether the correlation $\overline{\rho' w'}$ is still adequately representative of the vertical salt transport in a linear stratified fluid, or whether diffusion is coupled with advection. We discovered that, in a linear stratified system, layers seem to form at the top or bottom boundary layer and propagate vertically, mixing with the ambient fluid. We therefore could suggest that diffusive mixing may occur along the propagating fronts, while upwelling occurs within the depth of the layer. However these layers seem to travel much faster than the conductivity probe, which profiles the fluid continuously in time. This experimental limit did not allow us to measure the height and frequency of the layer appropriately. A series of conductivity probes could be mounted at different depth of the fluid, in order to measure the depth, frequency and celerity of the layer and compare them with the celerity of the wake-like perturbations forming across a density interface. To this end, an electronic device that prevents cross-talking proves fundamental.

The third aspect that should be clarified is how the missing TKE, $\mathcal{K}_T$, is converted in a two-layer fluid, as only a few percent of $\mathcal{K}_T$ seems to be transformed into potential energy through interfacial distortions. It could be interesting to investigate how the TKE is distributed in a linearly stratified system and compare it with the present analysis (may it be transferred to the mean motion with an inverse cascade process, feeding coherent structures different from the analyzed one? See Pouquet et al. (2013)).

Furthermore, a temperature gradient could be applied to the system by heating the fluid from below, in order to explore how the vertical buoyancy flux and buoyancy frequency could be influenced in steady-state. It would be intriguing to check whether there would still be two different rate-limiting regimes for the vertical salt and heat transport, and the conditions, if any, where the buoyancy flux still matches the flux across a density interface in a two-layer or multi-layer fluid, or across the interfaces forming in an initially

linear stratified fluid found by Woods et al. (2010); Oglethorpe et al. (2013).

We could also insert a vertical grid inside the Taylor-Couette in order to understand if and how the macro length scales could be affected.

Finally, we should say that, in literature, most of the experimental set-ups had a fixed outer cylinder (Woods et al., 2010; Oglethorpe et al., 2013; Petrolo and Woods, 2019). We suggest to let the outer cylinder counter-rotate with respect to the inner cylinder, or eventually, let the inner cylinder rotate only in the top (or bottom) half of the water column in order to generate non uniform turbulence along the vertical axis. In another possible scenario, we could generate turbulence only in the top and bottom boundary layers and keep the inner cylinder fixed in the interior of the fluid. In this way, we could simulate the stagnant ocean interior, the top turbulent boundary layer and the bottom turbulent continental shelves.

Bibliography

M.H. Alford, J.B. Girton, G. Voet, G.S. Carter, J.B. Mickett, and J.M. Klymak. Turbulent mixing and hydraulic control of abyssal water in the samoan passage. *Geophysical Research Letters*, 40(17):4668–4674, 2013. (Not cited.)

N.J. Balmforth, S.G.L. Smith, and W.R. Young. Dynamics of interfaces and layers in a stratified turbulent fluid. *Journal of Fluid Mechanics*, 355:329–358, 1998. (Not cited.)

J.A. Battjes and T. Sakai. Velocity field in a steady breaker. *Journal of Fluid Mechanics*, 111:421–437, 1981. (Not cited.)

B.M. Boubnov, E.B. Gledzer, and E.J. Hopfinger. Stratified circular couette flow: instability and flow regimes. *Journal of Fluid Mechanics*, 292:333–358, 1995. (Not cited.)

B.M. Boubnov, E.B. Gledzer, E.J. Hopfinger, and P. Orlandi. Layer formation and transitions in stratified circular couette flow. *Dynamics of Atmospheres and Oceans*, 23(1-4):139–153, 1996. (Not cited.)

D.A. Briggs, J.H. Ferziger, J.R. Koseff, and S.G. Monismith. Entrainment in a shear-free turbulent mixing layer. *Journal of Fluid Mechanics*, 310: 215–241, 1996. (Not cited.)

D.A. Briggs, J.H. Ferziger, J.R. Koseff, and S.G. Monismith. Turbulent mixing in a shear-free stably stratified two-layer fluid. *Journal of Fluid Mechanics*, 354:175–208, 1998. (Not cited.)

G.L. Brown and A. Roshko. On density effects and large structure in turbulent mixing layers. *Journal of Fluid Mechanics*, 64(4):775–816, 1974. (Not cited.)

M.J. Burin, H. Ji, E. Schartman, R. Cutler, P. Heitzenroeder, W. Liu, L. Morris, and S. Raftopolous. Reduction of ekman circulation within taylor-couette flow. *Experiments in Fluids*, 40(6):962–966, 2006. (Not cited.)

M. Carminati and P. Luzzatto-Fegiz. Conduino: affordable and high-resolution multichannel water conductivity sensor using micro usb connectors. *Sensors and Actuators B: Chemical*, 251:1034–1041, 2017. (Not cited.)

L.H.N. Cooper. Stratification in the deep ocean. *Science Progress (1933-)*, pages 73–90, 1967. (Not cited.)

P.F. Crapper and P.F. Linden. The structure of turbulent density interfaces. *Journal of Fluid Mechanics*, 65(1):45–63, 1974. (Not cited.)

C. De Boyer Montégut, G. Madec, A.S. Fischer, A. Lazar, and D. Iudicone. Mixed layer depth over the global ocean: An examination of profile data and a profile-based climatology. *Journal of Geophysical Research: Oceans*, 109(C12), 2004. (Not cited.)

S. Dong. Direct numerical simulation of turbulent taylor–couette flow. *Journal of Fluid Mechanics*, 587:373–393, 2007. (Not cited.)

S. Dong. Turbulent flow between counter-rotating concentric cylinders: a direct numerical simulation study. *Journal of Fluid Mechanics*, 615:371–399, 2008. (Not cited.)

R.J. Donnelly and K.W. Schwarz. Experiments on the stability of viscous flow between rotating cylinders-vi. finite-amplitude experiments. *Proceedings of the Royal Society of London. Series A. Mathematical and Physical Sciences*, 283(1395):531–556, 1965. (Not cited.)

G.D. Egbert and R.D. Ray. Significant dissipation of tidal energy in the deep ocean inferred from satellite altimeter data. *Nature*, 405(6788):775, 2000. (Not cited.)

M. Falder, N.J. White, and C.P. Caulfield. Seismic imaging of rapid onset of stratified turbulence in the south atlantic ocean. *Journal of Physical Oceanography*, 46(4):1023–1044, 2016. (Not cited.)

H.J.S. Fernando. Turbulent mixing in stratified fluids. *Annual Review of Fluid Mechanics*, 23(1):455–493, 1991. (Not cited.)

H.J.S. Fernando and R.R. Long. On the nature of the entrainment interface of a two-layer fluid subjected to zero-mean-shear turbulence. *Journal of Fluid Mechanics*, 151:21–53, 1985. (Not cited.)

H.J.S. Fernando and R.R. Long. Experiments on steady buoyancy transfer through turbulent fluid layers separated by density interfaces. *Dynamics of Atmospheres and Oceans*, 12(3-4):233–257, 1988. (Not cited.)

R. Ferrari. Oceanography: What goes down must come up. *Nature*, 513 (7517):179, 2014. (Not cited.)

R. Ferrari, A. Mashayek, T.J. McDougall, M. Nikurashin, and J.M. Campin. Turning ocean mixing upside down. *Journal of Physical Oceanography*, 46(7):2239–2261, 2016. (Not cited.)

E. Guyez, J.B. Flor, and E.J. Hopfinger. Turbulent mixing at a stable density interface: the variation of the buoyancy flux–gradient relation. *Journal of Fluid Mechanics*, 577:127–136, 2007. (Not cited.)

I.A. Hannoun, H.J.S. Fernando, and E.J. List. Turbulence structure near a sharp density interface. *Journal of Fluid Mechanics*, 189:189–209, 1988. (Not cited.)

J.M. Holford and P.F. Linden. Turbulent mixing in a stratified fluid. *Dynamics of Atmospheres and Oceans*, 30(2-4):173–198, 1999. (Not cited.)

G.O. Hughes. *Aspects of mixing in stratified flows*. PhD thesis, University of Cambridge, 1996. (Not cited.)

H. Jeffreys. On fluid motions produced by differences of temperature and humidity. *Quarterly Journal of the Royal Meteorological Society*, 51(216): 347–356, 1925. (Not cited.)

D. Kang and E.N. Curchitser. Energetics of eddy–mean flow interactions in the gulf stream region. *Journal of Physical Oceanography*, 45(4):1103–1120, 2015. (Not cited.)

A.B. Kara, P.A. Rochford, and H.E. Hurlburt. Mixed layer depth variability over the global ocean. *Journal of Geophysical Research: Oceans*, 108(C3), 2003. (Not cited.)

H. Kato and O.M. Phillips. On the penetration of a turbulent layer into stratified fluid. *Journal of Fluid Mechanics*, 37(4):643–655, 1969. (Not cited.)

E.L. Koschmieder. *Bénard cells and Taylor vortices*. Cambridge University Press, 1993. (Not cited.)

T. Kuhlbrodt, A. Griesel, M. Montoya, A. Levermann, M. Hofmann, and S. Rahmstorf. On the driving processes of the atlantic meridional overturning circulation. *Reviews of Geophysics*, 45(2), 2007. (Not cited.)

C. Leclercq, J.L. Partridge, P. Augier, C.P. Caulfield, S.B. Dalziel, and P.F. Linden. Nonlinear waves in stratified taylor–couette flow. part 1. layer formation. *arXiv preprint arXiv:1609.02885*, 2016a. (Not cited.)

C. Leclercq, J.L. Partridge, C.P. Caulfield, S.B. Dalziel, and P.F. Linden. Nonlinear waves in stratified taylor–couette flow. part 2. buoyancy flux. *arXiv preprint arXiv:1609.02886*, 2016b. (Not cited.)

G.S. Lewis and H.L. Swinney. Velocity structure functions, scaling, and transitions in high-reynolds-number couette-taylor flow. *Physical Review E*, 59(5):5457, 1999. (Not cited.)

P.F. Linden. Mixing in stratified fluids. *Geophysical & Astrophysical Fluid Dynamics*, 13(1):3–23, 1979. (Not cited.)

P.F. Linden. Mixing across a density interface produced by grid turbulence. *Journal of Fluid Mechanics*, 100(4):691–703, 1980. (Not cited.)

I. Lozovatsky, J.H. Lee, H.J.S. Fernando, S.K. Kang, and S.U.P. Jinadasa. Turbulence in the east china sea: the summertime stratification. *Journal of Geophysical Research: Oceans*, 120(3):1856–1871, 2015. (Not cited.)

R. Lumpkin and K. Speer. Global ocean meridional overturning. *Journal of Physical Oceanography*, 37(10):2550–2562, 2007. (Not cited.)

K.V. Mackenzie. Nine-term equation for sound speed in the oceans. *The Journal of the Acoustical Society of America*, 70(3):807–812, 1981. (Not cited.)

A. Maffioli, G. Brethouwer, and E. Lindborg. Mixing efficiency in stratified turbulence. *Journal of Fluid Mechanics*, 794, 2016. (Not cited.)

J. Marshall and K. Speer. Closure of the meridional overturning circulation through southern ocean upwelling. *Nature Geoscience*, 5(3):171, 2012. (Not cited.)

A. Mashayek, R. Ferrari, S. Merrifield, J.R. Ledwell, L. St Laurent, and A.N. Garabato. Topographic enhancement of vertical turbulent mixing in the southern ocean. *Nature Communications*, 8:14197, 2017. (Not cited.)

N. Mujica and D.P. Lathrop. Hysteretic gravity-wave bifurcation in a highly turbulent swirling flow. *Journal of Fluid Mechanics*, 551:49–62, 2006. (Not cited.)

W. Munk and C. Wunsch. Abyssal recipes ii: Energetics of tidal and wind mixing. *Deep Sea Research Part I: Oceanographic Research Papers*, 45 (12):1977–2010, 1998. (Not cited.)

W.H. Munk. Abyssal recipes. In *Deep Sea Research and Oceanographic Abstracts*, volume 13, pages 707–730. Elsevier, 1966. (Not cited.)

M. Nikurashin and G. Vallis. A theory of deep stratification and overturning circulation in the ocean. *Journal of Physical Oceanography*, 41(3):485–502, 2011. (Not cited.)

R.L.F. Oglethorpe. *Mixing in stably stratified turbulent Taylor-Couette flow.* PhD thesis, University of Cambridge, 2014. (Not cited.)

R.L.F. Oglethorpe, C.P. Caulfield, and A.W. Woods. Spontaneous layering in stratified turbulent taylor–couette flow. *Journal of Fluid Mechanics*, 721, 2013. (Not cited.)

T.R. Osborn. Estimates of the local rate of vertical diffusion from dissipation measurements. *Journal of Physical Oceanography*, 10(1):83–89, 1980. (Not cited.)

R.K. Pachauri, M.R. Allen, V.R. Barros, J. Broome, W. Cramer, R. Christ, J.A. Church, L. Clarke, Q. Dahe, P. Dasgupta, N.K. Dubash, O. Edenhofer, I. Elgizouli, C.B. Field, P. Forster, P. Friedlingstein, J. Fuglestvedt, L. Gomez-Echeverri, S. Hallegatte, G. Hegerl, M. Howden, K. Jiang, B. Jimenez Cisneroz, V. Kattsov, H. Lee, K.J. Mach, J. Marotzke, M.D. Mastrandrea, L. Meyer, J. Minx, Y. Mulugetta, K. O'Brien, M. Oppenheimer, J.J. Pereira, R. Pichs-Madruga, G.-K. Plattner, Hans-Otto Prtner, S.B. Power, B. Preston, N.H. Ravindranath, A. Reisinger, K. Riahi, M. Rusticucci, R. Scholes, K. Seyboth, Y. Sokona, R. Stavins, T. F. Stocker, P. Tschakert, D. Van Vuuren, and J.-P. van Ypserle. *Climate change 2014: synthesis report. Contribution of Working Groups I, II and III to the fifth assessment report of the Intergovernmental Panel on Climate Change.* Ipcc, 2014. (Not cited.)

Y.G. Park, J.A. Whitehead, and A. Gnanadeskian. Turbulent mixing in stratified fluids: layer formation and energetics. *Journal of Fluid Mechanics*, 279:279–311, 1994. (Not cited.)

D.H. Peregrine and I.A. Svendsen. *Spilling Breakers, Bores, and Hydraulic Jumps*, chapter 30, pages 540–550. 1978. (Not cited.)

D. Petrolo and A.W. Woods. Measurements of buoyancy flux in a stratified turbulent flow. *Journal of Fluid Mechanics*, 861, 2019. (Not cited.)

O.M. Phillips. Turbulence in a strongly stratified fluidis it unstable? In *Deep Sea Research and Oceanographic Abstracts*, volume 19, pages 79–81. Elsevier, 1972. (Not cited.)

E.S. Posmentier. The generation of salinity finestructure by vertical diffusion. *Journal of Physical Oceanography*, 7(2):298–300, 1977. (Not cited.)

Annick Pouquet, A Sen, D Rosenberg, Pablo Daniel Mininni, and J Baerenzung. Inverse cascades in turbulence and the case of rotating flows. *Physica Scripta*, 2013(T155):014032, 2013. (Not cited.)

L. Prandtl. Bemerkungen zur theorie der freien turbulenz. *ZAMM-Journal of Applied Mathematics and Mechanics/Zeitschrift für Angewandte Mathematik und Mechanik*, 22(5):241–243, 1942. (Not cited.)

S. Rahmstorf. Rapid climate transitions in a coupled ocean–atmosphere model. *Nature*, 372(6501):82, 1994. (Not cited.)

S. Rahmstorf. Thermohaline ocean circulation. encyclopedia of quaternary sciences. *Postdam Institute for Climate Impact Research*, 5, 2006. (Not cited.)

A. Randelhoff, I. Fer, and A. Sundfjord. Turbulent upper-ocean mixing affected by meltwater layers during arctic summer. *Journal of Physical Oceanography*, 47(4):835–853, 2017. (Not cited.)

C.R. Rehmann and J.R. Koseff. Mean potential energy change in stratified grid turbulence. *Dynamics of Atmospheres and Oceans*, 37(4):271–294, 2004. (Not cited.)

C.M. Risien and D.B. Chelton. A global climatology of surface wind and wind stress fields from eight years of quikscat scatterometer data. *Journal of Physical Oceanography*, 38(11):2379–2413, 2008. (Not cited.)

P.H. Roberts. The solution of the characteristic value problems (appendix of experiments on the stability of viscous flow between rotating cylinders by r.j. donnelly and k.w. schwartz). *Proceedings of the Royal Society of London. Series A*, 283:550, 1965. (Not cited.)

B.R. Ruddick, T.J. McDougall, and J.S. Turner. The formation of layers in a uniformly stirred density gradient. *Deep Sea Research Part A. Oceanographic Research Papers*, 36(4):597–609, 1989. (Not cited.)

J.W. Sandström. *Dynamische versuche mit meerwasser*, volume 36. Annalen der Hydrographie und Maritimen Meteorologie, 1908. (Not cited.)

W.J. Schmitz. On the interbasin-scale thermohaline circulation. *Reviews of Geophysics*, 33(2):151–173, 1995. (Not cited.)

K.L. Sheen, N.J. White, and R.W. Hobbs. Estimating mixing rates from seismic images of oceanic structure. *Geophysical Research Letters*, 36(24), 2009. (Not cited.)

K.N. Singh, P. Augier, C.P. Caulfield, S.B. Dalziel, C. Leclercq, and J.L. Partridge. Layering, instability, mixing, interfaces and turbulence in a stratified Taylor-Couette flow. In *International Conference on Rayleigh-Bénard Turbulence, Enschede, The Netherlands*, 2018. (Not cited.)

M. Sparrow, P. Chapman, and J. Gould. The world ocean circulation experiment (woce) hydrographic atlas series. *Southampton, UK: International WOCE Project Office*, 2005. (Not cited.)

U. Stefánsson and F.A. Richards. Distributions of dissolved oxygen, density, and nutrients off the washington and oregon coasts. In *Deep Sea Research and Oceanographic Abstracts*, volume 11, page 353. Elsevier, 1964. (Not cited.)

R.I. Tait and M.R. Howe. Some observations of thermo-haline stratification in the deep ocean. In *Deep Sea Research and Oceanographic Abstracts*, volume 15, pages 275–280. Elsevier, 1968. (Not cited.)

L.D. Talley. Closure of the global overturning circulation through the indian, pacific, and southern oceans: Schematics and transports. *Oceanography*, 26(1):80–97, 2013. (Not cited.)

G.I. Taylor. Stability of a viscous liquid contained between two rotating cylinders. *Philosophical Transactions of the Royal Society of London. A*, 233(605-615):289–343, 1923. (Not cited.)

H. Tennekes and J.L. Lumley. *A first course in turbulence*. MIT press, 1972. (Not cited.)

S.A. Thorpe. Experiments on instability and turbulence in a stratified shear flow. *Journal of Fluid Mechanics*, 61(4):731–751, 1973. (Not cited.)

S.A. Thorpe. Layers and internal waves in uniformly stratified fluids stirred by vertical grids. *Journal of Fluid Mechanics*, 793:380–413, 2016. (Not cited.)

J.R. Toggweiler and J. Russell. Ocean circulation in a warming climate. *Nature*, 451(7176):286, 2008. (Not cited.)

C.D. Troy and J.R. Koseff. The generation and quantitative visualization of breaking internal waves. *Experiments in Fluids*, 38(5):549–562, 2005. (Not cited.)

J.S. Turner. The coupled turbulent transports of salt and and heat across a sharp density interface. *International Journal of Heat and Mass Transfer*, 8(5):759–767, 1965. (Not cited.)

J.S. Turner. The influence of molecular diffusivity on turbulent entrainment across a density interface. *Journal of Fluid Mechanics*, 33(4):639–656, 1968. (Not cited.)

J.S. Turner and H. Stommel. A new case of convection in the presence of combined vertical salinity and temperature gradients. *Proceedings of the National Academy of Sciences*, 52(1):49–53, 1964. (Not cited.)

E. A. Variano and E. A. Cowen. Turbulent transport of a high-Schmidt-number scalar near an air–water interface. *Journal of Fluid Mechanics*, 731:259–287, 2013. (Not cited.)

A.F. Waterhouse, J.A. MacKinnon, J.D. Nash, M.H. Alford, E. Kunze, H.L. Simmons, K.L. Polzin, L.C. St. Laurent, O.M. Sun, R. Pinkel, L.D. Talley, C.B. Whalen, T.N. Huussen, G.S. Carter, I. Fer, S. Waterman, A.C. Naveira Garabato, T.B. Sanford, and C.M. Lee. Global patterns of diapycnal mixing from measurements of the turbulent dissipation rate. *Journal of Physical Oceanography*, 44(7):1854–1872, 2014. (Not cited.)

F. Wessels and K. Hutter. Interaction of internal waves with a topographic sill in a two-layered fluid. *Journal of Physical Oceanography*, 26(1):5–20, 1996. (Not cited.)

J.A. Whitehead and I. Stevenson. Turbulent mixing of two-layer stratified fluid. *Physics of Fluids*, 19(12):125104, 2007. (Not cited.)

E.J. Wolanski and L.M. Brush Jr. Turbulent entrainment across stable density step structures. *Tellus*, 27(3):259–268, 1975. (Not cited.)

A.W. Woods, C.P. Caulfield, J.R. Landel, and A. Kuesters. Non-invasive turbulent mixing across a density interface in a turbulent taylor–couette flow. *Journal of Fluid Mechanics*, 663:347–357, 2010. (Not cited.)

C. Wunsch and R. Ferrari. Vertical mixing, energy, and the general circulation of the oceans. *Annual Review of Fluid Mechanics*, 36:281–314, 2004. (Not cited.)

Y. Zellouf, P. Dupont, and H. Peerhossaini. Heat and mass fluxes across density interfaces in a grid-generated turbulence. *International Journal of Heat and Mass Transfer*, 48:3722–3735, 2005. (Not cited.)